The Pennsylvania State University
The Graduate School
College of Engineering

INVESTIGATION OF LASER-SUSTAINED PLASMA AND THE ROLE OF PLASMA IN CARBON DIOXIDE LASER NITRIDING OF TITANIUM

A Dissertation in
Engineering Science
by
Abdalla Ramadan Nassar

© 2012 Abdalla Ramadan Nassar

Submitted in Partial Fulfillment
of the Requirements
for the Degree of

Doctor of Philosophy

December 2012

The dissertation of Abdalla Ramadan Nassar was reviewed and approved* by the following:

Judith A. Todd
P. B. Breneman Department Head of Engineering Science and Mechanics
Dissertation Advisor, Chair of Committee

Stephen M. Copley
Senior Scientist, Applied Research Laboratory

John D. Mathews
Professor of Electrical Engineering

Albert E. Segall
Professor of Engineering Science and Mechanics
Engineering Science and Mechanics Graduate Officer

Vladimir V. Semak
Professor of Engineering Science and Mechanics

*Signatures are on file in the Graduate School.

Abstract

Applications of plasma discharges to materials processing can be seen in everything from circuit boards to drill bits. However, plasma formed near the focus of a continuous laser beam, laser-sustained plasma (LSP), has hardly been considered for materials processing applications. This despite several remarkable properties: very high maximum electron temperatures ($\sim$17,000 K); high electron densities (on the order of $10^{23}\,\mathrm{m}^{-3}$); and, the ability to be remotely moved simply by moving the focal point of the laser beam.

In this work, several aspects of LSP were investigated. The electron temperature and electron density within an argon LSP were measured. These measurements were compared to the predictions of a computational fluid dynamics model, taking into account, for the first time, the effects of different laser beam modes. A nitrogen LSP was employed to gain new insights into the role of near-surface plasma in laser nitriding of titanium, a process in which nitrogen is introduced into a melted region formed by a scanning laser beam to produce a functionally-graded, hardened layer. Employing these insights, the production of large-area, crack-free, deep and oxygen-free laser-nitrided layers was demonstrated.

The plasma temperature was measured via the relative intensities of excited atomic emission lines. This method, also known as a Boltzmann plot technique, relied on the assumption of local-thermodynamic equilibrium. The validity of this assumption was verified by measuring the spatially-resolved electron density using Stark broadening of the hydrogen-alpha emission line. However, reabsorption of plasma line emissions made temperature measurements using relative line intensities near the laser focus unreliable. That is, the region near the laser focus was found to be optically thick.

An axi-symmetric model of a LSP sustained in a flow of argon was also developed under the assumption of local-thermodynamic equilibrium. The electron temperature and total beam absorption predicted by the model compared well

with values from the literature and with the experimental results obtained using optical emission spectroscopy. The effect of several realistic laser beam modes were tested in the model using a "light pipe" technique. The validity of the technique was verified experimentally.

A major part of this work was the application of LSP to investigate laser nitriding of titnaium. Interactions of the LSP with a surface were distinguished from interactions of the laser beam with a surface under conditions where the laser beam did not result in plasma formation. By combining this approach with optical emission spectroscopy, it was possible to decouple the effect of plasma and the laser beam during nitriding of titanium. In this way, new light was shed on the role of near-surface plasma during CO_2 laser nitriding of titanium. Additionally, a new processing regime for near-stoichiometric, oxygen-free LSP nitriding of titanium was discovered.

The work presented here culminates by demonstrating large-area, crack-free and dendrite-free nitrided layers as thick as $600\,\mu$m. These layers were shown to have a hardness profile which is functionally graded. The effect of using a nitrogen-argon gas mixture, in place of pure nitrogen, on cracking, hardness, and microstructure was elucidated.

Table of Contents

List of Figures **viii**

List of Tables **xv**

Acknowledgments **xvi**

Chapter 1
Introduction **1**
1.1 Lasers in materials processing 1
1.2 Laser-sustained Plasma 2
1.3 LSP physics 4
1.3.1 Plasma at infrared and optical frequencies 5
1.3.2 Local thermodynamic equilibrium 6
1.3.3 Review of LSP research 8
1.3.4 Applications of LSP 10
1.4 Common experimental details 12
1.4.1 Characterization of the laser beam 13
1.4.2 Ignition and sustainment of LSP 14
1.5 Outline of Thesis 16

Chapter 2
Spectroscopic investigation of LSP **18**
2.1 Background and Introduction 18
2.1.1 Spectral line profile 19
2.1.2 Abel Inversion 22
2.1.3 Measurement of plasma parameters 27

2.1.3.1 Determination of temperature via relative intensities of excited atomic emission lines 27
2.1.3.2 Determination of electron density via Stark Broadening 29
2.2 Experimental setup 30
2.3 Data analysis 31
2.4 Results and Discussion 33
2.5 Conclusions 36

Chapter 3
Modeling of laser-sustained argon plasma 39
3.1 Background 40
3.2 Governing equations 42
3.3 Material Properties 42
3.3.1 Temperature-dependent properties 42
3.3.2 Properties dependent on electron density 45
3.4 Mesh and boundary conditions 48
3.5 Solution procedure 49
3.5.1 Propagation and absorption of laser power 50
3.6 Results and Discussion 53
3.6.1 Comparison with literature 53
3.6.2 Comparison with Experimental Results 55
3.6.3 Prediction of the effect of various beam modes on LSP . . . 57
3.7 Concluding Remarks 60

Chapter 4
Application of laser-sustained plasma to the nitriding of titanium 61
4.1 Laser nitriding 61
4.1.1 CO_2 Laser nitriding of titanium 64
4.2 The role of plasma in titanium nitriding 66
4.2.1 Experimental details 68
4.2.2 Results 72
4.2.3 Discussion 83
4.2.4 Conclusions 88
4.3 On the role of plasma in titanium nitriding with a nitrogen–argon gas mixtures 89
4.3.1 Experimental details 90
4.3.2 Single-trail results and analysis 91
4.3.2.1 High-speed (100–300 mm/s) nitriding using pure nitrogen 91

4.3.2.2 High-speed nitriding using a nitrogen–argon gas mixture . . . 99
4.3.2.3 Low-speed (15–75 mm/s) nitriding . . . 105
4.3.3 Conclusions . . . 108
4.4 Multi-trail nitriding of titanium . . . 111
4.4.1 Experimental details . . . 112
4.4.2 Results and discussion . . . 113
4.4.3 Conclusions . . . 126

Chapter 5
Conclusions and future work **129**
5.1 Conclusions . . . 129
5.2 Improvements and future work . . . 133

Appendix A
Calculation of excitation temperature and electron density **136**
A.1 Matlab Code: Calculating Excitation temperature via Boltzmann plot technique . . . 136
A.1.1 lines.txt . . . 146
A.2 Matlab Code: Calculating electron density via stark broadening of hydrogen-alpha line . . . 146

Appendix B
Axi-symmetric model code **156**
B.1 Header file . . . 156
B.2 C file . . . 156

Appendix C
Cross-sectional and top surface images **175**

Appendix D
Non-technical abstract **214**

Bibliography **216**

List of Figures

1.1 Plot of normalized Q mode intensity together with its subcomponents. The e-squared radius was arbitrarily defined as 30 14
1.2 Three-dimensional representation of a normalized Q mode intensity. The e-squared radius was arbitrarily defined as 30. 15
1.3 Laser beam profile measured at the focal plane. 15
1.4 Measured and expected laser beam radii. 16
1.5 Time sequence of ignition and sustainment of an argon LSP using 1.9 kW CO_2 laser beam recorded using a CCD camera with a welding filter. A tungsten ignition rod is inserted (from left to right) into the laser beam near the focus. Once ignited, the laser head moved upward and away from the ignition rod. 17

2.1 Definition of spectral terms 19
2.2 Plot of normalized Gaussian and Lorentzian profiles around 645 nm, each with a FWHM of 1 nm, and the resulting Voigt profile 22
2.3 The observed spectral radiance from a cross section of an axisymmetric plasma is a summation of the emissions along the line of observation. The z axis points into the page. 23
2.4 The test function versus the test function with noise. 26
2.5 A tenth-degree-even-powered-polynomial-sum fit and a Gaussian-second-degree-polynomial-sum fit to the noisy test function. 26
2.6 Comparison of transformations of the three methods. 27
2.7 Percent error of the three methods. The Nester-Olsen method is, by far, the least accurate. 27
2.8 Sample Boltzmann plot. The slope of the linear fit is equal to $-1/kT_{exc}$ 28
2.9 Photograph of OES collection system. 31
2.10 Measured LSP excitation temperature contours. LSP was sustained by a 1.9 kW laser in a 23.5 slpm argon gas mixture containing 0.5 % hydrogen. The color bar displays temperature in degrees Kelvin. . . 34

2.11 Measured excitation temperature without Abel inversion, as a function of radius, for every other recorded cross section. LSP was sustained by 1.9 kW laser in a 23.5 slpm argon gas mixture containing 0.5 % hydrogen. 35
2.12 Measured excitation temperature without Abel inversion, of LSP sustained by 1.9 kW laser in a 23.5 slpm argon gas mixture containing 0.5 % hydrogen. 35
2.13 Measured excitation temperature without Abel inversion, as a function of radius, for every other recorded cross section. LSP was sustained by 1.9 kW laser in a 23.5 slpm argon gas mixture containing 0.5 % hydrogen. 36
2.14 Measured electron density within LSP sustained by 1.9 kW laser in a 23.5 slpm argon gas mixture containing 0.5 % hydrogen. 37
2.15 Region of LTE within LSP according to the criterion that LTE exists where $n_e > 2.85 \times 10^{22}\,\mathrm{cm}^{-3}$ 38

3.1 Specific heat of Argon plasma according to the LTE assumption . . 43
3.2 Effective and thermal conductivity of argon LSP. 44
3.3 Argon plasma viscosity. 45
3.4 Electron density of argon plasma. 46
3.5 Inverse bremsstrahlung absorption coefficient of argon plasma. . . . 47
3.6 Sample domain with boundary conditions for LSP model. 48
3.7 Domain and mesh used for simulations using the PRC Q-mode . . . 49
3.8 Illustration of absorption within laser zone. 51
3.9 Comparison of Chen, Mazumder and Krier's [43,44] total beam absorption with model results. 54
3.10 Comparison of Chen, Mazumder and Krier's [43,44] plasma length with model results. 55
3.11 Comparison of the 11,000 K temperature contour predicted by the model with experimental results. 56
3.12 Comparison of Q-Mode total beam absorption within LSP as a function of laser power. 57
3.13 Depth profile of burns in acrylic caused by an output laser power of 1.75 kW and by the beam transmitted through an argon LSP. Little refraction of the beam was observed. 58
3.14 The effect of beam mode on LSP geometry using a 1.9 kW laser and a 5.0 m/s argon flow speed. The LSP sustained by TEM^*_{01} mode is longer and shifted further upstream than that generated by a Q-Mode. 59

3.15 The effect of beam mode on LSP geometry using a 1.9 kW laser and a 5.0 m/s argon flow speed. The LSP sustained by TEM_{00} mode is longer and shifted further upstream than that generated by a D-Mode. 59

4.1 Three different laser nitriding setups: (a) side gas nozzle; (b) coaxial gas nozzle; and, (c) enclosed chamber. Reprinted, with permission, from Xue, L., M. U. Islam, A. K. Koul, M. Bibby, and W. Wallace (1997) Materials and Manufacturing Processes, 4, pp. 25-47. [101]. . 63
4.2 "Determination of different process chains depending on the surface temperature T_i—(T_m, melting point; T_{ev}, evaporation point; α_i, absorption coeff; D_i, diffusion coeff.)". The subscripts refer to the different surface temperature ranges. Reprinted, with permission, from Höche, D. and Schaaf, P. (2011) Heat and Mass Transfer, 47(5), pp. 519-540. [120]. 64
4.3 SEM image of CO_2 laser nitrided sample showing the top surface (T), melt zone (MZ)and heat-affected zone (HAZ). Reprinted, with permission, from Mridha, S. and T. N. Baker (1991) Materials Science and Engineering: A, 142(1), pp. 115-124. [123]. 66
4.4 Experimental setup. 69
4.5 Optical spectrum, around 430 nm, recorded during processing of a titanium substrate at a translation speed of 75 mm/s and an off-focal distance of 4 mm (black) and of a three times magnified spectrum of a LSP sustained far away from any surface (dashed and grey). 70
4.6 Optical spectrum, around 870 nm, recorded during processing of a titanium substrate at a translation speed of 75 mm/s and an off-focal distance of 4 mm (black) and of a free-standing LSP sustained far away from any surface (dashed and grey). 71
4.7 Measured residual laser beam power as a function of off-focal distance. The estimated value of 1.9 kW is shown as a green, dashed line. 72
4.8 CCD images (a,b) taken during processing and surface image (c) of the processed trail at an off-focal distance of 8 mm and a translation speed of 90 mm/s with a pre-struck LSP: (a) atomic nitrogen species; (b) atomic titanium species; (c) top surface of the trail. . . 74
4.9 CCD images taken during processing (a,b) and surface image (c) of the processed trail at an off-focal distance of 8 mm and a translation speed of 10 mm/s: (a) atomic nitrogen species; (b) atomic titanium species; (c) top surface of the trail. 74

4.10 High-resolution XPS spectra from surfaces processed at an off-focal distance of 8 mm and a translation speed of (a) 90 mm/s and (b) 10 mm/s. The location and intensity of the N1s peak confirms the presence of titanium nitride in (a). 75
4.11 High-resolution XPS spectra from surfaces processed at an off-focal distance of 8 mm and a translation speed of (a) 90 mm/s and (b) 10 mm/s. The location and intensity of the O1s peak confirms greater surface oxidation in (b) than in (a). 76
4.12 XRD spectra of samples processed at an off-focal distance of 8 mm and a translation speed of 90 mm/s. No oxide phases of titanium were detected. 77
4.13 Irradiation of a stationary titanium substrate with a pre-struck nitrogen LSP, recorded using an 870 nm band pass filter. An upward shift and a dimming of the nitrogen-rich plasma region is observed with increasing vaporization of titanium. The time (sec.ms) and frame number are shown in the lower left and right, respectively, of each frame. 77
4.14 Surface images of processed trails at an off-focal distance of 8 mm and a translation speed of 90 mm/s without a pre-struck LSP: (a) top surface of the trail (3.5 kW); (b) top surface of a trail at 1.9 kW residual beam power. 78
4.15 CCD images taken during titanium nitriding at 4 mm off-focus and 90 mm/s: (a) atomic nitrogen; (b) atomic titanium; (c) top surface image. 80
4.16 A high-resolution XPS spectrum of the black nanopowder (solid line). Shifts of the Ti2p3/2 peak for TiO2, TiN_x, TiO, and Ti are noted between arrows. The two subcomponent shifts of the Ti2p3/2 peak confirm the presence of TiN_x (dotted line) and TiO_2 (dashed line). 80
4.17 TEM image of titanium nitride nanoparticles deposited at the side of some trails. 81
4.18 Cross-sectional optical images of the samples nitrided at 8 mm off-focus and 90 mm/s: (a) using a LSP; (b) without a LSP; and (c) with 1.9 kW residual laser beam power. 82
4.19 Cross-sectional image of a sample nitrided at 8 mm off-focus and 10 mm/s. 82
4.20 Schematics showing the convective flow within the melt pool: (a) low thermal diffusivity and high Prandtl number; (b) increased melt temperature and high Marangoni number. 85

4.21 Diagram of regions observed during CO_2 laser nitriding. Black nano-particulate was observed alongside trails processed within the striped region. Below the sold, black curve, oxide was observed at the surface and within the melt trail. Below the dashed, grey curve, surface-struck plasma formed during processing. Above both the black, solid and grey, dashed curves, oxygen contamination was prevented via pre-struck LSP processing. 87
4.22 Top surface images showing single-trail samples processed using nitrogen LSP as a function of off-focal position and translation speed. 92
4.23 Top surface images of single-trail samples processed using nitrogen LSP as a function using an off-focal distance of 6 mm and translation speeds of (a) 300 mm/s and (b) 150 mm/s. The decanted region and the reflective, smooth regions are labeled. (b) Black powder can be observed beyond the edges of the nitrided trail. . . . 93
4.24 Photograph, using oblique illumination, of the top surfaces of single-trail samples processed using nitrogen LSP as a function of off-focal position and translation speed. 94
4.25 Top surface images showing single-trail samples processed using CO_2 laser, without plasma formation, and nitrogen gas as a function of off-focal position and translation speed. 95
4.26 Cross-sectional micrographs of samples processed using nitrogen LSP as a function of off-focal position and translation speed. 97
4.27 Cross-sectional micrographs of samples processed using CO_2 laser and nitrogen gas, without plasma formation, as a function of off-focal position and translation speed. 98
4.28 XRD spectra of samples processed with and without prestruck-LSP, in pure nitrogen, at an off-focal distance of 8 mm and a translation speed of 200 mm/s 99
4.29 Top surface images of samples processed using a $49.2 \pm 2\,\%$ N_2–Ar LSP as a function of off-focal position and translation speed. 100
4.30 Top surface images showing single-trail samples processed using CO_2 laser, without plasma formation, and a $49.2 \pm 2\,\%$ N_2–Ar gas mixture as a function of off-focal position and translation speed. . . 101
4.31 Cross-sectional micrographs of samples processed using N_2-Ar LSP as a function of off-focal position and translation speed. 102
4.32 Cross-sectional micrographs of samples processed using CO_2 laser, without plasma formation, and N_2-Ar gas mixture as a function of off-focal position and translation speed. 103

4.33 XRD spectra of samples processed with and without prestruck-LSP, in 49.2% N_2-Ar gas mixture, at an off-focal distance of 8 mm and a translation speed of 100 mm/s 104
4.34 Optical images of top surface of LSP nitriding using $49.2 \pm 2\,\%$ nitrogen–argon mixture as a function of off-focal position and translation speed. 106
4.35 Photograph, using off–axis illumination, of the top surface of LSP nitriding using $49.2 \pm 2\,\%$ nitrogen–argon mixture at a translation speed of (a) 75 mm/s and (b) 50 mm/s. 106
4.36 Cross-sectional micrographs of LSP nitrided samples $49.2 \pm 2\,\%$ N_2-Ar mixture as a function of off-focal position and translation speed. 107
4.37 Cross-sectional image of sample processed using a $49.2 \pm 2\,\%$ N_2-Ar mixture at an off-focal distance of 8 mm and translation speed of 15 mm/s. 108
4.38 CCD images of nitrogen and argon emission lines around 870 nm as a function of processing speed and off-focal distance. 109
4.39 Illustration of the laser path during multi-trail nitriding experiments. 113
4.40 Cross-sectional micrographs of multi-trail samples processed using pure nitrogen with and without LSP as a function of off-focal position and translation speed. Cracking is clearly viable under all conditions tested. 114
4.41 Optical images of top surface of multi-trail, nitrided samples, with and without LSP, using pure nitrogen as a function of off-focal position and translation speed. Note: black areas are highly reflective gold color. 115
4.42 Optical images, with oblique illumination, of top surface of multi-trail, nitrided samples, with and without LSP, using pure nitrogen as a function of off-focal position and translation speed. 116
4.43 SEM image taken near the center of the surface processed at 8 mm OFD and a translation speed of 150 mm/s with a pre-struck nitrogen LSP. 117
4.44 Surface topography of the sample processed at 8 mm OFD and a translation speed of 150 mm/s. 118
4.45 Cross-sectional micrographs of multi-trail samples processed using a $49.2 \pm 2\,\%$ nitrogen–argon mixture, with and without LSP, as a function of off-focal position and translation speed. 118
4.46 Optical images of top surface of multi-trail samples nitride, with and without LSP, using a $49.2 \pm 2\,\%$ nitrogen–argon mixture as a function of off-focal position and translation speed. 119

4.47 Optical images, with oblique illumination, of top surface of multi-trail samples nitride, with and without LSP, using a 49.2 ± 2 % nitrogen–argon mixture as a function of off-focal position and translation speed. 120
4.48 (a) Top surface and (b,c,d) SEM images of multi-trail samples nitride using a pre-struck LSP formed in a 49.2 ± 2 % nitrogen–argon mixture. (c) SEM image of smooth, reflective region. (d) SEM image of transition from smooth to rough region. 121
4.49 Surface topography of the multi-trail samples nitride using a pre-struck LSP formed in a 49.2 ± 2 % nitrogen–argon mixture. 122
4.50 Hardness profiles of multi-trail samples processed using pure nitrogen and a 49.2 ± 2 % nitrogen–argon mixture for a transition speed 100 mm/s and two off-focal distances. 122
4.51 Cross-sectional micrographs of multi-trail samples processed using a 49.2 ± 2 % nitrogen–argon mixture at low translation speeds, as a function of off-focal position and translation speed. 123
4.52 Cross-sectional micrographs of sample with Vicker's hardness indentations. The sample was processed using a 49.2 ± 2 % nitrogen–argon mixture at a translation speed of 15 mm/s and an off-focal distance of 8 mm. 124
4.53 Hardness profiles of multi-trail samples processed using a 49.2 ± 2 % nitrogen–argon mixture at an off-focal distances of 8, 6 and 4 mm and a translation speed of 15 mm/s. 125
4.54 Hardness profiles of multi-trail samples processed using a 49.2 ± 2 % nitrogen–argon mixture at an off-focal distances of 8, 6 and 4 mm and a translation speed of 25 mm/s. Hardness profile of sample processed without plasma at an off-focal distance of 8 mm is shown. 125
4.55 XRD spectra of samples processed using a 49.2 ± 2 % nitrogen–argon gas mixture at an off-focal distance of 8 mm and translation speeds of 15 and 25 mm/s. 126
4.56 XRD spectra, collected after griding top surface, of samples processed using a 49.2 ± 2 % nitrogen–argon gas mixture at an off-focal distance of 8 mm and translation speeds of 15 and 25 mm/s. 127
4.57 XRD spectra of samples processed using a 49.2 ± 2 % nitrogen–argon gas mixture at an off-focal distance of 8 mm and translation speeds of 25 mm/s without plasma. Also shown is a cross-sectional micrograph of the sample 128

List of Tables

1.1 Common commercial lasers and some of their applications, modified from [2,3]. 1

2.1 Selected atomic argon emission lines with Einstein coefficients, statistical weights, and energy of the upper wavelength. 32

3.1 Parameter interpolation schemes. 49
3.2 Typical under-relaxation factors. 50
3.3 Percentage of total beam absorption within LSP generated by a 1.9 kW laser in a 5 m/s argon flow under various laser modes. 60

4.1 Categorization of publications on CO_2 laser nitriding of titanium. . 65
4.2 Highlight of experimental results. 83

Acknowledgments

First and foremost, I would like to thank my thesis advisor and committee chair, Dr. Judith A. Todd, for not only giving me the chance to work on this thesis topic, but for also providing support every step of the way. I must also thank Dr. Stephen A. Copley who, together with Dr. Todd, provided the technical guidance and criticism necessary to transform my hazy ideas and observations into scientific works. Knowing that anything I produced had to first meet their standards before seeing the light of day, forced me to become a better researcher, writer and presenter.

I also owe special thank to Dr. Ravindra Akarapu, who served as a post doctoral researcher during the first years of this endeavor. Together we spent countless hours in the lab conducting experiments and dealing with the many, many frustrating problems involved with setting up a laser processing system from the ground up. I am indebted to him for his enthusiasm, generosity with his time and constant encouragement. I also owe special thanks to Dr. Albert E. Segall, my undergraduate thesis advisor and doctoral committee member, for introducing me to the field of laser-materials interactions and encouraging me to undertake graduate studies. My remaining committee members, Dr. Vladimir V. Semak and Dr. John D. Mathews were chosen not only due to their expertise but also because they represent two of the finest teachers at Penn State. Dr. Semak's courses on laser optics and laser-materials processing, coupled with his natural skepticism, provided the foundation upon which I built and questioned much of my understanding of how lasers interact with matter. Dr. Mathew's introduction to plasmas course not only helped me better understand what a plasma is, but also allowed me to realize that plasma exists almost everywhere we look.

Finally, I would like to acknowledge all of my fellow research group members, the wonderful engineering support staff in the department of Engineering Science and Mechanics and the researchers at the Materials Characterization Lab who helped me with data collection and analysis. Much of this research was supported by the National Science Foundation Graduate Research Fellowship Program and the Office of Naval Research grant N00014-07-1-0121.

Chapter 1

Introduction

1.1 Lasers in materials processing

Shortly after the invention of the laser beam, in the early 1960's, potential applications of lasers to materials processing were quickly recognized [1]. Many of these early potential applications, such as cutting, welding, drilling and chemistry modification are today in widespread use [1]. Lasers are unique among light sources in that they provide coherent and monochromatic light which propagates with little divergence and can be highly focused. A list of some common commercial lasers and a few of their materials processing applications, modified from [2, 3], is shown in table 1.1.

Table 1.1. Common commercial lasers and some of their applications, modified from [2,3].

Laser	Primary Wavelength	Application
Ruby	694.3 nm	Processing of inorganic materials
Diode	UV to IR	Processing of semiconductors; welding; CD and DVD recording
CO_2	10.6 μm	Cutting; joining; drilling; atomic fusion
Nd:YAG	1064 nm	Cutting; joining; drilling
Nd-doped Fiber	1070 nm	Cutting; joining; drilling
Excimer laser	UV	Processing of organic material; photolithography; coloring

Lasers are indeed critical to modern materials processing. At the end of the first decade of the twenty-first century, world-wide sales of non-diode lasers for materials processing applications topped 1.6 billion U.S. dollars [3]. According to Steen and Mazumder [3], "The market for lasers in material processing has been a growth area for several years and is expected to continue to grow at 10-20 %."

Materials processing using lasers can be broken down into conventional and chemical processing. Conventional processing does not involve chemical modification of the substrate whereas chemical processing alters the substrate composition [4]. Conventional laser processing techniques include cutting, welding, scribing, and drilling as well as processes which involve heat treatment, such as annealing, transformation hardening and shock hardening [4]. Chemical processing includes techniques which do not involve chemical reactions, such as cladding, where material is melted and solidified atop a substrate, and techniques which involve inducement of chemical reactions, such as alloying. Applications presented in Section 4 of this thesis are examples of chemical processing.

1.2 Laser-sustained Plasma

A laser-sustained plasma (LSP) is a plasma sustained near the focus of a continuous laser beam without assistance from interaction between the laser beam and a nearby surface. LSP is sometimes referred to as a continuous optical discharges or an optical plasmatron [5]. Unlike plasmas sustained at microwave or radio frequencies, LSP can be sustained remotely, away from any structure or confining chamber. Most commonly, LSP is sustained by a continuous (CW) high-power carbon dioxide (CO_2) laser, operating at a wavelength of 10.6 μm.

Because electromagnetic waves can propagate into the interior region of a plasma only if the wave frequency is greater than the plasma frequency, using a CO_2 laser to sustain a plasma holds a key advantage over lower frequency sources, where the plasma frequency is higher than the wave frequency: LSP has a very high maximum electron temperatures ($\sim$17,000 K) in a small volume near the laser focus [5]. Deep penetration of CO_2 radiation within LSP is also aided by low inverse bremsstrahlung absorption ($<0.85\,\mathrm{cm}^{-1}$ within first-degree ionized LSP at 1 atm) [6]. Additionally, LSP can be remotely moved simply by moving the focal

position of the laser beam.

The unique characteristics of LSP have made it a suitable candidate for many potential applications, such as energy conversion and material processing [5], laser thruster propulsion [7] and spectrochemical analysies [8]. LSP generated in an argon:methane:hydrogen mixture ($Ar:CH_4:H_2$) has also been used in high-speed LSP deposition of polycrystalline and nanocrystalline diamond films at near–atmospheric pressures [9–12].

The primary means for diagnosing LSP is optical emission spectroscopy (OES). Optical emission spectroscopy relies on analysis of the optical emissions of excited atomic and ionic species within the plasma. By examining the wavelengths of line emissions, which are a result of bound-bound transitions, atomic and ionic components of the plasma can be identified. The intensities of the emission lines and their ratio provides information regarding the electron density and temperature within the plasma. The broadening of spectral lines can also be used to calculate the electron density within the plasma.

Further understanding of the physics of LSP can be gained though mathematical modeling and computer simulation of the phenomena. Modeling can shed light on how various input parameters, such as laser power, laser mode, processing gas and flow velocity, affect LSP. Through this understanding, experiments can be designed more efficiently and economically. Additionally, conditions can be simulated which would otherwise be difficult or expensive for exploratory studies.

An important but scarcely explored topic is application of LSP to materials processing. LSP uniquely allows distinguishing between the interaction of a plasma and a laser beam with a surface under conditions where the laser beam would not result in plasma formation. By combining this unique feature with OES, it is possible, as will be reported here, to decouple the effect of plasma from that of the laser beam in laser materials processing. For this reason, LSP will be used to investigate the role of near-surface plasma during CO_2 laser nitriding of titanium, as the role of plasma in laser nitriding is not well understood [13]. Additionally, the existence of plasma near a substrate during laser processing, under conditions where normal laser processing would not result in plasma formation, opens up a new processing window for laser nitriding, as will be discussed in Chapter 4.

1.3 LSP physics

A basic textbook definition of plasma is "a quasineutral gas of charged and neutral particles which exhibit collective behavior" [14]. Plasma differs from solids, liquids and gases in that it is comprised of particles interacting via collisions as well as charged particles interacting collectively via long-range coulomb forces.

The distance over which coulomb forces influence neighboring charges is defined as the Debye Length, λ_D.

$$\lambda_D = \left(\frac{\epsilon_0 kT}{n_e q_e^2}\right)^{1/2}. \tag{1.1}$$

Above, T is the electron temperature in Kelvin, n_e is the electron density, k is the Boltzmann constant, q_e is an electron's charge, and ϵ_0 is the permittivity of free space. Beyond a Debye length, the potential field around a point charge decreases exponentially, and is effectively shielded out; but, for distances smaller than λ_D the effective potential reduces to the coulomb potential.

A second critical plasma parameter is the plasma frequency, ω_p. The plasma frequency is related to the thermal velocity of electrons, v_e, and the Debye length by,

$$\omega_p = \frac{v_e}{\lambda_D} = \left(\frac{n_0 q_e^2}{\epsilon_0 m_e}\right)^{1/2}, \tag{1.2}$$

where m_e is the electron mass and n_0 is the plasma density. Since charge neutrality is typically assumed, the plasma density is equal to the electron density which is equal to the ion density, $n_0 = n_e = n_i$. If an electric field causes an electron to be displaced from its ideal shielded location, neighboring electrons will adjust to shield this nonequilibrium field. The resulting oscillations describe the plasma frequency, ω_p. If an incident electromagnetic field propagates at a frequency less than the plasma frequency, electrons can quickly adjust and the wave decays within a distance on the order of the skin depth, δ,

$$\delta = \frac{c}{\sqrt{\omega_p^2 - \omega^2}}, \tag{1.3}$$

where c is the speed of light and ω is the frequency of incident electromagnetic field.

Thus, plasma sustained by an electromagnetic field operating below the plasma

frequency, absorbs energy in a very thin outer skin which limits the maximum attainable temperature and results in a "flat temperature profile" [5]. The plasma becomes opaque for a frequency equal to the plasma frequency. Under this condition, most of the energy "is absorbed in a zone adjacent to the plasma layer of critical density" [15]. Above the plasma frequency, electromagnetic fields can be transmitted though the outer, less dense, regions of the plasma and be absorbed within the interior, more dense plasma regions. Most absorption of CO_2 laser radiation, operating at 28 THz, within LSP occurs near the laser focus where the electric field strength is very high. The ability of CO_2 laser radiation to penetrate into the plasma interior and produce strong electric fields near the focal point of the laser beam allows sustainment of temperatures higher than those generally achievable by other excitation sources [5, 6].

1.3.1 Plasma at infrared and optical frequencies

Plasma can be formed near the focal point of a laser beam via three mechanism. The first is photoionization, wherein a neutral, A, absorbs a single photon with an energy ($h\nu$) exceeding the neutral's ionization energy (ionization potential):

$$h\nu + A \rightarrow e^- + A^+. \tag{1.4}$$

To achieve a photon energy greater than the ionization energy of an argon atom, 15.76 eV, a wavelength less than 78.67 nm would be required. A lower probability means to achieve ionization is through a multiphoton process. This mechanism allows ionization via simultaneous absorption of two or more photons with a combined energy exceeding the neutral's ionization potential,

$$Nh\nu + A \rightarrow e^- + A^+, \tag{1.5}$$

where N is the required number of photons necessary to a exceed the ionization energy. To ionize a ground-state argon atom using a CO_2 laser would require the absorption of over 134 photons. The probability of this occurring at any practical laser irradiance (intensity) is virtually zero. Practically speaking, multiphoton ionization need only be considered at wavelengths less than 1 μm [16].

The third mechanism by which breakdown can occur at optical frequencies is cascade (or avalanche), breakdown. Here, free electrons, accelerated by a laser's electromagnetic field, collide with neutrals resulting in ionization and a doubling of the number free electrons,

$$e^- + A \rightarrow 2e^- + A^+. \tag{1.6}$$

Inelastic collisions between neutrals and electrons, accelerated by the laser's electromagnetic field though inverse bremsstrahlung absorption,

$$h\nu + e^- + A \rightarrow (e^-)^* + A, \tag{1.7}$$

continue to produce more electrons until a sufficient density of ions is achieved. The notation $(e^-)^*$, in equation 1.7, is used to indicate an electron with increased kinetic energy. At this point, the plasma is heated through the more efficient [5, 6, 15] electron-ion inverse bremsstrahlung process,

$$h\nu + e^- + A^+ \rightarrow (e^-)^* + A^+, \tag{1.8}$$

resulting in a sharp increase in the degree of ionization and sustainment of the plasma [15]. Inverse bremsstrahlung absorption is discussed in more detail in Chapter 3. It has long been recognized that the ablation of a metal wire or substrate near the focus of a CO_2 laser is a reliable means by which to initiate the electron avalanche [17]. According to Arzuov et al. [17] and others [15], the lowering of the threshold for breakdown near a solid is primarily due to the vaporization and ionization of surface defects, such as metal oxides and thermally isolated regions.

1.3.2 Local thermodynamic equilibrium

In Section 1.3, the electron temperature, T, was introduced. For a system of particles, the kinetic temperature describes the Maxwellian velocity distribution of those particles. Temperature therefore describes the mean kinetic energy of a system of particles. This description however requires that the mean distance between particles, the mean free path, be much smaller than the size of the sys-

tem. Additionally, the particles must undergo many collisions such that the time between collisions is much shorter than any other characteristic time [18]. Since, this description generally holds for electrons in a laboratory plasma [19], the electron temperature describes the Maxwellian velocity distribution of free electrons. However, the same is not generally true for the ion kinetic temperature [18]. In fact, Zerkle and Krier [20], argue that kinetic equilibrium should not be expected in LSP.

In addition to the transfer of energy though collisions, energy is also transferred via radiation. If radiation emitted by a region of plasma is completely reabsorbed by neighboring regions before escaping the plasma, a radiation equilibrium exists. In other words, if the radiation mean–free path is much smaller than the size of the plasma, a radiation temperature can be defined [18]. In such a case the system is essentially a black body. However, most plasma, including LSP, can be considered as, at least partially, optically thin. That is, radiation emitted by species within the plasma is not absorbed, but contributes to the observed spectrum [21].

Complete thermodynamic equilibrium requires that kinetic, radiation as well as chemical equilibrium exist. Chemical equilibrium is established if the population of bound states follows a Maxwell-Boltzmann distribution which can be defined by an excitation temperature. Therefore, in complete equilibrium, the electron, ion, excitation and radiation temperatures are all equal. Since plasma radiation "almost never resembles that of a black body" [19], complete equilibrium almost never exists. In high-density plasmas however, collisions processes dominate and radiative processes become negligible [18]. In this case, local thermodynamic equilibrium (LTE) can be said to exist.

LTE is defined as a state where the population density distribution of electrons and the velocity distribution of electrons and ions are exclusively determined by particle collisions which are rapid, such that there is an instantaneous response of the electron distribution to any changes in the plasma condition [19, 22]. In other words, "the times associated to the establishment of kinetic balances are smaller than that of the plasma variations" [23]. Under LTE, complete thermodynamic equilibrium can be assumed in a small neighborhood of a point.

According to Zerkle et al. [20], LTE can be assumed for neutrals and ions at electron densities of $3.87 \times 10^{17}\,\mathrm{cm}^{-3}$ and $2.85 \times 10^{16}\,\mathrm{cm}^{-3}$, respectively, within

LSP [20]. The assumption of LTE significantly reduces complexity in spectral analysis and modeling of plasma. Under this assumption, several techniques exist for estimating both electron density and temperature. These include (i) determination of electron density from spectral line width, (ii) determination of electron density from absolute continuous radiation, (iii) determination of electron temperature via doppler broadening of spectral lines and (iv) determination of electron temperature from absolute and relative spectral line intensity. With respect to modeling, LTE allows the definition of all plasma properties in terms of a single temperature, greatly reducing complexity and computational time.

1.3.3 Review of LSP research

Generation of a LSP was first reported by Generalov et al. [24] in 1970. Generalov et al. [24] refereed to the LSP as a "continuous optical discharge." The LSP was ignited in a high-pressure, xenon-filled chamber using a Q-switched CO_2 laser and sustained using a seperate CW 150 W CO_2 laser. These first experiments came only months after Raizer [25] had argued for the feasibility of sustaining LSP in xenon at high pressures based on a one-dimensional model. In this section, key experimental works into LSP will be reviewed. More comprehensive reviews concerning spectroscopic investigation of LSP, mathematical modeling and applications of LSP to nitriding are given in Chapters 2, 3 and 4, respectively.

Early research on LSP centered on several main topics: thresholds for generation and maintenance [26–31]; characterization of plasma density and temperature [20, 27, 32]; and, the influence of focusing beam geometry, laser power, gas flow and gas composition on plasma paramters [7, 27, 31, 33–36]. According to Keefer [5], the requirement for a high-power(>1 kW) laser, coupled with unclear practical applications, limited research into LSP.

In the early days, experiments were conducted in high-pressure chambers, similar to that used by Generalov et al. [24], with < 2 kW lasers [26, 29, 30, 37] or in open atmosphere with multi-kilowatt lasers [27, 28, 32]. An example of a study conducted in a high-pressure chamber is that of Carlhoff et al. [29]. In this study, a 2 kW CO_2 laser was used to study the minimum power necessary to maintain LSP in helium at pressures up to 210 bar. The major advantage of using a high-pressure

chamber was the ability to operate using sub-kilowatt powers [24].

Notable among experiments conducted at atmospheric pressure, Fowler and Smith [27] showed that LSP sustained in atmospheric air absorbed approximately 50 % of the total beam intensity. They [27] also showed that total beam absorption increased with laser power and, using an interferometric technique to measure spatially-resolved electron densities, argued that refraction takes place near the laser focus [27]. The maximum electron density and temperature measured by Fowler and Smith [27] were 17,000 K and $2.1 \times 10^{17}\,\mathrm{cm}^3$ using a 6.2 kW laser with a near-gaussian beam mode. The LSP size, maximum density and maximum temperature decreased with a decrease in laser power.

Keefer et al. [32] also determined the spatially-resolved temperature of a LSP sustained in air by a 6 kW, near-gaussian mode, laser by measuring the absolute continuum intensity near 512.5 nm. Similar to the results of Fowler and Smith [27], Keefer et al. [32] found that the maximum electron temperature was approximately 17,000 K near the focal point of the laser beam. Additionally, Keefer et al. showed that the plasma diameter, defined by the 10,500 K temperature contour was approximately 3 mm. Glumb [38] has, however, raised doubt as to the accuracy of the absolute continuum technique due to the need for calibration.

Generalov et al. [28] found that the minimum power required to sustain LSP in open atmosphere increased with air flows coaxial with and perpendicular to the laser beam. It was also shown that the least stable configuration was with the flow directed opposite the direction of laser propagation. This observation agreed well with the earlier works of Raizer [30] and Fowler [27].

According to Raizer [30], the first demonstration of a LSP sustained in a forced convective (argon) flow was by Kozlov [37]. This LSP was refereed to as an optical "plasmatron" [37] or "plasmotron" [30]. Following the work of Kozlov, other researchers also demonstrated LSP in forced convective flows of Ar [7, 31, 35, 36], N_2 [31, 39, 40], nitrogen-argon mixture [41], CO_2 [31], xenon [42] and oxygen-argon mixture [42]. In the most common configuration, the laser beam propagating upwards, along the same direction one would expect buoyancy effects, into a quartz chamber [7, 35, 36, 38]. An important finding, first reported by Well, Keefer and Peters [36], determined that total beam absorption was strongly affected at flow rates above those associated with natural buoyancy—in this research [36], the laser

beam propagated upwards. In addition, Welle, Keefer and Peters [36] speculated that total beam absorption was dependent upon laser beam mode. However, no systematic research studying the effect of laser beam mode on LSP has been conducted [5].

Research into the influence of flow and laser beam geometry on the total beam absorption continued well into the 1980's. Krier et al. [35] found that total beam absorption increased with laser power and converged to a value of approximately 80 %, at 8 kW (the highest laser power used). This was true at pressures near 1.1, 2.0 and 3.5 atm and at flow rates of 0.15 and 0.25 m/s. The most systematic experimental work concerning the effect of flow on temperature and total beam absorption was conducted by Chen, Mazumder and Krier [43, 44]. In their works [43, 44], total beam absorption and spatially-resolved plasma temperature were measured for LSP sustained in a 2 to 10 m/s forced convective flow of argon directed coaxial to, and in the same direction as, the laser beam. An annular, $TEM_{01}{}^{*}$, laser beam operating at powers of 2.5 and 5 kW and an F-number of f/7 was used. Their experimental results [43, 44] showed that a total beam absorption around 80 % could be obtained at flow rates above 4 m/s.

1.3.4 Applications of LSP

Many researchers were motivated by the potential application of LSP to laser propulsion [5,7,33,35,36,38]. These researchers tended to be interested in hydrogen due to its low molecular weight. Advantages of a LSP propulsion system include the potential for high thrust, high specific impulse and the ability to provide power remotely [45]. Interest in this application still persists [46].

Another application of LSP was for the production of a high energy, low mass atom beam [42]. Cross and Cremers [42] used xenon and an argon-oxygen gas mixture at a pressure of 3 atm to produce high kinetic energy Xe, O_2 and O species. According to Keefer [5], the work of Cross and Cremers [42] generated particle fluxes similar to those experienced by satellites in low-earth orbitals. Application of LSP for spectrochemical analyses of species which are otherwise difficult to excite has also been suggested by Cremers et al. [47]. Drawing analogy with other plasma sources, Keefer [5] has additionally proposed potential application of LSP

to plasma chemistry and light sources.

The first insight into the application of LSP to materials processing was provided by Giren [40, 41], who investigated nitriding of steel using nitrogen and nitrogen-argon mixtures. Giren [40] found that nitriding with LSP resulted in a different microstructure and hardness than processing with a laser beam alone [40]. This was attributed to the activation of mass-transport processes due to the presence of LSP. Additionally, it was claimed that processing with a LSP led to a 30 % increase in the surface microhardness of SAE grade 1045 steel [40]. Giren [41] also argued that nitriding with a nitrogen-argon mixture, rather than pure nitrogen, may be beneficial for two reasons: 1) the threshold irradiance for sustainment of LSP decreases with the addition of argon; and, 2) the concentration of ionized, atomic nitrogen decreases relative to the population of neutral nitrogen, the latter of which can pass more easily though the potential barrier at the substrate surface.

More recently, a novel deposition technique for diamond film synthesis, using LSP, has emerged. Advantages cited for LSP diamond deposition included the ability to operate at atmospheric pressure, using a kilowatt-range laser, in gas mixtures where Ar or Xe are the predominant species [48]. The ability to generate plasma with an electron temperature higher than in conventional CVD was also expected to result in deposition rates much higher than for conventional CVD [48].

In initial reports, an LSP was generated using a 2.5 kW CW CO_2 laser opperating at 1.5 kW in a 2 to 4 l/min gas flow. A gas mixture of Xe:H_2:CH_4=330:27:1, by volume, was used to deposit a "rainbow" -colored, smooth polycrystalline film on tungsten at a rate of up to 0.5-0.83 μm/min [10, 49]. Xenon was found to be the predominant component of the mixture due to its lower threshold for plasma formation. Further studies claimed that, under optimized conditions, continuous, polycrystaline diamond films could also be deposited on molybdenum, silicon, and cemented carbides at deposition rates up to 2 μm/min [11].

Two different deposition configurations were used. The laser beam and coaxial gas flow were directed perpendicular to (up-down configuration) or parallel to (horizonal configuration) a horizontally positioned substrate. It was shown that the perpendicular configuration allowed plasma sustainment over a wider range of gas velocities. A minimum gas velocity of 0.135 m/s for a (H_2+CH_4)/Xe ratio of 2-10 % was required to deposit diamond [48]. In all experiments, the substrate was

placed below the visibly dense plasma core, in the transparent surrounding plume—this region was found to contain a high concentration of C_2 radicals, although a quantitative analysis was not conducted [9].

A major problem cited was film non-uniformity due to the residual laser beam heating of the substrate [50]. More uniform films were synthesized via a modified mirror system which produced an annular beam [12]. This system allowed uniform deposition within the inner circular area of the annular beam. Further uniformity was achieved via chemical pretreatment [12].

While these works are very exciting [9–11, 48, 49], the lack of evidence that the observed films were indeed vapor deposited is troubling. Because substrates were seeded with diamond prior to processing, the observed film could have been due to a transformation of the diamond used to seed the substrate. In reproducing some of these works [9–11, 48, 49] for his Honor's thesis, Alan Githens [51] was unable to show explicitly that the resultant diamond films were produced by LSP vapor deposition.

1.4 Common experimental details

In this research, all experiments were conducted using a 5 kW PRC Laser Corp. STS5000 CO_2 laser. The laser beam was guided to a laser-processing chamber using several uncoated, water-cooled copper mirrors and a quarter-waveplate mirror designed to change the laser's linearly-polarized light to circularly-polarized light within the processing chamber. Circular polarization was used to ensure equal absorption of laser power, during materials processing, regardless of substrate's direction of travel relative to the laser beam. It is well known that laser absorption is higher when the direction of polarization is parallel to the substrate's direction of travel. This arises when the melt front is oriented at an angle less than 90 degrees with respect to the incoming laser beam (which results in greater absorption of p-polarized light at the melt front) due to high vapor pressure directly above the melt.

A 5 in focal length, 2 in diameter zinc selenide (ZnSe) lens, enclosed in a Precitec Inc. CM2" (Z) laser cutting head, was used to focus the laser beam. Translation of the laser head and specimens within the processing chamber was conducted using

three Aerotech, Inc. ATS1000 series linear stages. Processing gas was supplied to the laser head from which it flowed coaxially out of a 10 mm diameter laser-head nozzle. The gas flow rate was controlled via an Omega Engineering, Inc. FMA5400 series mass flow meter.

Prior to all experiments, the laser output power was measured as a function of input power using a Coherent Inc. PM5K thermopile sensor. Laser power was measured after transmission though the ZnSe lens. All laser powers reported in this thesis were measured in this way.

1.4.1 Characterization of the laser beam

The output beam produced by the STS5000 CO_2 laser is known as a Quadramodal (Q-mode) beam. This Q-mode is a superposition of four transverse (TEM) modes:

$$I_{\text{Q-mode}} = 0.16 \times \text{TEM}_{00} + 0.16 \times \text{TEM}_{10} + 0.36 \times \text{TEM}^*_{01} + 0.36 \times \text{TEM}^*_{02}. \quad (1.9)$$

An illustration of the four TEM modes as well as the Q mode are shown in figure 1.1. A three-dimensional representation of the Q mode is also shown in figure 1.2. In both figures, the e-squared radius ($1/e^2$) was arbitrarily defined as 30.

In addition to being a Q-mode, according to the 2009 PRC laser corporation product manual, the laser beam has an M-squared number of 3.2 and a $1/e^2$ focused beam radius of 0.12 mm, for the focusing geometry described in Section 1.4. The M-squared number, also known as the beam quality factor, is defined as the ratio of a laser's beam parameter product (the product of the half-angle divergence and the focal spot radius) to the beam parameter product of a gaussian beam at the same wavelength.

A verification of both the radius and M-squared number was conducted using a PRIMES ® FOCUS MONITOR. The measured beam profile at the focal plane is shown in figure 1.3 and a comparison of the expected and measured beam radius is shown in figure 1.4. The manufacturer's specification match well with the collected data.

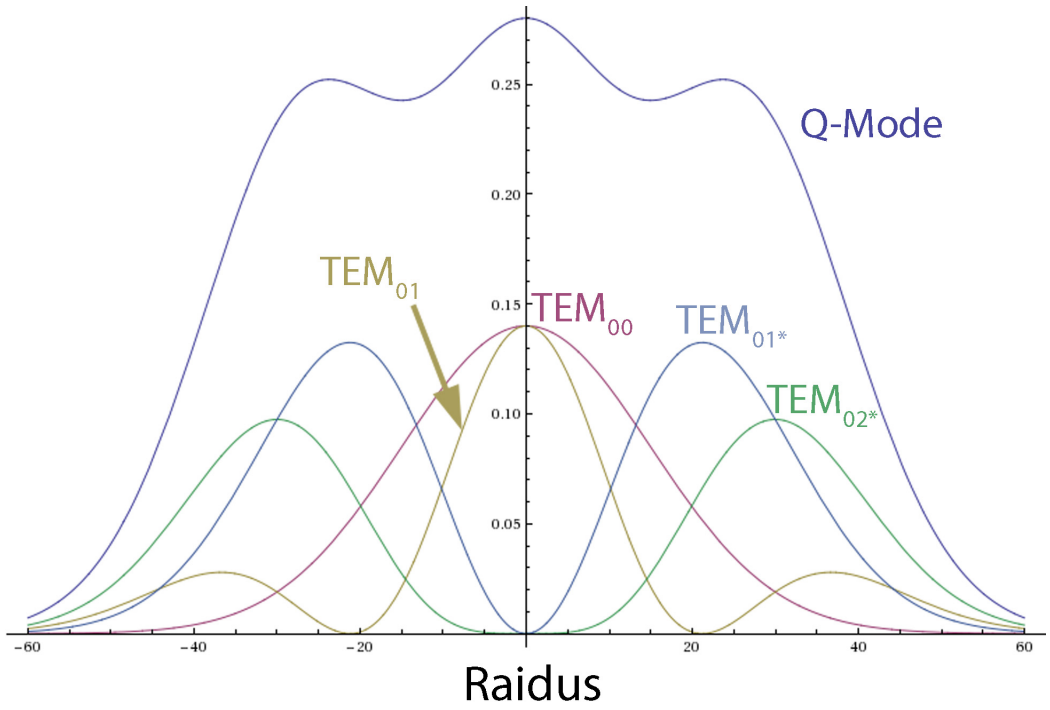

Figure 1.1. Plot of normalized Q mode intensity together with its subcomponents. The e-squared radius was arbitrarily defined as 30

1.4.2 Ignition and sustainment of LSP

In this research, it was found that laser-sustained plasma could be generated or "sparked" using a variety of techniques. The most common technique employed involved translation of a titanium substrate below the focused laser beam at a speed below 90 mm/s and an off-focal distance, defined from the focal position of the beam to the surface of the substrate, of 4 mm. LSP could also be ignited by irradiating a titanium substrate at an off-focal distance less than 4 mm for less than one second then moving the laser head upwards. Another technique involved the insertion of a 1.5 mm thick titanium wire into the focal plane of the laser beam. The insertion of a tungsten wire or using a secondary, nanosecond-pulsed, laser beam were other techniques used to ignite the plasma. LSP was generated in a variety of gases including coaxially-flowing nitrogen, argon, an Ar:CH_4:H_2 gas mixture and an Ar:CO_2 gas mixture. LSP was also generated in stationary air. A time sequence of the ignition and sustainment of a LSP in a coaxial flow of argon gas is shown in figure 1.5. The frame number and time (the last three digits are in

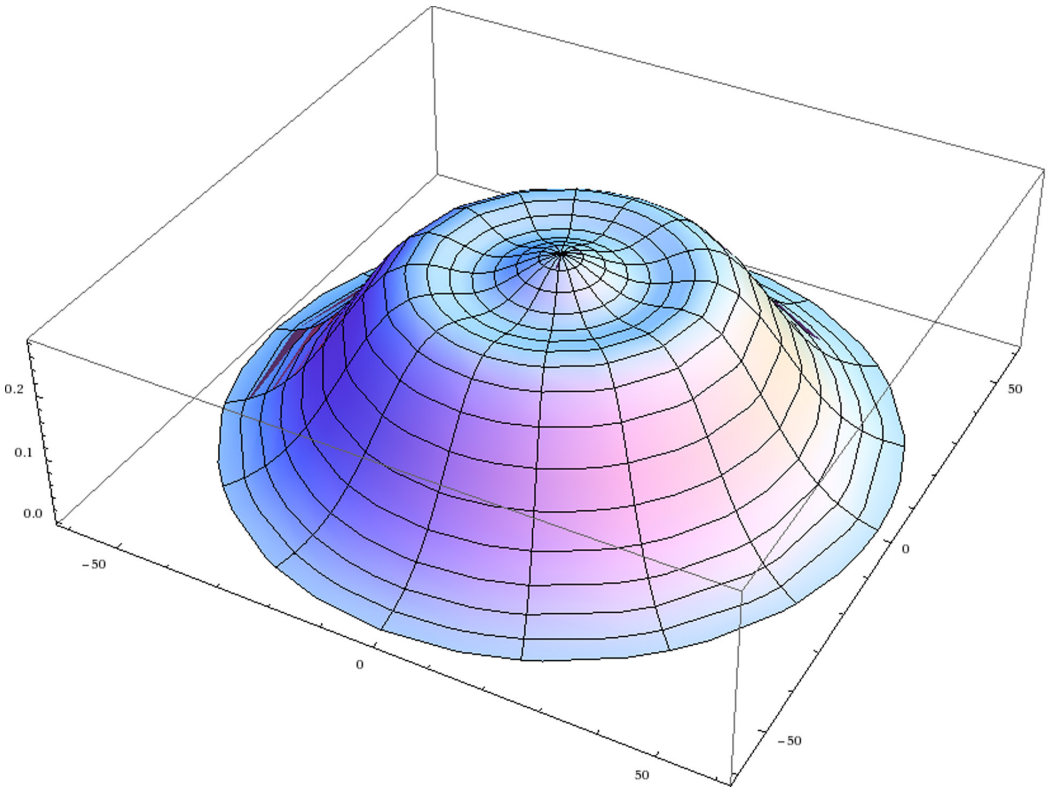

Figure 1.2. Three-dimensional representation of a normalized Q mode intensity. The e-squared radius was arbitrarily defined as 30.

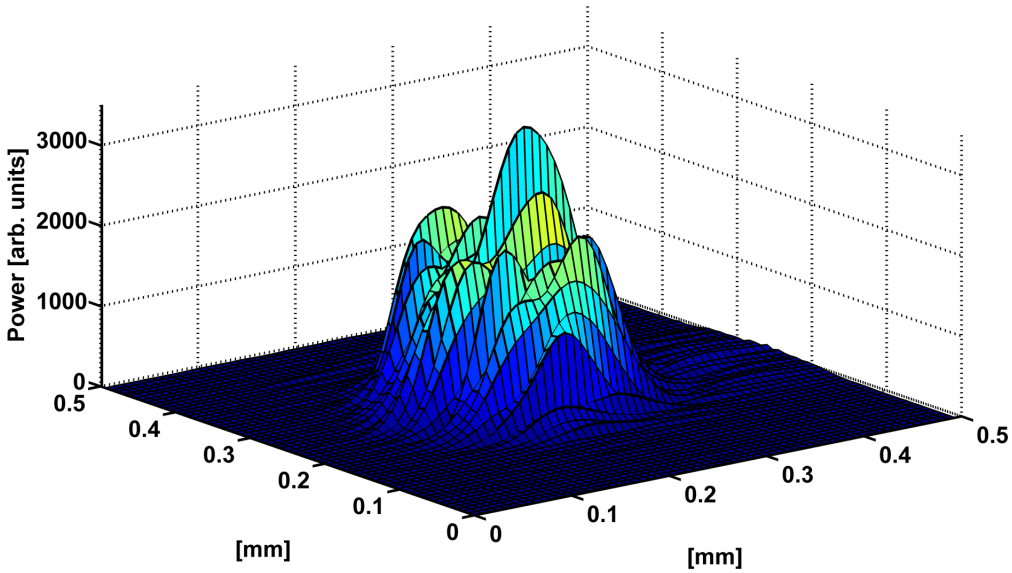

Figure 1.3. Laser beam profile measured at the focal plane.

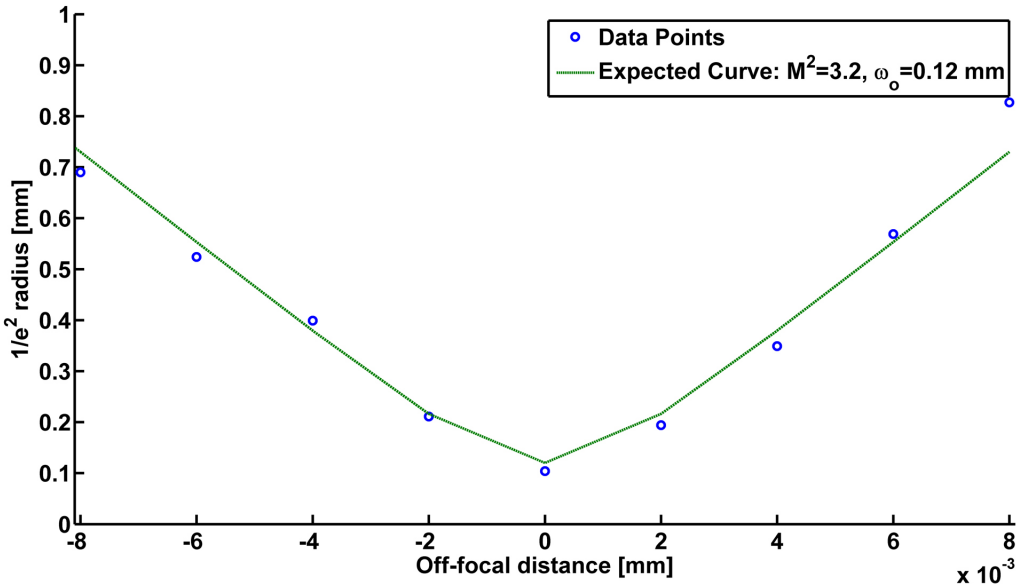

Figure 1.4. Measured and expected laser beam radii.

milliseconds) is shown below each frame. In this case, the LSP was ignited using a tungsten rod using a laser output power of 1.9 kW. Once ignited, the laser head traversed upwards and away from the ignition rod.

1.5 Outline of Thesis

This thesis is organized into five chapters. In Chapter 1, topics pertinent to modeling and characterization of LSP were introduced. Experimental details and laser parameters used throughout the remainder of the thesis were also provided. Chapter 2 focuses on characterization of LSP via optical emission spectroscopy. Here, experimentally measured temperature and density data are reported. A computational fluid dynamic model of an argon LSP is presented in Chapter 3. The subject of Chapter 4 is the application of LSP to understanding laser nitriding of titanium as well as the utilization of LSP to nitride under conditions otherwise not possible.

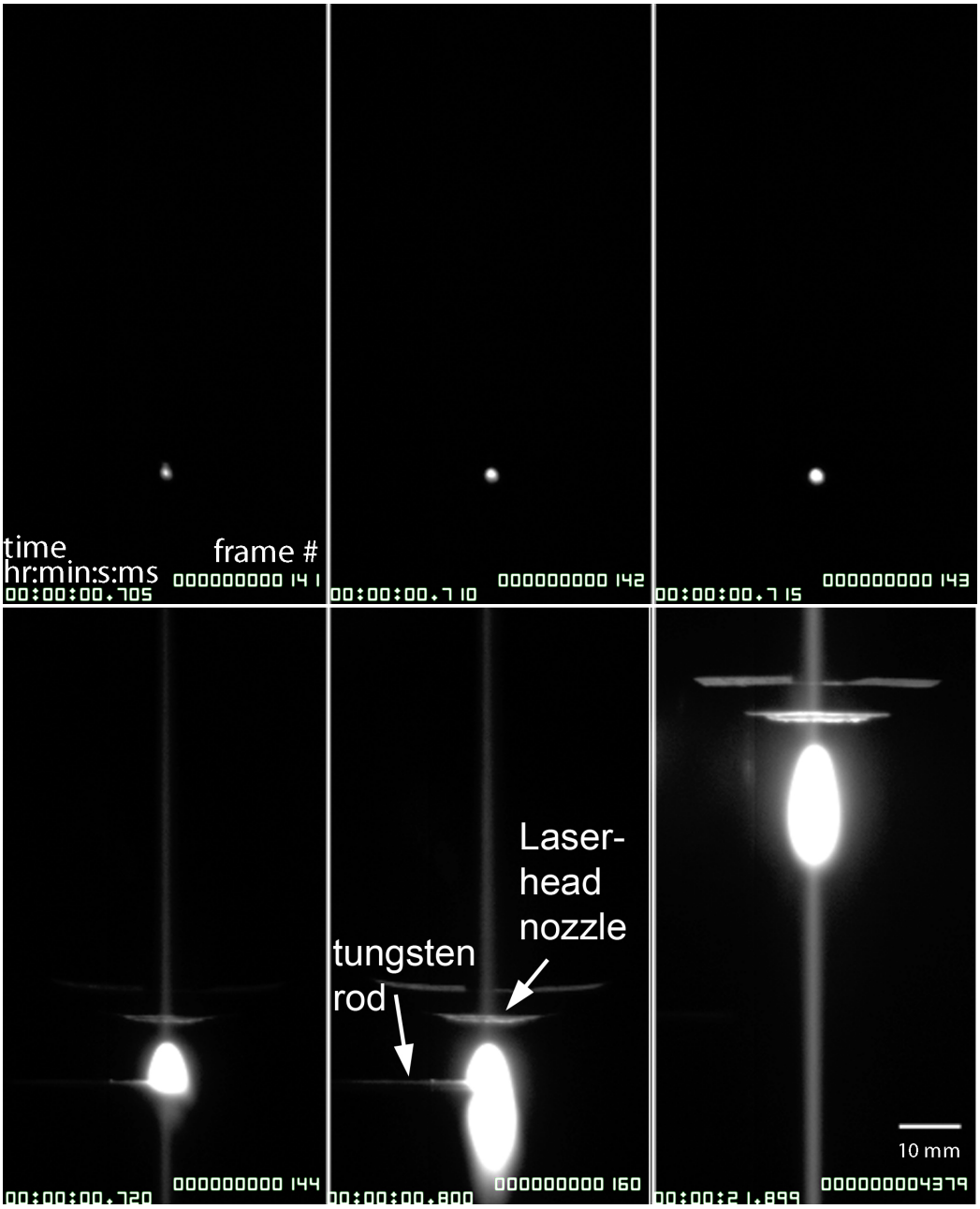

Figure 1.5. Time sequence of ignition and sustainment of an argon LSP using 1.9 kW CO_2 laser beam recorded using a CCD camera with a welding filter. A tungsten ignition rod is inserted (from left to right) into the laser beam near the focus. Once ignited, the laser head moved upward and away from the ignition rod.

Chapter 2

Spectroscopic investigation of LSP

2.1 Background and Introduction

Optical emission spectroscopy (OES) is a powerful tools for diagnosis of plasma composition and parameters. It can yield a wealth of knowledge regarding plasma parameters [21, 52]: The location of spectral lines can be used to determine constituent atomic or molecular species; Broadening of spectral lines provides information on the electron density and kinetic temperature of the emitting atom; Particle density and excitation temperature can be derived from the total intensity of a spectral line or ratio of spectral line intensities; The background radiation gives information regrading the electron density. An additional advantage is that, unlike Langmuir probe techniques, OES is complectly passive.

A definition of spectral terms is provided in figure 2.1. Important spectral parameters include the center wavelength (λ_0), maximum line intensity (I_{max}), total line intensity, defined as the integral of the spectral profile above the continuum, and Full Width at Half Maximum (FWHM).

Plasma emission spectra depend both on the properties of the emitting atom or ion as well as its local environment [18, 52, 53]. As noted in Section 1.3, the local environment can be approximated as the area within a Deybe length of the emitting species. Within this distance, coulombic interactions influence the energy levels and population densities of emitting species resulting in spectral line shifts and broadening [53], continuum emission and forbidden line emission [18]. Before a discussion of these effects, it is necessary to discuss briefly how radiation is emitted

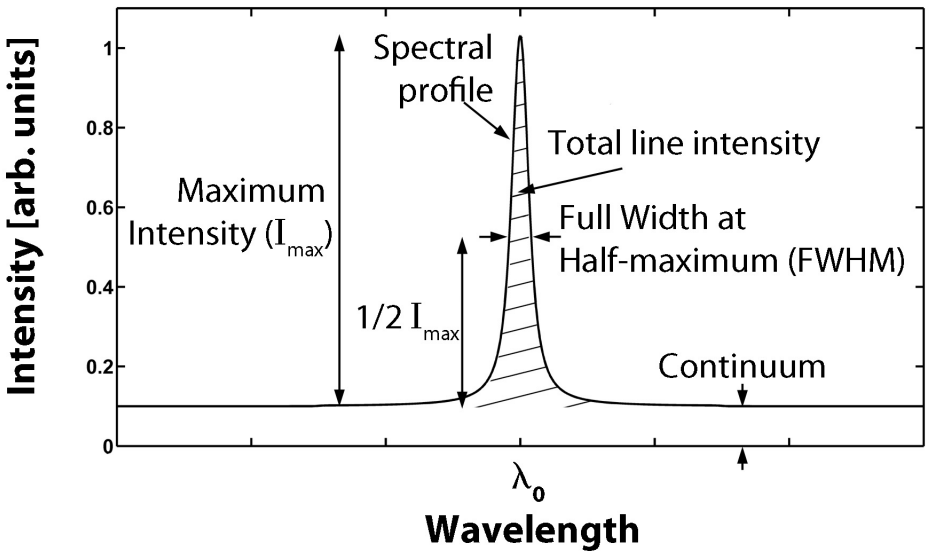

Figure 2.1. Definition of spectral terms

from plasma.

Plasma emissions are a result of free-free transitions, free-bound transitions or bound-bound transitions. Free-free transitions are a result of acceleration of charged particles, also known as bremsstrahlung radiation. Free-bound transitions occur when a free electron recombines with an ion. Both free-free and free-bound transitions contribute to the continuum. Line radiation occurs from bound-bound transitions. That is, transitions between two bound energy levels where the energy difference between the upper and lower levels equals $h\nu_{upper \rightarrow lower}$.

2.1.1 Spectral line profile

Since individual spectral lines result from bound-bound transitions, one may reasonably expect the profile of a spectral lines to resemble a Dirac delta function about a wavelength equal in energy to the difference between the upper and lower state. However, due to uncertainty principle ($\Delta t \Delta E \geq h/2\pi$), the energy of each state, for a given time of occupation of the upper state (Δt) , is a range rather than a concrete value. The broadening of a spectral line due to the uncertainty principle is called natural broadening. Natural broadening results in a Lorentzian

spectral profile,

$$I_N(\nu) = \frac{\gamma}{4\pi^2}\left[\frac{1}{(\nu-\nu_0)^2+(\gamma/4)^2}\right], \tag{2.1}$$

where γ is the sum of the spontaneous transition probabilities of upper and lower states [52,54], ν is frequency and ν_0 is the center frequency. Natural line broadening is typically so small ($< 10^{-4}$ nm), that it can almost always be neglected in the case of laboratory plasmas [18, 52].

Another broadening mechanism which is always present is Doppler broadening. Doppler broadening comes about from the thermal motion of the emitting atom or ion. The resulting spectral profile is gaussian and given by Griem [52], in a normalized form, as

$$I_D(\lambda) = \left(\frac{Mc^2}{2\pi kT\lambda_0^2}\right)^{1/2} \exp\left[-\frac{Mc^2}{2kT\lambda_0^2}(\Delta\lambda)^2\right]. \tag{2.2}$$

Where, M is the mass of the emitting species. Based on equation (2.2), the FWHM can be defined as

$$\left(\frac{2kT\ln 2}{Mc^2}\right)^{1/2}\lambda_0. \tag{2.3}$$

It is important to note that the temperature, T, in equations (2.2) and (2.3) is the temperature of the emitting species which is not necessarily equal to the electron temperature [18]. Doppler broadening is typically dominant in low-density plasmas, but can be completely neglected in dense plasmas [52].

A third broadening mechanism is Stark broadening. Stark broadening, also referred to as pressure broadening, results from interaction of radiating species with neighboring electrons and ions. Neighboring charged particles generate electric fields which perturb the radiating species resulting in a Lorenzian profile of the form

$$I_L(\lambda) = \frac{\alpha_L}{\pi}\left[\frac{1}{(\lambda-\lambda_0)^2+\alpha_L^2}\right]. \tag{2.4}$$

The above equation is normalized and α_L is the half-width at half-maximum (FWHM/2) of the broadened line. Stark broadening line widths, as a function of electron density and temperature, are readily available for a large number of atomic and ionic emission lines, most notably hydrogen lines, [52, 53, 55–57]. Since broadening is much more heavily dependent on electron density than temperature,

Stark broadening is useful in measuring electron density.

In addition to the mentioned mechanisms, the spectrometer used to collect plasma emissions also contributes to observed spectral line broadening. This broadening is called "instrumental broadening." Spectrometers can be classified by their optical resolution, spectral range and signal-to-noise ratios. These parameters are determined by spectrometer components. Light enters a spectrometer through an entrance slit and is collected using lenses and/or an optical fiber. In a typical configuration, light enters the spectrometer, is collimated by a spherical mirror and diffracted via an optical grating. The diffracted light is then imaged onto a linear array of Charge-Coupled Device (CCD) pixels. Each CCD pixel collects photons over a narrow range of wavelengths based on its location. The flux of photons for each pixel is then integrated for a period of time, know as the integration time, and a digital spectrum is produced.

Optical resolution and spectral range are dependent on the groove density of the optical grating, the dimensions of the entrance optics and the number of light measuring (typically CCD) pixels. There is always a trade off between optical resolution and spectral range—increased resolution will result in a decreased spectral range. There is also a trade off between the size of the entrance optics and signal intensity—a decrease in the size of the entrance optics, or slit size, will improve resolution but reduce signal intensity. It may be noted that in the case of very bright sources, as in the case of a LSP, signal intensity is rarely a problem. Optical resolution can be calculated by multiplying the grating dispersion by the pixel resolution. Grating dispersion is given by a grating's spectral range divided by the number of detector pixels, while the pixel resolution is typically provided by the spectrometer manufacturer for a given entrance optics, or slit size. Instrumental broadening can then be approximated as a gaussian with a FWHM equal to the optical resolution.

The measured spectral line profile is equal to the convolution of the natural, Doppler, Stark and instrumental broadening profiles. Since both Doppler and instrumental broadening produce gaussian profiles, if natural and Stark broadening can be ignored, the measured FWHM can be described simply by

$$\sqrt{\mathrm{FWHM}^2_{\mathrm{doppler}} + \mathrm{FWHM}^2_{\mathrm{instrumental}}}.$$

In the case of a convolution of a gaussian and a Lorentzian profile, the result is the so called Voigt profile:

$$\int_{-\infty}^{\infty} \frac{e^{-y^2} dy}{(x-y)^2 + (\alpha_L/\alpha_G)^2}, \tag{2.5}$$

where, α_G is related to the FWHM of the gaussian contribution ($\mathrm{FWHM_G}$) by $\mathrm{FWHM_G} = 2\sqrt{\ln 2}\alpha_G$. Again, α_G is not the half-width at half-maximum of the gaussian contribution as has been erroneously reported in [58]. A plot of a normalized Gaussian and Lorentzian profile around 645 nm, each with a FWHM of 1 nm, and the resulting Voigt profile are plotted in figure 2.2.

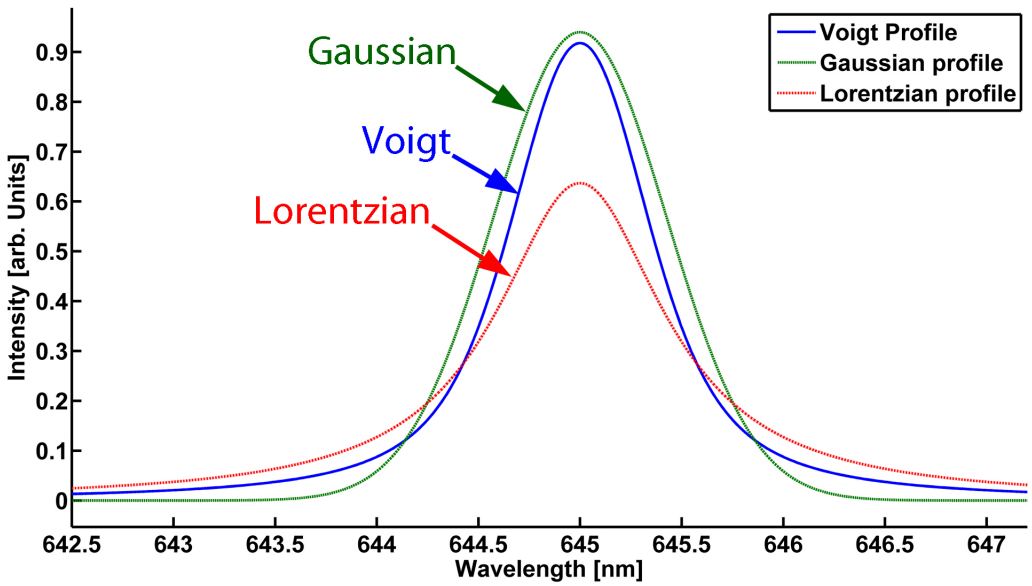

Figure 2.2. Plot of normalized Gaussian and Lorentzian profiles around 645 nm, each with a FWHM of 1 nm, and the resulting Voigt profile

2.1.2 Abel Inversion

In studying spectral emissions from plasma, one is almost always interested in determining the spatial distribution of plasma properties. When the plasma can be considered axisymmetric, the problem of determining the spatial distribution of parameters reduces to determining the radial distribution of its spectral emissions. Figure 2.3 shows a cylindrical plasma.

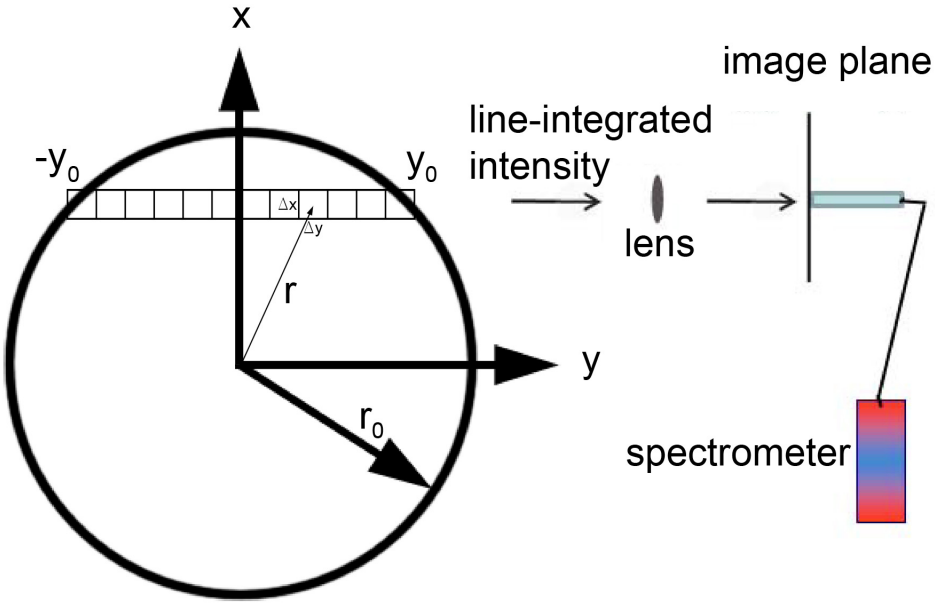

Figure 2.3. The observed spectral radiance from a cross section of an axi-symmetric plasma is a summation of the emissions along the line of observation. The z axis points into the page.

An observer sees the line-integrated radiance, $I\,[\frac{W}{m^2nm}]$ in the y direction along a line of length $2y_0$, which is a constant distance from the y axis. If the plasma is optically-thin, meaning that there is no absorption within the plasma, the line integrated radiance of the plasma is related to the plasma emissivity, $\epsilon(r)\,[\frac{W}{m^3nm}]$ by [59]

$$I(x)\Delta x\Delta z = \sum_{-y_0}^{y_0} \epsilon(r)\Delta x\Delta y\Delta z. \tag{2.6}$$

Equation (2.6) can be written in integral form as

$$I(x) = 2\int_0^{y_0} \epsilon(r)\,dy = 2\int_x^{r_0} \frac{\epsilon(r)r}{\sqrt{(r^2-x^2)}}\,dr. \tag{2.7}$$

Where $y = \sqrt{r^2 - x^2}$. To solve equation (2.7) we first need to find the inverse of a homogenous Volterra-type integral equation of the first kind, which can be written

as

$$g(x) = \int_x^{r_0} \frac{f(r)}{\sqrt{(r^2 - x^2)}}\, dr = A(x,r) f(r) \tag{2.8}$$

where $A(x,r)$ is the Abel-type integral operator [60]. The goal is to invert equation (2.8) to obtain $f(r)$ and $A^{-1}(r,x)$.

As equation (2.8) sufferers from two branch points at $x = \pm r$, inversion though classical function analysis methods is problematic [60]. However if we let

$$x^2 = \xi, \quad r^2 = \tau, \quad r_0^2 = R, \quad F(\tau) = \frac{f(\sqrt{\tau})}{2\sqrt{\tau}} \quad \text{and} \quad G(\xi) = g(\sqrt{\xi}), \tag{2.9}$$

equation (2.8) can be rewritten as [60]

$$G(\xi) = \int_\xi^R \frac{F(\tau)\, d\tau}{\sqrt{\tau - \xi}}. \tag{2.10}$$

Equation (2.10) can now be inverted using fractional calculus. To invert, we start with the definitions of the right-sided Riemann-Louville fractional integral of order α, ${}_tJ_a^\alpha$ and the right-sided Riemann-Louville fractional derivative of order α, ${}_tD_a^\alpha$ [61].

$$\begin{aligned}
{}_tJ_a^\alpha f(t) =& \frac{1}{\Gamma(\alpha)} \int_t^a (\tau - t)^{(\alpha-1)} f(\tau)\, d\tau, \ t < a, \ \alpha \in \mathbb{R}^+, \\
{}_tD_a^\alpha f(t) =& \begin{cases} (-\frac{d}{dt})^m \, {}_tJ_a^{m-\alpha} f(t) = \frac{1}{\Gamma(m-\alpha)} (-\frac{d}{dt})^m \int_t^a \frac{f(\tau)}{(\tau-t)^{(\alpha+1-m)}}\, d\tau \\ \qquad\qquad\qquad\qquad\qquad\qquad\qquad\qquad (m-1) < \alpha < m, \\ (-\frac{d}{dt})^m f(t), \\ \qquad\qquad\qquad\qquad\qquad\qquad\qquad\qquad \alpha = m = 1, 2, 3, ..., \\ {}_tJ_a^{-\alpha} f(t) = \frac{1}{\Gamma(-\alpha)} \int_a^t \frac{f(\tau)}{(\tau-t)^{(\alpha+1)}}\, d\tau \\ \qquad\qquad\qquad\qquad\qquad\qquad\qquad\qquad \alpha < 0, \end{cases}
\end{aligned} \tag{2.11}$$

Where $\Gamma(\alpha)$ is the gamma function and a is a fixed point. Using equation (2.11), equation (2.10) can be rewritten as

$$G(\xi) = \int_\xi^R \frac{F(\tau)\, d\tau}{(\tau - \xi)^{(1-1/2)}} = \Gamma(1/2)\, {}_\xi J_R^{1/2} F(\xi), \tag{2.12}$$

where $\alpha = 1/2$. Therefore,

$$F(\xi) = \frac{1}{(\Gamma(1/2))^2}\frac{-d}{d\xi}\int_{\xi}^{R}\frac{G(\tau)\,d\tau}{(\tau-\xi)^{(1-1/2)}} = \frac{-1}{\pi}\frac{d}{d\xi}\int_{\xi}^{R}\frac{G(\tau)\,d\tau}{\sqrt{(\tau-\xi)}} \tag{2.13}$$

and

$$f(r) = \frac{-2}{\pi}\frac{d}{dr}\int_{r}^{r_0}\frac{g(x)x}{\sqrt{(x^2-r^2)}}\,dr = A^{-1}(r,x)g(x) \tag{2.14}$$

Multiplying each side of equation (2.7) by $\frac{-1}{\pi}\frac{d}{dx}$, we get

$$\frac{-1}{\pi}\frac{d}{dx}I(x) = \frac{-2}{\pi}\frac{d}{dx}\int_{x}^{r_0}\frac{\epsilon(r)r}{\sqrt{(r^2-x^2)}}\,dr = A^{-1}(x,r)\epsilon(r). \tag{2.15}$$

And, finally

$$\epsilon(r) = \frac{-1}{\pi}A(r,x)\frac{d}{dx}I(x) = \frac{-1}{\pi}\int_{r}^{r_0}\frac{dI(x)}{dx}\frac{1}{\sqrt{(x^2-r^2)}}\,dr. \tag{2.16}$$

There are a variety of numerical techniques used to calculate $\epsilon(r)$ via equation (2.16). One of the more common techniques discretizes the cylindrical source into a finite number of concentric annuli each with a constant emission coefficient, ϵ_k. Using this technique together with a variable transformation and an assumption that the measured intensity varies linearly within each zone, of width a, along the x-axis, Nester and Olsen [62] reduced equation (2.16) to a summation with a set of tabulated coefficient, $B_{k,n}$.

$$\epsilon_k = -\frac{2}{\pi a}\sum_{n=k}^{N}B_{k,n}I_n \tag{2.17}$$

An alternative technique relies on fitting the measured intensity data to a function which can be analytically evaluated once operated on by $A(r,x)\frac{d}{dx}$. Two possible functions are a gaussian and a sum of even-powered polynomials [63].

To determine the best approach, Abel transformation of a noisy test function using the Nester and Olsen [62] technique (equation (2.17)), an analytical solution of a tenth-degree-even-powered-polynomial-sum fit (equation (2.18)) and an analytical solution of a Gaussian-second-degree-polynomial-sum fit (equation (2.19))

will be briefly presented.

$$I(x) = a_1 + a_2x^2 + a_3x^4 + a_4x^6 + a_5x^8 + a_6x^{10} \tag{2.18}$$

$$I(x) = a_1 \exp\{-(x/c_1)^2\} + a_2x^2 \tag{2.19}$$

The noisy test function is a summation of a test function and random noise,

$$I(x) = (100(1 - x^2)) + 5\delta(x),\ x \in [0, 1] \text{ and } \delta(x) \in [-1, 1] \tag{2.20}$$

Where $\delta(x)$ is a random number generated for each discrete x. A plot of the test function with and without noise is shown in figure 2.4. A plot of a tenth-degree-even-powered-polynomial-sum fit and a Gaussian-second-degree-polynomial-sum fit is shown in figure 2.5. As shown in figure 2.5, the tenth-degree-even-powered-polynomial-sum fit exhibits some oscillations while the Gaussian-second-degree-polynomial-sum fit does not. A reduction in the oscillations of the polynomial fit may be obtained using fewer terms in the series.

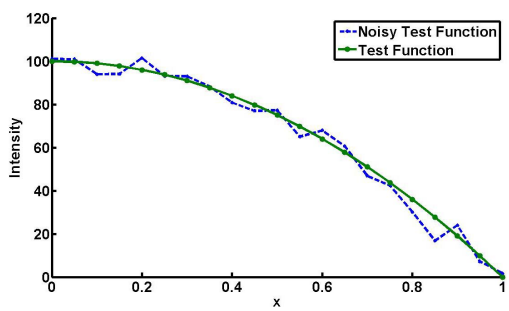

Figure 2.4. The test function versus the test function with noise.

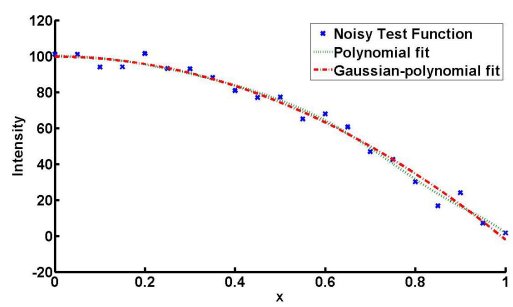

Figure 2.5. A tenth-degree-even-powered-polynomial-sum fit and a Gaussian-second-degree-polynomial-sum fit to the noisy test function.

Figure 2.6 shows the Abel transformation for the analytical test function and the three transformations of the noisy test function. The relative error, defined as $|\epsilon_{exact} - \epsilon_{approximate}|/\epsilon_{exact}$, is shown in Figure 2.7. It is clear that, for this noisy test function, the Gaussian-second-degree-polynomial-sum fit inversion is slightly more accurate than the the tenth-degree-even-powered-polynomial-sum fit, which exhibits small oscillations as expected. By far, the least accurate method is the

Nester-Olsen method. In fact, even a small amount of noise results in a significant error. From this exercise, it can be readily concluded that for the analysis of real spectra, it is a good idea to fit the spectra to a function which can be analytically inverted. This approach appears to reduce noise significantly in the final solution.

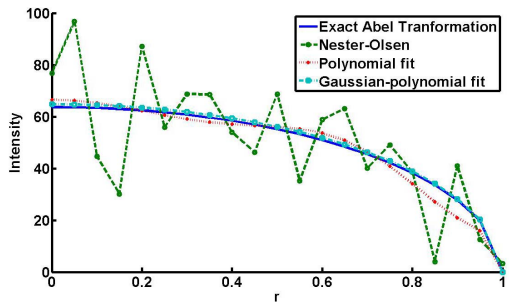

Figure 2.6. Comparison of transformations of the three methods.

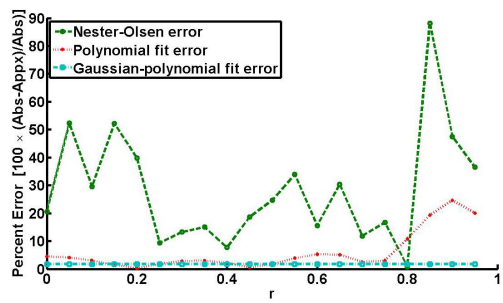

Figure 2.7. Percent error of the three methods. The Nester-Olsen method is, by far, the least accurate.

2.1.3 Measurement of plasma parameters

Once local plasma emissivity has been determined using Abel inversion, location-dependent properties can be determined via several quantitative spectroscopic techniques. Here, the Boltzmann plot technique and the Stark broadening technique are introduced for the determination of excitation temperature and electron density, respectively.

2.1.3.1 Determination of temperature via relative intensities of excited atomic emission lines

The oldest and most common technique for determination of plasma temperature is measurement of the relative total intensities of emission lines [52]. If LTE is assumed, the total line intensity of a spectral line resulting from a transition from an upper level, u, to a lower level l is

$$I_{u\to l} = \frac{h\nu A_{u\to l} N_u g_u}{Z(T_{exc})} \exp(-E_u/kT_{exc}). \tag{2.21}$$

Where, $A_{u\rightarrow l}$ is the Einstein emission coefficient for the transition, N_u is the population density of the upper state, g_u is the statistical weight of the upper level, E_u is the energy of the upper level and $Z(T)$ is the partition function. Taking the natural logarithm of both sides of equation (2.21), results in

$$\ln\left(\frac{I_{u\rightarrow l}}{h\nu A_{u\rightarrow l} g_u}\right) = Const - \frac{E_u}{kT_{exc}}. \tag{2.22}$$

Equation (2.22) assumes that the line intensity is not reabsorbed by the plasma. In other words, the plasma is optically thin. Determination of the excitation temperature of a given plasma species can therefore be determined using a semi-log plot of the left hand side of equation (2.22) versus the upper energy level for several emission lines. The slope of linear fit gives $-\frac{1}{kT_{exc}}$. A sample Boltzmann plot, used in calculating the argon excitation temperature in a region of a LSP, is shown in figure 2.8.

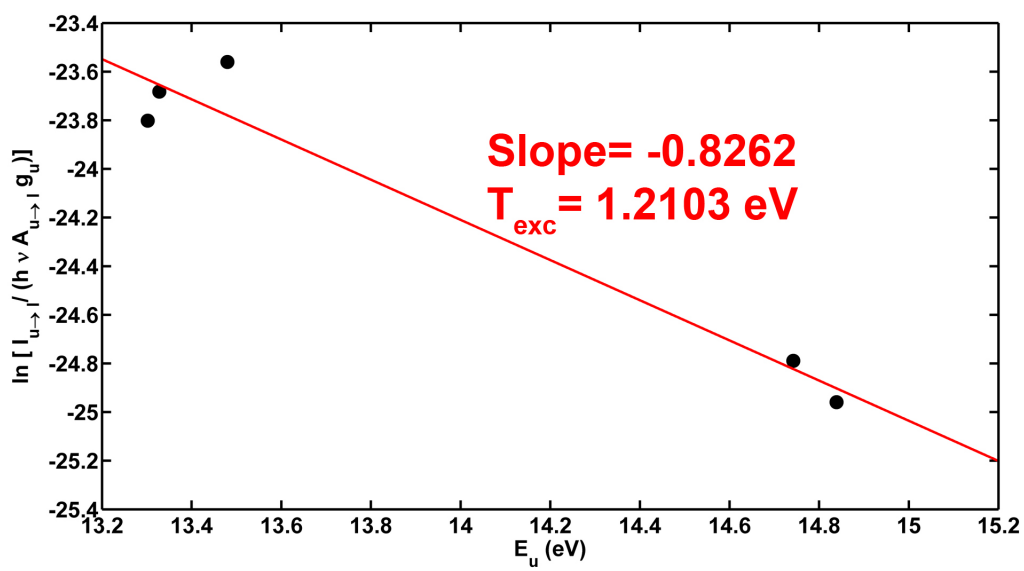

Figure 2.8. Sample Boltzmann plot. The slope of the linear fit is equal to $-1/kT_{exc}$

According to Griem [52], the relative intensities technique is typically accurate within ten percent. However, Cooper [18] argues that the technique is "rather insensitive and inaccurate" due to uncertainties in transition probability and energy differences less than kT_{exc} between upper energy levels of emission lines within a typical spectrum. Cooper's [18] former point is no longer valid due to improved

accuracy and wide availability of transition probabilities [64]. Moreover, the relative intensities technique has been consistently used to measure the temperature of LSP under conditions where LTE can be assumed [20, 65, 66].

2.1.3.2 Determination of electron density via Stark Broadening

Like the relative intensities technique, Stark broadening is a well known and very popular quantitative spectroscopic technique which has been employed for over half a century [52]. Stark broadening allows determination of electron density for an arbitrary chemical composition under non-LTE conditions as long as Stark-broadening parameters for a given emission line are well known. Stark broadening parameters, i.e. FWHM and spectral shift, are available in tabulated form for several emission lines of hydrogen [55, 57] as well as many atomic species [52], including argon [56, 67].

The hydrogen-beta line (486.13 nm) is among the most popular line for analysis due to a very low overall error ($< 5\%$) and large broadening (FWHM on the order of 1 nm for an electron density of $10^{22}\,\mathrm{m}^{-3}$) [52, 55]. Another important line is the hydrogen-alpha line (656.27 nm). Although the uncertainty associated with this line is higher than that for the hydrogen-beta line, large broadening (on the order of 0.2 nm) still makes it useful. Less useful are the argon lines, which exhibit a Stark broadened FWHM of less than 0.1 nm at typical LSP densities [67].

In any case, accurate determination of the Stark broadened FWHM requires deconvolution of natural, Doppler, Stark and instrumental broadening profiles. However, under conditions where Stark broadening dominates, the observed line profile can be directly fitted to a Lorentzian profile (equation (2.4)). As noted in Section 2.1.1, natural broadening can be neglected in almost all cases. With respect to the hydrogen-alpha and -beta lines, Doppler broadening can also be neglected under typical conditions within LSP. For example, even at a temperature of 15,000 K, Doppler broadening (equation (2.3)) results in a FWHM of only 0.056 nm. If a high-resolution spectrometer is used, instrumental broadening may also be ignored. Of course, to resolve broadening accurately, the spectrometer resolution must be much smaller than the Stark broadened FWHM.

2.2 Experimental setup

In the experiments reported here, LSP was ignited, as described in Section 1.4, and sustained in an argon gas mixture containing 0.5 % hydrogen. A gas flow rate of 23.5 slpm was used. The estimated gas speed though the 10 mm diameter laser nozzle was calculated to be 5 m/s. An output laser power of 1.9 kW was measured prior to the experiment.

A high-resolution HR4000 spectrometer with a spectral range from 600 to 710 nm and an optical resolution less than 0.06 nm (FWHM) was used to study spectral line profiles. The spectrometer was equipped with a 200 μm diameter optical fiber. Wavelength calibration was conducted using an Ocean Optics, Inc. HG-1 Mercury Argon Calibration Source. An Ocean Optics, Inc. DH-2000-CAL Deuterium Tungsten Halogen Calibration Standard was used to determine the instrument response function of each spectrometer. That is, the number of counts recorded, for a given number of photons, at each wavelength of incident light. Once determined, a calibration file was generated to compensate for nonuniformities in spectral responses.

To study LSP emissions as a function of spatial location, line-integrated spectra were imaged onto the end of the optical fiber using a 25.4 mm diameter, 100 mm focal-length UV fused silica lens. Prior to collection of plasma emissions, a dark spectrum was collected to measure the spectrometer's baseline response. An aperture stop, with a 1 mm opening, was used to maximize the depth-of-field. The depth of field attainable with this setup was approximately 96 mm. Collections were made along a cross-section of the LSP by translating the collection system a small distance, Δx =0.2 mm, as shown in figure 2.3. The total number of data points along each cross section was twenty-one and the total number of cross-sections was fourteen. The distance between each cross-section was 2 mm. An integration time of 4 ms was used and 250 spectra were collected at each data point. The 250 spectra were averaged to produce one spectrum at each data point. A photograph of the collection system is shown in figure 2.9.

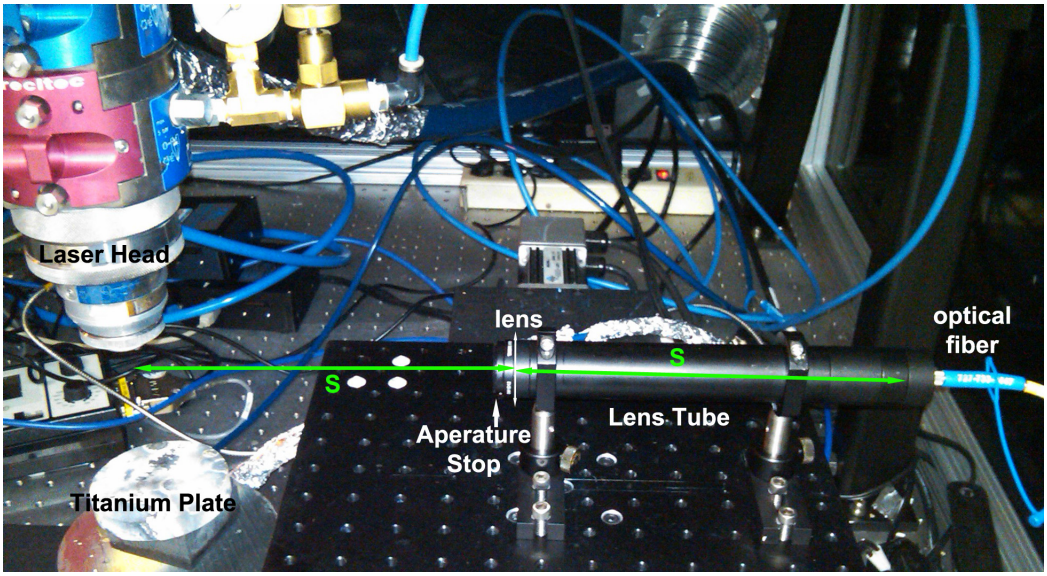

Figure 2.9. Photograph of OES collection system.

2.3 Data analysis

Emission lines collected from the spectrometer was identified using the NIST Atomic Spectra Database (version 4.1) [64] and with the aid of the Spectrum Analyzer, version 1.7 software [68]. Present atomic and ionized species were determined by overlapping known spectral lines with LSP emissions. Wavelength corrections were not necessary.

Quantitative determination of plasma temperature and density required several steps. The first steps in analyzing line-integrated emissions data involved averaging and calibrating the data. All spectra collected at each data point were averaged. Once averaged, the dark spectrum was subtracted from the data. The spectrometer's instrumental response function was corrected by multiplication of a calibration curve. Smoothing the calibration curve, using a twenty point moving average, was necessary so as not to introduce additional noise into the data.

Prior to Abel inversion, the total (integrated) line intensities of prominent atomic argon emission lines were calculated. The selected emission lines are shown in table 2.1. The domain of integration was manually, and globally, identified for each emission line. The contribution of continuum emissions to the line intensity was approximated using a linear fit and subtracted.

Total line intensities, as a function of LSP radius at each cross section, were

Table 2.1. Selected atomic argon emission lines with Einstein coefficients, statistical weights, and energy of the upper wavelength.

State	Wavelength [nm]	A_u[1/s]	g_k	E_u[ev]
Ar I	641.6307	1160000	5	14.83881
Ar I	667.7288	236000	1	13.47989
Ar I	675.2834	1930000	5	14.74254
Ar I	696.5430	6390000	3	13.32786
Ar I	706.7217	3800000	5	13.30223

Abel inverted using the tenth-degree-even-powered-polynomial fit (equation (2.18)) scheme described in Section 2.1.2—the polynomial fit was better than the Gaussian -second-degree-polynomial fit for the line-integrated data. Once inverted, radial emission data were used to measure the argon excitation temperature using the relative intensities of excited atomic emission lines, i.e. the Boltzmann plot technique. Points where the R-squared value of the linear fit to the Boltzmann plot was less than 0.85 were eliminated. For a linear, fit,

$$\text{R-squared} = \frac{\sum(y_i - y_{fit,i})^2}{\sum((y_i - \bar{y}_i)^2)}, \tag{2.23}$$

where y_i is the value corresponding to each data point, i, $y_{fit,i}$ is the fitted value and $\bar{y}_i$ is the mean value corresponding to all data points. The procedure, which has been thus described, was implemented using a MATLAB code, included in Appendix A.

Electron density was determined using the Stark broadening of the hydrogen-alpha (656.2725 nm) emission line. Here too, emissions data were first averaged and calibrated as already described. However, as opposed to Abel inverting the total line intensity, spectral emissions within a domain of 656.28±3.8 nm were inverted at each recorded wavelength within the domain using the tenth-degree-even-powered-polynomial fit scheme.

After inversion, the hydrogen-alpha spectral profile, at each data point, was fitted to a Lorentzian curve (equation (2.4)) to determine the FWHM. As noted in Section 2.1.3.2, deconvolution of the curve was not necessary. Once determined, the measured FWHM were matched to the tabulated data of Gigosos et al. [55] to calculate the electron densities.

2.4 Results and Discussion

The output of the Boltzmann plot technique is the excitation temperature of neutral argon species within the LSP. Since, LTE is assumed this temperature is assumed equal to the electron and ion temperatures. A contour plot of the measured plasma temperature is presented in figure 2.10.

The maximum temperature measured, ≈15,000 K, was less than the 16,000 to 20,000 K reported by some authors under similar conditions [43, 44]. In these cited publications [43, 44], temperature was measured using the line-to-continuum intensity of the 415 nm Ar I line. However, a more recent study by Zerkle and Krier [20] found that the excitation temperature of an argon LSP sustained by a 5 kW laser was close to 14,000 K. Zerkle and Krier [20] used an iterative algorithm to determine the non-LTE temperature of the LSP based on measurement of relative line ratios of neutral and ionized argon, respectively, and determination of the electron density via Stark broadening of the hydrogen-alpha line.

The contour temperature plot also shows an off-axis peak in the temperature. This is more apparent in figure 2.11. This peak is mostly likely an artifact of data processing or due to the assumption that the observed line radiation is optically-thin. Moreover, the peak falls within the 10 % error generally attributed to the Boltzmann plot technique [52].

Using the Boltzmann plot technique without Abel inversion, figures 2.12 and 2.13, did not show an off-focal temperature peak. Interestingly enough, similar temperature profiles are nevertheless obtained with or without Abel inversion. This comparison indicates that the off-axis maximum temperature can be attributed primarily to the optically-thin assumption. Since, as will be described in Section 3.1, reabsorption of optically-thick radiation plays an important role in radiation transfer within LSP, the center of the plasma is likely to be optically thick. Another, less likely, possibility is that the temperature within the center of the LSP is nearly uniform, measuring around 14,000 K. This conclusion is improbable because direct absorption of laser energy only takes place along the laser beam path, which occupies a small region near the center axis of the plasma. The temperature should be highest at locations where the energy source exists.

Unlike plasma temperature, the electron density profile, measured via Stark

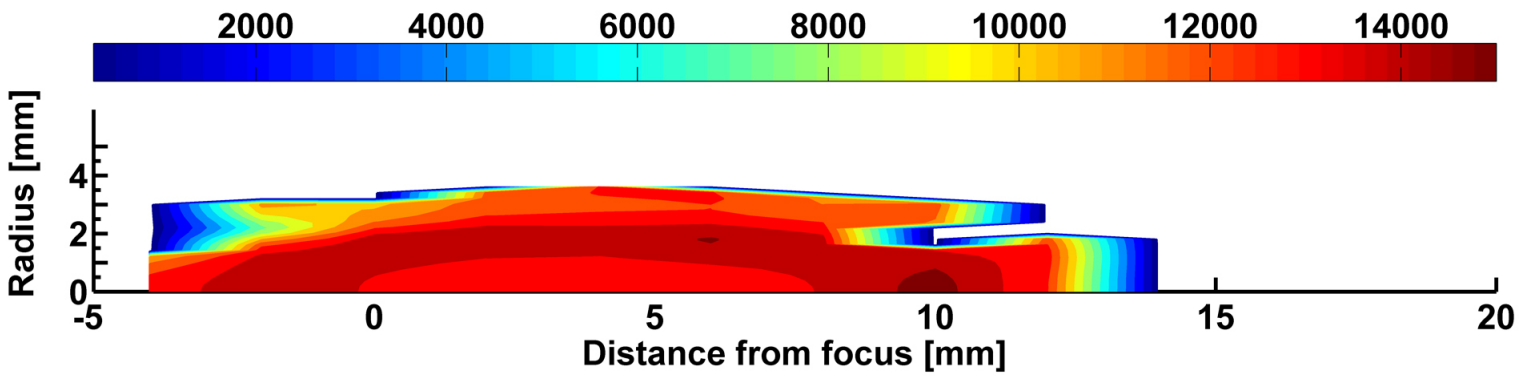

Figure 2.10. Measured LSP excitation temperature contours. LSP was sustained by a 1.9 kW laser in a 23.5 slpm argon gas mixture containing 0.5 % hydrogen. The color bar displays temperature in degrees Kelvin.

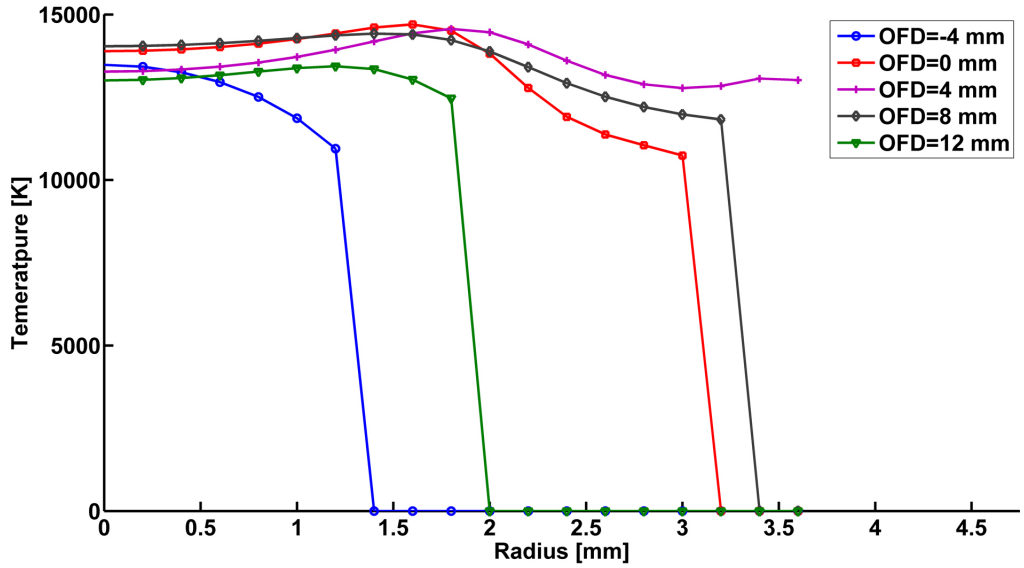

Figure 2.11. Measured excitation temperature without Abel inversion, as a function of radius, for every other recorded cross section. LSP was sustained by 1.9 kW laser in a 23.5 slpm argon gas mixture containing 0.5 % hydrogen.

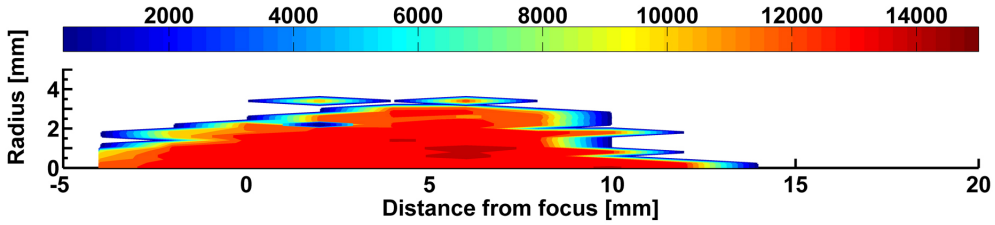

Figure 2.12. Measured excitation temperature without Abel inversion, of LSP sustained by 1.9 kW laser in a 23.5 slpm argon gas mixture containing 0.5 % hydrogen.

broadening of the hydrogen-alpha line, did not show an off-axis peak. The shape of the electron density contours, shown in figure 2.14, conform well to an intuitive understanding, based on visual observation of the plasma, on how the contours should look. The maximum electron density, $5.6 \times 10^{22}\,\mathrm{m}^{-3}$ was located 2 mm downstream of the laser focus.

Based on the Stark broadening results, the measured electron densities were approximately at or above $1 \times 10^{22}\,\mathrm{m}^{-3}$ within the region where plasma temperature was above 10,000 K. According to Zerkle and Krier [20], LTE can be assumed above an electron density of $2.85 \times 10^{22}\,\mathrm{cm}^{-3}$ within an argon LSP. Recall that the Stark broadening technique does not rely on any assumption of LTE. Using the

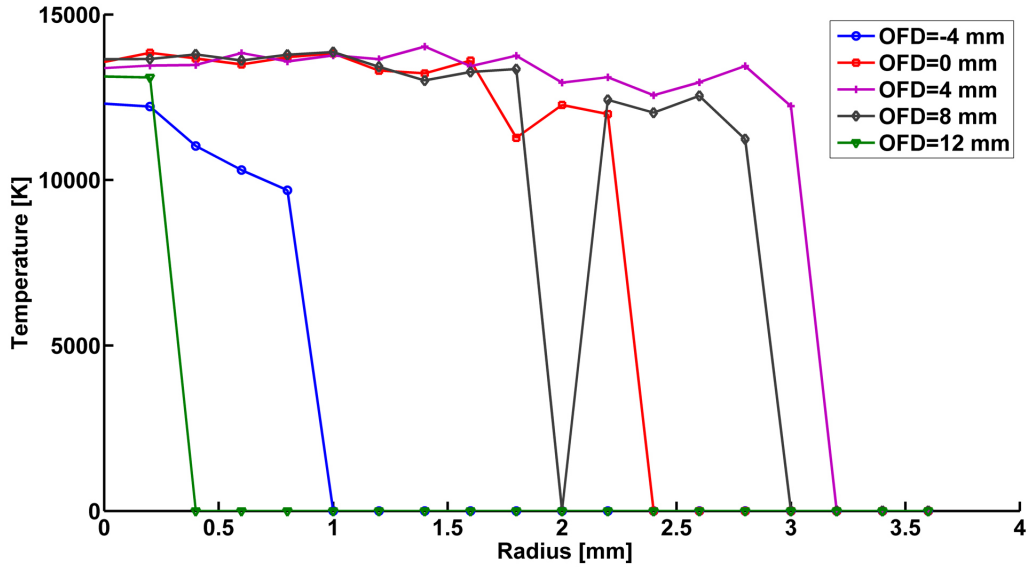

Figure 2.13. Measured excitation temperature without Abel inversion, as a function of radius, for every other recorded cross section. LSP was sustained by 1.9 kW laser in a 23.5 slpm argon gas mixture containing 0.5 % hydrogen.

criterion given by Zerkle and Krier [20], the portion of the plasma where LTE can be assumed, and where the Boltzmann plot technique can be applied, is shown in figure 2.15. However, as also noted by Zerkle and Krier [20], when energy transfer via optically-thick radiation is considered in an argon LSP, the criteria for LTE is lowered by one order of magnitude. Given this, the Boltzmann plot technique is considered valid within the domain where it was used.

2.5 Conclusions

In addition to the LSP temperature and density measurements presented here, several broader conclusions can be drawn.

- The tenth-degree-even-powered-polynomial fit is an effective technique to Abel invert line-integrated emissions from LSP.
- While measurement of LSP temperature using the Boltzmann plot technique may be valid in outer regions of the plasma where LTE exists, the technique is likely not accurate near the center of the LSP due to reabsorption of optically thick radiation.

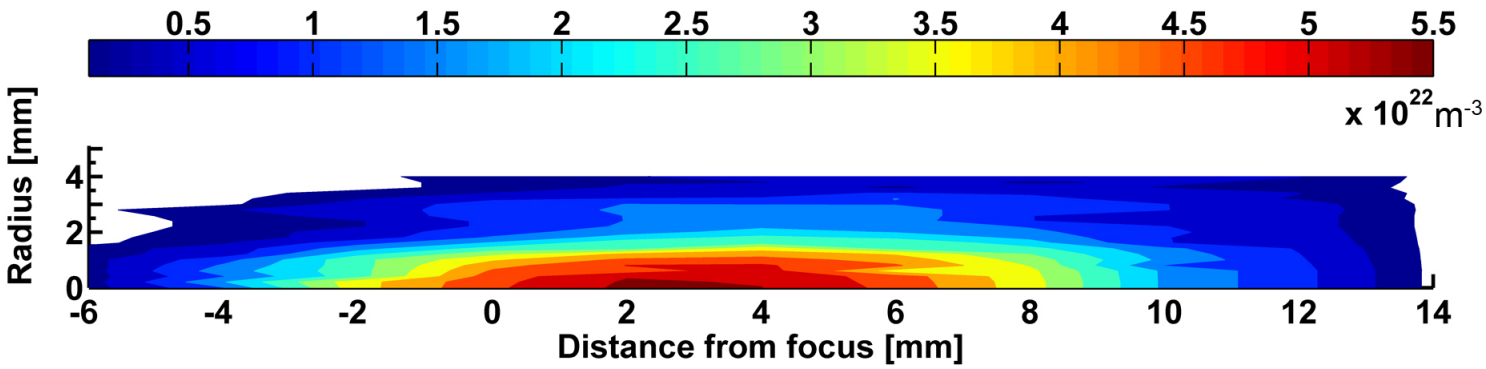

Figure 2.14. Measured electron density within LSP sustained by 1.9 kW laser in a 23.5 slpm argon gas mixture containing 0.5 % hydrogen.

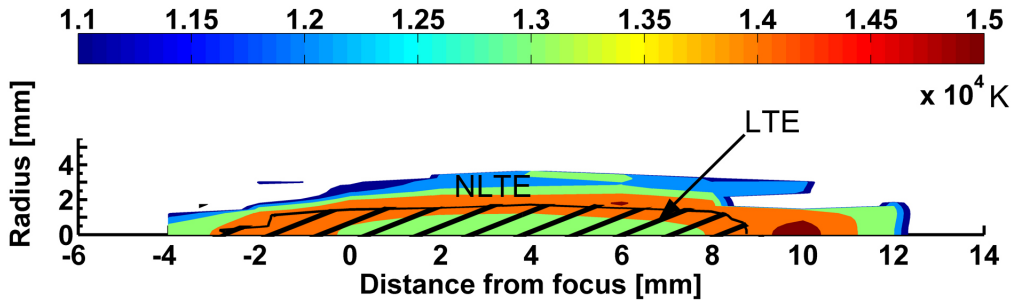

Figure 2.15. Region of LTE within LSP according to the criterion that LTE exists where $n_e > 2.85 \times 10^{22}\,\mathrm{cm}^{-3}$

- LTE can be reasonably assumed within regions of the LSP above 10,000 K.

These conclusions hold important consequences for further investigation of LSP parameters as well as for mathematical modeling. Among the most important findings was that the assumption of LTE within LSP is reasonable. However, the assumption that LSP radiation is optically-thin is not. Therefore, temperature must be determined by a technique which does not use relative intensities of excited atomic emission lines. Alternatively, it may be possible to measure the optical thickness of the plasma, as a function of wavelength, and to compensate for it within the Abel inversion algorithm. Additionally, direct comparison of experimentally measured LSP temperatures with model predictions is likely not possible near the center of the LSP. However, comparison of an outer temperature contour, for example 11,000 K, is likely to be accurate. Moreover, the results indicate that the assumption of LTE for LSP modeling is valid but the contribution of optically-thick radiation to energy transfer within the LSP must be taken into account.

Chapter 3

Modeling of laser-sustained argon plasma

While conducting laboratory experiments with LSP is essential to understand LSP phenomena mathematical, modeling is required to verify and further that understanding. Not only can a model shed light on how various input parameters, such as laser power, laser mode, processing gas and flow velocity, affect LSP; it can do so more inexpensively than experimentation. Moreover, an accurate model is an invaluable resource in evaluating the feasibility of, directing and optimizing real-world processes.

In this chapter, a computational hydrodynamic model of a LSP will be introduced. The model assumes axial symmetry, LTE, and negligible refraction of the laser beam. The validity of these assumptions will be discussed and verified experimentally. Novel aspects of this work include the algorithm, an alternative to the ray tracing method, used to calculate the laser power absorbed within the plasma. Using this algorithm, LSPs sustained by single and multi-mode beams are simulated. Model outputs, such as total beam absorption and plasma temperature, are compared with previously published results as well as with the experimental results of Chapter 2, with good agrement.

It may be noted that an earlier version of the model was published [69]. Nassar's primary contributions to that work were the devisement of the laser beam propagation and absorption algorithm as well as incorporation of temperature-dependent plasma properties. The results presented here, which include several

corrections and modifications to the original model, were computed using a different domain and mesh, and present new results for comparison with experimental data.

3.1 Background

The first model to emerge after the discovery of LSP by Generalov et al. [24] was developed by Raizer [70]. Drawing a close analogy with a slow-burning combustion process, Raizer presented a one-dimensional model of a hydrogen LSP sustained in an unfocused, nondivergent laser beam based on the energy and continuity equations. The primary output of the model was the temperature distribution along the axis of laser beam propagation. A closed-form solution was presented assuming that radial velocity, radiative heat transfer and radiative losses were zero, radial heat-conduction loss was a constant and that the specific heat divided by thermal conductivity (c_p/k) was also constant. Results of a numerical calculation for LSP sustained by a focused beam were also presented [70].

A tremendous improvement to Raizer's numerical model was made by Jackson and Nelson [71] who incorporated a radiative conductivity term, based on a diffusion approximation of radiation transfer, to account for optically-thick radiation. This addition resulted in a much improved agreement with experiments [5]. Jackson and Nelson's [71] model was later used to model a hydrogen LSP, using realistic gas properties, at pressures of 1, 3, 10 and 30 atm by Kemp and Root [72,73]. Keefer et al. [74] enhanced the model of Kemp and Root [72,73] by using a numerical technique with improved convergence throughout the domain [5]. Regardless of this improvement, Keefer et al. [74] concluded that two dimensional models were necessary to accurately model laser beam interactions and energy transport.

According to Keefer [5], the first two-dimensional model was developed by Batteh and Keefer [75] for LSP in air. This model included radial heat conduction losses, allowing calculation of the radial and axial temperatures [75]. However, like the work of Raizer [70], the model assumed a collimated laser beam, (c_p/k) was a constant and did not include radiative conductivity—presumably this work was completed prior to knowledge of the work of Jackson and Nelson [71]. Also, because the radial velocity was defined as zero, the model was only quasi-two-

dimensional. The Batteh-Keefer model [75] was later extended to hydrogen [76]. Further improvement was made by Muller and Uhlenbusch [77] who defined thermal conductivity as a function of temperature and replaced the collimated beam with a converging gaussian.

By far, the most comprehensive quasi-two-dimensional model was developed by Glumb and Krier [7, 38]. They used temperature-dependent gas properties, absorption coefficients, radiative conductivity and radiation losses. The model also incorporated a focused laser beam using a ray-tracing technique. Using this technique, the effect of a top-hat and an annular, $TEM_{01}{}^{*}$, beam modes were compared. However, the technique had a major drawback—it could not "account for radial non-uniformities in absorption" [38]. This was a consequence of calculating the total beam absorption using one absorption coefficient, across the entire beam width, for each point along the beam propagation axis [38].

The first full two-dimensional model was developed by Jeng and Keefer [78, 79] for an argon LSP sustained by an annular laser beam. Using a finite difference scheme, they solved the axi-symmetric forms of continuity, momentum, and energy equations using temperature dependent gas properties derived from experimental data. Later, the model was expanded to a hydrogen LSP sustained by a gaussian beam [79, 80]. As in the work of Glumb and Krier [7, 38], geometric ray tracing was used to model the propagation of their annular laser beam and energy deposition. Refraction of the laser beam was neglected.

Later models were introduced which incorporated diffraction-limited, gaussian beams [81, 82]. Conrad et al [39] built upon these analyses by using a parabolic refractive index assumption to estimate the increase in the gaussian beam width due to refraction. These studies, as well as later ones using similar approaches [83], considered only the effect of a gaussian laser beam. Additionally, rigorous comparison with experimental results, by for example comparing computed and experimentally measured total beam absorption or temperature contours, was lacking.

3.2 Governing equations

A LSP sustained in flowing argon by a CO_2 laser was modeled using the steady-state, incompressible form of the continuity, momentum, and energy equations,

$$\nabla \cdot (\rho \mathbf{v}) = 0, \tag{3.1}$$

$$\rho \mathbf{v} \cdot \nabla \mathbf{v} = -\nabla p + \nu \nabla^2 \mathbf{v}, \tag{3.2}$$

$$\nabla \cdot (\rho \mathbf{v} h) - \nabla \cdot (\frac{k_{eff}}{c_p} \nabla h) = \alpha I_{laser} - \dot{Q}_{rad}, \tag{3.3}$$

where, ρ was density, $\mathbf{v}$ was the velocity vector, p was pressure, ν was viscosity, h was enthalpy, c_p was the specific heat and k_{eff} was the effective thermal conductivity.. Within the energy equation, the source terms were represented by the energy deposition due to inverse bremsstrahlung absorption (αI_{laser}) and energy loss due to radiation emission ($-\dot{Q}_{rad}$).

3.3 Material Properties

3.3.1 Temperature-dependent properties

Several temperature dependent material properties were required to solve equations (3.1), (3.2) and (3.3): density, specific heat, thermal conductivity and viscosity. These parameters were assumed to vary based on a single plasma temperature. In other words, LTE was assumed. Additionally, it was assumed that the plasma was charge-neutral (ion density = electron density) and only first-degree ionization took place within the LSP.

Argon was assumed to be an incompressible ideal gas. Its density was defined as

$$\rho(T) = \frac{P_{op}}{\frac{R}{M_w} T}. \tag{3.4}$$

Where T was the temperature in degrees Kelvin, P_{op} was the operating pressure, defined as 101,325 Pa, R was the universal gas constant and M_w was the molecular weight of the argon (39.948 g/mol).

Specific heat was approximated using a twenty-one point piece-wise linear func-

tion from 200 K to 28,125 K by fitting the data of Derllishak et al. [84]. It may be noted that around 20,000 K, a minimum was observed, signalling the complete first-degree ionization of the plasma and the beginning of second-degree ionization. Since only first-degree ionization was assumed within the LSP, solution temperatures above 20,000 K, would have been considered invalid. Fortunately, such solutions did not occur.

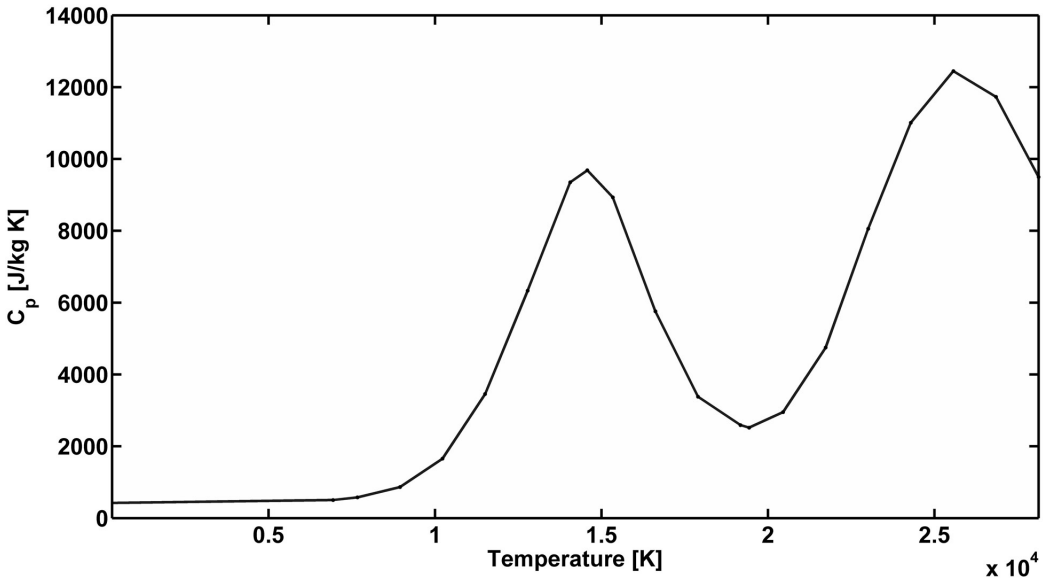

Figure 3.1. Specific heat of Argon plasma according to the LTE assumption

The effective thermal conductivity was considered to be the sum of thermal conductivity and a radiative conductivity. Thermal conductivity data were approximated as a fourth degree polynomial,

$$c_p = 1.1575 \times 10^{-2} + 1.7186 \times 10^{-5}\, T + 1.1024 \times 10^{-8}\, T^2 - 3.0111 \times 10^{-12}\, T^3 + 2.3465 \times\ 10^{-16}\, T^4, \quad (3.5)$$

using the data of Devoto [85] and Murphy [86] from 100 K to 11,000 K. Above 11,000 K, optically-thick radiation contributes to the effective thermal conductivity. Because optically thick radiation emitted from a region within the plasma is absorbed by a neighboring region, it transports energy. A diffusion approximation

for the radiative transport of energy is [87]

$$\frac{dQ}{dt} = -\frac{4}{3}acT^3\bar{l}\nabla T, \tag{3.6}$$

where a is the radiation density, c is the speed of light, T is temperature and $\bar{l}$ is the Rosseland mean radiation path length. Unfortunately, calculation of the Rosseland mean radiation path length is difficult [88]. Instead of calculating this parameter, the effective thermal conductivity was approximated as a line,

$$k_{eff} = -23.10204 + 2.204 \times 10^{-3}\,T \text{ for } T > 11,000\,\text{K}, \tag{3.7}$$

above 11,000 K using the data of Glumb and Krier [7]. A graph of the effective thermal conductivity is shown in figure 3.2

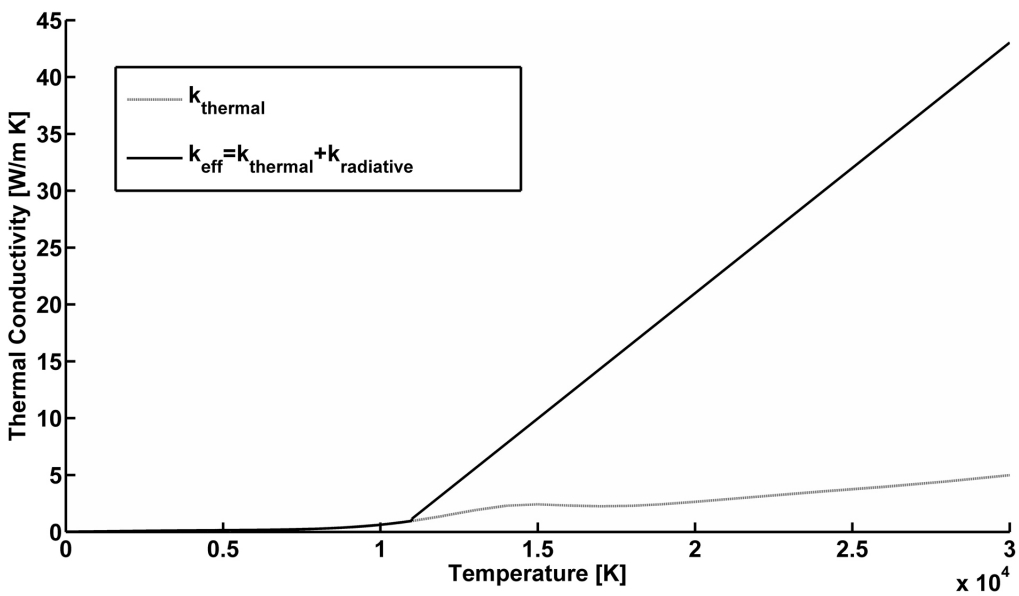

Figure 3.2. Effective and thermal conductivity of argon LSP.

Viscosity data in the range 100-20,000 K were approximated using a six-degree piecewise polynomial taken directly from Chen et al. [89]. Although model results were only considered valid below 20,000 K, viscosity values from 20,000 K to 30,000 K, based on a linear approximation of the data of Murphy and Arundell [86], were also included in the model. A graph of viscosity as a function of temperature is shown in figure 3.3

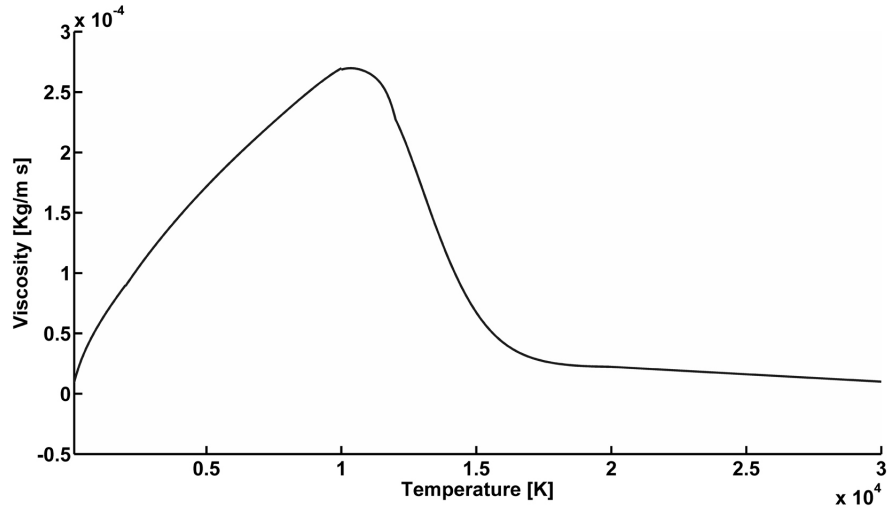

Figure 3.3. Argon plasma viscosity.

3.3.2 Properties dependent on electron density

While density, specific heat, thermal conductivity and viscosity can be considered, within the developed model, to depend solely on the plasma temperature, calculation of radiative losses and absorption within the plasma necessitates knowledge of the electron density. Based on the assumption of LTE and first-degree ionization, the electron density can be expressed using the Saha ionization equation [90],

$$\frac{n_e^2}{n_{Ar}} = \frac{2}{\Lambda^3}\frac{g_{Ar}}{g_{Ar^+}} \exp\frac{-E_{ion}}{T_e}, \tag{3.8}$$

where, n_e is the electron density, n_{Ar} is the neutral argon atom density, Λ is the thermal de Broglie wavelength, E_{ion} is the first ionization energy of argon, and T_e is the temperature in energy units. The partition function ratio of neutral and ionized argon, expressed $\frac{g_{Ar}}{g_{Ar^+}}$, was approximated by fitting the ratio of Ar I and Ar II partition functions obtained from the NIST Atomic Spectra Database (version 4.1) [64] versus temperature:

$$\frac{g_Ar}{g_(Ar^+)} = -2.3077\times10^{-29}\,T^7 + 2.3474\times10^{-24}\,T^6 - 8.8453\times10^{-20}\,T^5$$
$$+1.4851\times10^{-15}\,T^4 - 9.843\times10^{-12}\,T^3 - 1.2477\times10^{-8}\,T^2 + 0.00047534\,T + 3.7971 \tag{3.9}$$

A plot of electron density is shown in figure 3.4.

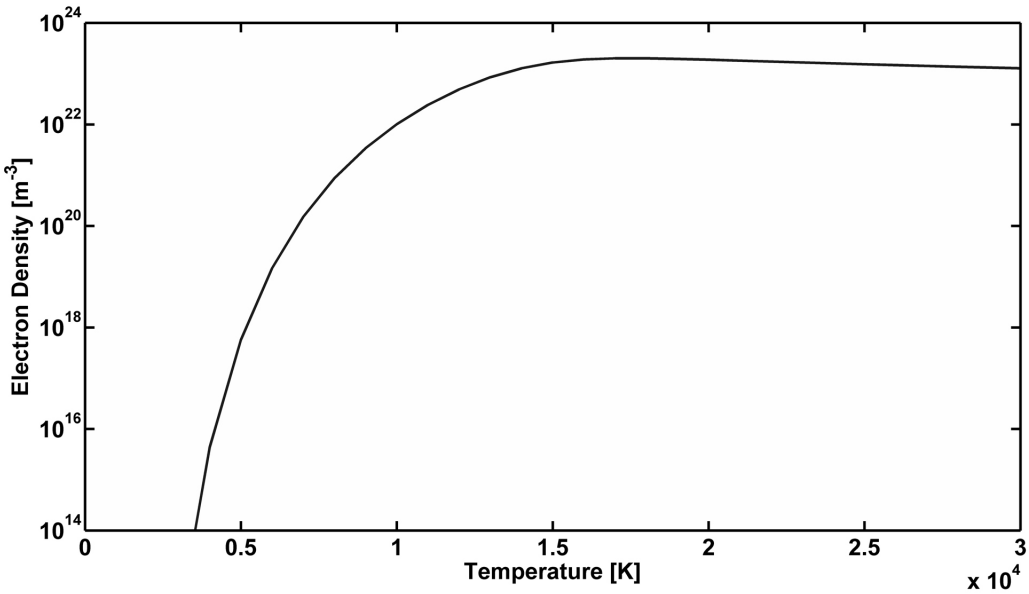

Figure 3.4. Electron density of argon plasma.

Once known, the electron density was then used to calculate the inverse bremsstrahlung absorption coefficient, α, and energy loss due to radiation emission, $-\dot{Q}_{rad}$, which appear in equation (3.3). The inverse bremsstrahlung absorption coefficient [91]

$$\alpha = \frac{7.8 \times 10^{-7} Z n_e^2 \ln \Lambda}{\nu^2 T_e^{3/2}} \frac{1}{\left(1 - \frac{\nu_p^2}{\nu^2}\right)^{1/2}}, \tag{3.10}$$

is dependent on the electron temperature in electron volts, T_e, the ionic charge, Z (set equal to one for first-degree ionization), the electron density, n_e in cm^{-3}, the laser frequency, ν, the plasma frequency, ν_p, and the coulomb logarithm for electron-ion collision, $\ln \Lambda$. The plasma frequency was approximated as $\nu_p = 8980\sqrt{n_e}$ and the coulomb logarithm was approximated as $23 - \ln(ne^2 Z T_e^{3/2})$ [92]. Figure 3.5 plots the inverse bremsstrahlung absorption coefficient up to 30,000 K. It should however be noted that since second-degree ionization begins to occur around 20,000 K, the plotted absorption values are only valid below this temperature.

Three types of radiative mechanisms exist within plasma: bremsstrahlung (free-free), free-bound transitions and bound-bound transitions. The first two

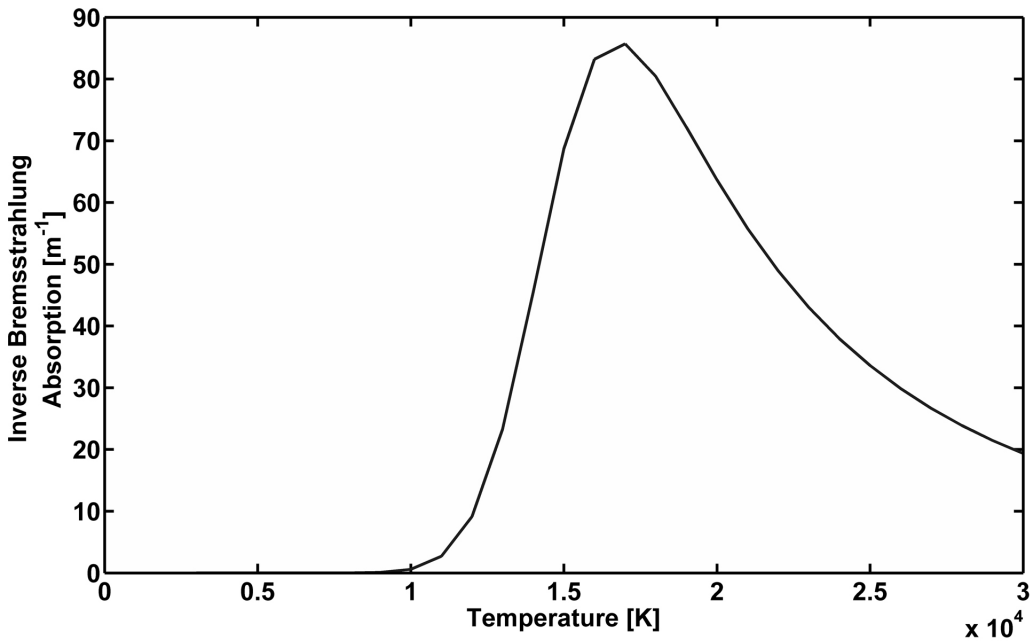

Figure 3.5. Inverse bremsstrahlung absorption coefficient of argon plasma.

mechanism collectively contribute to the continuum radiation. Oettinger and Bershader [93] cite Horn [94] as having derived an expression for the collective bremsstrahlung and free-bound radiation loss, which can be rewritten as,

$$q_r = \frac{64e^6\pi^{3/2}}{3c^3m_e^{3/2}(6T_e)^{1/2}}n_e^2(\nu_c + \frac{T_e}{h})Z_{eff}^2. \tag{3.11}$$

It should be noted that equation (3.11) is given in terms of atomic units (eV, cm, s). So for example, m_e is the mass of an electron in eV s^2 cm^{-2}. The term Z_{eff} is the ratio of the effective nuclear charge to the proton charge. A value for Z_{eff} of $\sqrt{1.5}$ is appropriate for argon [93, 94]. Additionally, ν_c, is the cutoff frequency. For argon, this cutoff-frequency corresponds to the transition from ionization to the 4p atomic level: 6.89×10^{14} Hz (2.85 eV) [93, 94]. Transitions beyond this frequency are considered to be optically thick [7]. Radiation loss from bound-bound transitions have been found to be approximately equal to continuum radiation losses [7, 93, 94]. Therefore, the total radiation loss was approximated as twice the loss from continuum radiation. Below 8,000 K, the total radiation loss was found to be negligible and set to zero within the model.

3.4 Mesh and boundary conditions

A sample domain, with boundary conditions, for the numerical model is shown in figure 3.6. The domain of the model consisted of a cylindrical pipe. At the left of the domain, a velocity inlet was designated. The velocity was uniform, constant and flowed into the domain (positive z direction). The top of the domain was an insulating, frictionless wall. The right of the domain was an atmospheric pressure outlet.

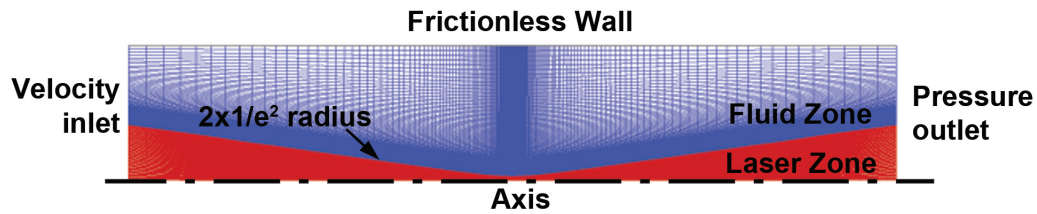

Figure 3.6. Sample domain with boundary conditions for LSP model.

Within the domain interior, two zones were designated: a laser zone and an outer fluid zone. To account for 99% of the laser power, the laser zone conformed to twice the $1/e^2$ beam radius of a focused beam with a known beam mode, waist size and M-squared value. That is, the width of the laser zone was

$$2 \times w_0 \sqrt{1 + \left(\frac{M^2 \lambda z}{\pi w_0^2} \right)^2}. \tag{3.12}$$

Within the laser zone, both the source term, αI_{laser} and $-\dot{Q}_{rad}$, were included in the energy equation (equation (3.3)). Within the fluid zone, only the radiative loss term was included. The solution procedure within each zone is discussed in further detail in section 3.5.

The size of the domain and the mesh size were chosen based on the focusing geometry and spot size of the laser beam. In the case of a PRC 5000 STS laser with Q-Mode (see section 1.4.1), a domain radius of 50 mm, a length of 100 mm downstream of focus and a length of 50 mm upstream of focus were used. In all cases, an exponentially graded discretization scheme was used, such that the highest density of cells appeared near the laser focus. Figure 3.7 shows the domain and mesh used for simulations using the Q-mode. Not shown in figure 3.7 is a

center line, at z=0, connecting the tops of the fluid and laser zones. This center line was divided into 120 divisions, with an exponential ratio of 0.17.

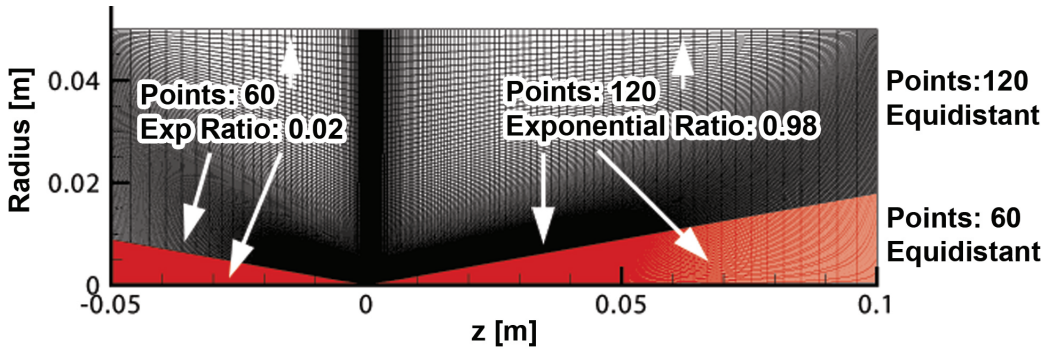

Figure 3.7. Domain and mesh used for simulations using the PRC Q-mode

3.5 Solution procedure

The continuity and momentum equation were solved in Ansys Fluent [95] using the pressure-based, finite-volume method. In the pressure-based scheme, the continuity and momentum equations were used to derive a pressure equation from which the velocity field was obtained. Multiple iterations ere required for the velocity field to satisfy continuity. As shown in table 3.1, a second-order, upwind scheme was used for both velocity and enthalpy interpolation, a second-order scheme was used for pressure interpolation and the SIMPLE (Semi-Implicit Method for Pressure Linked Equations) algorithm [96] was used for pressure-velocity coupling. In all cases, a second-order scheme was used for improved accuracy of the final solution.

Table 3.1. Parameter interpolation schemes.

Model Parameter	Scheme
Velocity interpolation	Second-order upwind
Enthalpy interpolation	Second-order upwind
Pressure interpolation	Second-order
pressure-velocity coupling	SIMPLE

To initialize the problem, a constant axial velocity and a zero radial velocity were assigned to all cells. Additionally, a temperature of 300 K was assigned to

all cells except for a small region near the focal region of the laser beam. This is analogous to sparking a LSP under experimental conditions. Without this high-temperature region, CO_2 laser radiation would not be absorbed anywhere in the domain due to the very low electron density, and inverse bremsstrahlung absorption, at 300 K. The high-temperature region was typically as wide as the laser beam diameter, one to three millimeters in length and 14,000 K. Varying the size of the high-temperature region did not have an effect on the steady-state solution.

Under-relaxation was used to stabilize the solution convergence. That is, new values for predicted variables were reduced, or relaxed, based on an explicit relaxation factor: $Used\ Value = Old\ Value + Relaxation\ Factor \times (Predicted\ Value - Old\ Value)$. Typical under-relaxation factors used are shown in table 3.2—these factors were chosen by trial and error such as to minimize the number of iterations required for convergence while maintaining a stable solution. It was not found to be necessary to modify the default solution limits on pressure (1 Pa to 5×10^{10} Pa,). However, a minimum and maximum temperature limit of 290 K and 29,000 K was imposed. Iterations were performed until a converged solution was obtained. The solution was considered to have converged when the energy flux out of the domain was within 1 % of the total energy absorbed minus the radiative losses of the LSP.

Table 3.2. Typical under-relaxation factors.

Variable	Typical under-relaxation factor
Pressure	0.15 to 0.25
momentum	0.35 to 0.45
Energy	0.90 to 0.95

3.5.1 Propagation and absorption of laser power

As discussed in section 3.4, the computational grid consisted of two zones: the laser zone and the outer fluid zone. The radius of the laser zone was defined as twice the $1/e^2$ beam radius, to account for 99% of the laser power. The laser zone is shown magnified in figure 3.8. The laser zone consisted of equally-sized partitions, light pipes, along the radial direction. The laser power was tracked along each light pipe. In the absence of absorption, the fraction of laser power

propagating through a light pipe, at any point along the axis, remained constant. Now, consider an arbitrary cell, c, within light pipe A-A' (see figure 3.8). If the fraction of power entering this light pipe is P_A and n is the number of cells in the laser path before cell c, the laser power incident on cell c, is

$$P_{indident}(c) = P_A \times \exp\left[\sum_{i=1}^{n} -\alpha_i l_i\right]. \tag{3.13}$$

Where, α_i is defined by equation (3.10) and l_i is the cell length for each cell i. Using equation (3.13), The power absorbed within cell c can then be defined as

$$P_{absorbed}(c) = P_{indident}(c) \times (1 - \exp[\alpha_c l_c]). \tag{3.14}$$

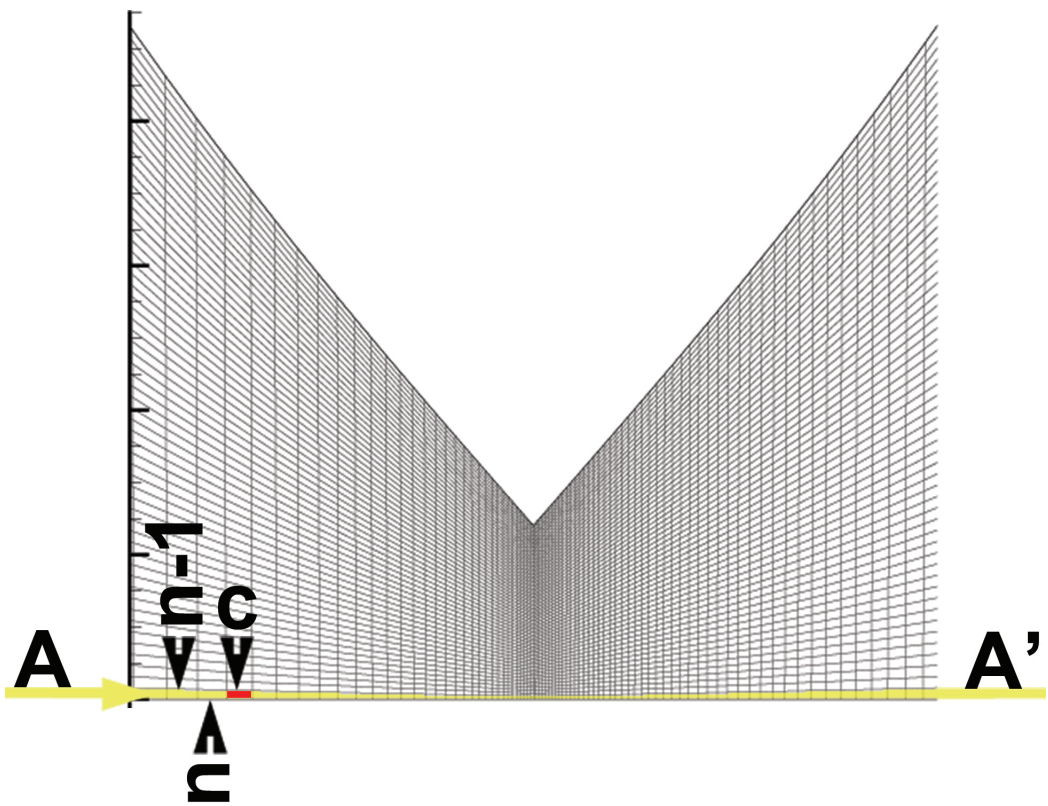

Figure 3.8. Illustration of absorption within laser zone.

Calculation of the fraction of power entering a light pipe is dependent on the laser mode irradiance and the number of light pipes within a beam $1/e^2$ radius.

For a TEM_{00}, Gaussian beam, the irradiance distribution is

$$I(r) = \frac{2P}{\pi w(z)^2} \exp\left[\frac{-2r^2}{w(z)^2}\right]. \tag{3.15}$$

Where, P is the total beam power and $w = w(z)$ is the $1/e^2$ beam radius at a position along the beam direction (z). Integrating equation (3.15) over all angles and across the width of one light pipe, from $r = w_1$ to $r = w_2$,

$$\int_0^{2\pi} \int_{w_1}^{w_2} \frac{2P}{\pi w^2} \exp\left[\frac{-2r^2}{w^2}\right], \tag{3.16}$$

results in an expression for the amount of power contained within a light pipe i,

$$P_i(\mathrm{TEM}_{00}) = P\left(\exp\left[\frac{-2w_1^2}{w^2}\right] - \exp\left[\frac{-2w_2^2}{w^2}\right]\right). \tag{3.17}$$

A similar analysis was used to calculate the fraction of power entering a light pipe for higher order modes. For a TEM_{01}^*, doughnut mode,

$$P_i(\mathrm{TEM}_{01}^*) = P \times \left[e^{-\frac{2{w_1}^2}{w^2}} - e^{-\frac{2{w_2}^2}{w^2}} + e^{-\frac{2{w_1}^2}{w^2}} - e^{-\frac{2{w_2}^2}{w^2}}\right]. \tag{3.18}$$

For a diamodal, D-Mode, beam,

$$P_i(\mathrm{D}) = 0.6 \times P_i(\mathrm{TEM}_{01}^*) + 0.4 \times P_i(\mathrm{TEM}_{00}). \tag{3.19}$$

For a quadramodal mode, Q-mode, beam,

$$P_i(\mathrm{Q}) = 0.14 \times P_i(\mathrm{TEM}_{00}) + 0.14 \times P_i(\mathrm{TEM}_{10}) + 0.36 \times P_i(\mathrm{TEM}_{01}^*) + 0.36 P_i(\mathrm{TEM}_{02}^*). \tag{3.20}$$

Where,

$$P_i(TEM_{10}) = P \times \left[e^{-\frac{2{w_1}^2}{w^2}} - e^{-\frac{2{w_2}^2}{w^2}} + \frac{4e^{-\frac{2{w_1}^2}{w^2}}{w_1}^4}{w^4} - \frac{4e^{-\frac{2{w_2}^2}{w^2}}{w_2}^4}{w^4}\right] \tag{3.21}$$

and

$$P_i(TEM_{02}^*) = P \times \left[e^{-\frac{2{w_1}^2}{w^2}} - e^{-\frac{2{w_2}^2}{w^2}} + \frac{2e^{-\frac{2{w_1}^2}{w^2}}{w_1}^2}{w^2} + \frac{2e^{-\frac{2{w_1}^2}{w^2}}{w_1}^4}{w^4} - \frac{2e^{-\frac{2{w_2}^2}{w^2}}{w_2}^2}{w^2} - \frac{2e^{-\frac{2{w_2}^2}{w^2}}{w_2}^4}{w^4} \right] \quad (3.22)$$

The code used to incorporate the the source terms in equation (3.3) as well as the temperature-dependent material properties into Ansys Fluent is included in Appendix B.

3.6 Results and Discussion

The primary outputs of the described model included the axi-symmetric temperature profile and the total laser beam absorption within the LSP. In addition to the primary outputs, which could be compared with experimental results, additional outputs included the axial velocity, radial velocity and pressure within the domain.

3.6.1 Comparison with literature

To verify the model, predictions were compared with the experimental results of Chen, Mazumder and Krier [43, 44]. These experimental results [43, 44] were used because they contained total absorbtion values and spatial temperature profiles for LSP sustained in flowing argon. Additionally, sufficient data to model the laser beam mode, power and geometry were available [43, 44]. Szymanski and Filipkowski [97] have similarly compared their model predictions with the results of Chen, Mazumder and Krier [43, 44].

In their experiments, Chen, Mazumder and Krier [43,44] used a TEM_{01}^*, annular beam with an F/7 f-number and a focal beam diameter of approximately 1 mm. Based on the description of the laser beam [44], an M-squared value of 10.58 was derived. The beam was modeled using a mesh consisting of sixty light pipes. The width of each pipe was defined as $w(z)/30$. The initial power entering a light pipe was calculated using equation (3.18).

The experimental results [43, 44] of the total beam absorbtion and plasma length, defined by the 11,600 K contour generated by a 5 kW CO_2 laser, were compared with the model for a flow range of 1.97 to 9.85 m/s. The most reliable

results presented by Chen, Mazumder and Krier [43, 44] were the total beam absorbtion data, to which a 5 % experimental error was attributed. The temperature contour measurements were less reliable. In addition to the claim of a 10 % experimental error, the temperature contours were near-rectangular rather than the expected tear-drop shape.

A comparison of the predicted total beam absorbtion with the data of Chen, Mazumder and Krier [43, 44] is shown in figure 3.9. The model results compare very well with the experimental results for all flows. At a flow 3.94 m/s the model under predicts the experimental results but is almost within the estimated 5% experimental error. The total beam absorption is about 80% for all cases and displays a local maximum at around 3.94 m/s. A local maximum was also observed at the same flow speed by Chen, Mazumder and Krier [43, 44], although it was noted in their studies that the experimental error made the determination of a local maximum unreliable.

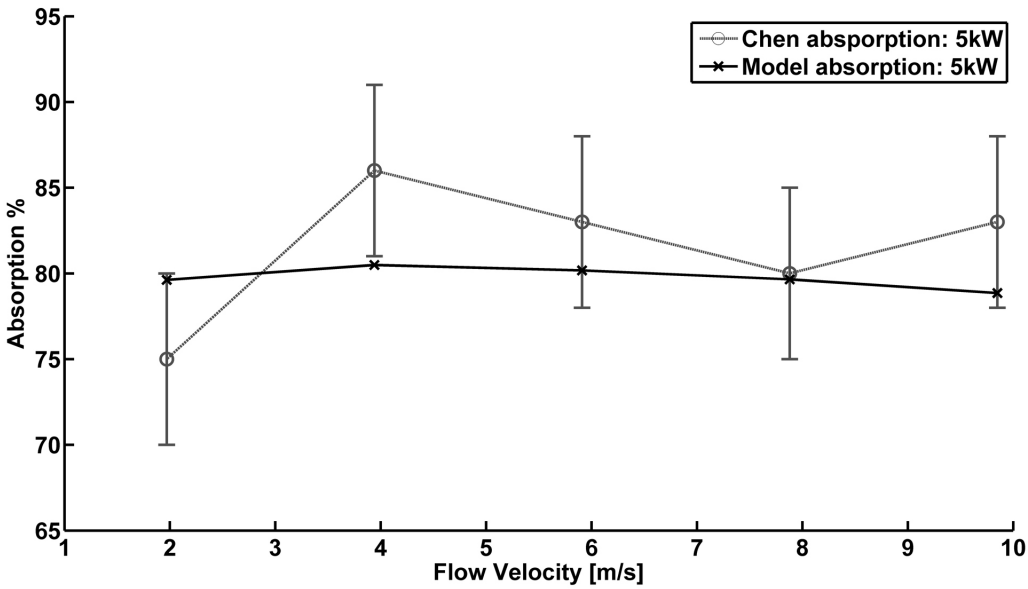

Figure 3.9. Comparison of Chen, Mazumder and Krier's [43,44] total beam absorption with model results.

Chen, Mazumder and Krier [43,44] defined the size of their LSP by the 11,600 K (1 eV) temperature contour. As noted above, the temperature contour measurement, especially along the radial direction, did not appear very reliable. However,

since temperature measurement along the central axis can be somewhat less sensitive to errors due to Abel inversion [98], it was concluded that the measurements of plasma length were less prone to error than measurements of the plasma radius. Therefore, plasma length, rather than radius, was used to compare the model results to the results of Chen, Mazumder and Krier [43, 44]. To account for the estimated 10 % error in experimental measurements of the temperature contours, the results of Chen, Mazumder and Krier [43,44] were plotted against the 11,600 K, 10,400 K and 12,760 K temperature contours predicted by the model. Figure 3.10 shows that the predicted plasma length matched well with the experimental results. It can therefore be concluded that the described axi-symmetric LSP model can accurately predict the temperature and laser beam absorption with LSP using the assumption of LTE.

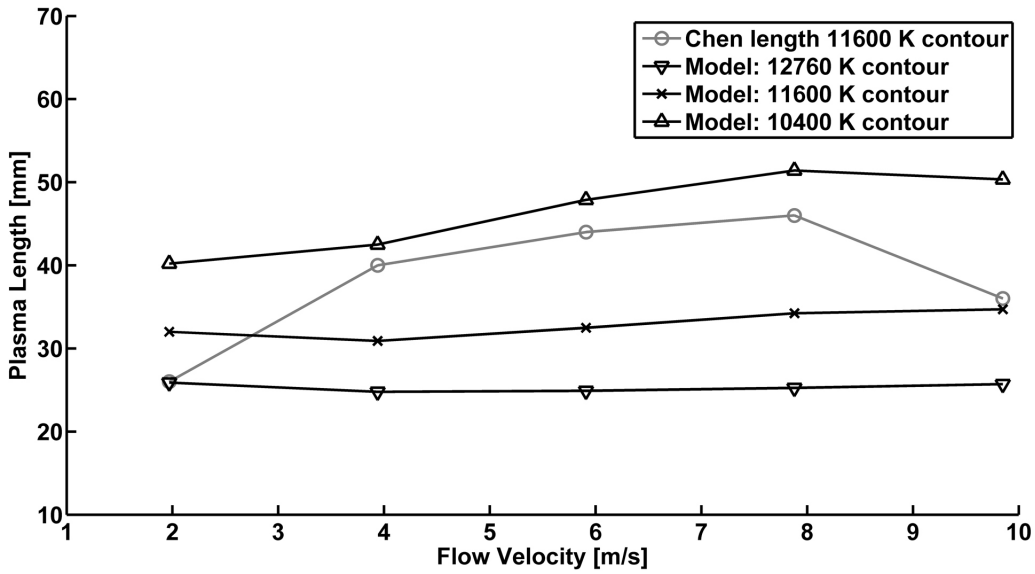

Figure 3.10. Comparison of Chen, Mazumder and Krier's [43,44] plasma length with model results.

3.6.2 Comparison with Experimental Results

In addition to validating the model by comparison with published results [43, 44], the model was also compared with experimental measurements of the LSP temperature and absorption, presented in Chapter 2. In this case, the LSP was

sustained using a 1.9 kW, Q-Mode, beam in 5 m/s argon gas mixture containing 0.5 % hydrogen. Further details were provided in Section 2.2.

Comparison of the measured 11,000 K temperature contour with the model results, figure 3.11, showed remarkable agreement. As noted in Chapter 2, direct comparison of temperatures near the center of the LSP was not possible due to reabsorption of optically thick radiation.

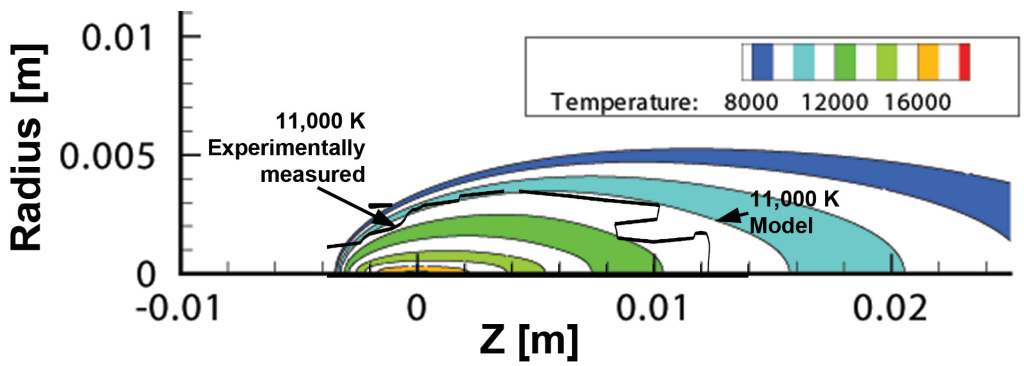

Figure 3.11. Comparison of the 11,000 K temperature contour predicted by the model with experimental results.

Along with temperature, the total beam absorption within the LSP was compared to experimentally measured absorption values. Total beam absorption was derived by measuring the portion of the laser beam transmitted through the LSP to a calorimeter located approximately 150 mm downstream of the laser focus. Moving the calorimeter further downstream from the focal position had no impact on the measurement. Measured and total beam absorption is compared with the model results in figure 3.12. While the model underpredicted the total beam absorption at an output laser power of 1.9 kW, predicted absorption fell in line with experimental results at higher laser powers. The reason for the discrepancy at 1.9 kW is unclear.

Experiments were also conducted to test the validity of assuming no beam refraction within the LSP. These experiments were performed using pure argon flowing at 5 m/s and a measured output laser power of 1.75 kW. A burn was made in a clear acrylic block at the measured output laser power (without LSP) for thirty seconds. The amount of power transmitted though an argon plasma sustained using the same output power was measured to be 0.87 kW. A second burn was

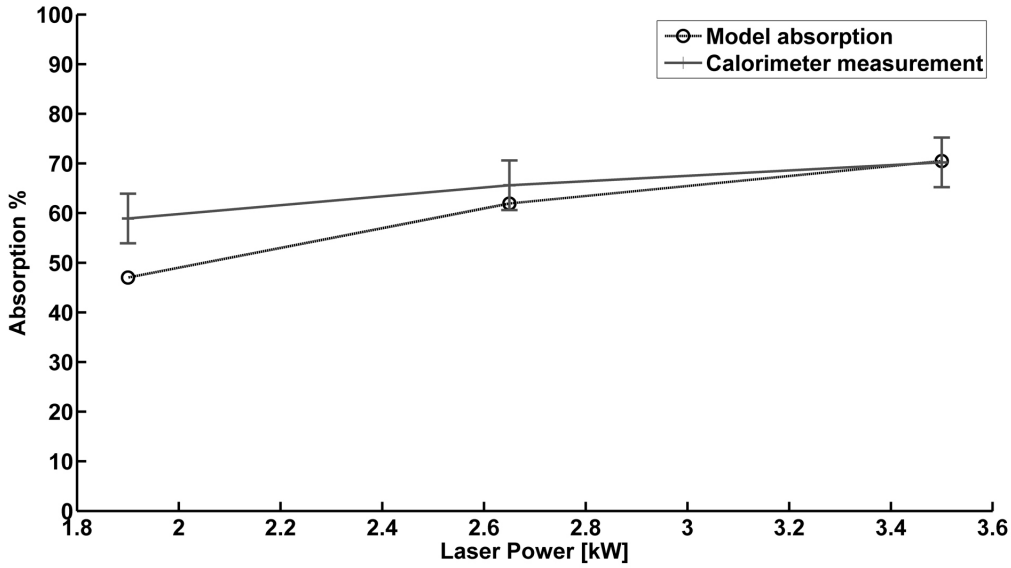

Figure 3.12. Comparison of Q-Mode total beam absorption within LSP as a function of laser power.

made at the same off-focal distance as the first burn but for a length of time adjusted such that the total power incident on the acrylic block was equal for both burns. The depth profiles of both burns are shown in figure 3.13. The FWHM of the burn profile made with the LSP was less than 10 % larger than the burn made with the laser beam alone. Based on this result, it was concluded that neglecting beam refraction within the model was valid.

3.6.3 Prediction of the effect of various beam modes on LSP

As noted in section 3.1, various authors have modeled the effect of gas flow speed and focusing geometry on LSP absorption and size. However, it does not appear that anyone has investigated the effect of laser beam mode, taking into account non-uniform beam absorption across the laser beam width. An advantage of the light-pipe approach used in the described LSP model is the ease with which it is possible to model various laser beam modes, as described in Section 3.5.1. To investigate this effect, three beam modes, TEM_{00}, TEM^*_{01} and a D-mode, were compared with the results of the LSP generated by a Q-Mode beam. In all cases,

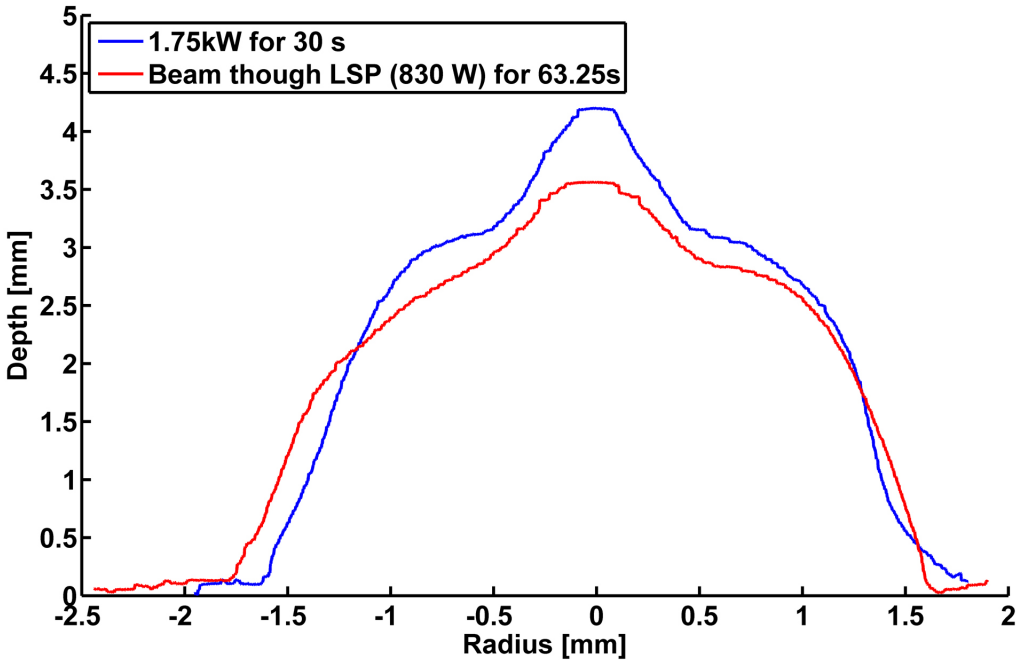

Figure 3.13. Depth profile of burns in acrylic caused by an output laser power of 1.75 kW and by the beam transmitted through an argon LSP. Little refraction of the beam was observed.

the laser geometry was set to be the same as for the Q-Mode.

Figure 3.14 juxtaposes temperature contours of a LSP generated by a 1.9 kW Q-Mode laser with that generated by a TEM_{01}^{*} laser mode with the same power. Both LSPs were modeled in a 5 m/s argon gas flow. Figure 3.15 shows the temperature contours for a plasma generated under the same conditions but with TEM_{00} mode and D-Mode laser beams. It can be observed that the LSP generated by the TEM_{00} mode beam was shifted further upstream than any of the other modeled beams. Along with this, the plasma length and volume, arbitrarily defined by the 11,600 K contour, was larger than any other modeled mode. A comparison of the total beam absorption versus the modeled beam modes is shown in table 3.3. Absorption was highest for the TEM_{00} mode, followed by the D-Mode, TEM_{01}^{*} and Q-Mode. Thus, if maximum absorption of the total laser beam is desired, as is the case in many LSP applications, it would behoove the experimentalist to select a TEM_{00} mode laser beam.

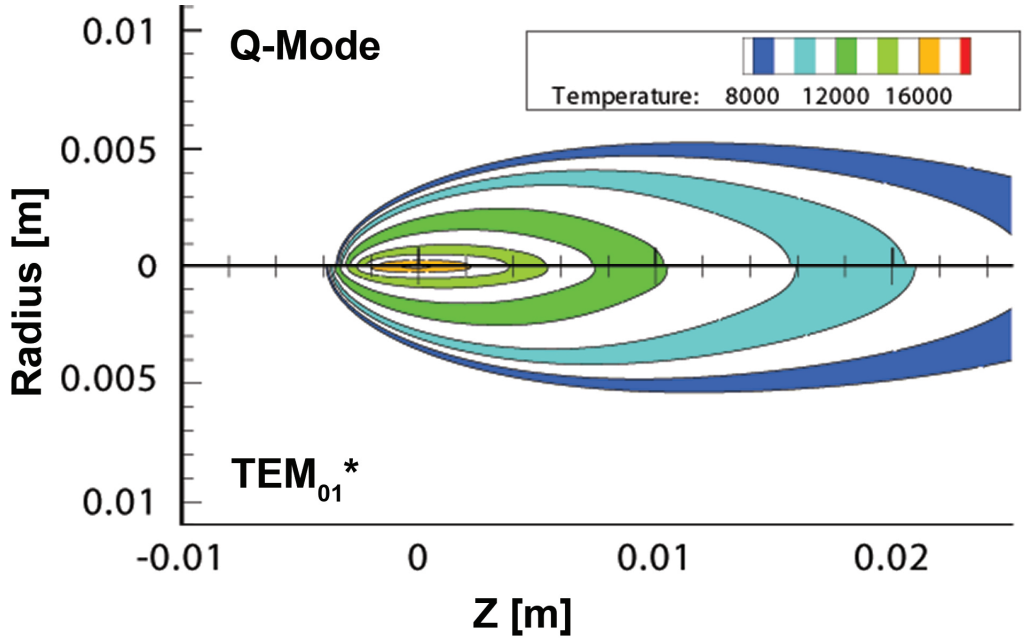

Figure 3.14. The effect of beam mode on LSP geometry using a 1.9 kW laser and a 5.0 m/s argon flow speed. The LSP sustained by TEM_{01}^{*} mode is longer and shifted further upstream than that generated by a Q-Mode.

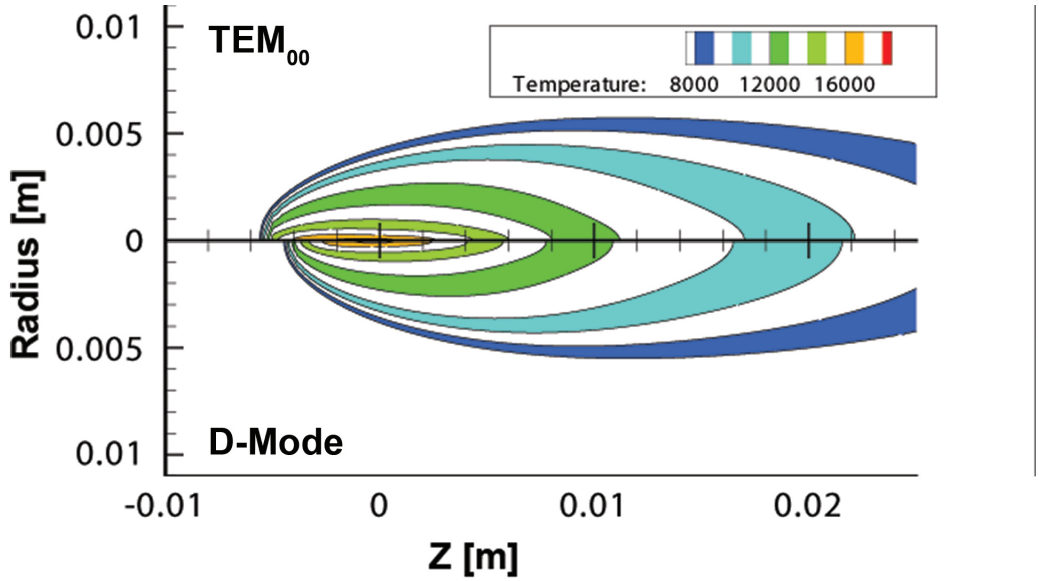

Figure 3.15. The effect of beam mode on LSP geometry using a 1.9 kW laser and a 5.0 m/s argon flow speed. The LSP sustained by TEM_{00} mode is longer and shifted further upstream than that generated by a D-Mode.

Table 3.3. Percentage of total beam absorption within LSP generated by a 1.9 kW laser in a 5 m/s argon flow under various laser modes.

Laser mode	Percent of total beam absorption
Q-Mode	47%
D-Mode	52%
TEM_{01}^{*}	49%
TEM_{00}	58%

3.7 Concluding Remarks

The developed numerical model predicted the temperature distribution and total beam absorption within a laser-sustained plasma in a forced convective flow of argon under various flow speeds. The model was solved within the ANSYS FLUENT software package using the finite volume method. Temperature dependent thermal and transport properties of argon plasma were used under the assumption of LTE.

Model results (total beam absorbtion and plasma temperature) compared very well with the experimental results of Chen, Mazumder and Krier [43, 44]. Results were also in good agreement with the measured 11,000 K temperature contour presented in Chapter 2. Total beam absorbtion of the laser beam within the LSP also agreed well with experimental results at laser powers above 1.9 kW. The model however underpredicted total beam absorbtion at 1.9 kW.

The steady-state LSP model assumed axial symmetry, LTE, and negligible refraction of the laser beam. Good agreement with experiments adds creditability to these assumptions. The assumption of negligible beam refraction was further verified experimentally. The algorithm, an alternative to the ray tracing method, used to calculate the laser power absorbed by the plasma, allowed modeling of various laser beam modes. Numerical investigation of the effect of various laser beam modes on total beam absorbtion and temperature distribution predicted that maximum absorption could be achieved using a TEM_{00} laser beam mode.

Chapter 4

Application of laser-sustained plasma to the nitriding of titanium

Thus far, the majority of this thesis has dealt with finding and modeling LSP properties and parameters. To simplify the task, an argon LSP was studied and numerically modeled. However, the ultimate goal of this work, as outline in Chapter 1, is to utilize LSP for materials processing applications. While applications of a pure argon LSP to materials processing may be possible, perhaps in heat treating or surface structuring of components, using a chemically reactive gas in place of or in addition to argon enables chemical transformation of the substrate and the ability to tailor surface and subsurface properties. An example of such a process is the nitriding of titanium. The following sections cover the topics of single-trail and multi-trail nitriding of titanium using a LSP.

Portions of Sections 4.1 and 4.2 have been previously published by Nassar et al. [99]. Nassar's contributions to that work included conducting all experiments, analyzing and reporting experimental results as well as formulating hypotheses based on observations.

4.1 Laser nitriding

Laser nitriding has long been recognized as a method for forming titanium nitride at the surface of titanium and titanium alloys [100]. The laser beam is scanned across the surface of a titanium substrate in a nitrogen atmosphere. Nitrogen is

incorporated into the melt trail, which solidifies to form a layer of titanium nitride at the surface with an underlying layer of titanium nitride dendrites surrounded by a titanium-nitrogen solid solution.

Nitrogen is typically supplied to the substrate in one of the three ways illustrated in figure 4.1 [101]. A deficiency of the side-nozzle arrangement (figure 4.1 (a)) is difficulty with alignment and turbulence [101]. Misalignments can lead to oxidation [101]. According to Bell et al. [102], to prevent oxidation, the gas stream exiting the nozzle must cover at least three times the width of the melt trail. The coaxial arrangement (figure 4.1 (b)) does not suffer from alignment issues but turbulence has been cited as resulting in poor surface finish [101]. The enclosed chamber (figure 4.1 (c)) eliminates both misalignment and turbulence issues but places restrictions on the size of the substrate and may require vacuum pumping to eliminate gas contamination. An alternative to these techniques is the use of shielding, bell-jar devices [103, 104] or specially designed nozzles with varying degrees of sophistication [105, 106]. In all cases, limiting oxygen contamination is critical.

A variety of laser systems have been employed in laser nitriding of titanium: pulsed and continuous-wave (CW) CO_2 [100–102, 105, 107–113]; neodymium-doped yttrium aluminum garnet (Nd:YAG) [101, 114–116]; Ti-sapphire [115]; excimer [107, 115, 117]; and free-electron lasers [115, 118–120].

Laser nitriding is a complex process which, following Liu et al. [121], has been described with minor variations in interpretation by Kloosterman and DeHossen [111] and Höche and Schaaf [120] as involving the following sequence of steps:

1. surface absorption: $[Ti] + N_2 \rightarrow [Ti]+[N_2]$
2. nitrogen decomposition: $[N_2] \rightarrow 2[N]$
3. nitrogen transference: $[N]_{surface} \rightarrow [N]_{inside}$
4. titanium nitride precipitation: $[Ti(N)] \rightarrow TiN + [Ti(N)]'$
5. melt solidification: $[Ti(N)]' \rightarrow TiN + \alpha\ Ti(N)$

where [ ] refers to a solution and (N) represents N in titanium structure (notation due to Liu [121]).

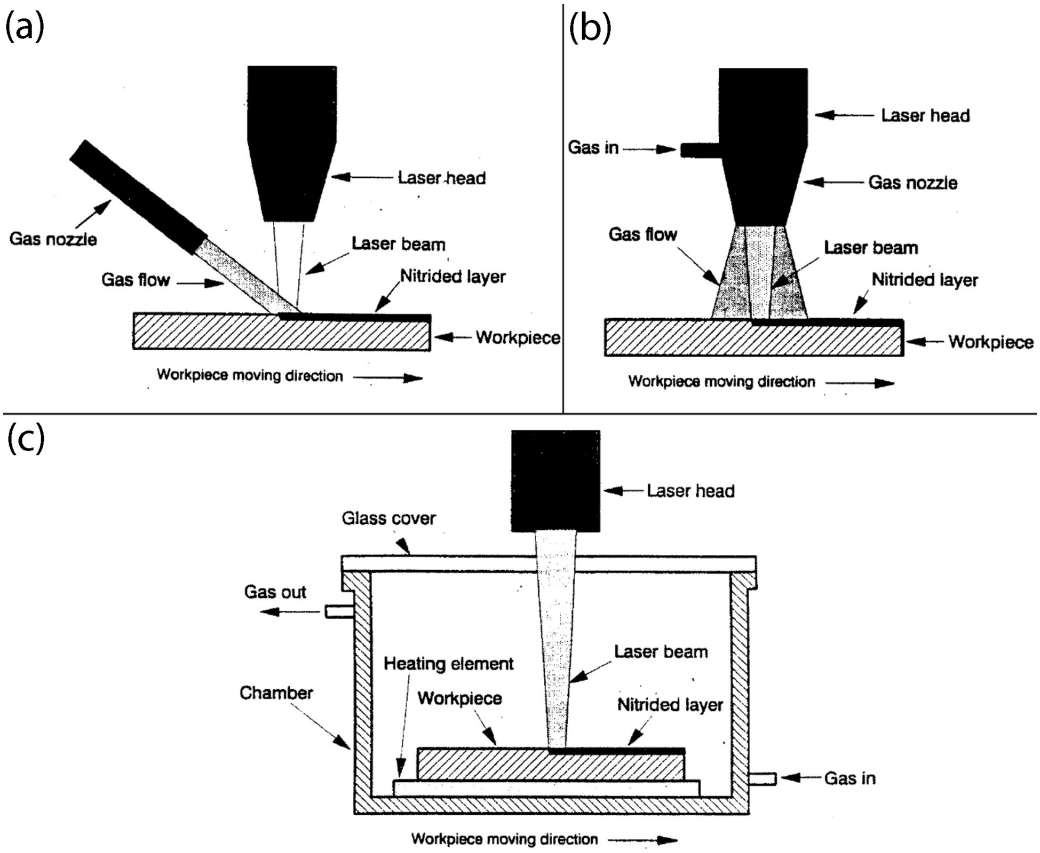

Figure 4.1. Three different laser nitriding setups: (a) side gas nozzle; (b) coaxial gas nozzle; and, (c) enclosed chamber. Reprinted, with permission, from Xue, L., M. U. Islam, A. K. Koul, M. Bibby, and W. Wallace (1997) Materials and Manufacturing Processes, 4, pp. 25-47. [101].

Höche and Schaaf [120] describe three generalized process chains based on their own works and the research literature, shown in figure 4.2, for laser nitriding. All three processes are described as being solely dependent on local surface heating and the resulting surface temperature of the substrate—this is in contrast to the work described here where plasma can be sustained independently of and prior to surface heating of the substrate. According to Höche and Schaaf [120], if the substrate surface temperature is below the melting point, the process is governed by nitrogen diffusion. However, if melting is achieved, convection enhances the transference of nitrogen into the melt. Finally, if the substrate temperature is sufficient to achieve significant vaporization (presumably, the so-called "evaporation temperature" is the boiling point), plasma is said to form, resulting in atomic nitrogen, which is

absorbed more readily than molecular nitrogen but may also result in a reduction of energy reaching the substrate due to "plasma shielding." While all three cases can result in a nitrided surface, nitriding above the "evaporation temperature" is recommended by Höche and Schaaf [120], with the caveat that keyhole formation should be avoided.

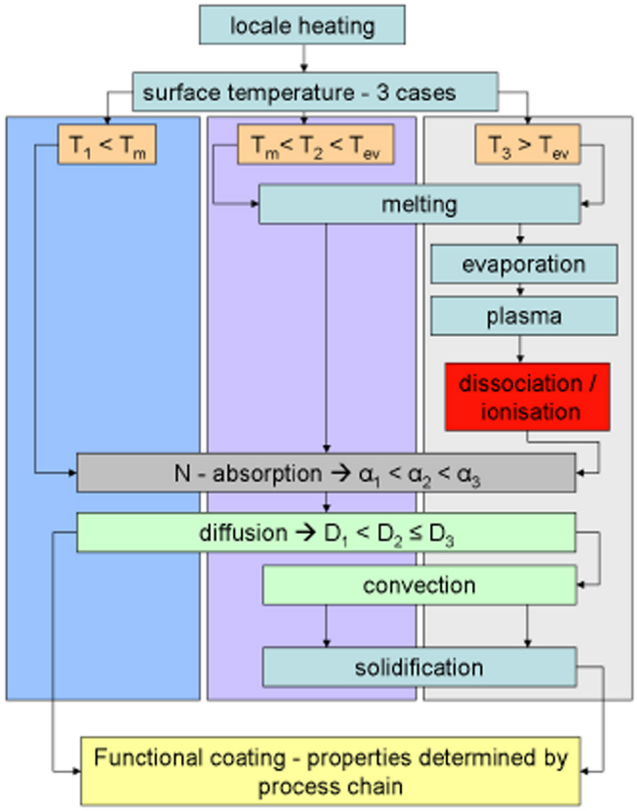

Figure 4.2. "Determination of different process chains depending on the surface temperature T_i—(T_m, melting point; T_{ev}, evaporation point; α_i, absorption coeff; D_i, diffusion coeff.)". The subscripts refer to the different surface temperature ranges. Reprinted, with permission, from Höche, D. and Schaaf, P. (2011) Heat and Mass Transfer, 47(5), pp. 519-540. [120].

4.1.1 CO_2 Laser nitriding of titanium

A great deal of research has been published on CO_2 laser nitriding of titanium. Table 4.1 categorizes some prominent publications based on the mode of operation (CW or pulsed) and the substrate material. In addition to commercially pure

(CP) titanium (IMI115) and Ti-6Al-4V (IMI318), Ti-5.5Al-3.5Sn-3Zr-1Nb-0.3Si (IMI829) has also been studied [105].

Table 4.1. Categorization of publications on CO_2 laser nitriding of titanium.

CW/Pulsed	Substrate	Citation
CW	Commercially pure Ti	[100, 105, 108, 109, 111, 122–124]
CW	Ti-6Al-4V	[101–104, 110, 112, 121, 123]
Pulsed	Commercially pure Ti	[107, 125, 126]
Pulsed	Ti-6Al-4V	[101, 104]

With respect to CP titanium, the microstructure of the nitride layer consists of a thin layer of solid titanium nitride at the surface with titanium nitride dendrites extending into an alpha titanium matrix below. The titanium matrix may also contain alpha-prime, also known as martensitic titanium. A typical top surface and cross-section is shown in figure 4.3 [123]. As shown in figure 4.3, the melt zone is non-hemispherical and asymmetric. This is very typical of laser nitrided titanium samples [101,104,108,109,111,115,121] and has been attributed to capillary action within the melt pool due to surface tension [111, 123]. Flow within the melt pool is also complicated by the incorporation of nitrogen and formation of dendrites within the melt. The nature of the melt zone shape will be expanded on in the section 4.2.3.

The volume percentage of dendrites can be reduced by using nitrogen-argon gas mixtures in place of pure nitrogen. This has also been observed to have an effect on the melt pool shape and cracks within the nitride layer [104, 105, 108, 120, 122]. Cracks within the nitrided layer are a persistent problem but can be mitigated using low concentration of nitrogen or reducing the nitrogen flow rate [105, 109, 111, 112, 122, 123]. Reduction of the nitrogen concentration or flow rate, however comes at the expense of hardness. Hardness values, for nitriding of CP titanium with pure nitrogen, higher than 1900 Vickers Pyramid Number (HV) have been reported [108, 122, 123].

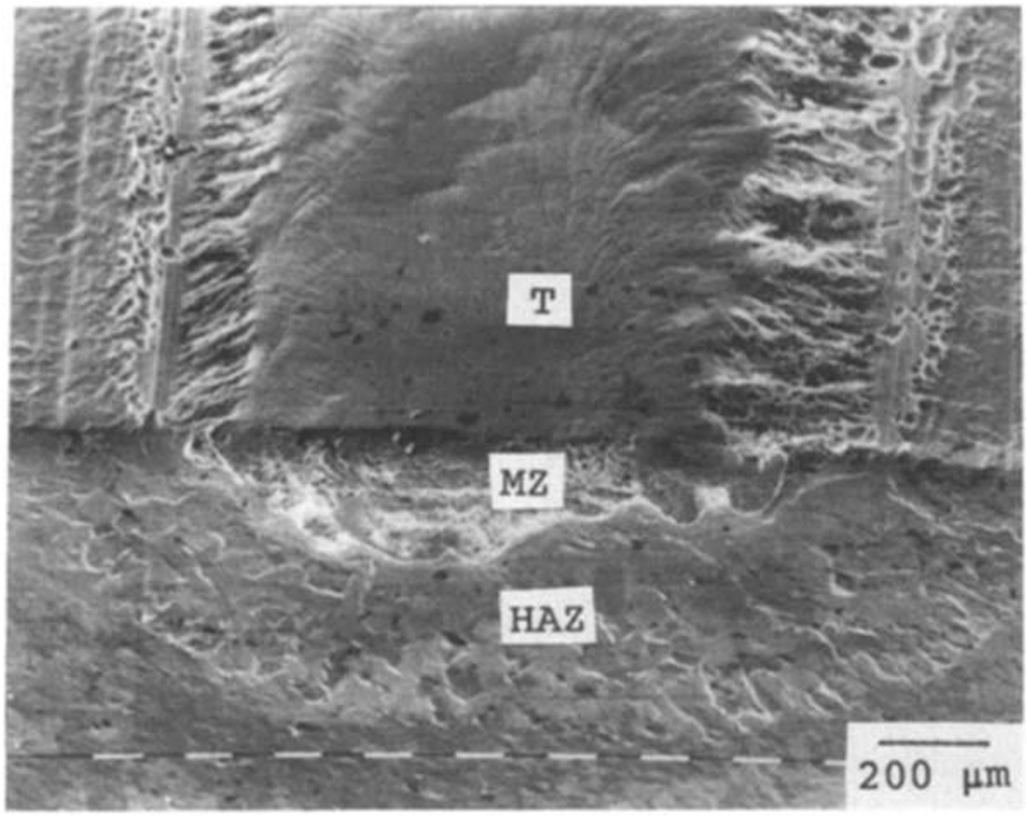

Figure 4.3. SEM image of CO_2 laser nitrided sample showing the top surface (T), melt zone (MZ)and heat-affected zone (HAZ). Reprinted, with permission, from Mridha, S. and T. N. Baker (1991) Materials Science and Engineering: A, 142(1), pp. 115-124. [123].

4.2 The role of plasma in titanium nitriding

The role of near-surface plasma during CO_2 laser nitriding of titanium is not well understood [13]. While some authors suggest that plasma may aid the laser nitriding process, arguing that near-surface plasma allows for a more efficient coupling of energy between a CO_2 laser and the surface of a metal [40, 41, 107, 125, 127], others ignore its role [100, 101, 103, 105, 108–110, 121–123] or try to prevent its formation [104, 111], arguing that it reduces power reaching the substrate [104, 111]. Plasma is expected to play a more important role in CO_2 laser nitriding than in nitriding with shorter wavelength lasers due to greater absorption of the laser beam within the plasma by inverse bremsstrahlung. For example, given reasonable approximations of an electron temperature of 1.5 eV and an electron density

of 10^{17} cm^3, equation (3.10) gives $\alpha = 0.2$ cm^{-1} for a CO_2 laser and $\alpha = 0.002$ cm^{-1} for a 1.06 μm Nd:YAG laser.

Several mechanisms can be argued to improve energy transfer from the laser beam to the substrate in the presence of plasma. Giren [40, 41] and Thomann et al. [107, 125] suggest that hot ions and atoms, generated by the plasma, impact the surface and activate mass-transport processes within the surface layer, which may be molten [40, 41, 107, 125]. It has also been pointed out [40, 107, 125], with some reference made to the work of Nielsen [128], that titanium's absorption of UV radiation emitted from the laser plasma is much higher than for 10.6 μm CO_2 laser radiation. Additionally, the shock wave generated by plasma ignition may also promote nitrogen incorporation and diffusion into molten titanium in the case of nitriding with a pulsed laser [107,125]. Since no shockwave is generated in nitriding with a CW laser beam, the last mechanism is not expected to play a role in the work discussed here. Höche and Schaaf [120] have also argued that plasma leads to dissociated, atomic nitrogen which more efficiently bonds with the substrate due to its higher adsorption capacity compared to molecular nitrogen.

It may be noted, that to the best of the author's knowledge, Giren [40, 41] is the only author who has explicitly attempted to use LSP (he refereed to it as a continuous optical discharge) for nitriding—in his case, the substrate was steel [40]. Although his research garnered very few external citations (according to ISI Web of Knowledge citation index), it does champion the view that LSP processing results in a different microstructure and hardness than processing with a laser beam alone [40]. This was attributed to the activation of mass-transport processes due to the presence of LSP. Additionally, it was claimed that processing with a LSP led to a 30 % increase in the surface microhardness of structural 45 steel [40]. Prior to the works of Giren [40, 41], it was, and still largely is, the view of most researches, as expressed by Raizer [30], that LSP formed during materials processing "absorbs a noticeable part of incident radiation, and as a result the surface is shielded from radiation. It makes the difficulties in the surface treatment by laser radiation" [30].

The presence of plasma near a substrate surface has also been proposed as a means to reduce oxygen contamination. Liu et al. [129] and Yu et al. [124] have, respectively, demonstrated nitriding of iron and titanium using a CO_2 laser beam

and a plasma gun simultaneously in open atmosphere. Yu et al. [124] argue that, in open atmosphere, titanium reacts more readily with excited nitrogen atoms and ions than with the surrounding, unexcited, oxygen. Thus, the presence of nitrogen plasma above a titanium surface, coupled with surface heating and melting from a CO_2 laser, allows for titanium nitriding in open atmosphere without oxidation.

In the following sections, a series of novel experiments are described to explore the hypotheses discussed above. A laser-sustained nitrogen plasma will be used to investigate the effects of plasma during laser nitriding. Conditions will be explored where (1) titanium metal can be nitrided using a pre-struck laser-sustained nitrogen plasma traversing a titanium substrate, (2) comparable conditions where nitriding occurs without a plasma being struck at the surface, and (3) nitriding occurs with a surface-struck plasma. These experiments will enable comparison of the resultant microstructures and exploration of the mechanisms of nitride formation with and without plasma. Reactant species in the plasma and near-surface regions will also be explored using CCD imaging to shed further light on the nitriding mechanisms. These experiments were designed to provide new insights regarding the role of plasma absorption, the importance of nitrogen dissociation during the laser nitriding process and the role of plasma in transferring energy to the substrate. The results may be applied to identify optimal processing regimes for the formation of near-stoichiometric titanium nitride surfaces with minimal oxidation during CO_2 laser nitriding.

4.2.1 Experimental details

The experimental setup used in this investigation and a CCD image of a nitrogen LSP are shown in figures 4.4(a) and 4.4(b), respectively. Refer to Section 1.4 for details on the characterization of the laser beam and ignition of LSP. Nitrogen gas (99.995% purity) was supplied to the laser cutting head at a flow rate of 16 slpm. It may be noted that the flow rate given in [99] was incorrectly reported as 10 slpm. The nitrogen gas flowed coaxially out of a 10 mm diameter laser-head nozzle above the titanium substrate. A measured output power of 3.5 kW was used for processing unless otherwise stated. The laser beam was focused via a 50.8 mm diameter, 127 mm focal-length, ZnSe lens. The focal plane was

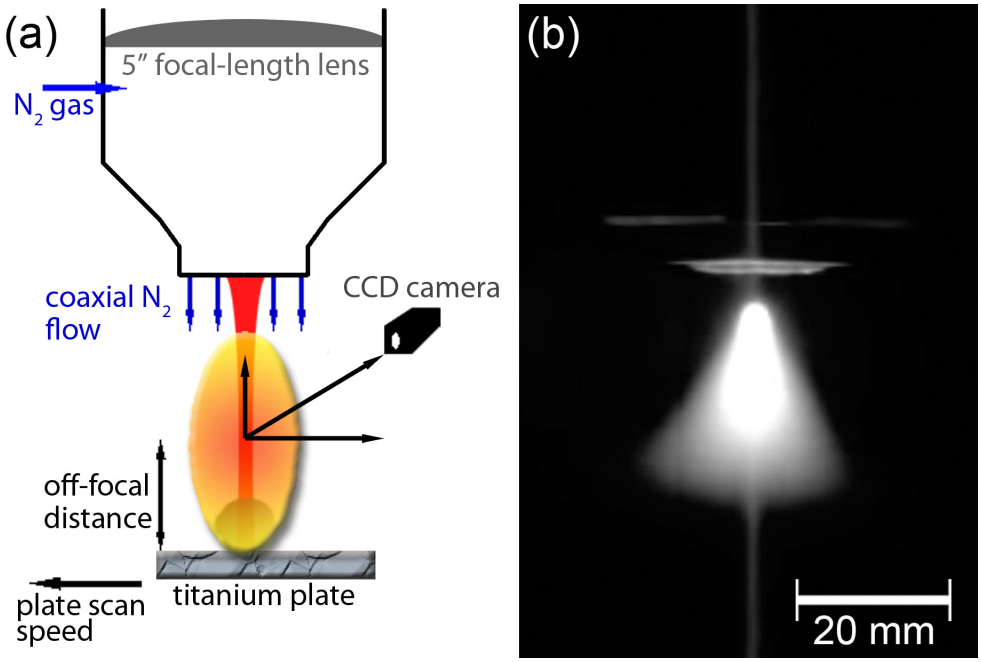

Figure 4.4. Experimental setup.

13 mm below the nozzle head. Commercially pure (also known as CP, Grade 2 or IMI115) titanium samples of 3.175 mm thickness were mechanically polished to a 600 (P1200) grit and cleaned with acetone and isopropyl alcohol before processing. As shown in figure 4.4(a), the titanium samples were placed at varying off-focal distances (OFDs), measured from the focal plane of the laser beam.

A nitrogen LSP was generated by one of the methods described in Section 1.4. Once generated, the LSP was sustained indefinitely near the focus of the laser, isolated from confining walls or a substrate. The titanium samples were translated under and perpendicular to the laser beam and coaxial LSP, at speeds varying from 10 to 120 mm/s. An Ocean Optics, Inc. HR4000 CG UV-NIR spectrometer with a spectral range from 200 to 1100 nm and an optical resolution of 0.50 nm (FWHM) was used for identification of excited and ionized species within the LSP. The process was also monitored with a JAI TM-6740CL CCD camera equipped with a 430 nm (10 nm FWHM) band pass filter and a 870 nm (10 nm FWHM) band pass filter. A 0.6 optical density, neutral density (ND) filter was used with the 870 nm filter and a combination of 0.6 and 0.4 optical density ND filters was used with the 430 nm filter to prevent image bloom. Prior to selection of the band pass filter, an

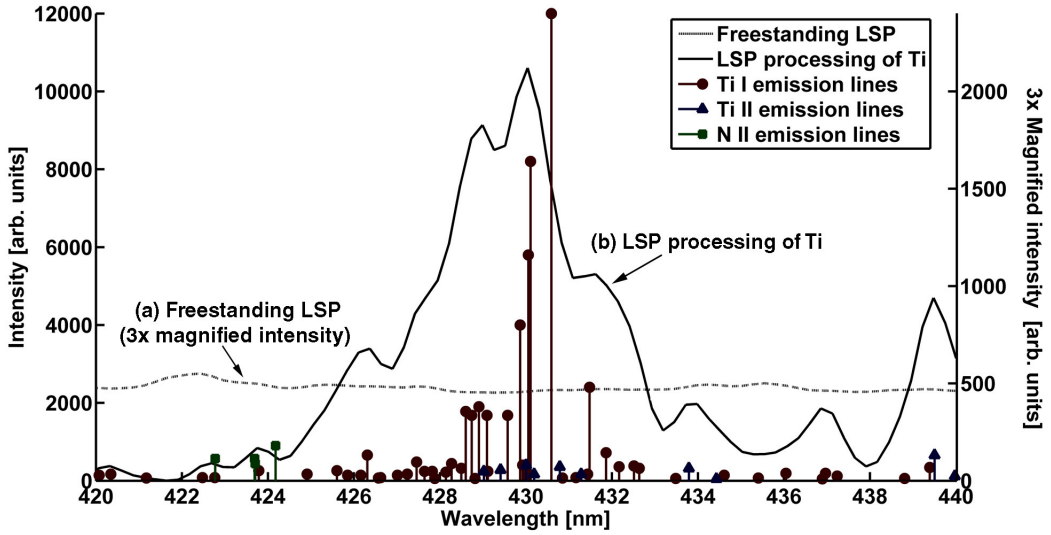

Figure 4.5. Optical spectrum, around 430 nm, recorded during processing of a titanium substrate at a translation speed of 75 mm/s and an off-focal distance of 4 mm (black) and of a three times magnified spectrum of a LSP sustained far away from any surface (dashed and grey).

analysis of the overall optical emissions from LSP was conducted as described in Section 2.2. Figure 4.5 compares (a) an optical emission spectrum around 430 nm from a freestanding nitrogen LSP sustained far away from any surface, with (b) an optical emission spectrum recorded during processing of a titanium substrate with a pre-struck nitrogen LSP at a translation speed of 75 mm/s and an off-focal distance of 4 mm. Around 430 nm, the observed emission peaks from the pre-struck LSP processing of Ti spectrum were attributable to excited, atomic (Ti I lines) and ionized titanium (Ti II lines), with a few ionized nitrogen (N II lines) below 425 nm. Figure 4.6 compares both spectra around 870 nm, where the observed emission peaks were attributed to excited, atomic nitrogen (N I lines). In all cases, bremsstrahlung radiation was also observed. Based on these observations, a CCD camera with a 430 nm band pass filter was used to study the location of excited atomic titanium species and a 870 nm band pass filter was used to study the location of excited atomic nitrogen during the nitriding process. It can be noted that although several emission lines from molecular nitrogen ions could arise around 430 nm, they were neither observed nor expected due to the rapid dissociation of molecular nitrogen during the nitriding process, agreeing with

research by Thomann et al. [126].

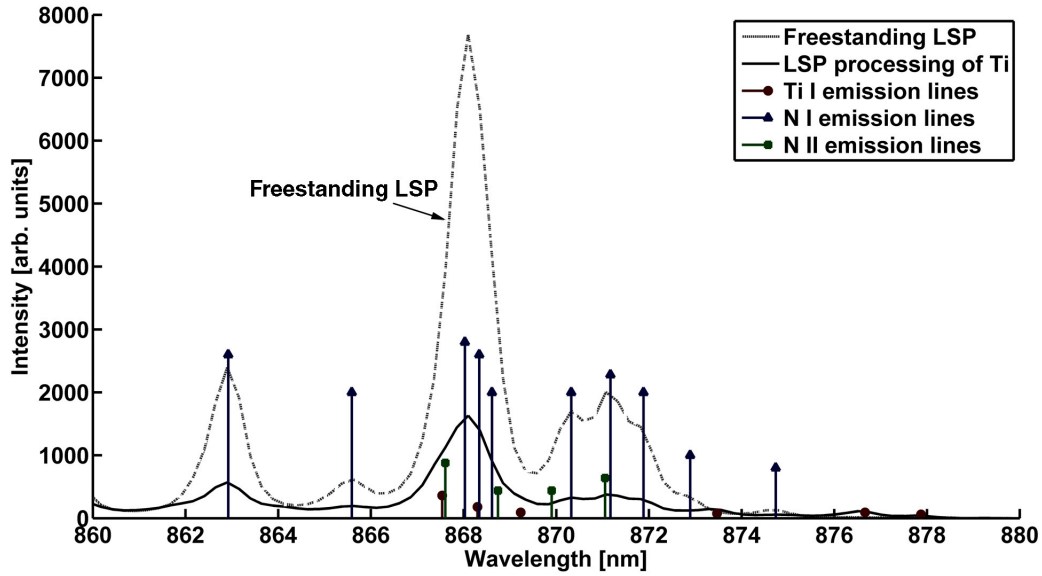

Figure 4.6. Optical spectrum, around 870 nm, recorded during processing of a titanium substrate at a translation speed of 75 mm/s and an off-focal distance of 4 mm (black) and of a free-standing LSP sustained far away from any surface (dashed and grey).

To estimate the amount of laser radiation transmitted though the LSP, a calorimeter was used to measure the residual beam power, i.e. the portion of the laser beam not absorbed by the plasma, which passed through a LSP formed in a 16 slpm flow of nitrogen using a 3.5 kW CO_2 laser beam. During the measurement, the LSP was sustained far away from the calorimeter to limit the amount of plasma radiation absorbed by the calorimeter. A plot of the measured residual beam power is shown in figure 4.7 as a function of off-focal distance, measured from the surface of the calorimeter to the laser beam focus.

Optical photographs were taken of the processed samples. A transverse cross-section of each processed sample was cut and polished. Care was taken to cut the cross-section near the middle of the trail length to avoid edge effects. The treated samples were cleaned with acetone and alcohol and were polished using standard metallographic techniques and etched in a 5 ml HF, 5 ml HNO_3 and 85 ml H_2O solution.

X-ray photoelectron spectroscopy (XPS) analyses were performed on the top surface of the processed trails. The analyses were performed using a Kratos Ana-

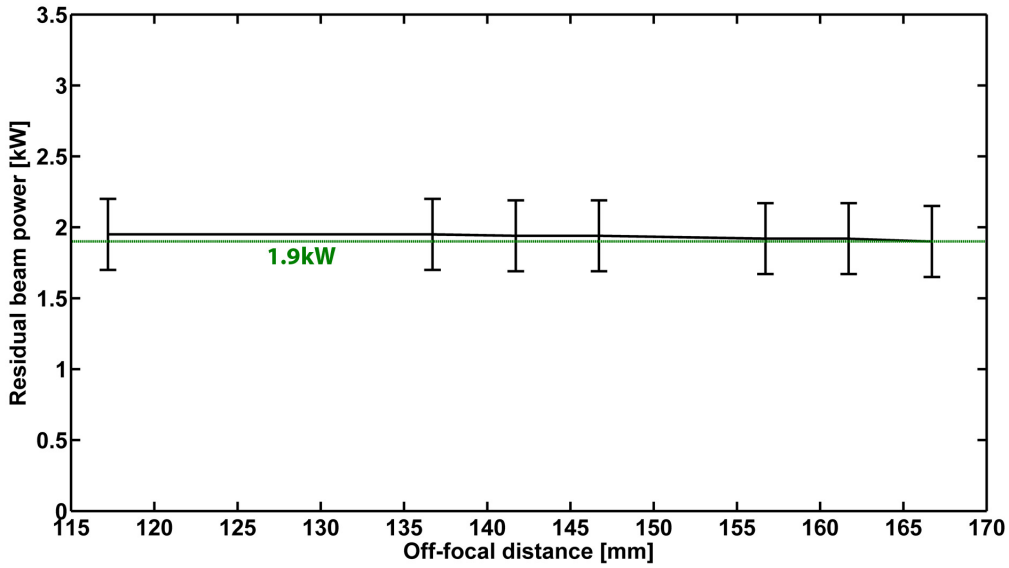

Figure 4.7. Measured residual laser beam power as a function of off-focal distance. The estimated value of 1.9 kW is shown as a green, dashed line.

lytical Axis Ultra instrument. Prior to XPS analysis, the surface of the trail was cleaned with acetone and isopropyl alcohol. To further reduce surface contamination, the cleaned samples were etched with an argon ion beam for 100 seconds. Black nanoparticulate observed during the nitriding process was collected on an aluminium stub placed 3 mm from the center of a trail nitrided at 90 mm/s and an off-focal distance of 4 mm. These powder samples were immediately stored in a vacuum desiccator after processing. They were not etched prior to analysis. The XPS data were calibrated by defining the adventitious carbon C1s peak as 284.5 eV [130]. The nanoparticulate was also imaged using a Philips (FEI) EM420T transmission electron microscope (TEM). Particles were collected onto a TEM slide by submerging the processed titanium sample in alcohol, agitating in an ultrasonic bath then dispensing a drop of the alcohol onto the slide. X-ray diffraction (XRD) analyses were conducted using a PANalytical Empyrean XRD system with automatic slits set to 0.5 mm and a beam mask of 5 mm.

4.2.2 Results

CCD imaging revealed that two distinct plasma regions, one rich in nitrogen (figure 4.8(a)) and the other rich in titanium (figure 4.8(b)), were formed during the

nitriding process. Figures 4.8(a) and 4.8(b) show CCD images taken during nitriding at an off-focal distance of 8 mm and a sample translation speed of 90 mm/s with a pre-struck LSP. An 870 nm band pass filter was used in figure 4.8(a) and a 430 nm band pass filter was used in figure 4.8(b). A top surface image of the processed sample is shown in figure 4.8(c). At this off-focal distance and translation speed, plasma could not be ignited during the translation of the titanium sample under the laser beam. To produce plasma near the surface of the sample, LSP was ignited using a titanium rod, as described in Section 1.4, prior to the translation of the titanium sample below the laser beam and LSP. Figure 4.8(a) shows that excited atomic nitrogen, N I, was very close, if not in contact with, the titanium sample during processing. Note that a slight reflection of light from the plasma is also observed on the surface of the substrate. Figure 4.8(b) shows very faint background, continuum radiation from the nitrogen LSP as well as excited and ionized titanium vapor very close to the substrate. From figure 4.8(b), it can be observed that titanium vapor was emitted from the sample during processing, but did not appear to be present within the nitrogen LSP. It may also be noted that neither CCD imaging nor emission spectroscopy showed any atomic or ionized titanium species within the LSP once the titanium ignition rod was removed.

Figures 4.9(a) and 4.9(b) show CCD images taken during processing at an off-focal distance of 8 mm and a sample translation speed of 10 mm/s. Also shown is an image of the processed surface in figure 4.9(c). It can be observed from figures 4.9(a) and 4.9(b) that under conditions where emissions from Ti I are bright (figure 4.9(b)), the emissions from N I near the surface are reduced (figure 4.9(a)). Compared to the sample translated at 90 mm/s, the titanium vapor emitted from the sample translated at 10 mm/s was greater in quantity and brighter. The size of the nitrogen LSP was smaller for the 10 mm/s case. By comparing the brightness of nitrogen near the sample for the 90 mm/s translation speed (figure 4.8(a)) with the 10 mm/s case (figure 4.9(a)), it could be concluded that there was a lower amount of excited, atomic nitrogen near the surface of the sample processed at 10 mm/s.

Under conditions where a nitrogen-rich plasma was formed near the surface of the substrate, the processed trail was smooth and uniformly gold-colored (figure 4.8(c)). At an off-focal distance of 8 mm and a translation speed of 90 mm/s, the

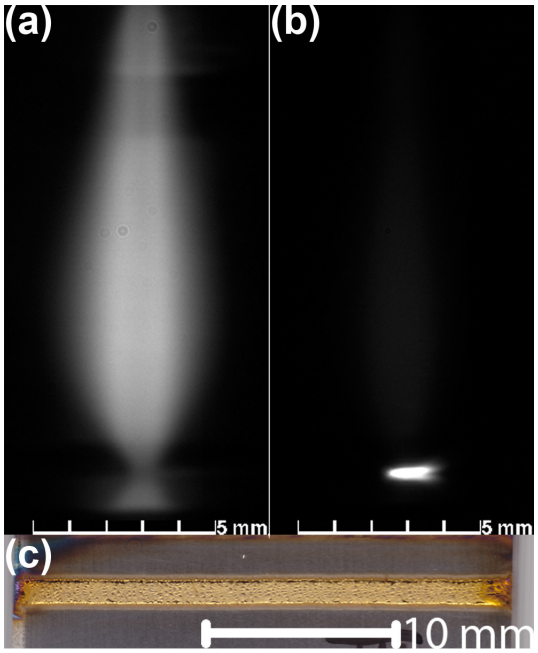

Figure 4.8. CCD images (a,b) taken during processing and surface image (c) of the processed trail at an off-focal distance of 8 mm and a translation speed of 90 mm/s with a pre-struck LSP: (a) atomic nitrogen species; (b) atomic titanium species; (c) top surface of the trail.

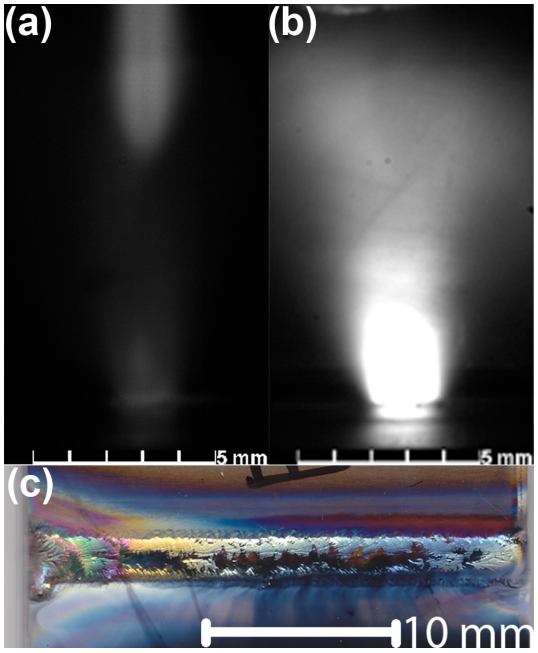

Figure 4.9. CCD images taken during processing (a,b) and surface image (c) of the processed trail at an off-focal distance of 8 mm and a translation speed of 10 mm/s: (a) atomic nitrogen species; (b) atomic titanium species; (c) top surface of the trail.

surface of the sample processed with a pre-struck LSP, shown in figure 4.8(c) was gold-colored. At the same off-focal distance but a translation speed of 10 mm/s, shown in figure 4.9(c), the sample surface was a non-uniform, greyish-blue with some hints of purple and gold. A black, non-adherent powder was deposited alongside the 10 mm/s trail.

The smooth, gold-colored layer was titanium nitride whereas the rough, white, blue and gold-colored layer contained titanium oxide. Figures 4.10 and 4.11 show high-resolution XPS spectra taken at the surfaces of the samples processed at (a) 90 and (b) 10 mm/s. The shifts and relative peak intensities of the N1s (figure 4.10) and O1s (figure 4.11) spectral peaks confirm that the surface layer of the sample processed at 10 mm/s (b) was highly oxidized, whereas the surface of the samples processed at 90 mm/s (a) consisted primarily of titanium nitride [130, 131]. It should be noted that the small oxygen O1s signal observed for the 90 mm/s surface in figure 4.11(a) corresponded to that of a native oxide layer, approximately 50 Å thick, and/or water adsorption that occurs on a titanium nitride surface stored in air [131].

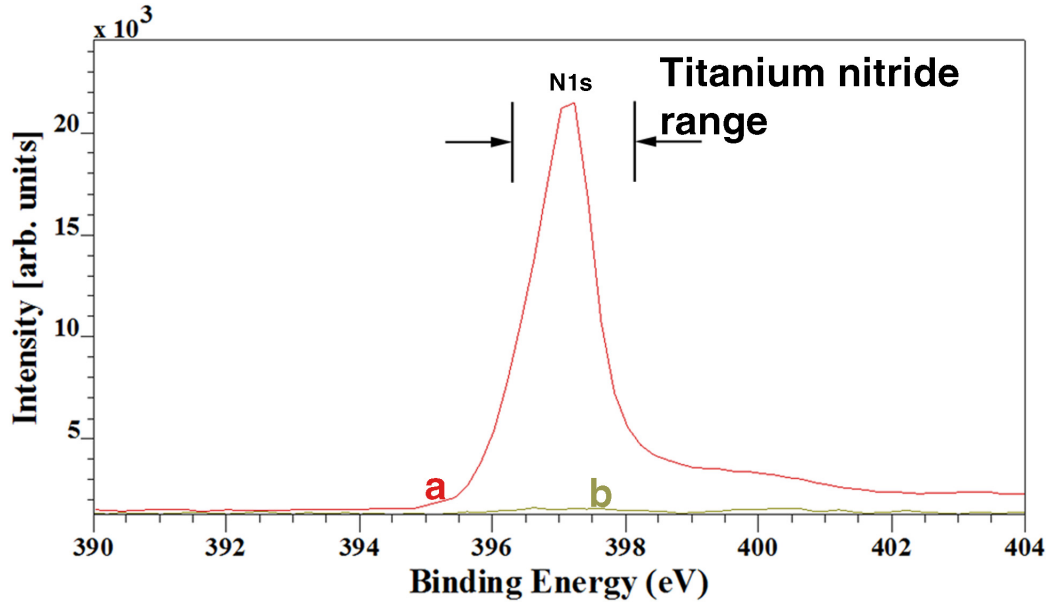

Figure 4.10. High-resolution XPS spectra from surfaces processed at an off-focal distance of 8 mm and a translation speed of (a) 90 mm/s and (b) 10 mm/s. The location and intensity of the N1s peak confirms the presence of titanium nitride in (a).

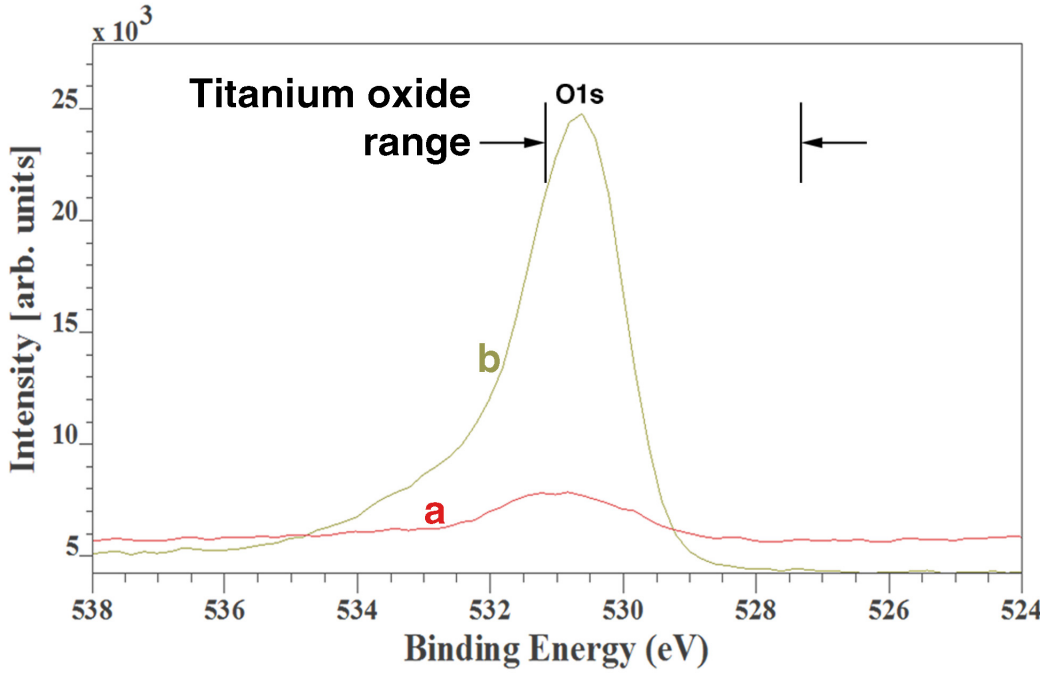

Figure 4.11. High-resolution XPS spectra from surfaces processed at an off-focal distance of 8 mm and a translation speed of (a) 90 mm/s and (b) 10 mm/s. The location and intensity of the O1s peak confirms greater surface oxidation in (b) than in (a).

X-ray diffraction from the 90 mm/s surface, shown in figure 4.12, was unable to detect the presence of titanium oxide. Both TiN and Ti peaks were clearly identified. It should be noted that the Ti_2N phase was not observed, as expected, due to the rapid cooling of the processed trail. These results, together with energy-dispersive X-ray spectroscopy analyses and film color, indicated that the surface processed at 90 mm/s was near-stoichiometric titanium nitride.

At an off-focal distance of 8 mm, there was a threshold speed for processing with a pre-struck LSP of approximately 60 mm/s, above which a continuous gold-colored surface was observed. Increasing amounts of grey and blue were observed as the sample translation speed was decreased below this threshold value. The threshold speed was found to increase with decreasing off-focal distance. Below this threshold speed, an upward shift and a dimming of the nitrogen-rich plasma region was observed. A similar effect was observed in irradiating a stationary titanium sample with a pre-struck nitrogen LSP, shown in figure 4.13. Here too, an upward shift and a dimming of the nitrogen-rich plasma region was observed

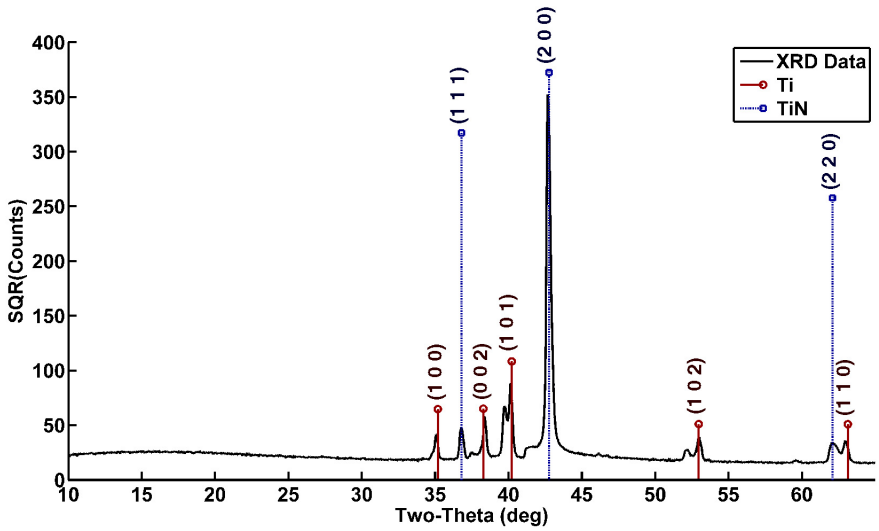

Figure 4.12. XRD spectra of samples processed at an off-focal distance of 8 mm and a translation speed of 90 mm/s. No oxide phases of titanium were detected.

with increasing vaporization of the titanium.

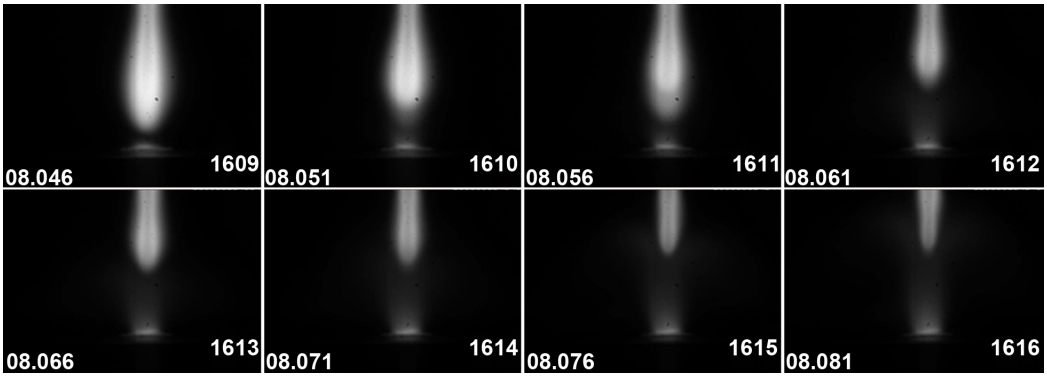

Figure 4.13. Irradiation of a stationary titanium substrate with a pre-struck nitrogen LSP, recorded using an 870 nm band pass filter. An upward shift and a dimming of the nitrogen-rich plasma region is observed with increasing vaporization of titanium. The time (sec.ms) and frame number are shown in the lower left and right, respectively, of each frame.

To further ascertain the role of nitrogen and titanium species during the nitriding process, specifically the role of plasma absorption and heating of the substrate, a titanium sample was processed at an off-focal distance of 8 mm and a translation speed of 90 mm/s without a pre-struck LSP. At this off-focal distance and translation speed, the laser power density at the sample surface was insufficient

to generate a plasma during translation of the titanium sample under the laser beam. No emissions around 430 or 870 nm were observed using the CCD camera. An additional sample was processed, at the same off-focal distance and translation speed, without a LSP, using a power approximately equal to the residual laser beam power, which was found to be approximately 1.9 kW.

The size of the pre-struck LSP, as observed with the 870 nm band-pass filter, during nitriding at 8 mm off-focus and a translation speed of 90 mm/s (4.8(a)) was similar to that of the free-standing LSP (figure 4.4(b)). (It should be noted that in figure 4.4(b) the plasma is viewed though a welding filter and so may appear different in size than the plasma observed though the 870 nm filter.) Consequently, the power transmitted through the free-standing plasma was expected to be similar to that reaching the substrate during processing at 8 mm off-focus and 90 mm/s translation speed. Such an estimate assumes little absorption by titanium vapor emitted from the sample.

The samples processed without a LSP, at 3.5 kW and 1.9 kW are shown in figures 4.14(a) and 4.14(b), respectively. Whereas the sample processed at 3.5 kW using a pre-struck LSP, figure 4.8(c), exhibited a continuous gold-colored surface layer, the sample processed without a LSP, figure 4.14(a), exhibited a multi-colored layer with clearly visible ripples. Both trails were 1.3 mm wide. The sample processed at 1.9 kW (figure 4.14(b)) was 1 mm wide. It exhibited a dull, non-uniform color along its length indicating a non-uniform surface coverage of titanium nitride [111]. The blue color in figure 4.14(a) indicated the presence of oxygen in the surface layer.

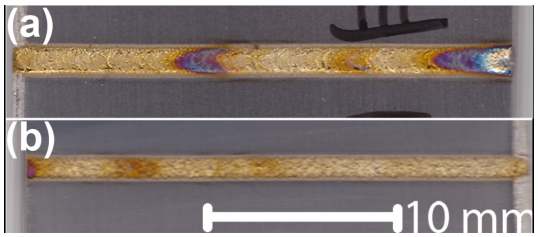

Figure 4.14. Surface images of processed trails at an off-focal distance of 8 mm and a translation speed of 90 mm/s without a pre-struck LSP: (a) top surface of the trail (3.5 kW); (b) top surface of a trail at 1.9 kW residual beam power.

Pre-ignition of a LSP was not always necessary for a nitrogen-rich plasma to form at the substrate surface. At and below an off-focal distance of 6 mm, and at

a translation speed below 90 mm/s, plasma could be struck at the surface without pre-ignition of a LSP. Such a plasma could be sustained after passing over the titanium sample. A continuous, gold-colored, surface titanium nitride layer formed when excited atomic nitrogen was present near the sample surface, regardless of whether the plasma (a) formed as the titanium sample was translated below the laser beam, or (b) was pre-struck prior to the translation of the sample. At and below a 6 mm off-focal distance and 90 mm/s translation speed, identical surfaces were observed for pre-struck LSP and for surface-ignited plasma.

Figure 4.15 shows CCD images taken with (a) 870 nm and (b) 430 nm band pass filters near the middle of the trail length and (c) a top surface image of a titanium sample processed using an off-focal distance of 4 mm and a translation speed of 90 mm/s. Excited atomic nitrogen near the sample surface and titanium emissions were observed (figures 4.15(a) and (b)). The gold-colored trail was 1.2 mm wide. The XPS spectrum from the trail surface was nearly identical to that shown in figures 4.10(a) and 4.11(a). As can be observed in figure 4.15(c), a black, non-adherent powder was deposited alongside the trail. An XPS analysis of powder collected on an aluminium stub placed 3 mm from the center of the trail nitrided at 90 mm/s and an off-focal distance of 4 mm is displayed in figure 4.16. This high resolution spectrum contained the Ti2p3/2 and Ti2p1/2 spectral peaks (solid line) together with two subcomponents of the Ti2p3/2 spectral peak (dotted and dashed lines), fitted using the CasaXPS Version 2.3.12 program. Typical binding energies for TiO_2 TiN_x, TiO and Ti are identified at the top of the diagram. The binding energies of the fitted subcomponents of the Ti2p3/2 spectral peak show that the powder was a mixture of titanium nitride and titanium dioxide [130, 132, 133]. Examination by transmission electron microscopy determined that the black particles, shown in figure 4.17, were tens of nanometers in size.

Cross-sectional micrographs of the processed samples provided further insight into the role of plasma in transferring energy to the substrate. Figure 4.18(a) shows a cross-sectional micrograph taken near the middle of the trail processed at 8 mm off-focus and 90 mm/s with a pre-struck LSP (figure 4.8(c)). Figure 4.18(b) shows a cross-sectional micrograph taken near the middle of the trail processed at 8 mm off-focus and 90 mm/s without a LSP (figure 4.14(a)). Figure 4.18(c) shows a cross-sectional micrograph taken near the middle of the trail processed

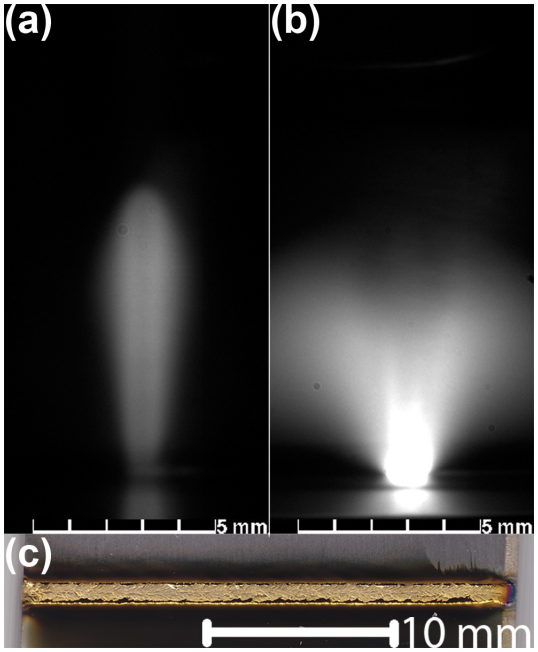

Figure 4.15. CCD images taken during titanium nitriding at 4 mm off-focus and 90 mm/s: (a) atomic nitrogen; (b) atomic titanium; (c) top surface image.

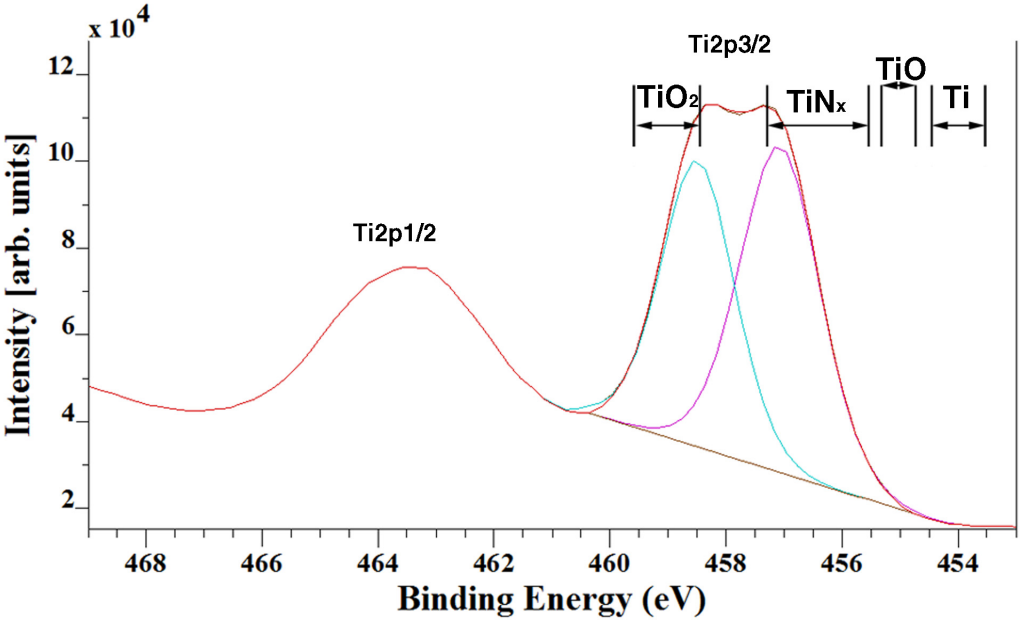

Figure 4.16. A high-resolution XPS spectrum of the black nanopowder (solid line). Shifts of the Ti2p3/2 peak for TiO2, TiN_x, TiO, and Ti are noted between arrows. The two subcomponent shifts of the Ti2p3/2 peak confirm the presence of TiN_x (dotted line) and TiO_2 (dashed line).

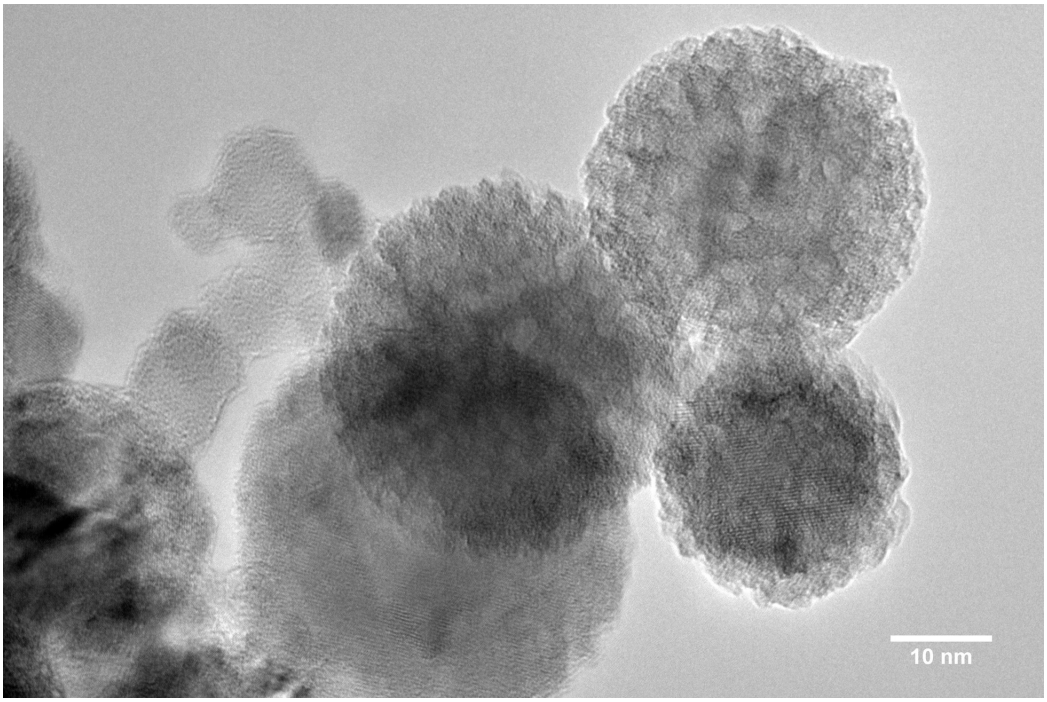

Figure 4.17. TEM image of titanium nitride nanoparticles deposited at the side of some trails.

at 8 mm off-focus and 90 mm/s using an output laser power of 1.9 kW, equivalent to the residual beam power (figure 4.14(b)). Figures 4.18(a) and (b) show a thin nitrided layer at the trail center with TiN rich lobes at both edges of the trail. Titanium nitride dendrites extended from the surface into the substrate across the width of the trail. Dendrites were oriented along flow lines within the melt, which was non-uniform. Similar features have been reported by many authors [101, 104, 108, 109, 111, 115, 121]. Figure 4.18(c) shows a rougher surface and much shallower melt layer with dendrites extending from the surface into the melt. Convective flow lines were not observed in this melt trail.

Figure 4.19 presents a cross-sectional micrograph taken near the middle of the trail processed at 3.5 kW, 8 mm off-focus and 10 mm/s. Here, dendrites were observed near the surface and within the melt, which was non-uniform and contained many pores. The cross-section of the sample processed at 3.5 kW, 4 mm off-focus and a translation speed of 90 mm/s exhibited similar features to those in figures 4.18 (a) and (b) and is not shown.

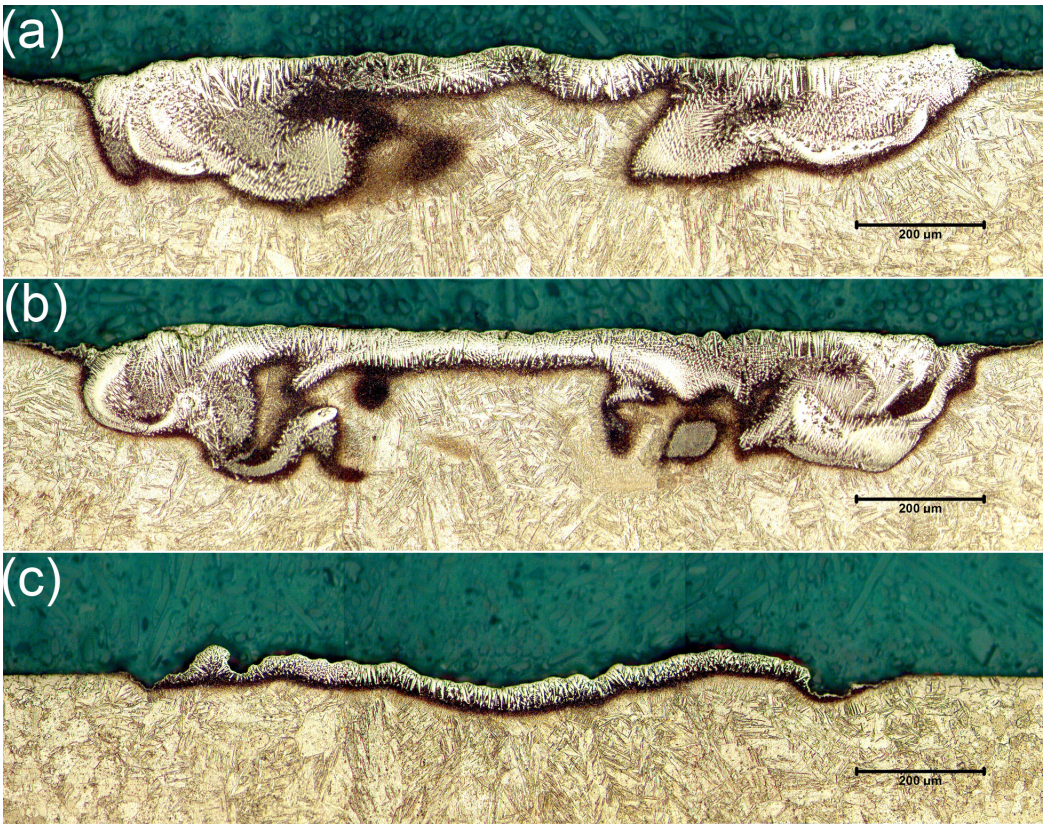

Figure 4.18. Cross-sectional optical images of the samples nitrided at 8 mm off-focus and 90 mm/s: (a) using a LSP; (b) without a LSP; and (c) with 1.9 kW residual laser beam power.

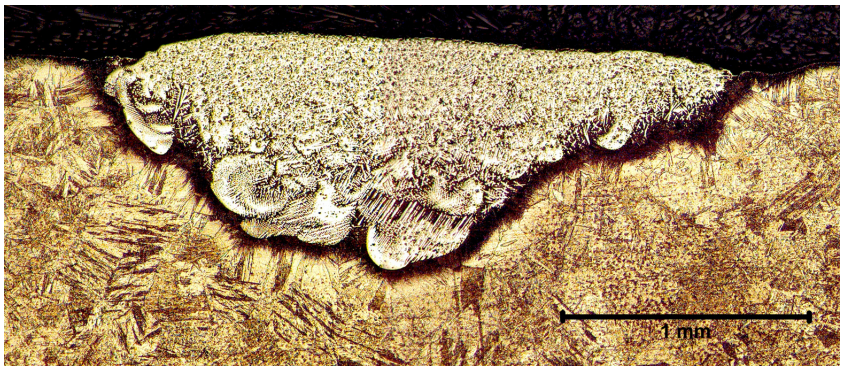

Figure 4.19. Cross-sectional image of a sample nitrided at 8 mm off-focus and 10 mm/s.

4.2.3 Discussion

The experimental results are summarized in Table 4.2. The CCD imaging technique, together with the surface and cross-sectional analyses presented in Section 4.2.2, demonstrated that although nitriding is possible regardless of whether atomic or molecular nitrogen exists near the surface of the substrate, the presence of a nitrogen-rich plasma near the surface results in a smooth, near-stoichiometric titanium nitride layer.

Table 4.2. Highlight of experimental results.

Power (kW)	OFD (mm)	Speed (mm/s)	Surface color	Cross section	Species near substrate
3.5	8	90	Gold	figure 4.18(a)	N, N^+
3.5	8	10	Gray/Blue	figure 4.19	Ti, Ti^+
3.5	8	90	Multi-colored	figure 4.18(b)	N_2 (no plasma)
1.9	8	90	Dull gold	figure 4.18(c)	N_2 (no plasma)
3.5	8	90	Gold	—	N, N^+, Ti, Ti^+

Comparisons showed that cross sections of the nitrided trails formed at 3.5 kW beam power, 8 mm off-focus, 90 mm/s speed with no plasma (figure 4.18(b)), and with pre-struck LSP (figure 4.18(a)) were remarkably similar in terms of melt volume, dendrite density and dendrite distribution. This indicated that, despite absorption of the laser beam power by the plasma, heat input to both samples was approximately the same. Had only residual beam power been available to heat the sample, a nitrided trail similar to that produced at 1.9 kW beam power, 8 mm off-focus and 90 mm/s speed would have been observed. Consequently, it appears that processes such as particle impact and re-radiation in the UV do transfer equivalent power to the substrate, essentially replacing the laser beam power lost through absorption by the plasma and diminished by the power lost through beam reflection from the substrate. In other words, the presence of a nitrogen-rich plasma did not significantly reduce the power absorbed by the substrate.

The shape of the melted regions with and without plasma was almost identical indicating that the spatial distribution of heat input and the induced convective flow were similar. Not only was the size and shape similar, the volume fractions of TiN dendrites appeared the same indicating similar nitrogen transport into the

sample. Thus, the presence of atomic nitrogen can arise from either dissociation of molecular nitrogen in the laser-sustained plasma or at the melt surface, with subsequent incorporation into the melt trail. This contrasts with Höche et al.'s [120] conclusion that dissociation of molecular nitrogen above a titanium substrate, due to plasma formation, during laser nitriding results in increased absorption of atomic nitrogen into the melt. Our results indicate that while the presence of dissociated nitrogen above the surface appears to prevent oxidation of the top surface layer (compare the oxidation observed in figure 4.8(c) to that observed without LSP in figure 4.14(a)), it does not appear to affect the degree of nitriding within the melt (figures 4.18(a) and (b)).

The origin of the shape and constitution of the melt trails shown in figures 4.18 and 4.19 has many unknowns. The spatial distribution of heat and mass transfer from the plasma to the melt is not well characterized. The kinetics of the various reaction steps discussed in the introduction is uncertain as are the relative contributions of diffusion and convection to heat and mass transfer in the melt. One explanation for the unusual, wavy melt pool observed in figures 4.18(a) and (b) may be inferred from the work of Arora, Roy and DebRoy [134]. Figure 4.20(a) presents a sketch of convective flow lines observed during processing under conditions where strong convective currents dominate melt pool geometry, e.g. the thermal diffusivity is low and the Prandtl number is high [134]. In titanium-nitrogen solutions, the surface tension increases with decreasing temperature causing flow at the surface from hotter to cooler regions. Thus, hot liquid moves away from the center of the melt trail towards the edge where it transfers some of its heat to the surrounding solid titanium causing it to melt. Hydrostatic pressure increases at the edge due to the inflow of liquid and the specific volume increase upon melting. This results in a return flow of cooler liquid towards the center, where it is reheated and again flows outwards. Thus, convection within the melt pool cools the center of the melt trail while melting additional material near the edges. This circulation of the melt explains the plateau region along the center line of the melt trail and also the widespread distribution of TiN dendrites that form as the nitrogen concentration increases, and nitrogen solubility decreases upon cooling (figures 4.18(a) and 4.18(b)).

Increased melt temperature, which results in a higher Marangoni number, ap-

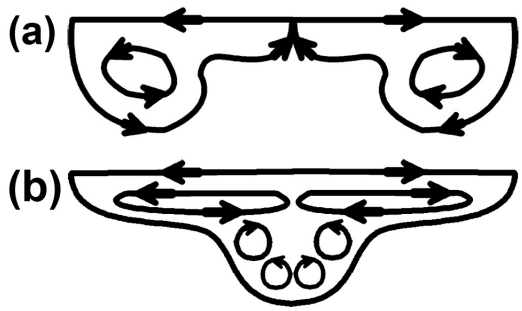

Figure 4.20. Schematics showing the convective flow within the melt pool: (a) low thermal diffusivity and high Prandtl number; (b) increased melt temperature and high Marangoni number.

pears to produce multiple eddies in the melt (figure 4.19). The upper shallow loops excite multiple lower loops circulating in the opposite directions, as shown in figure 4.20(b). Under conditions where the melt is not circulated and the outward flowing melt solidifies as it approaches the outer edges of the trail, a dip in the center of the melt trail is observed (figure 4.18(c)).

An explanation for the translation speed threshold for the formation of titanium nitride, rather than oxides or oxy-nitrides at the surface of the sample, is suggested by the observed formation of a substantial plume of atomic titanium (figure 4.9(b)) at speeds below the threshold. The flux of titanium vapor appears to reduce the amount of excited atomic and ionic nitrogen reaching the substrate and is also indicative of a very high surface temperature. The absence of excited atomic and ionized nitrogen near the surface then reduces nitrogen shielding and prevents the formation of a protective coating of titanium nitride. Thus, the trail surface becomes oxidized as the sample is translated away from the beam and the protective flow of nitrogen into open atmosphere. In the absence of a nitrogen-rich plasma and at speeds above the threshold, molecular nitrogen reaches the sample surface, dissociates and is incorporated into the melt forming titanium nitride. In some areas along the trail, sufficient titanium nitride is formed to be protective during cool down and thus a gold colored trail results.

As noted, it does appear that the presence of a nitrogen-rich plasma near the substrate surface has a beneficial effect with respect to minimizing oxidation and reducing roughness of the laser nitrided trail surface. This suggests that such plasma may getter any oxygen entrained in, or at the outer boundary of, the

gas flow. Also, sputtering by the plasma may remove oxides and reduce surface roughness. The trail formed at 3.5 kW beam power, 8 mm off-focus, 90 mm/s speed without plasma was significantly oxidized (figure 4.14(a)) while the trail formed with LSP was not (figure 4.8(c)). The black TiN nanoparticles formed at the sides of some trails (figure 4.17) imply chemical reaction within the plasma. In addition to the formation of a protective titanium nitride surface layer via reaction of atomic or molecular nitrogen within the melt, it is also likely that titanium nitride was deposited onto the trail as the sample was translated away from the beam. Decreasing the off-focal distance or lowering the scan speed would be expected to increase the surface temperature of the melt and thus the flux of titanium vapor, increasing the concentration of titanium to the point where TiN particles nucleated and grew in the plasma. This correlated well with the observation that more black powder was deposited as the off-focal distance or the translation speed was decreased.

These observations are summarized in figure 4.21, which plots translation speed (for the range 10 – 120 mm/s) versus off-focal distance (for the range 0 – 8 mm). Multiple phenomena can be identified in this figure:

1. below the dashed, grey curve, surface-struck plasma was formed during processing;

2. below the solid, black curve, oxide formed on the single trails, designated by open circles;

3. in the striped region, black nanoparticulate was observed adjacent to the processed trails;

4. above the solid black line, gold-coloured TiN trails were observed, designated by the symbol N;

5. in the region above the black curve and below the dashed grey curve, gold-coloured TiN trails were formed without oxidation by surface-struck plasma; and

6. above both the black and the dashed grey curves, nitriding occurred without oxide contamination using a pre-struck laser-sustained plasma.

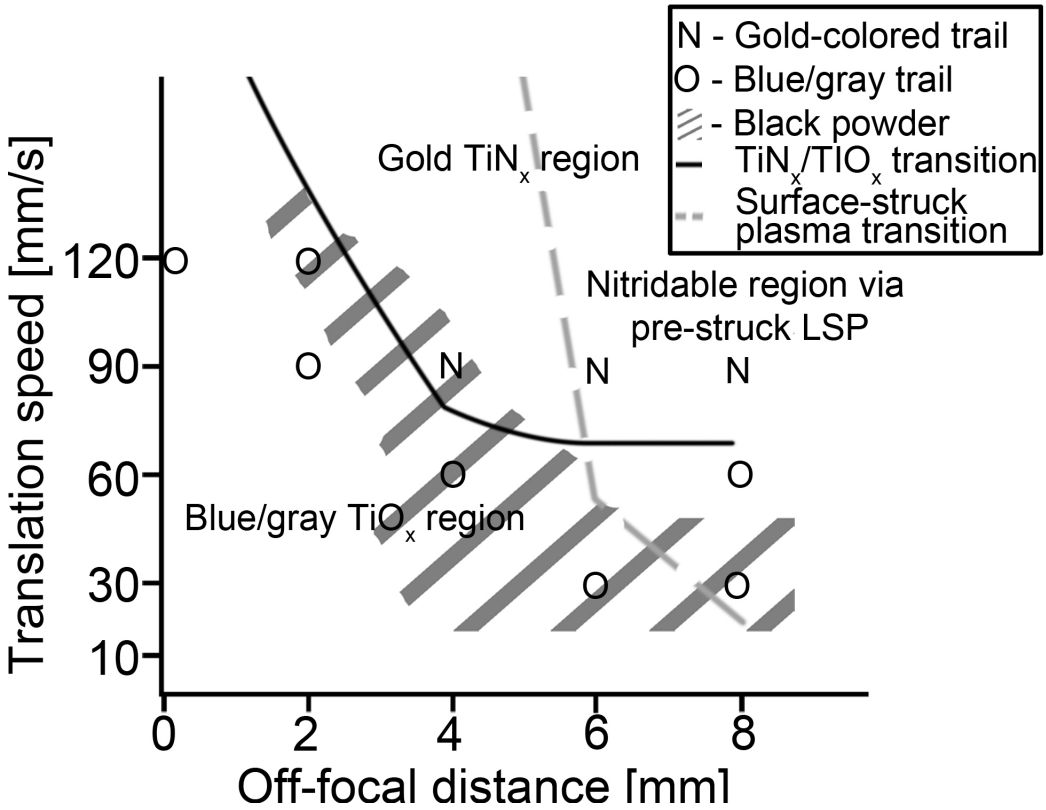

Figure 4.21. Diagram of regions observed during CO_2 laser nitriding. Black nanoparticulate was observed alongside trails processed within the striped region. Below the sold, black curve, oxide was observed at the surface and within the melt trail. Below the dashed, grey curve, surface-struck plasma formed during processing. Above both the black, solid and grey, dashed curves, oxygen contamination was prevented via pre-struck LSP processing.

As shown in figure 4.21, at high translation speeds and large off-focal distances, the titanium nitride surface was gold-colored with no evidence of surface oxidation when the LSP was pre-stuck. At sufficiently high translation speeds (above the solid black curve) and with the laser-beam focus sufficiently close to the surface of the substrate (below the grey, dashed curve), a nitrogen, surface-struck plasma was formed and prevented oxidation of the processed trail. Formation of oxide-free, titanium nitride surfaces at large off-focal distances (above 6 mm) was only possible via processing with a pre-struck, nitrogen LSP.

The results presented in this thesis provide necessary guidance, with respect to the off-focal distance and translation speed for the formation of near-stoichiometric titanium nitride layers. We have distinguished the effects of processing: 1) using

a pre-struck LSP; 2) with a laser beam and no plasma formation; and 3) with a surface-struck plasma. For the first time, we have shown how to control the size, shape and interaction zone between the nitrogen plasma and the titanium emissions from the substrate to produce a near-stoichiometric titanium nitride surface film. Such control is demonstrated by the CCD images in figure 4.8. We have identified a new processing regime (above the grey and black curves in figure 4.20) where nitriding can be conducted in an open atmosphere using a pre-struck LSP. Not only does the LSP shield the substrate from oxygen contamination when in contact with the substrate, but the LSP also efficiently transfers power to the substrate, thus generating a melt pool of similar size to that formed with the laser beam alone. The higher off-focal distance of the pre-struck LSP permits wider surface coverage and faster nitriding than the surface-ignited plasma.

4.2.4 Conclusions

From experimental studies of titanium laser nitriding using a pre-struck laser-sustained plasma, a surface struck plasma, and the laser beam without plasma, it can be concluded that:

- laser-sustained plasma provides a novel tool for studying the formation of titanium nitride layers;
- a threshold translation speed was identified, as a function of off-focal distance, above which:(a) nitrogen-rich pre-struck plasma was located near the titanium substrate surface; and (b) a near-stoichiometric titanium nitride surface with dendritic sub-surface structures was formed in open atmosphere;
- below the threshold speed, the surface showed a high susceptibility to oxidation and compositional variation;
- nitriding with pre-struck LSP and without plasma demonstrated that the presence of atomic nitrogen could arise from either dissociation of molecular nitrogen in the LSP or at the melt surface (no plasma), with subsequent incorporation into the melt trail;

- conditions were identified where the degree of titanium nitride formation within the melt was similar for the pre-struck LSP (dissociation taking place within the plasma, i.e. above the surface) and without plasma (dissociation at the melt surface, where decomposition of nitrogen in the melt is the rate limiting step);
- energy input into and its distribution within the sample did not appear to be attenuated by the presence of a nitrogen-rich plasma;
- formation of titanium nitride nanoparticulate provided evidence for reaction of nitrogen within the plasma with titanium vaporized from the substrate;
- a processing window (above the black curve and above the grey, dashed curve in figure 4.21) for the formation of near-stoichiometric, oxide-free TiN surfaces was identified for surface-struck plasma;
- for the first time, it has been shown that laser-sustained plasma can access nitriding conditions beyond those achieved with surface-struck plasma (above the grey, dashed curve in figure 4.21), or in the absence of plasma, to produce uniform, near-stoichiometric, titanium nitride layers; and
- the pre-struck LSP processing window occurs at larger defocussing conditions than the surface-ignited plasma processing window, enabling greater surface coverage and faster nitriding of titanium.

4.3 On the role of plasma in titanium nitriding with a nitrogen–argon gas mixtures

As noted in Section 4.2, nitrogen–argon gas mixture have been used in place of pure nitrogen to reduce cracking [105, 109, 111, 112, 122, 123]. The microstructure, size, hardness and shape of the melt zone have also been shown to be significantly affected by gas composition [104, 105, 108, 120, 122]. It is well known that argon has a lower optical breakdown threshold than nitrogen as well as higher total beam absorption—compare the measured 70 % total beam absorption of the argon LSP sustained at 3.5 kW (figure 3.12) with the 46 % absorption of the nitrogen LSP

sustained at 3.5 kW, calculated from the data reported in Section 4.2.2. However, there is a paucity of literature pertaining to the effects of plasma, LSP or surface-struck plasma on laser nitriding with a nitrogen–argon gas mixtures.

In this section, single-trail nitriding, with and without plasma, using pure nitrogen will be compared to nitriding using a nitrogen–argon gas mixture. Evidence will be presented concerning the role of plasma in reducing oxygen contamination during processing. A hypothesis concerning vapor deposition of titanium nitride due to LSP-substrate interaction will be introduced with supporting evidence. Also, it will be demonstrated, for the first time, that in addition to suppressing cracking and affecting the microstructure, size hardness and shape of the melt zone, the addition of argon to the processing gas results in a reduction in the threshold processing speed below which nitrided surfaces become oxidized. This permits the formation of nitrided layers of greater depths. In the following sections, analysis is provided as results are presented.

4.3.1 Experimental details

The setup for experiments was identical to that shown in figure 4.4(a) and as described in Section 4.2.1, with the exception that a $49.2 \pm 2\,\%$ nitrogen-argon mixture was used in place of pure nitrogen, where indicated. Here too, an output laser power of 3.5 kW and a gas flow rate of 16 slpm were used. Samples were processed at speeds between 15 and 300 mm/s. To ascertain the microstructure and composition of the samples, metallographic and XRD analyses were conducted as described in Section 4.2.1. With respect to XRD analysis, as in Section 4.2.1, X-rays were incident upon the top, processed surface of the substrate. Within this section, the term "high-speed" will be used to refer to nitriding using a translation speed above 75 mm/s whereas "low-speed" refers to speeds at and below 75 mm/s (slightly above the threshold speed shown in figure 4.21 for an OFD between 4 and 8 mm).

An 870 nm (10 nm FWHM) filter was used to monitor the location of excited atomic nitrogen species during processing with the nitrogen-argon LSP. Within the range of the band pass filter, only one relatively weak argon emission line around 866.79 nm was observed. Unfortunately however, a wavelength window

of at least 10 nm where titanium emission lines dominated, without overlap by argon lines, and where an inexpensive and commercially-available bandpass filter could be purchased did not exist. That is, argon or nitrogen emission lines overlapped with titanium emission lines, within a 10 nm window, around all visible wavelengths for which inexpensive bandpass filters were available. The presence of nitric oxide (NO) and nitrogen dioxide (NO_2) were monitored, respectively, using a BW Technologies Inc. Gas Alert Extreme, nitric oxide and a nitrogen dioxide gas detector. The detectors were place approximately 30 mm away from the laser beam focus during processing.

4.3.2 Single-trail results and analysis

4.3.2.1 High-speed (100–300 mm/s) nitriding using pure nitrogen

To better understand the role of plasma and gas composition on the nitriding process, the top surface of samples processed at various off-focal distances and translation speeds with and without a pre-struck LSP were compared. It may be noted, that for the laser power and flow conditions used, once struck by any of the methods discussed in Section 4.2.1, the plasma could be sustained indefinitely. All samples were processed at a translation speed above the threshold speed defined by figure 4.21—the region where gold-colored TiN trails were observed. In figure 4.22, magnified top-surface images of single-trail samples processed with a pure nitrogen LSP are shown. Several features are noteworthy and are labeled in figure 4.23 . It can be readily observed that the trail width increased as the translation speed was decreased, due to greater local energy input; however, the relationship between trail width and off-focal distance was less clear. Whereas the trail width increased as off-focal distance increased at a speed of 100 mm/s, the relationship did not hold at higher speeds. At all constant speeds and varying OFDs, a porous, decanted region, where melt flowed back towards the center of the trail upon cooling, could be observed along the trail edges [123]. Beyond the decanted region, black powder, shown to contain titanium nitride nanopowder in Section 4.2.2, was observed alongside trails processed at lower speeds and shorter OFDs.

The presence of titanium nitride nanopowder could be explained by the reaction of titanium and atomic nitrogen, dissociated by the LSP, in the gas phase,

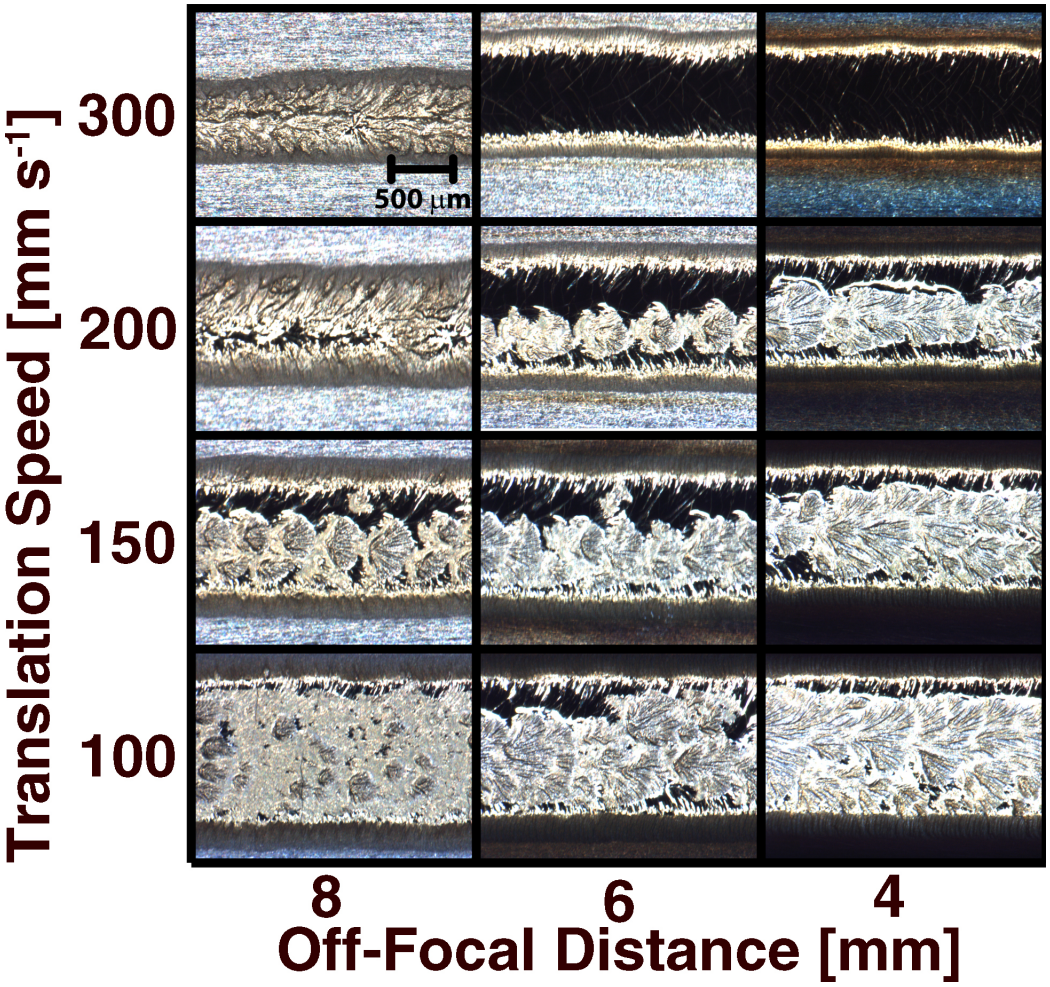

Figure 4.22. Top surface images showing single-trail samples processed using nitrogen LSP as a function of off-focal position and translation speed.

as postulated in Section 4.2. Also observed along the edges of (8 mm and 150, 100 mm/s, 6 mm and 200, 150, 100 mm/sand 4 mm and 200, 150, 100 mm/s) or in the middle of (6 mm and 300 mm/a and 4 mm and 300 mm/s) the processed trails were smooth, reflective regions (appearing black in figure 4.22). Oblique illumination, as was used in figure 4.24, revealed the shininess of this region. Smooth, reflective regions, which appear black in the micrographs but which are actually a highly-reflective gold color, appeared to cover the entire center of trails processed at the highest translation speed (300 mm/s) and OFDs of 6 and 4 mm. It should be noted that figure 4.24 was taken after samples were cleaned with alcohol and distilled water, thus removing the non-adherent powder alongside some trails. It

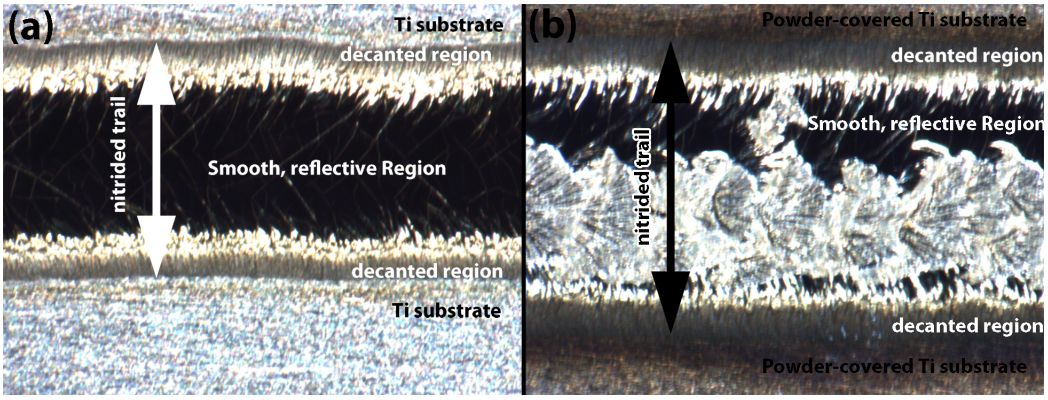

Figure 4.23. Top surface images of single-trail samples processed using nitrogen LSP as a function using an off-focal distance of 6 mm and translation speeds of (a) 300 mm/s and (b) 150 mm/s. The decanted region and the reflective, smooth regions are labeled. (b) Black powder can be observed beyond the edges of the nitrided trail.

is likely that the reflective and the the black nanoparticulate-covered regions arose from related processes. They are likely due to the gas-phase deposition of titanium nitride upon a cooling surface: (1) where the surface was sufficiently hot (but not molten) nucleation and growth of a continuous film occurred; (2) where the surface was colder, condensation took place and nanoparticulate was formed; (3) where the surface was molten, titanium nitride was incorporated into the melt.

The hypothesis that gas-phase deposition of titanium nitride took place due to the interaction of excited atomic nitrogen with titanium, in the case of processing with LSP, is further supported by the surface morphologies of the samples processed without plasma (figure 4.25). Here, powder was entirely absent alongside the processed trails. Additionally, the amount of surface covered by the smooth, reflective regions was dramatically less. If the proposed hypothesis is correct, the continued existence of these smooth, reflective regions, although with much less surface coverage, suggests that a gas-phase reaction still took place very near the surface of the trails, even when processing without plasma. In the case of nitriding without LSP, such a reaction could only take place at locations where hot titanium vapor, emitted from the substrate, dissociated and reacted with incoming molecular nitrogen, since there is no mechanism for cold nitrogen to directly absorb laser radiation under these experimental conditions. In the event that titanium nitride vapor landed on molten titanium (which was likely to happen since the reaction likely took place directly above melt), it would have been incorporated into

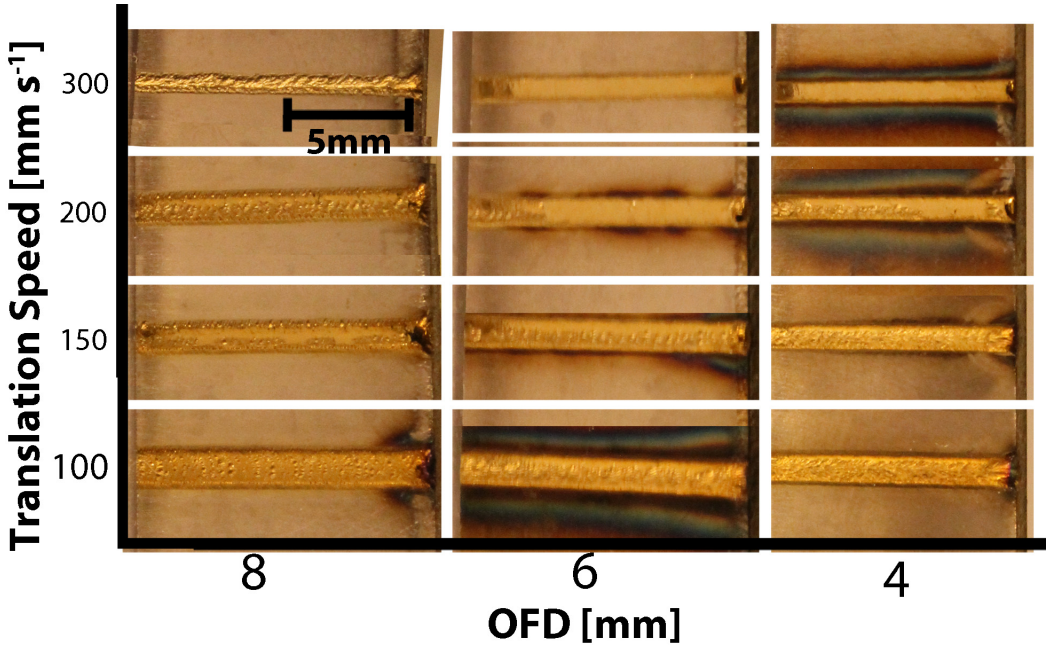

Figure 4.24. Photograph, using oblique illumination, of the top surfaces of single-trail samples processed using nitrogen LSP as a function of off-focal position and translation speed.

the melt. In fact, only when the vapor landed upon solidified or nearly-solidified regions of the trail were the smooth, reflective regions observed.

To be clear, the suggestion here is that melt pool and plasma dynamics resulted in regions along the processed trail of varying temperatures and cooling rates. The formation of ripples, the decanted regions and other surface features of the processed trails were also a consequence of these dynamics. It should then not be surprising that the formation of titanium nitride of varying morphologies varied with surface features such as ripples. According to Copley et al. [135], instabilities at the front edge of the melt pool result in waves which ripple backwards. The resulting semicircular ripples in (solidified) laser melted trails indicate prior positions of back edges of the melt pools [135]. In regions where titanium nitride vapor landed on a ripple, it became incorporated into the melt. However where smooth, reflective regions were observed, titanium nitride landed on a very hot but solidified trail, forming a film.

Along with the proposed gas-phase reaction of nitrogen with titanium, another gas-phase reaction took place during processing with plasma. Nitric oxide (NO)

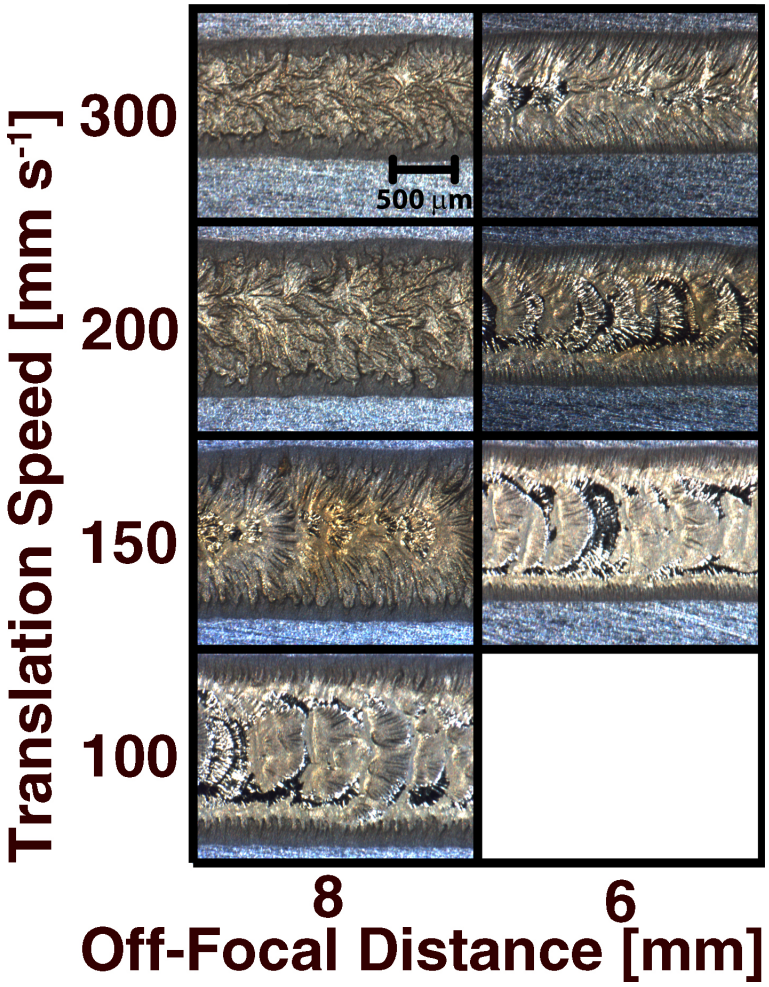

Figure 4.25. Top surface images showing single-trail samples processed using CO_2 laser, without plasma formation, and nitrogen gas as a function of off-focal position and translation speed.

and nitrogen dioxide (NO_2) sensors detected the presence of both species during processing with LSP. Nitric oxide was detected in concentrations higher than 25 parts per million. A second or so after the detection of NO, the NO_2 sensor also registered concentrations higher than 5 parts per million. Based on this, it is proposed that the presence of excited, atomic nitrogen above the substrate, provided by the LSP, reduced oxygen contamination by interacting with atmospheric oxygen to produce NO which then converted into nitrogen dioxide via the reaction: $2\ NO + O_2 \rightarrow 2\ NO_2$. Thus, the nitrogen LSP effectively shielded the substrate from oxidation both by interacting with (gettering) atmospheric oxygen as well as

by participating in the formation of a protective titanium nitride film upon the cooling trail.

Cross-sectional micrographs of the samples presented in figure 4.22 are shown in figure 4.26. Magnified images of these cross sections are included in Appendix C. The melt zone microstructures consisted of dendrites in a matrix comprised of acicular alpha titanium containing interstitial nitrogen. Dendrite-rich side lobes within the melt pool were also observed. Below the melt zone, an acicular alpha titanium heat affected zone was observed. While some processing parameters produced relatively smooth surfaces (ie. 8 mm OFD and a translation speed of 100 mm/s), most cross sections were rough. Cracks were also observed in all cases except for the sample processed at the largest OFD and the fastest speed.

Similar microstructures were observed in cross sections of trails processed without LSP, shown in figure 4.27. Magnified images of these cross sections are also included in Appendix C. Here too, cracking and rough surface features were observed. The observation that nitriding with a nitrogen LSP did not reduce the total energy absorbed by the substrate was also reaffirmed here—the melt volume of trails nitrided without LSP or surface-struck plasma was equal to or less than the melt volume of trails nitrided with LSP or surface struck plasma. While this does not suggest that this observation is universal, it again points out that the view that plasma results in a less energy-efficient process [104, 111] may not be true for all processing conditions.

Comparison of XRD spectra of samples processed with and without prestruck-LSP also supported the hypothesis presented here concerning deposition of titanium nitride via a gas-phase reaction of nitrogen with titanium. Figure 4.28 shows the XRD spectra of samples processed with and without a prestruck-LSP, in pure nitrogen, at an off-focal distance of 8 mm and a translation speed of 200 mm/s. While both spectra show the presence of alpha titanium and titanium nitride (one cannot be entirely certain that the peaks labeled $TiN_{0.26}$ are correctly identified), the relative strengths of the strongest TiN and Ti lines in each figure strongly indicates that more titanium nitride existed in the sample processed with, than in the sample processed without, LSP. It may however be argued that this comparison is unfair because the sample processed without LSP has a smaller cross section—this counterpoint will be addressed in Sections 4.3.2.2 and 4.4.

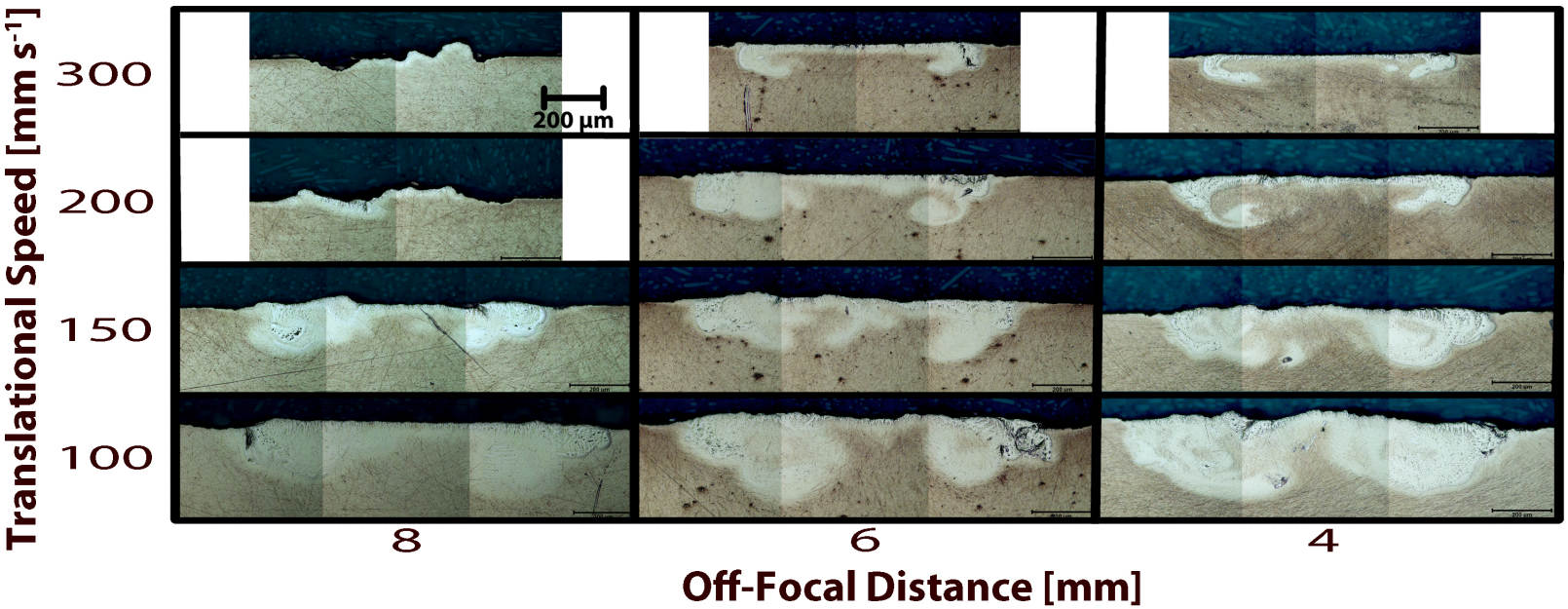

Figure 4.26. Cross-sectional micrographs of samples processed using nitrogen LSP as a function of off-focal position and translation speed.

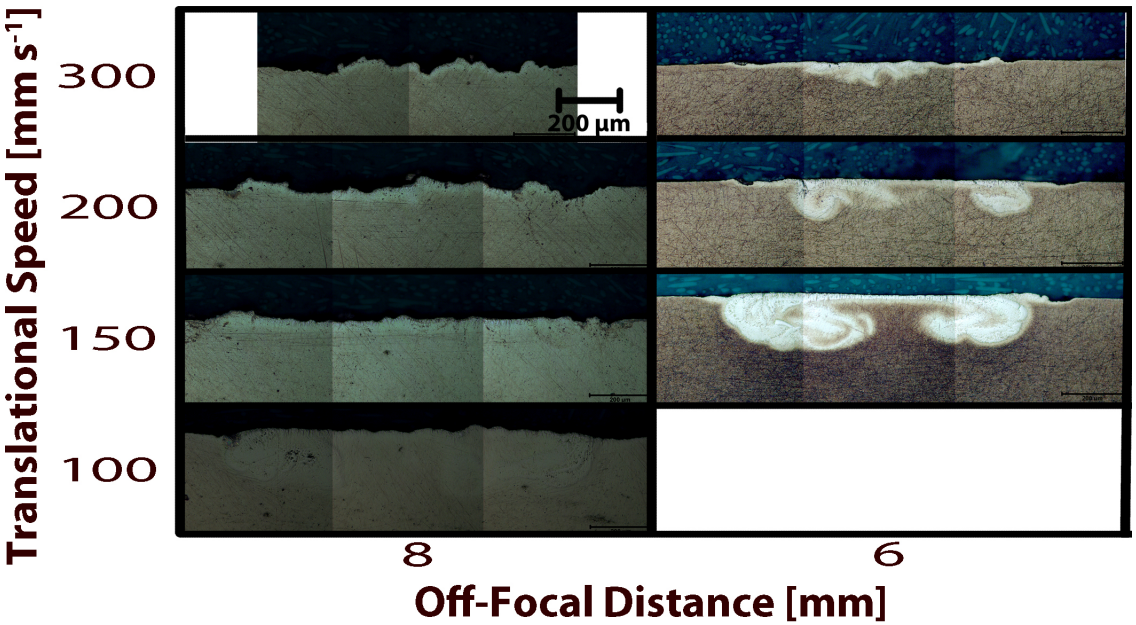

Figure 4.27. Cross-sectional micrographs of samples processed using CO_2 laser and nitrogen gas, without plasma formation, as a function of off-focal position and translation speed.

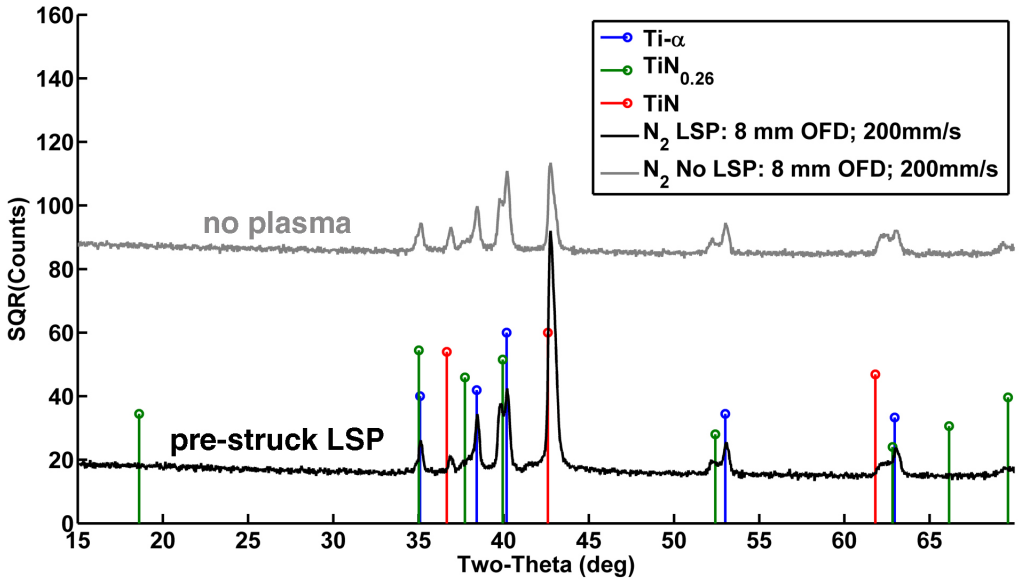

Figure 4.28. XRD spectra of samples processed with and without prestruck-LSP, in pure nitrogen, at an off-focal distance of 8 mm and a translation speed of 200 mm/s

4.3.2.2 High-speed nitriding using a nitrogen–argon gas mixture

As in the case of nitriding with pure nitrogen, nitriding with a 49.2% N_2-Ar gas mixture resulted in different surface and sub-surface features depending on whether or not a plasma existed near the substrate surface. Figure 4.29 shows top surface images, as a function of off-focal position and translation speed, of samples processed using a pre-struck N_2-Ar LSP. The decanted region observed in samples processed using pure nitrogen (figure 4.22), can also be observed alongside trails shown in figure 4.29 at OFDs of 6 and 4 mm. The region is however less evident at 8 mm OFD and speeds of 200 and 300 mm/s, indicating that the melt solidified at the trail edges rather than draining back towards the center. Here too, smooth, reflective regions, appearing black but actually gold colored, were observed in all trails except those processed at an OFD of 8 mm and translation speeds of 200 and 300 mm/s. However, unlike the samples processed with a pure nitrogen, pre-struck LSP, black, nanoparticulate was not observed alongside any trail.

It is striking that trails processed without a pre-struck or surface-struck LSP in a 49.2% N_2-Ar gas mixture (figure 4.30) showed no indication of the smooth, reflective regions. Black powder was also not observed. Additionally, the surfaces

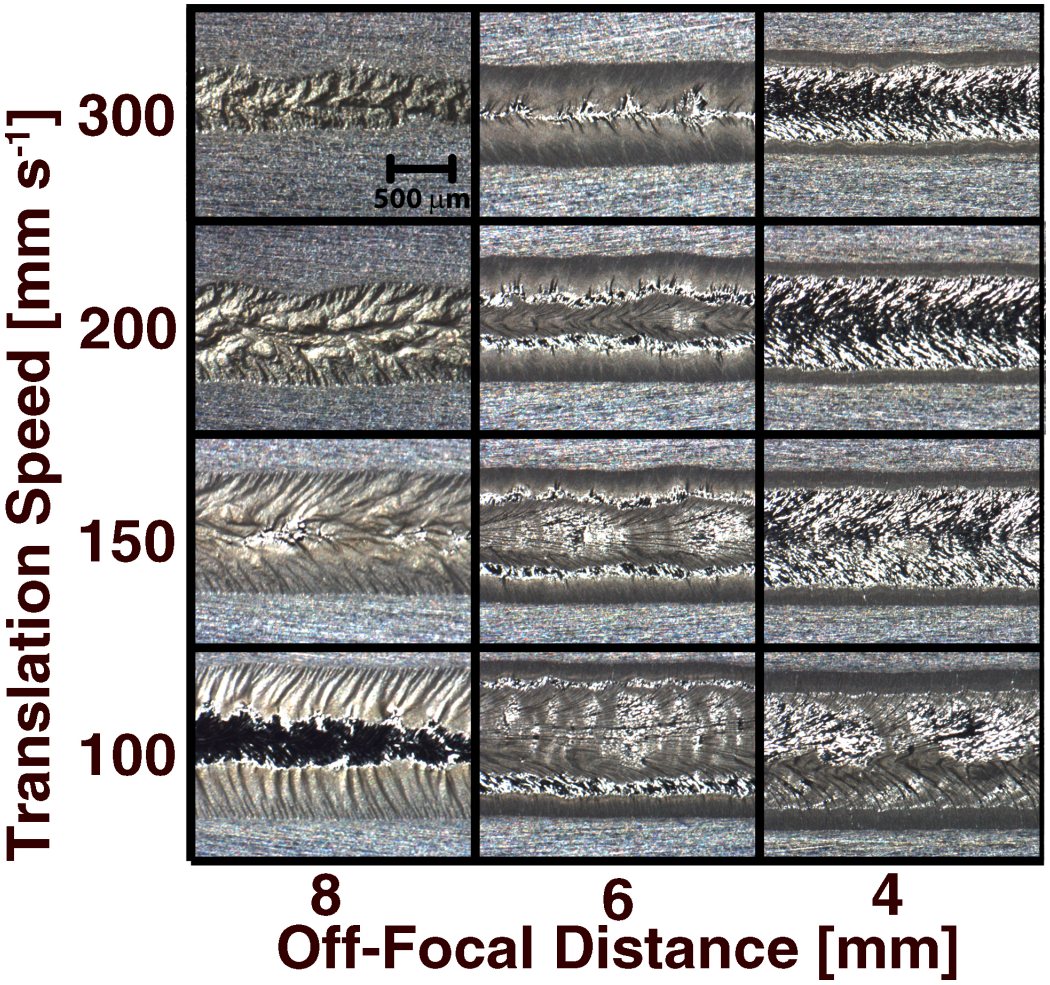

Figure 4.29. Top surface images of samples processed using a $49.2 \pm 2\,\%$ N_2–Ar LSP as a function of off-focal position and translation speed.

were dull colored, indicating little to no surface coverage of titanium nitride [111].

Comparison of cross sections with (figure 4.31) and without (figure 4.32) a pre-struck plasma reaffirmed that plasma participated in energy transfer to the substrate. Magnified images of the cross sections are included in Appendix C. For example, at an off-focal distance of 8 mm, the depth of nitriding in samples processed with LSP was greater than those processed without at all speeds. However, the reverse appears to be true at an OFD of 6 mm. Unfortunately, quantifying the difference in melt volume is difficult because the transition between the melt zone and the heat-affect zone was difficult to determine based purely on the microstructure of CP titanium. Nevertheless, the result was readily observed qualitatively.

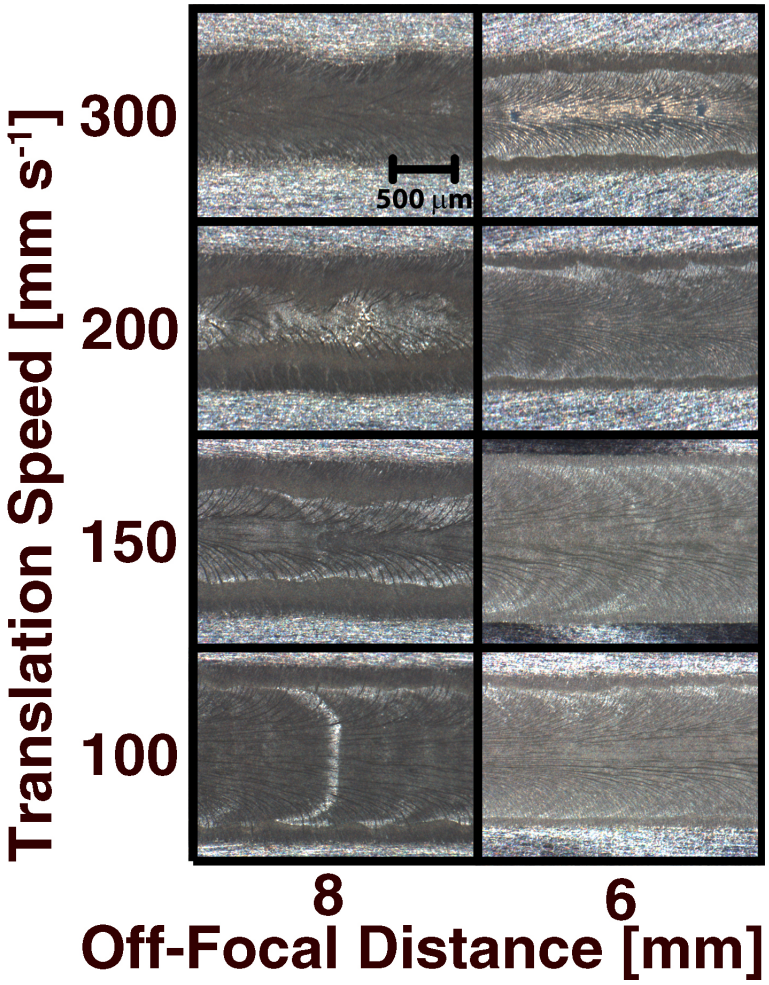

Figure 4.30. Top surface images showing single-trail samples processed using CO_2 laser, without plasma formation, and a $49.2 \pm 2\,\%$ N_2–Ar gas mixture as a function of off-focal position and translation speed.

XRD analyses of the trails processed with and without prestruck LSP in a nitrogen-argon gas mixture, shown in figure 4.33, not only adds further proof to the hypotheses presented here, but also disqualifies the counterpoint introduced at the end of Section 4.3.2.1. The spectrum of the sample processed with a pre-struck LSP showed that TiN was present in that sample. However, TiN was not present in the sample processed without a pre-struck plasma. Since the XRD spectra were recorded with the surface of each sample facing the X-ray source and the subsurface microstructure of both samples appeared similar, plasma was almost certainly responsible for the formation of TiN at the surface of the sample to which

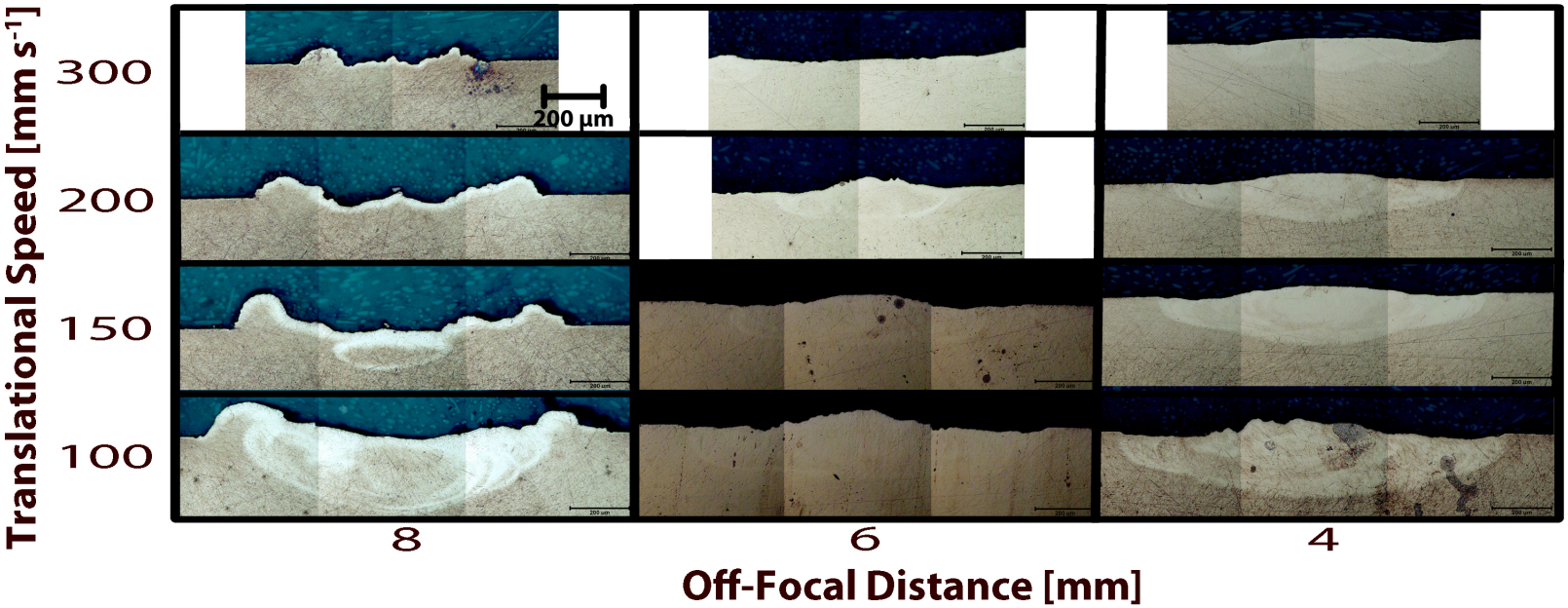

Figure 4.31. Cross-sectional micrographs of samples processed using N_2-Ar LSP as a function of off-focal position and translation speed.

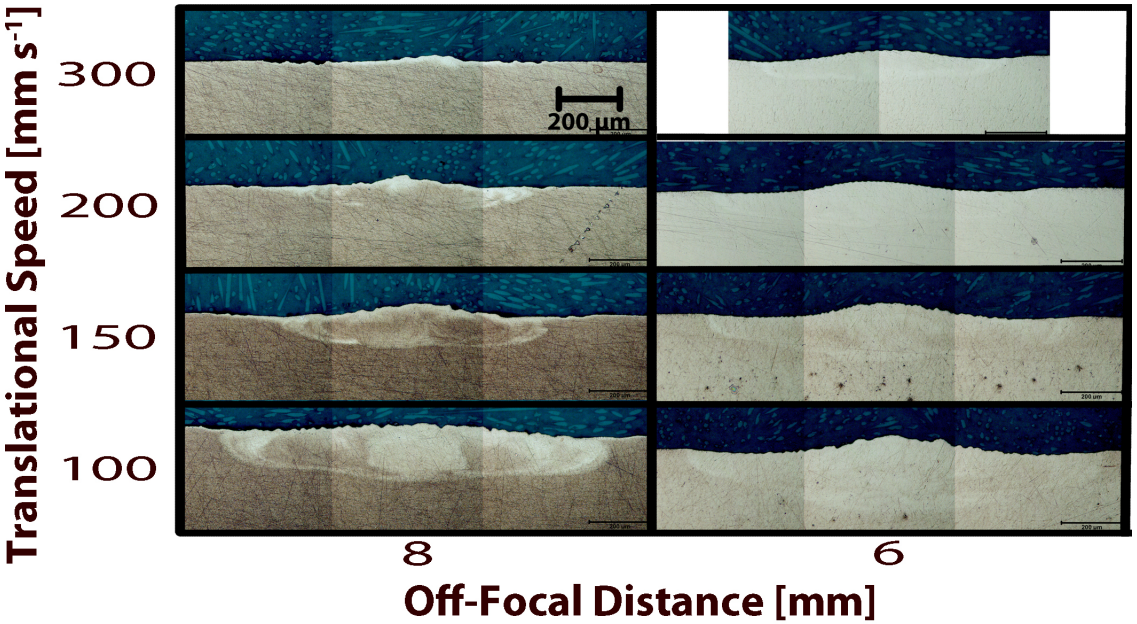

Figure 4.32. Cross-sectional micrographs of samples processed using CO_2 laser, without plasma formation, and N_2-Ar gas mixture as a function of off-focal position and translation speed.

it was exposed! It may also be noted that, as was the case during processing with a pure nitrogen LSP, both NO and NO_2 were detected in concentrations higher than 25 and 5 parts per million, respectively, during processing with, but were not detected during processing without, LSP.

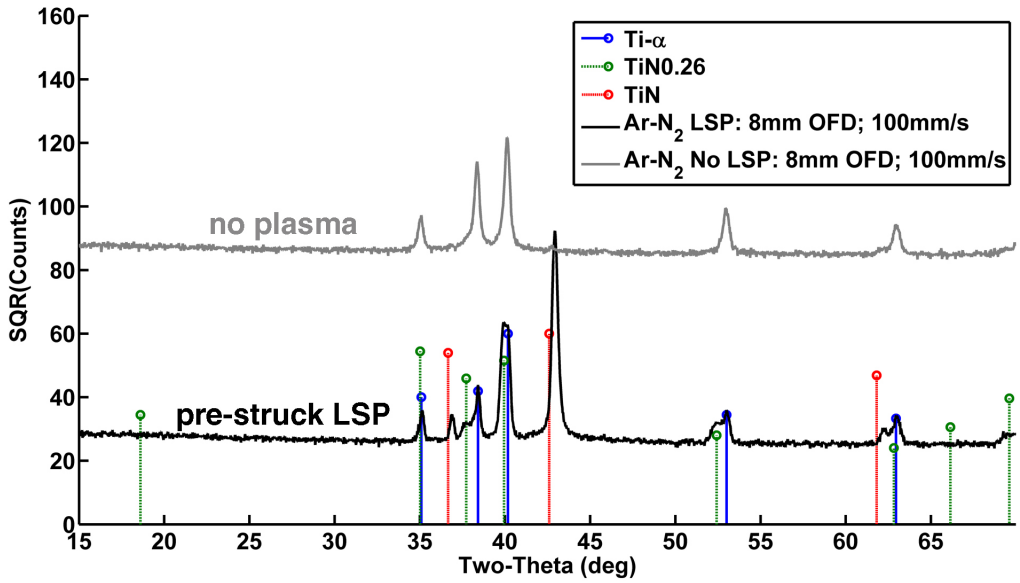

Figure 4.33. XRD spectra of samples processed with and without prestruck-LSP, in 49.2% N_2-Ar gas mixture, at an off-focal distance of 8 mm and a translation speed of 100 mm/s

4.3.2.3 Low-speed (15–75 mm/s) nitriding

At speeds of and below 75 mm/s, surface compositions of the processed samples, together with CCD images of excited atomic nitrogen species, provided further insight into the influence of argon addition to the processing gas on the nitriding process. Figure 4.34 presents images of the processed surfaces at off-focal distances of 4, 6 and 8 mm and translation speeds of 15, 25, 50 and 75 mm/s. Images were recorded at five times magnification. All surfaces, except for the sample processed at 4 mm OFD and 15 mm/s displayed a light-gold color. The sample processed at 4 mm OFD and 15 mm/s and, to a lesser extent, the one processed at 4 mm OFD and 25 mm/s contained hints of blue and purple. As explained in Section 4.2.2, this indicates surface oxidation. Also, as in the case of surface images of samples processed at high speeds, the regions which appeared black in figure 4.34 were actually gold-colored with oblique illumination, as shown in figure 4.35.

Cross sections of the processed samples are shown in figure 4.36. The melt zones of the samples processed at low speeds were larger, more symmetric and more semi-circular in shape than those of samples process at high speeds (figure 4.31). Also, as in the case of high-speed nitriding with the nitrogen-argon mixture, sub-surface dendrites were not observed. The substructure consisted primarily of acicular alpha titanium, containing interstitial nitrogen, with clearly visible previous beta grain boundaries. A 200X magnified cross section of the sample processed at an off-focal distance of 8 mm and a translation speed of 15 mm/s is shown in figure 4.37 with some previous beta grain boundaries indicated. A thin, continues layer at the surface of this trial can also be observed.

Based on the surface colors and subsurface morphologies of the processed trails, it appears that oxygen-free nitriding of titanium at speeds far below the threshold speed identified in figure 4.21 was enabled via the dilution of the nitrogen processing gas with argon. CCD imaging of the location of nitrogen species during processing, shown in figure 4.38, provided an insight as to how this might have been possible. At an off-focal distance of 8 mm and 6 mm, respectively, the shape of the nitrogen-argon plasma above the substrate is virtually unchanged at all tested speeds. However, at an OFD of 4 mm, plasma begins to narrow and shift upwards below a speed of 25 mm/s. This correlates with the observation of surface oxidation, at the same off-focal distance, below a speed of 25 mm/s. The main

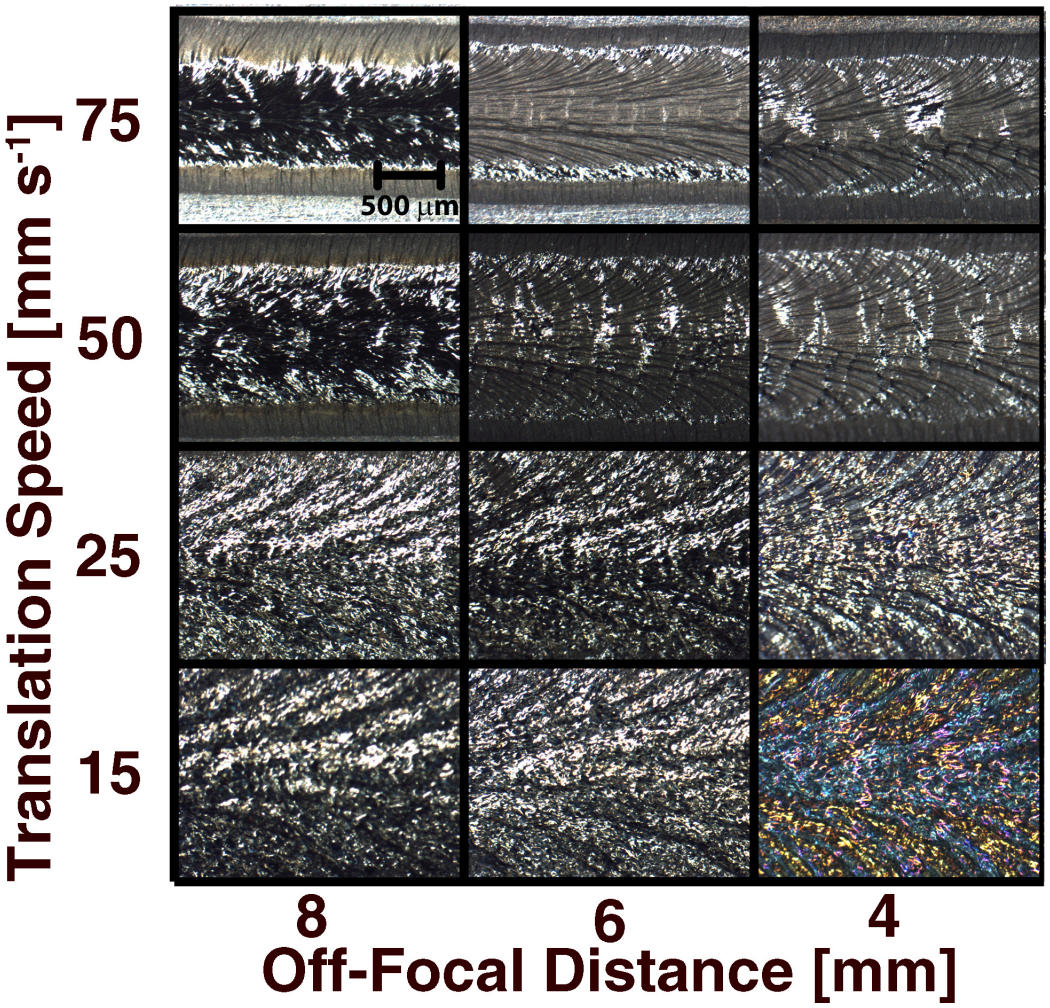

Figure 4.34. Optical images of top surface of LSP nitriding using $49.2 \pm 2\,\%$ nitrogen–argon mixture as a function of off-focal position and translation speed.

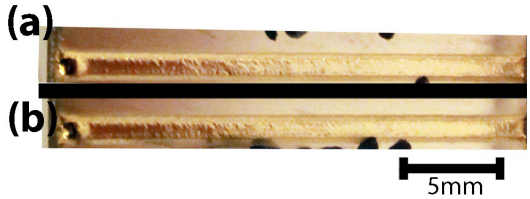

Figure 4.35. Photograph, using off–axis illumination, of the top surface of LSP nitriding using $49.2 \pm 2\,\%$ nitrogen–argon mixture at a translation speed of (a) 75 mm/s and (b) 50 mm/s.

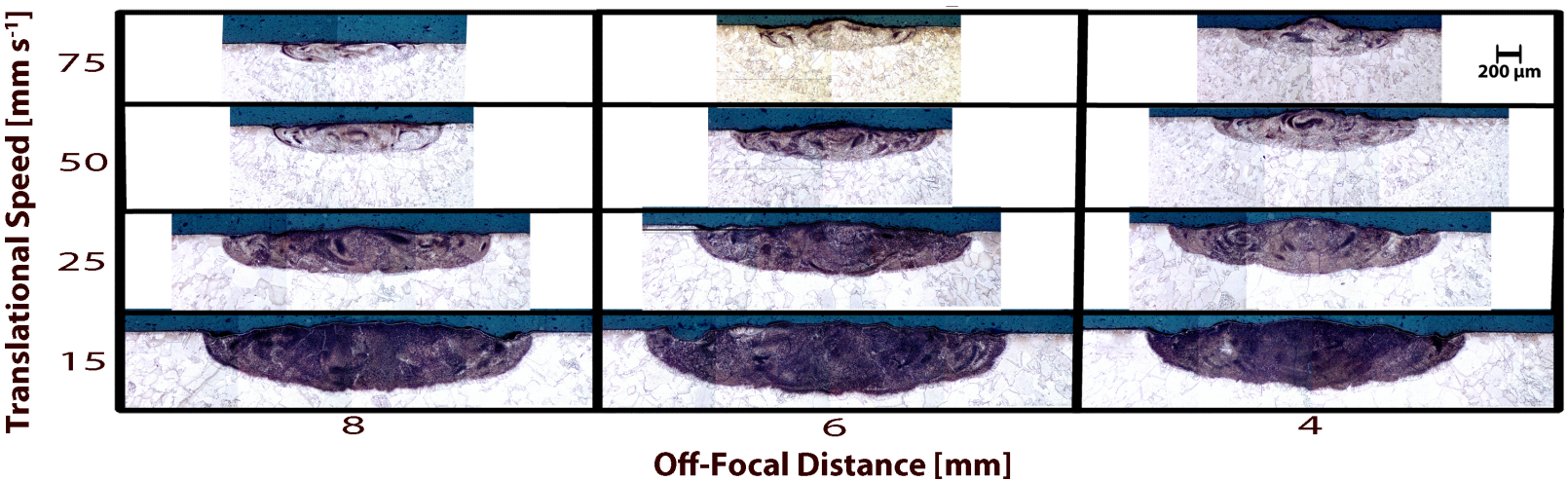

Figure 4.36. Cross-sectional micrographs of LSP nitrided samples $49.2 \pm 2\,\%$ N_2-Ar mixture as a function of off-focal position and translation speed.

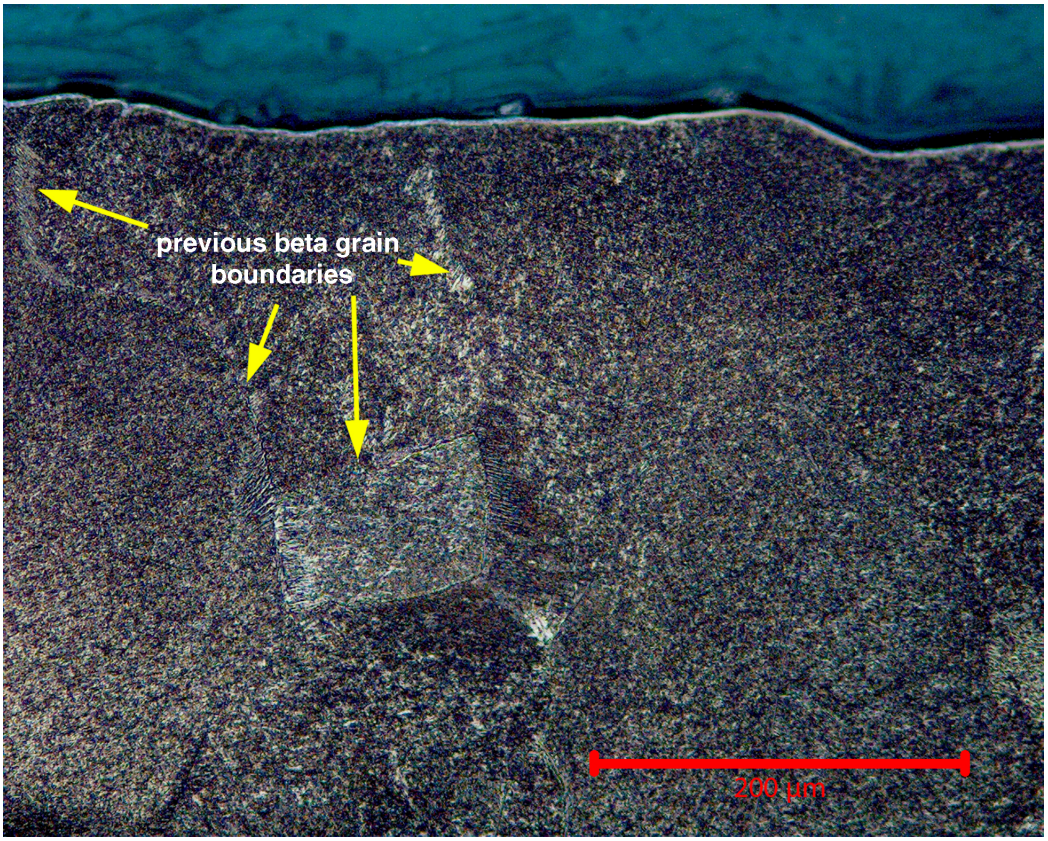

Figure 4.37. Cross-sectional image of sample processed using a 49.2 ± 2 % N_2-Ar mixture at an off-focal distance of 8 mm and translation speed of 15 mm/s.

point however, is that excited nitrogen and argon species were located near the surfaces of the substrates processed at speeds as low as 15 mm/s. At these same OFDs, a pure nitrogen plasma would have been blown up and away from the surface by titanium vapor emitted from the substrate at a speed below approximately 60 mm/s (the transition speed identified in figure 4.21.

4.3.3 Conclusions

From the above experimental studies, several conclusions were drawn regarding the role of plasma, and argon addition to a nitrogen plasma, in the nitriding process.

- Nitrogen-rich plasma, located near the surface of a titanium substrate, shielded the substrate from oxidation both by interacting with (gettering) atmospheric oxygen as well as by participating in the formation of a protective

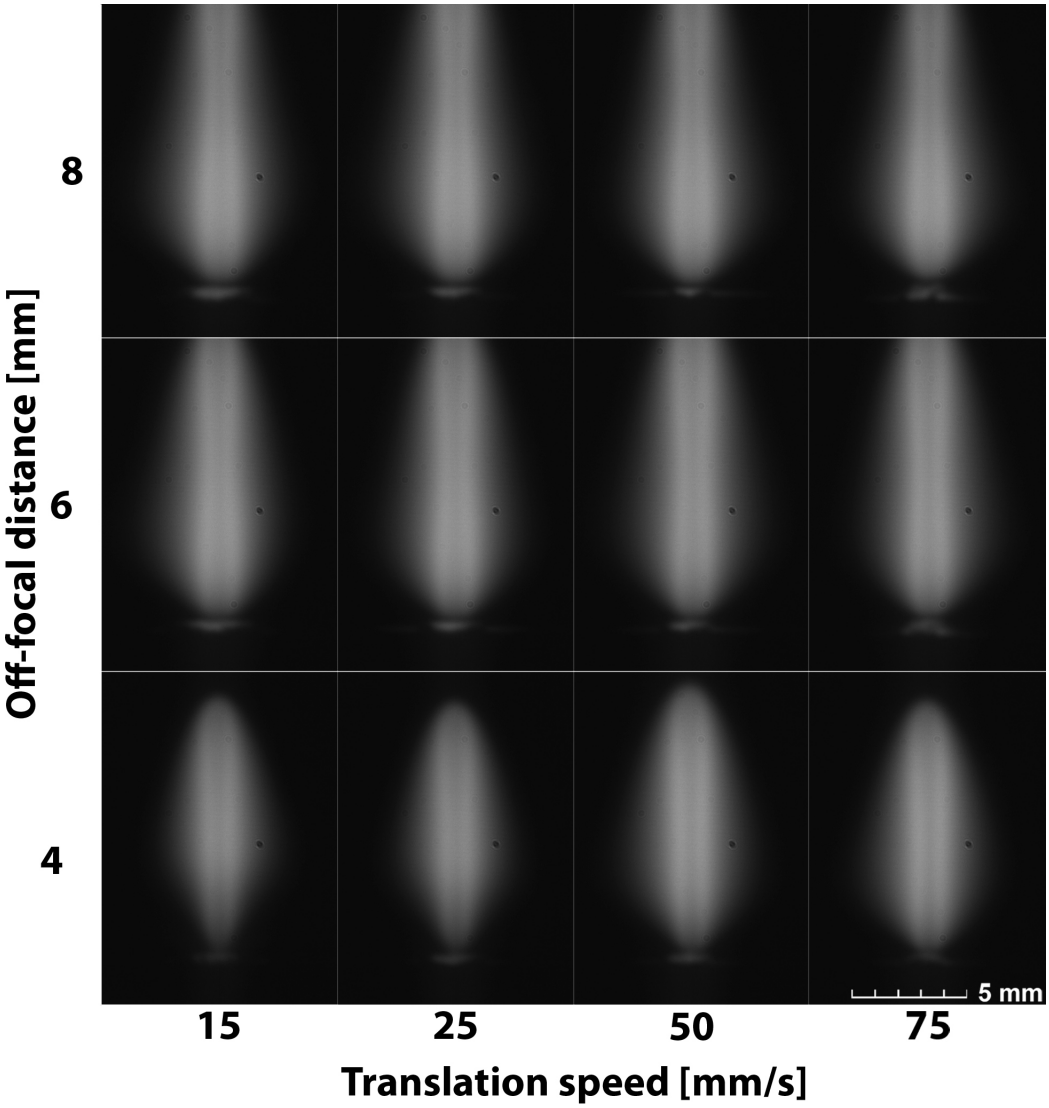

Figure 4.38. CCD images of nitrogen and argon emission lines around 870 nm as a function of processing speed and off-focal distance.

titanium nitride film upon the cooling trail, possibly via N(g) +Ti(g) $\rightarrow$ TiN(s).

- Vapor deposited titanium nitride: 1) formed a continuous surface where the substrate surface was sufficiently hot but not molten; 2) condensed into nanoparticulate where the surface was too cold for nucleation and growth to take place; and, 3) was incorporated into the melt where the surface was molten.

- The presence of excited, atomic nitrogen above titanium, provided by the LSP, reduced oxygen contamination by interacting with atmospheric oxygen to produce NO which then converted into nitrogen dioxide.
- Plasma participated in energy transfer from the laser beam to the substrate and did not necessarily reduce the total energy absorbed by titanium during laser nitriding.
- Addition of argon to pure nitrogen gas resulted in a reduction of the threshold processing speed for oxygen-free nitriding of titanium. A nitrogen–argon plasma allowed for oxygen- and crack-free nitriding of titanium at speeds as low as 15 mm/s.

4.4 Multi-trail nitriding of titanium

Ultimately, the goal of any nitriding process is to achieve large-area surface hardening of components. In the case of a pulsed laser beam, this is done by overlapping multiple laser spots; while in the case of a CW laser, this can be done by overlapping multiple laser trails. A spinning beam, where the laser spot is rotated while the substrate is translated below, can also be used [110]. As in single-trail nitriding, a major problem which can be expected when overlapping laser trails is cracking. According to Kloosterman [111], cracking in overlapping trails is due to a stepwise buildup of tensile stress with each overlap. The likelihood of cracking is further increased due to increasing concentration of nitrogen in the melt pool with each successive overlap [105, 109, 111, 112, 122, 123].

This is perhaps a reason why research into multi-trail nitriding of titanium using a CW CO_2 laser beam has been limited [103, 109, 110]. Multi-trail laser nitriding of Ti-6Al-4V was studies by Bonss et al. [103] using a 3.1 kW laser, translation speeds of 3 to 13 mm/s, nitrogen-argon gas ratios of 0 to 0.8, by volume, and a trail overlap of 2.25 mm within a specially-designed bell jar. Raaif et al. [109] used the same experimental setup but with a trail overlap of 2.75 mm, nitrogen concentrations of 40, 60 and 80 % and reported a gas flow of 100 slpm.

Bonss et al. [103] observed dendrites within the melt at nitrogen concentration above 25 % and reported hardness values within the melt zone to vary almost linearly from 350 HV (base metal hardness of Ti-6Al-4V) to 830 HV with nitrogen concentration from 0 to 80 %. Raaif et al. [109] reported surface hardness of approximately 1060 HV at 80 %, 750 HV at 60 % and 500 HV at 40 % nitrogen concentration.

Selamat et al. [110] has also studied multi-trail nitriding of Ti-6Al-4V produced by a spinning laser beam, rotating at 1500 rotations per minute, with a substrate translation speed of 3 mm/s. Using a 50 % trail overlap in a 20 % nitrogen environment, hardness values from 800 to 500 HV were achived more than 600 microns below the surface. Unfortunately, cracking was not discussed in any of the above references [103, 109, 110]. It it reasonable to assume that cracking may not have occurred at the reported hardness values since, according to Bell et al. [102], cracking becomes problematic above 650 HV. It is also possible that cracking was ignored.

In this section, results concerning high-speed and low-speed, multi-trail nitriding of titanium using a pure nitrogen and a $49.2 \pm 2\,\%$ nitrogen–argon gas mixture will be reported. As in the case of single-trail nitriding, the presence of plasma as well as the nitrogen concentration is shown to influence surface and sub-surface microstructure. Using the advantageous effects of a nitrogen-argon mixture, such as lowering of the threshold speed for oxygen-free nitriding and reduction in the likelihood of cracking, the production of a hard, nearly-uniform, and crack-free nitrided layer of up to $700\,\mu$m in depth is reported.

4.4.1 Experimental details

The setup for experiments was identical to that described in Section 4.3.1. Here too, "high-speed" is used to refer to nitriding at a translation speeds above 75 mm/s and "low-speed" refers to speeds at and below 75 mm/s. In all experiments, one of two gases was used: either pure nitrogen or a $49.2 \pm 2\,\%$ nitrogen-argon gas mixture. An output laser power of 3.5 kW and a gas flow rate of 16 slpm were used for all experiments. Metallographic and XRD analyses were conducted as described in Section 4.2.1. Hardness measurements of polished cross sections were made using a Leco M-400 H hardness testing machine. All measurements were made using 300 gram-force, applied for 15 seconds. Three indentations, approximately $100\,\mu$m apart, were made, starting $50\,\mu$m from the top surface, at each reported depth. Each reported hardness value is an average of the three measurement. Scanning Electron Microscope (SEM) images were taken using a Philips XL30 environmental SEM. Optical profilometry was performed using a Zygo NewViewTM 7300 instrument.

Multiple laser-nitrided trails were produced atop CP titanium following the scheme shown in figure 4.39. The titanium substrate was translated below the laser beam such that the entire plate length was covered. An overlap distance equal to half the trail width was used for all experiments. That is, a 50 % overlap was used. Trail widths, as a function of off-focal distance and processing speed, were determined using the cross-sectional micrographs of individual trails. The dwell time between successive trails was varied from approximately 10 to 20 s.

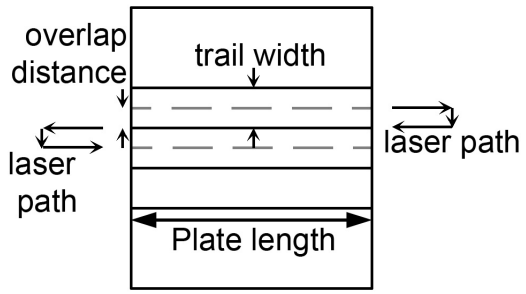

Figure 4.39. Illustration of the laser path during multi-trail nitriding experiments.

4.4.2 Results and discussion

As in the case of single-trail nitriding, multi-trail nitriding using pure nitrogen produced a mixture of titanium nitride dendrites and alpha-titanium within the melt pool. The melt pools were also highly-nonuniform and contained many cracks. Cross-sectional micrographs of multi-trail samples processed using pure nitrogen, with and without LSP, as a function of off-focal position and translation speed, are shown in figure 4.40. Cracking and non-uniformity were observed regardless of whether or not plasma existed during processing. Increasing the trail overlap to 75 % (not shown) resulted in increased cracking and did not improve uniformity. As was the case in single-trail nitriding, comparison of the melt volume produced with and without LSP showed that plasma participated in energy transfer to the substrate. Moreover, plasma also appeared to influence distribution of the sub-surface dendrites.

The top surfaces of the multi-trail samples also maintained many of the features observed in single-trail nitriding with pure nitrogen. Optical images of the top surface of multi-trail samples nitrided with and without LSP, using pure nitrogen, as a function of off-focal position and translation speed, are shown in figure 4.41. In keeping with the hypotheses presented in Section 4.3, smooth, reflective regions were much more pronounced when a pre-struck LSP was used. As shown in figure 4.42, the smooth, reflective regions were a highly reflective gold color when viewed using oblique illumination. Also, black nanoparticulate (not shown in figure 4.41 due to cleaning prior to imaging) was also only observed during processing with plasma. Additionally, the surface processed at a translation speed of 150 mm/s and an OFD of 8 mm without plasma was more dull-colored than the surface processes

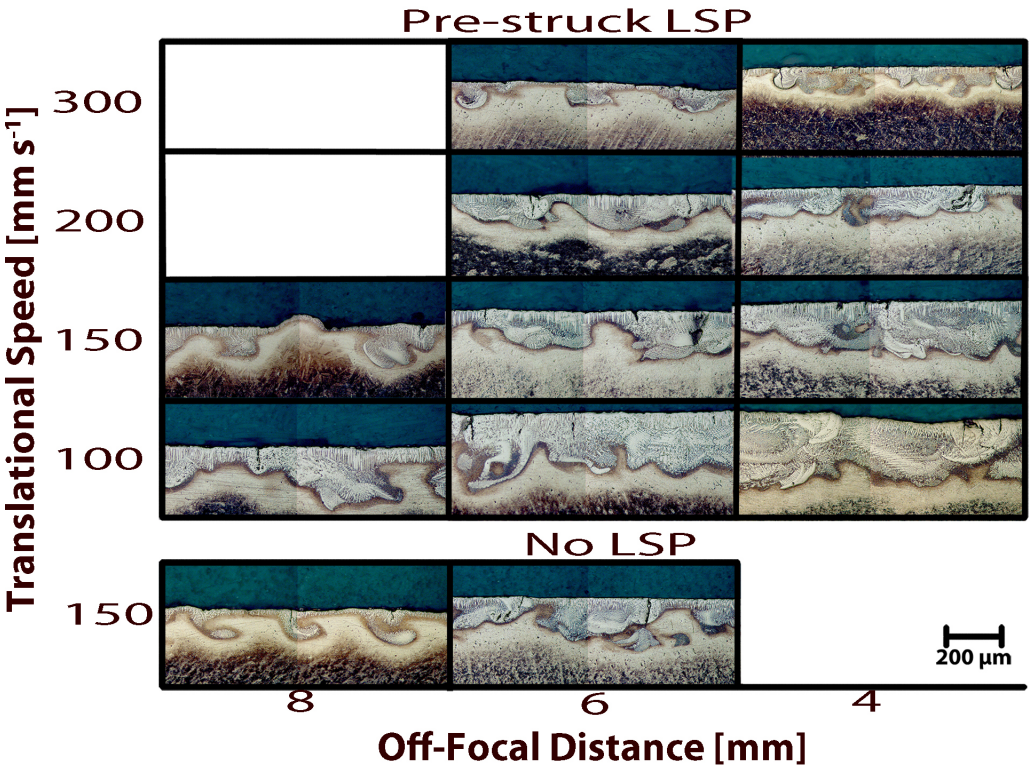

Figure 4.40. Cross-sectional micrographs of multi-trail samples processed using pure nitrogen with and without LSP as a function of off-focal position and translation speed. Cracking is clearly viable under all conditions tested.

with a pre-struck LSP—indicating greater coverage of the LSP-processed surface with titanium nitride.

Additional details regarding the morphologies of the processed surfaces were obtained via SEM imaging and optical profilometry. An SEM image taken near the center of the surface processed at 8 mm OFD and a translation speed of 150 mm/s with a pre-struck nitrogen LSP is shown in figure 4.43. The SEM images revealed smooth and rough regions along the surface. Within the smooth regions, several cracks were readily observed. These cracks were also observed in the optical micrographs shown in figure 4.41. Optical profilometry of the same sample, shown in figure 4.44, revealed a surface arithmetic average roughness (R_a) below 0.5 μm within the smooth region but an average roughness of 3.07 μm for the total surface.

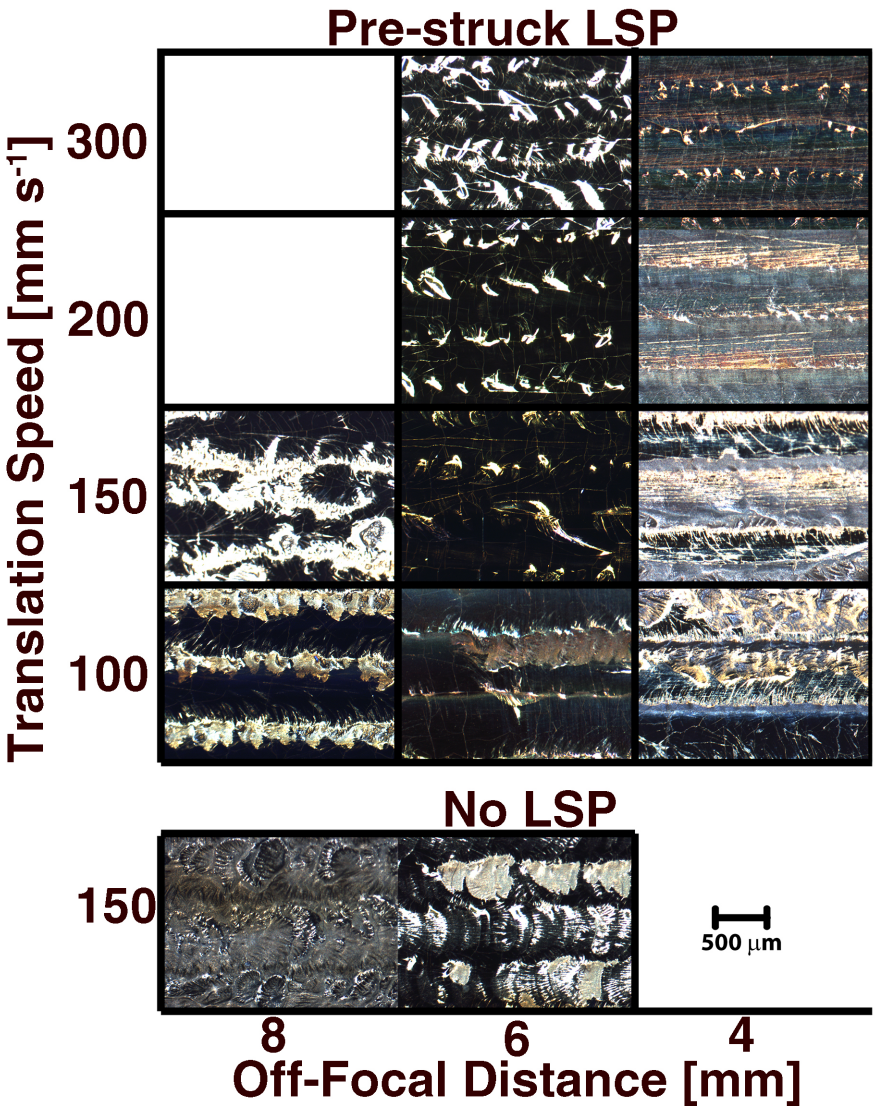

Figure 4.41. Optical images of top surface of multi-trail, nitrided samples, with and without LSP, using pure nitrogen as a function of off-focal position and translation speed. Note: black areas are highly reflective gold color.

As expected, using a $49.2 \pm 2\,\%$ nitrogen–argon mixture significantly affected the microstructure and shape of the melt pool. Cross-sectional micrographs of multi-trail samples processed using a $49.2 \pm 2\,\%$ nitrogen–argon mixture, with and without LSP, as a function of off-focal position and translation speed are shown in figure 4.45. Cracking, indicated with an arrow in figure 4.45, was only observed at a translation speed of 200 mm/s and an OFD of 6 mm. All other cases appeared free

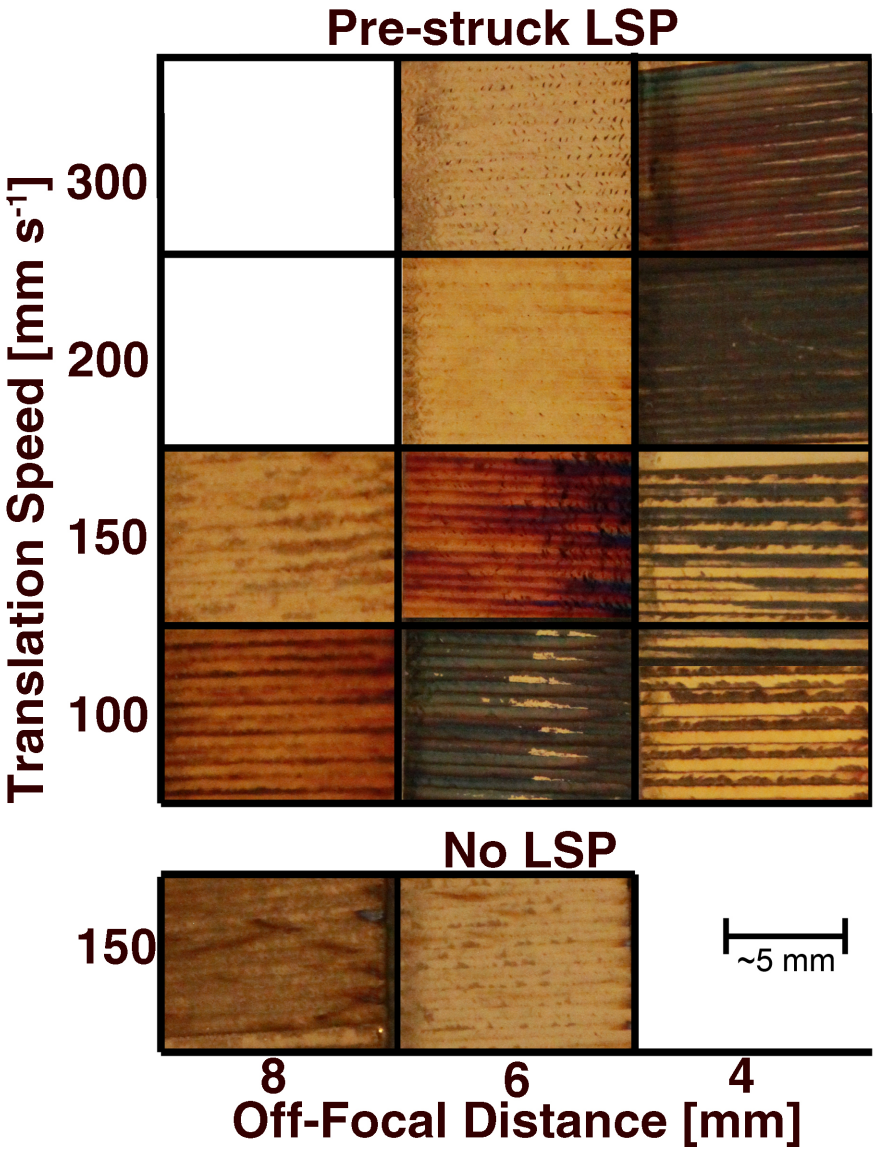

Figure 4.42. Optical images, with oblique illumination, of top surface of multi-trail, nitrided samples, with and without LSP, using pure nitrogen as a function of off-focal position and translation speed.

of cracks. See Appendix C for magnified cross-sectional image. Within the melt pool, the microstructure consisted of alpha titanium with no evidence of titanium nitride dendrites. Within tens of microns from the surface however, dendrites were observed. As in the case of nitriding with pure nitrogen, the presence of plasma was observed to influence the melt pool shape and size. At a translation speed of 150 mm/s and OFDs of 8 mm and 6 mm, processing without plasma appeared to

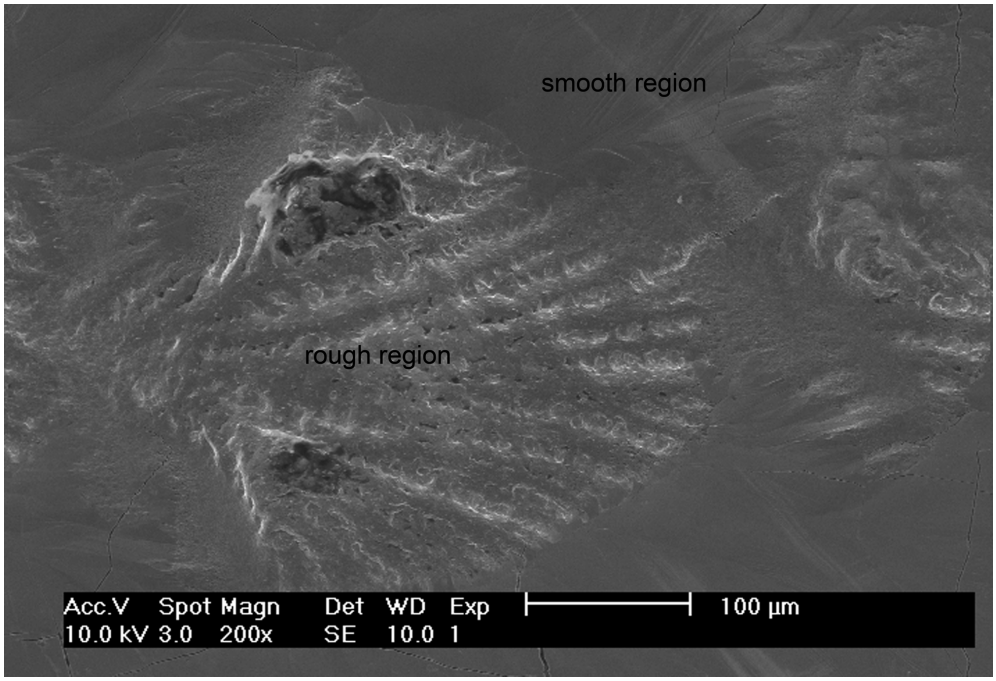

Figure 4.43. SEM image taken near the center of the surface processed at 8 mm OFD and a translation speed of 150 mm/s with a pre-struck nitrogen LSP.

produce a deeper melt pools. Based on a comparison of the depths of trails nitrided with and without LSP, it is again clear that plasma participates in energy transfer to the substrate. Depending on processing parameters and gas composition, plasma can either decrease or increase the total energy absorbed by the substrate.

Figure 4.46 shows optical images of top surface of multi-trail samples nitride, with and without LSP, using a $49.2 \pm 2\,\%$ nitrogen–argon gas mixture. Again, smooth, reflective regions, which were a highly reflective gold when viewed with oblique illumination as shown in figure 4.47, were more evident when a pre-struck LSP was used. As in the case of single-trail nitriding using a nitrogen-argon mixture, black nanoparticulate was not observed under any processing condition.

Scanning electron microscopy of the surface of the samples processed using a $49.2 \pm 2\,\%$ nitrogen–argon gas mixture at 8 mm OFD and a translation speed of 100 mm/s (figure 4.48), together with optical profilometry (figure 4.49),verified that the reflective regions located along some trails were indeed smooth. The smooth regions were bordered by rougher ridges formed at the edges of successive melt pools.

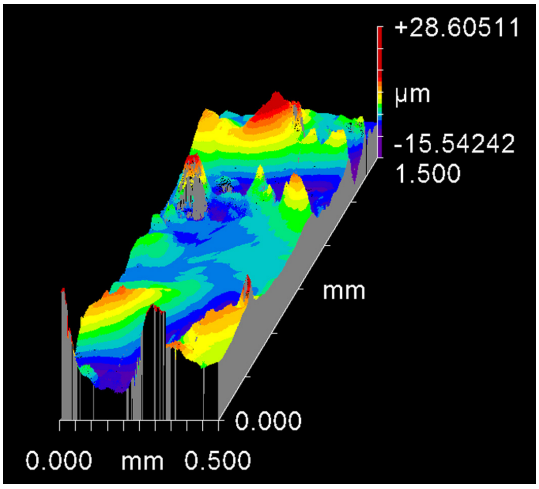

Figure 4.44. Surface topography of the sample processed at 8 mm OFD and a translation speed of 150 mm/s.

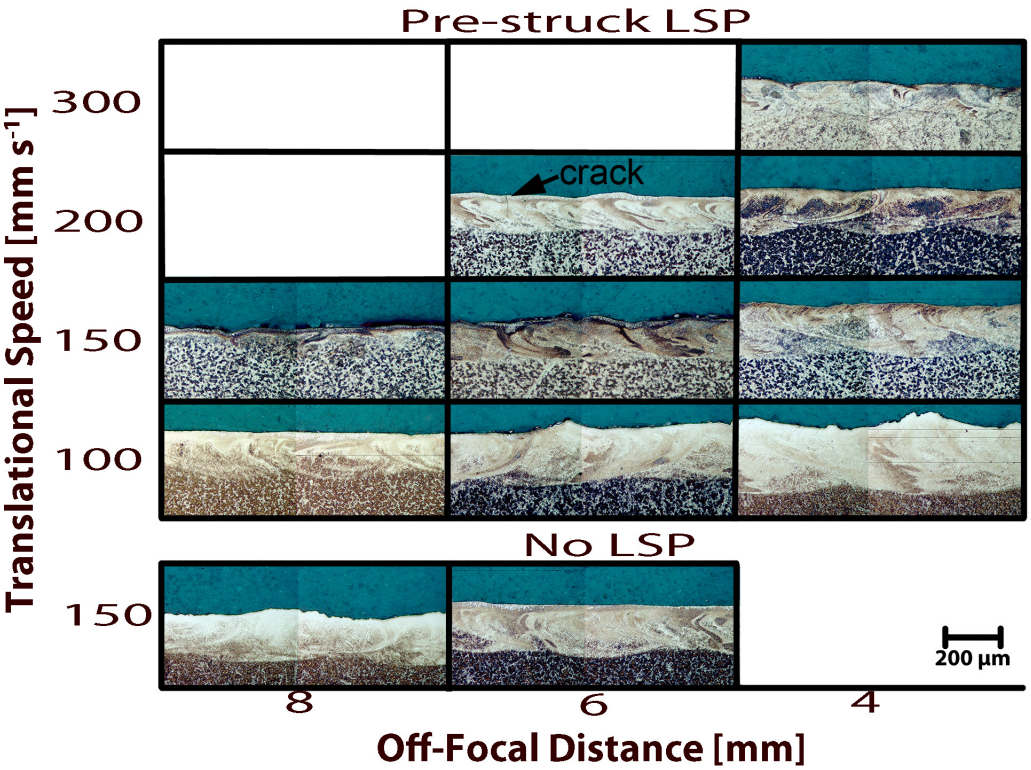

Figure 4.45. Cross-sectional micrographs of multi-trail samples processed using a 49.2± 2 % nitrogen–argon mixture, with and without LSP, as a function of off-focal position and translation speed.

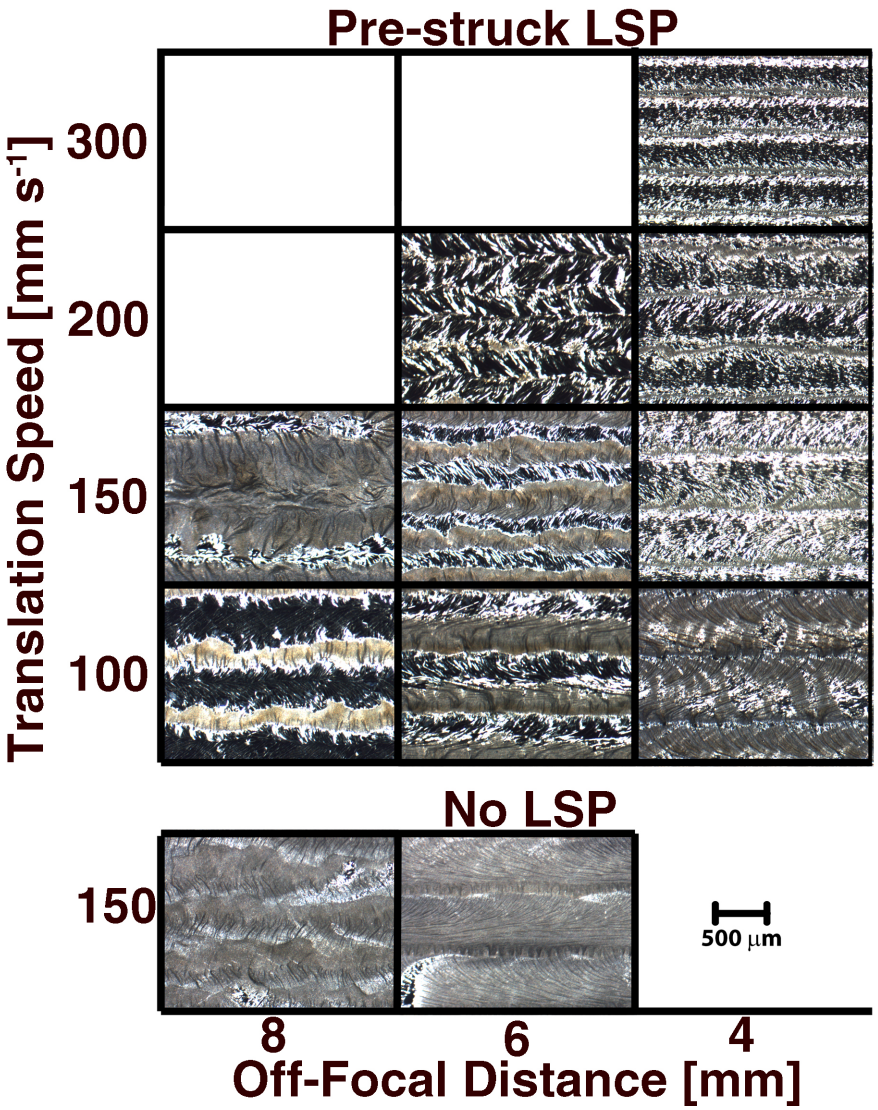

Figure 4.46. Optical images of top surface of multi-trail samples nitride, with and without LSP, using a 49.2±2 % nitrogen–argon mixture as a function of off-focal position and translation speed.

Based on the microstructures of the trails processed with pure nitrogen versus a nitrogen-argon gas mixture, it was expected that the melt-trail hardness would be higher in the samples processed with pure nitrogen. Indeed, this was the case. Hardness profiles of multi-trail samples processed using pure nitrogen and 49.2 ± 2 % nitrogen–argon mixture for a transition speed of 100 mm/s and OFDs of 6 and 4 mm are shown in figure 4.50. In all cases, hardness values decreased to

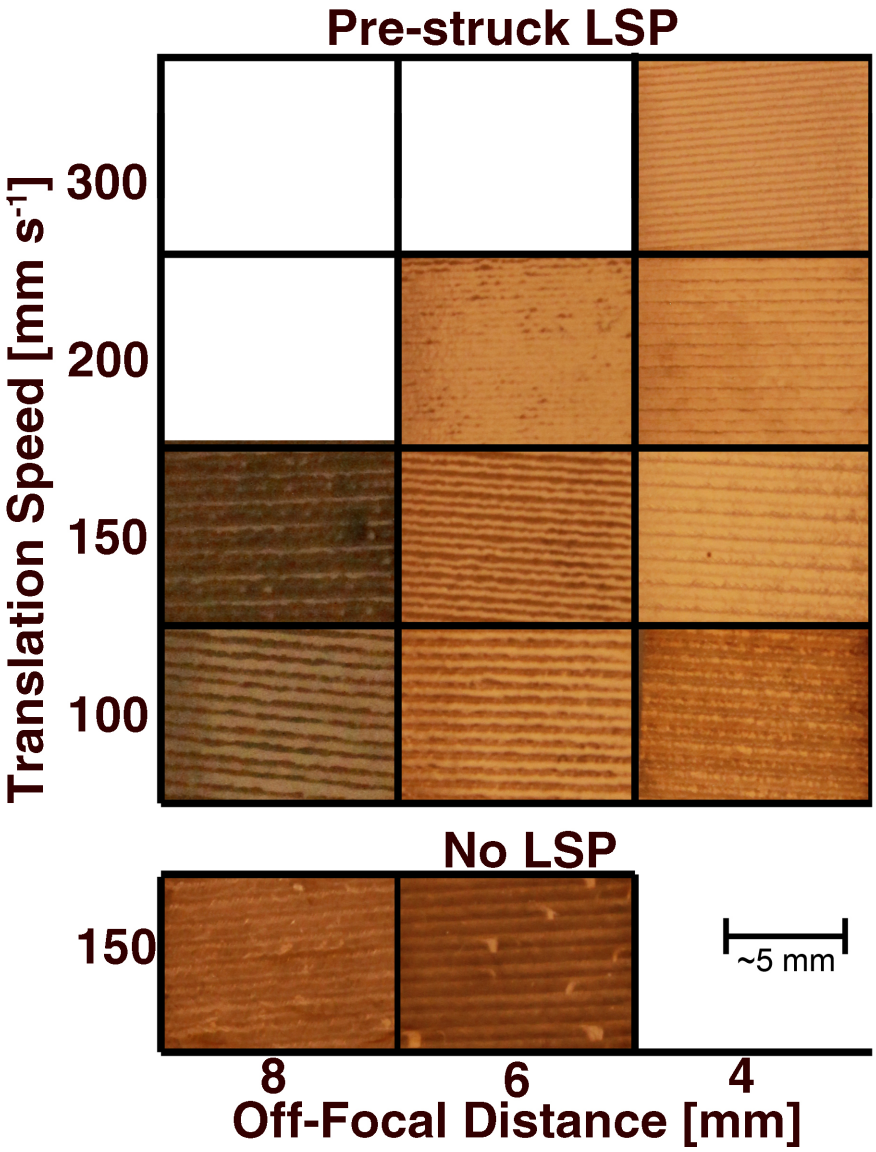

Figure 4.47. Optical images, with oblique illumination, of top surface of multi-trail samples nitride, with and without LSP, using a $49.2 \pm 2\,\%$ nitrogen–argon mixture as a function of off-focal position and translation speed.

the substrate hardness of 200 HV at a depth of 300-400 μm. The hardness near the surface of trail processed with pure nitrogen at an OFD of 6 mm was approximately twice harder than both trail processed with the nitrogen–argon mixture. However, this trail's hardness profile did not decrease smoothly due to the uneven distribution of dendrites below the surface. Moreover, cracking within the samples processed with pure nitrogen rendered their practical application unlikely.

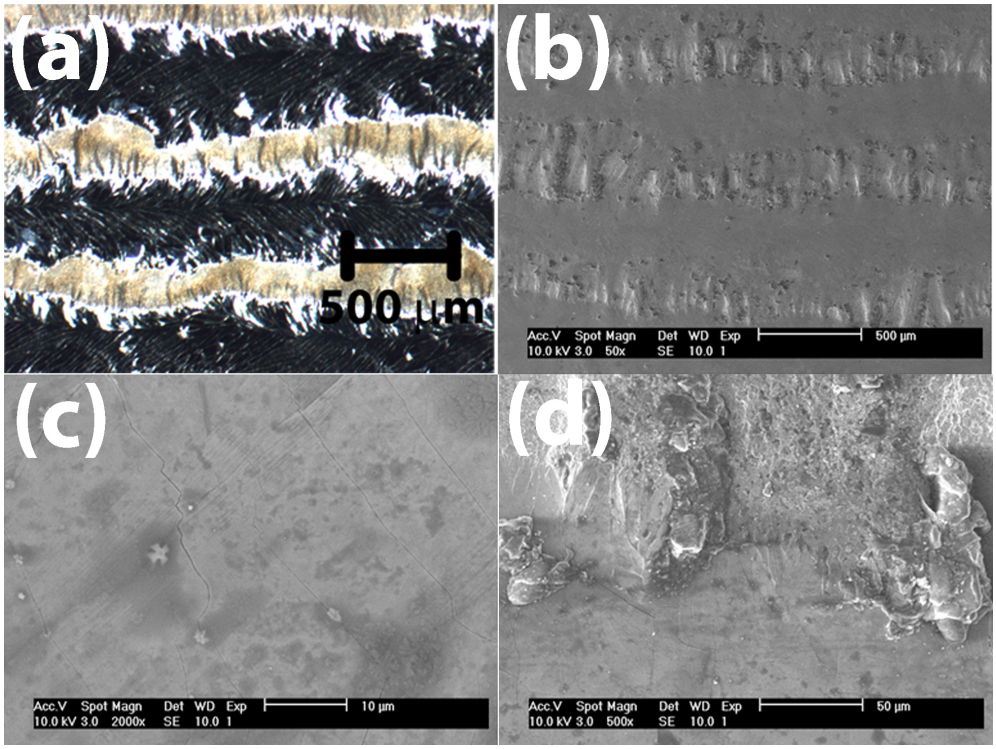

Figure 4.48. (a) Top surface and (b,c,d) SEM images of multi-trail samples nitride using a pre-struck LSP formed in a $49.2 \pm 2\,\%$ nitrogen–argon mixture. (c) SEM image of smooth, reflective region. (d) SEM image of transition from smooth to rough region.

In addition to crack reduction, a major advantage of using an nitrogen-argon gas mixture instead of pure nitrogen, first reported in Section 4.3, was the lowering of the threshold processing speed for oxygen-free nitriding of titanium. Taking advantage of this phenomenon, crack-free nitrided layers of more than $600\,\mu$m in depth were achieved at low translation speeds using a nitrogen-argon mixture, together with a pre-struck LSP. Cross-sectional micrographs of multi-trail samples processed at translation speeds of 25 and 15 mm/s are shown in figure 4.51. While a thin layer of titanium nitride dendrites could be observed near the surface of some trails, dendrites were not observed within the melt pool. Below the dendrites, the melt pool consisted of acicular alpha with alpha-prime (martensitic) titanium needles. Previous beta grain boundaries were also observed.

Not only were cracks not evident in the cross sections processed using a N_2-Ar gas mixture at low speeds, cracks were also not observed during microhardness indentation. Figure 4.52 shows a cross-sectional micrograph of the sample processed

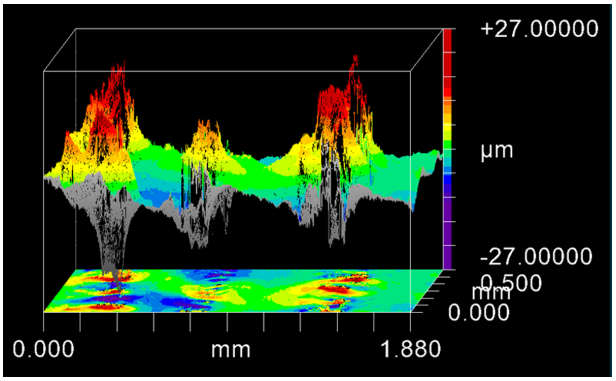

Figure 4.49. Surface topography of the multi-trail samples nitride using a pre-struck LSP formed in a $49.2 \pm 2\,\%$ nitrogen–argon mixture.

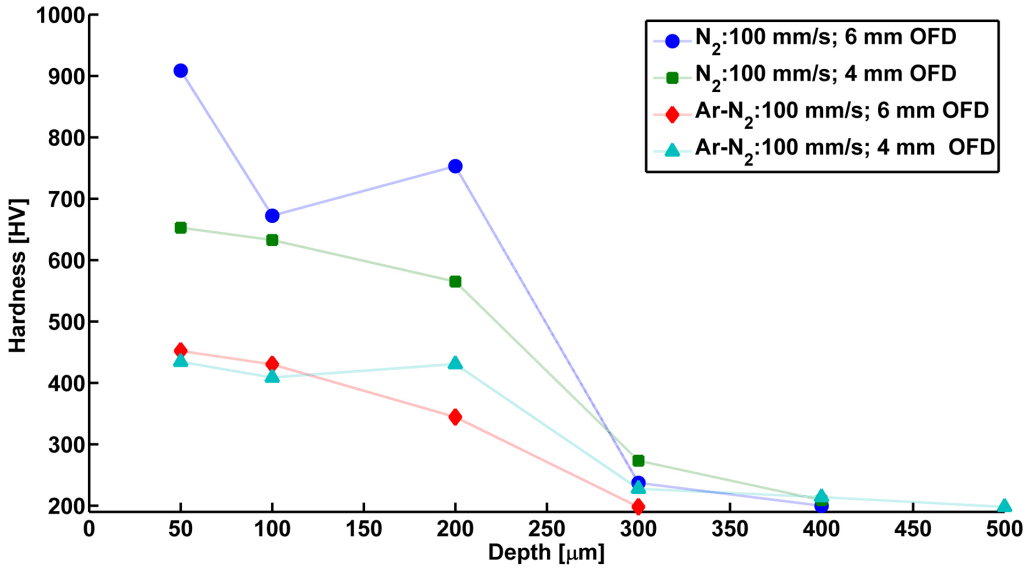

Figure 4.50. Hardness profiles of multi-trail samples processed using pure nitrogen and a $49.2 \pm 2\,\%$ nitrogen–argon mixture for a transition speed 100 mm/s and two off-focal distances.

at a translation speed of 15 mm/s and an OFD of 8 mm with Vickers hardness indentations. The fact that cracking was not observed is very promising and suggests that cracking will not be readily induced in a practical application.

Hardness profiles of samples processed at low speeds with the nitrogen-argon gas mixture are shown in figures 4.53 and 4.54. The hardness profile within the melt pool averaged around 550 HV at a translation speed of 15 mm/s. The substrate hardness, of 200 HV, was reached at a depth of 600 to 700 μm. At a transla-

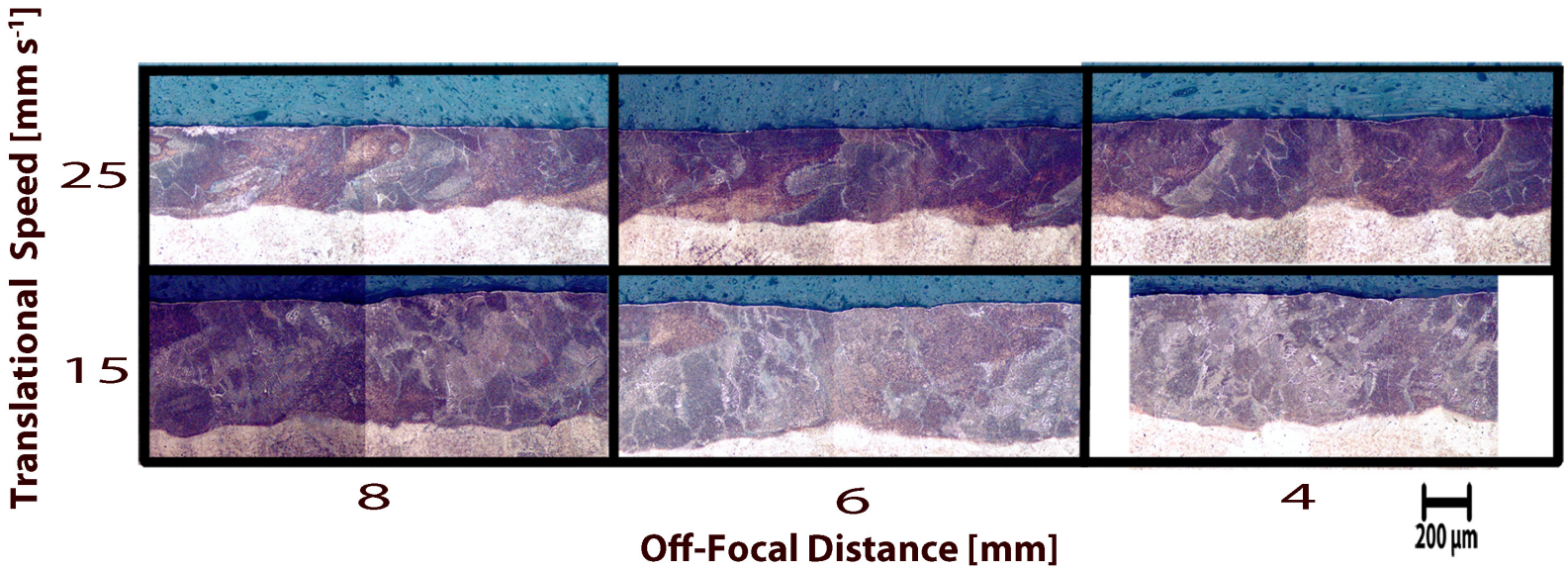

Figure 4.51. Cross-sectional micrographs of multi-trail samples processed using a $49.2 \pm 2\,\%$ nitrogen–argon mixture at low translation speeds, as a function of off-focal position and translation speed.

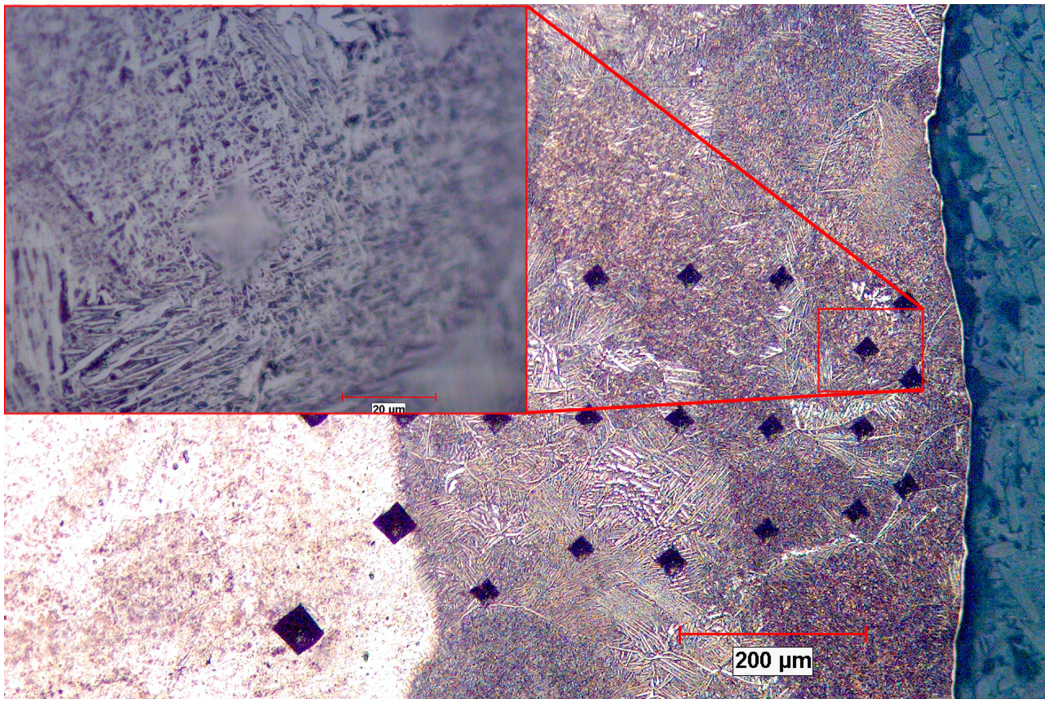

Figure 4.52. Cross-sectional micrographs of sample with Vicker's hardness indentations. The sample was processed using a $49.2 \pm 2\,\%$ nitrogen–argon mixture at a translation speed of 15 mm/s and an off-focal distance of 8 mm.

tion speed of 25 mm/s, the average hardness was approximately 50 HV lower and substrate hardness was reached at a depth of 400 to 600 μm.

To better assess the microstructures of the melt pool, XRD was performed on the top surfaces of the two samples after processing and also after flat-grinding. The XRD spectra taken after processing, shown in figure 4.55 revealed the presence of alpha titanium as well as titanium nitride. After flat-grinding, there were no detectable diffraction lines associated with titanium nitride. This leads to the conclusion that titanium nitride was only confined to the surface layer of the processed samples. Below this, a nitrogen-titanium solid solution existed.

Throughout Section 4.3, it was hypothesized that nitrogen or nitrogen–argon plasmas produced a thin layer of vapor-deposited titanium nitride during processing. Much evidence, including the observations of nanoparticulate, surface appearance and XRD spectra was given to support this hypothesis. Here further evidence is provided. While there were strong titanium nitride reflections in the XRD spectra of the sample processed with a pre-struck LSP at a translation speed

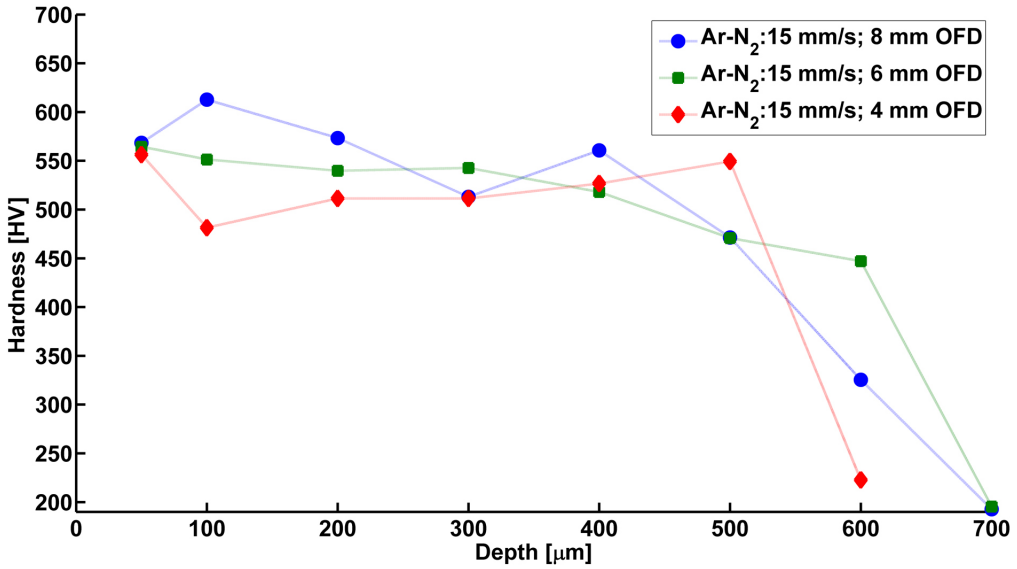

Figure 4.53. Hardness profiles of multi-trail samples processed using a $49.2 \pm 2\,\%$ nitrogen–argon mixture at an off-focal distances of 8, 6 and 4 mm and a translation speed of 15 mm/s.

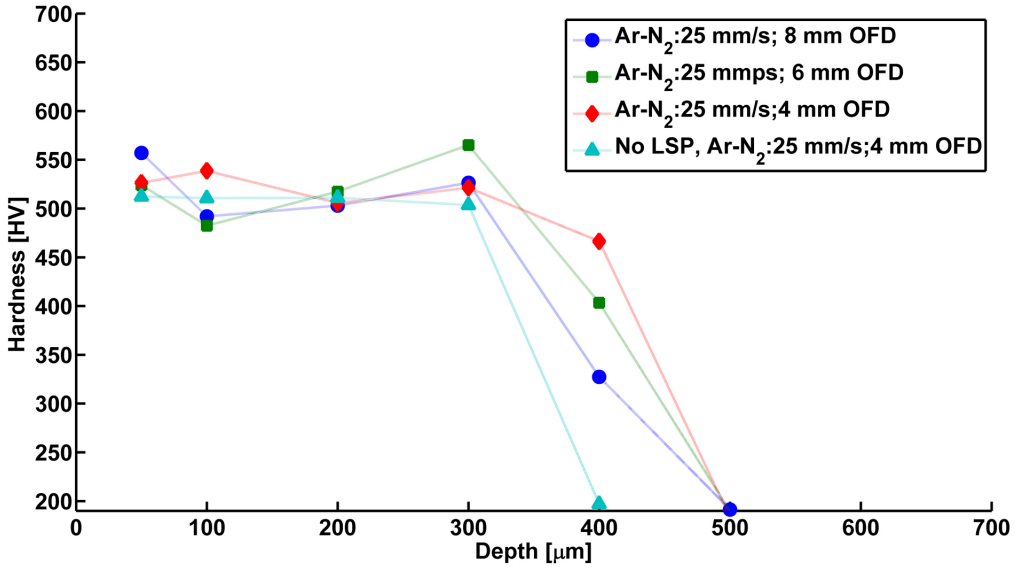

Figure 4.54. Hardness profiles of multi-trail samples processed using a $49.2 \pm 2\,\%$ nitrogen–argon mixture at an off-focal distances of 8, 6 and 4 mm and a translation speed of 25 mm/s. Hardness profile of sample processed without plasma at an off-focal distance of 8 mm is shown.

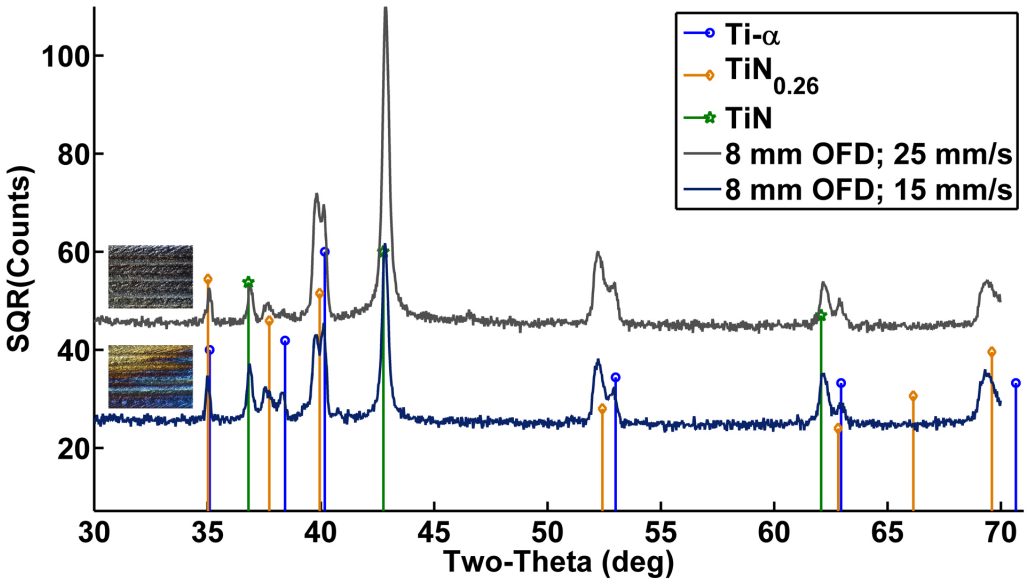

Figure 4.55. XRD spectra of samples processed using a $49.2 \pm 2\,\%$ nitrogen–argon gas mixture at an off-focal distance of 8 mm and translation speeds of 15 and 25 mm/s.

of 25 mm/s and an OFD of 8 mm (figure 4.55), the reflections disappeared after grinding off the top surface (figure 4.56) and when processing without plasma formation (figure 4.57).

4.4.3 Conclusions

The work described here built upon the basic science revealed and the hypotheses presented in Sections 4.2 and 4.3. Using data regarding single-trail nitriding with pure nitrogen and with a $49.2 \pm 2\,\%$ nitrogen-argon mixture, multi-trail nitriding of titanium was performed. Further evidence was provided to support the hypotheses that plasma participates significantly in energy transfer to the substrate during laser nitriding (when plasma is pre-struck or surface-struck) and is responsible for vapor deposition of titanium nitride.

The goal of this work was to produce wide-area, hard, functionally-graded and crack-free layers atop titanium. Through systematic study, this goal was achieved. Taking advantage of the lowering of the threshold speed for oxygen-free nitriding using a $49.2 \pm 2\,\%$ nitrogen-argon mixture, in place of pure nitrogen, layers more than 600 μm thick with functionally-graded hardness profiles, peaking around 550 HV near the surface, were produced. The layers were shown to be

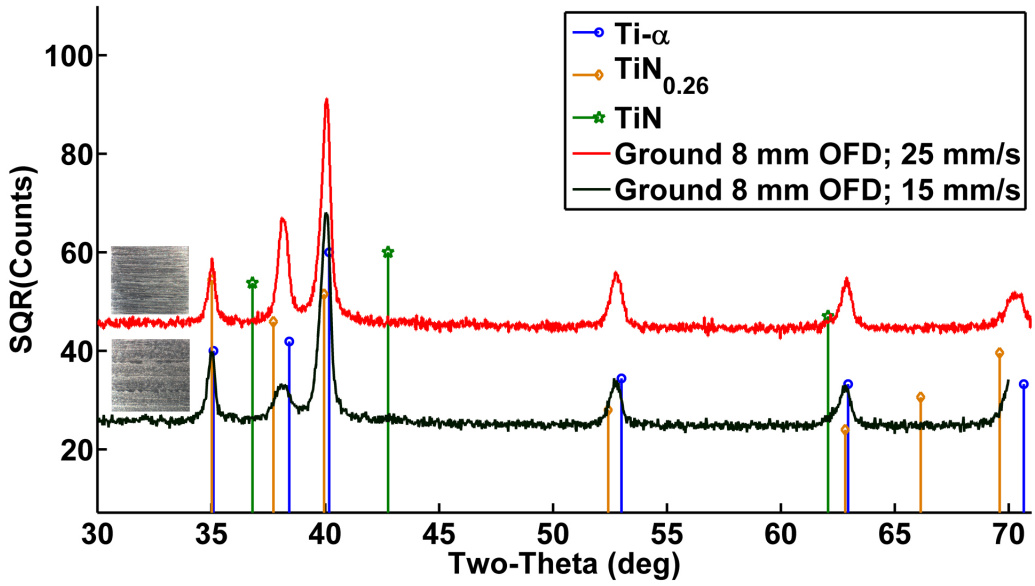

Figure 4.56. XRD spectra, collected after griding top surface, of samples processed using a $49.2 \pm 2\,\%$ nitrogen–argon gas mixture at an off-focal distance of 8 mm and translation speeds of 15 and 25 mm/s.

crack-free and dendrite-free. The production of crack-free layers less than 400 μm thick, was also demonstrated.

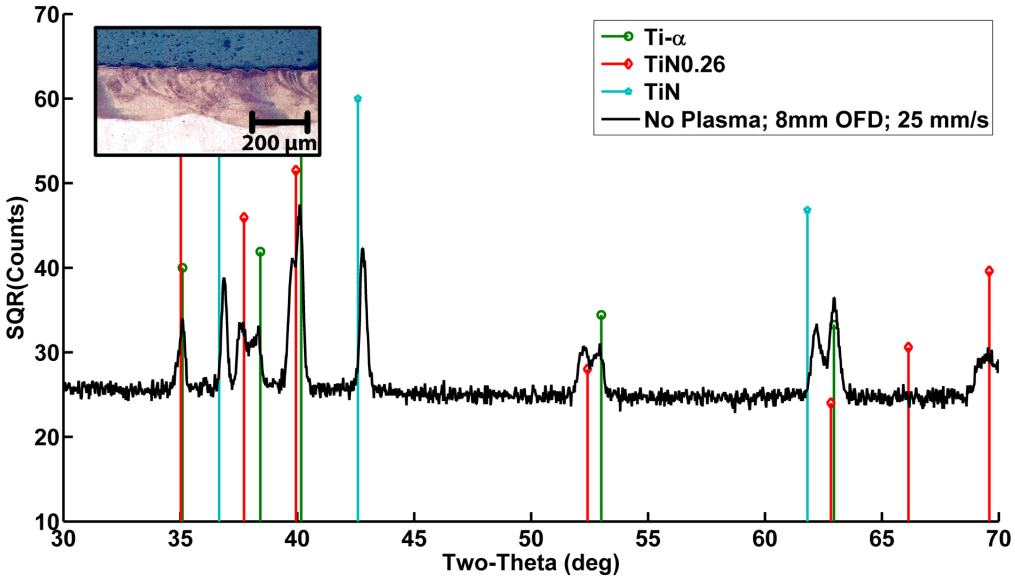

Figure 4.57. XRD spectra of samples processed using a $49.2 \pm 2\,\%$ nitrogen–argon gas mixture at an off-focal distance of 8 mm and translation speeds of 25 mm/s without plasma. Also shown is a cross-sectional micrograph of the sample

Chapter 5

Conclusions and future work

5.1 Conclusions

The overall goal of the work presented in this dissertation was to provide a basis for understanding upon which the application of LSP for materials processing can be based. This goal was achieved by combining experimental determination of LSP parameters, computational fluid dynamics modeling and investigation of laser nitriding of titanium using optical emission spectroscopy and LSP. This work represents a significant step forward towards understanding the role of plasma in laser processing of materials, in general, and specifically in laser nitriding of titanium. With respect to the nitriding of titanium, a similar set of experiments to those presented here does not exist anywhere in the literature. Key and novel conclusions, drawn from this research, are highlighted in this section.

Spatially-resolved temperature and density of a laser-sustained plasma, formed in forced convective flow of argon with 0.5 % hydrogen, was determined using optical emission spectroscopy. The plasma temperature, assuming LTE, was determined using the relative intensities of excited atomic emission lines. The electron density was determined, without assumption of LTE, using the Stark broadening of the hydrogen-alpha emission line. Three important findings arose from these spectroscopic investigations:

- An optically-thick region existed near the focal point of the laser beam. Within this region, temperature measurement via the Boltzmann plot tech-

nique results was not valid.

- Abel inversion of spectroscopic data via the tenth-degree-even-powered- polynomial fit was effective and introduced little error.

- Regions of the LSP where the temperature was above 10,000 K were in LTE. Modeling of the LSP using the assumption of LTE should be valid within this domain but the influence of optically-thick radiation on energy transfer within the LSP must be accounted for.

A computational fluid dynamics model of an axi-symmetric LSP, sustained in a forced convective flow of argon, was also developed and tested against published and experimental results. Predicted LSP temperature contours and total-beam absorbtion compared well with the experimental results of Chen, Mazumder and Krier [43, 44] and with experimental results reported in this dissertation. The model incorporated temperature-dependent thermal and transport properties of an argon plasma under LTE. Major assumptions used within the model, LTE and negligible refraction of the laser beam, were tested and verified experimentally. Novel contributions of this work included

- the development of a computational-efficient "light pipe" method to model laser beam propagation and absorption within the domain, assuming negligible beam refraction. The assumption of negligible beam refraction was verified experimentally.

- Using the "light pipe" method, the effects of Gaussian, annular, Dimodal (D-Mode) and Quadramodal (Q-Mode) beam modes on LSP were compared for the first time. A Gaussian beam was found to produce the largest plasma and the greatest total-beam absorption.

The third portion of the work focused on the application of LSP in CO_2 laser nitriding of titanium. As part of this work, novel experiments were conducted to test conflicting hypotheses regarding the role of plasma during laser nitriding of titanium. The formation of oxygen-free nitrided layers with near-stoichiometric surfaces was also demonstrated. Utilizing the unique properties of LSP, a series of novel experiments were used to shed light on the role of plasma absorption,

the role of plasma in transferring energy to substrate, the importance of nitrogen dissociation during the laser nitriding process and the influence of translation speed and off-focal distance on the processed layers:

- nitrogen-rich plasma contributed to the transfer of energy to the substrate and, under some conditions, energy input into and its distribution within the sample did not appear to be attenuated by the presence of a nitrogen-rich plasma;
- nitriding with pre-struck LSP and without plasma demonstrated that the presence of atomic nitrogen could arise from either dissociation of molecular nitrogen in the LSP or at the melt surface (no plasma), with subsequent incorporation into the melt trail;
- conditions were identified where the degree of titanium nitride formation within the melt was similar for the pre-struck LSP (dissociation taking place within the plasma, i.e. above the surface) and without plasma (dissociation at the melt surface, where decomposition of nitrogen in the melt is the rate limiting step);
- A threshold translation speed was identified, as a function of off-focal distance, above which:(a) nitrogen-rich pre-struck plasma was located near the titanium substrate surface; and (b) a near-stoichiometric titanium nitride surface with dendritic sub-surface structures was formed in open atmosphere;
- below the threshold speed, the surface showed a high susceptibility to oxidation and compositional variation;
- formation of titanium nitride nanoparticulate provided evidence for reaction of nitrogen within the plasma with titanium vaporized from the substrate;
- a processing window (above the black curve and above the grey, dashed curve in figure 4.21) for the formation of near-stoichiometric, oxide-free TiN surfaces was identified for surface-struck plasma;
- for the first time, it has been shown that laser-sustained plasma can access nitriding conditions beyond those achieved with surface-struck plasma (above

the grey, dashed curve in figure 4.21), or in the absence of plasma, to produce uniform, near-stoichiometric, titanium nitride layers; and

- the pre-struck LSP processing window occurs at larger defocussing conditions than the surface-ignited plasma processing window, enabling greater surface coverage and faster nitriding of titanium.

Nitriding of titanium using a LSP formed in a nitrogen-argon gas mixture led to additional understanding regarding the role of plasma and argon addition within the nitriding process.

- Reaction of atomic nitrogen, provided by the plasma, with oxygen resulted in the formation of nitric oxide and nitrogen dioxide which aided in the prevention of oxidation of the nitride trails.

- Formation of a surface titanium nitride film, tens of micrometers thick, atop nitrided trails was hypothesized to result from interaction of atomic nitrogen, provided by the plasma, with titanium vapor emitted from the substrate.

- The morphology of titanium nitride at the surface of the nitride trails was related to surface temperatures during processing: vapor-deposited titanium nitride formed a continues surface where the substrate surface was sufficiently hot but not molten; condensed into nanoparticipants where the surface was too cold for nucleation and growth to take place; and, was incorporated into the melt where the surface was molten.

- Plasma was again shown to participated in energy transfer from the laser beam to the substrate and did not necessarily reduce the total energy absorbed by titanium during laser nitriding despite higher total-beam absorption of a nitrogen-argon LSP, as compared to a pure-nitrogen LSP .

- Addition of argon to nitrogen gas resulted in a reduction of the threshold processing speed for oxygen-free nitriding of titanium. The reduction in threshold processing speed allowed the formation of deep nitrogen-containing, solid-solution layers, several hundred microns thick.

The ultimate goal set out in this work, the formation of large-area, hard, functionally-graded and crack-free layers atop titanium, was achieved using plasma formed in a $49.2 \pm 2\,\%$ nitrogen-argon gas mixture. By overlapping laser trails, large-area, crack-free and dendrite-free layers as thick as $600\,\mu$m were demonstrated. The layers had functionally-graded hardness profiles, with a near-surface hardness around 550 HV.

5.2 Improvements and future work

Several recommendations may be given for the refinement of the work done here. Results of Chapters 2 and 3 made clear that consideration of optically-thick radiation is important in analysis of optical emission data as well as in modeling of LSP. If accurate measurement of temperature within the core of the LSP is to be made using the Boltzmann plot technique, the opacity of each emission line needs to be quantitatively determined. A general approach to determine the opacity of an emission line involves imaging the plasma onto itself using a concave mirror while recording the spectral emissions [136].

Alternatively, other techniques, not involving the measurement of emission line intensity may be considered for the measurement of temperature. Keefer et al. [32] appeared to have had success in determining the spatially-resolved temperature of a LSP sustained in air using the continuum intensity near 512.5 nm. Caution must however be used, as this technique requires calibration using an emission source with a known temperature. Glumb [38] has also raised doubt regarding the accuracy of this approach.

Another attractive technique is the measurement of the shift-to-width ratio of Stark-broadened argon lines. This technique is independent of the LTE assumption and can be used reliably to determine the electron temperature within 10 % [18]. It does however require a spectrometer with excellent ($<$0.01 nm) resolution. This technique also requires the use of an emission line known to be optically thin or measurement of the line opacities.

Several improvements and expansions can also be suggested for the numerical model presented in Chapter 3. Although the assumption of LTE was appropriate at temperatures above 10,000 K, it will likely fail in the outer regions of the plasma.

Modeling of LSP-substrate interactions will however require knowledge of temperature in outer plasma regions. After all, these regions are the first to interact with a substrate. Additionally, knowledge of the gas temperature, which is likely to be much lower than the electron temperature, is necessary. A non-LTE model will require incorporation of multiple temperatures and determination of non-LTE thermal and transport properties. Many of these properties can be derived using the work of Devoto [137]. Incorporation of surface reactions between a substrate and LSP would also be very powerful.

A less arduous task, with respect to improvement of the axi-symmetric numerical model, is the expansion to a fully three-dimensional model. Such a transition would allow modeling of cross-flows of gas and interaction of LSP with arbitrarily-shaped substrates. Of course, this additional capability comes at the expense of computational speed. Transition from two-dimensional axial-symmetry to three dimensions should however be straight forward. Additionally, the "light pipe" method can be easily expanded to three dimensions if the mesh is appropriately designed. Less arduous still, is the incorporation of a more realistic flow velocity into the model.

Finally, a great deal of additional work can be recommended with respect to the application of LSP to laser nitriding. The experiments presented here all used a constant flow rate and laser power. Varying the laser power and flow rate would result in a more complete parametric study. It should also be noted that titanium alloy systems, as well as other refractory metals should be amenable to LSP nitriding. Pre-heating and temperature control during processing may also be a means to reduce the likelihood of cracking. The incorporation of additional energy sources, such as lasers of differing wavelengths, direct or alternating current fields and magnetic fields may also be used to control or enhance the nitriding process.

A critical parameter was the ratio of argon to nitrogen. Varying the argon-nitrogen gas ratio is expected to influence significantly the resultant microstructure and its properties, e.g. hardness. Along with this, it is recommended that the sub-surface atomic concentration of nitrogen and oxygen be measured in the nitrided layers. Unfortunately, this can not be accomplished using the most common technique, energy dispersive X-ray spectrometry, due to the nearness of oxygen,

nitrogen and titanium peaks near 0.45 keV. Potentially, the improved resolution associated with wavelength dispersive X-ray spectroscopy or electron probe microscopy may allow for accurate atomic concentration mapping.

A final consideration for the application of functionally-graded nitrided layers is their mechanical properties. In addition to hardness, the wear, corrosion, and elastic properties of the layers should to be characterized prior to application. Once an understanding of how processing parameters affect the properties of the nitridied layers is gained, processing parameters can be customized to produce tailored microstructures for tailored applications.

Appendix A

Calculation of excitation temperature and electron density

A.1 Matlab Code: Calculating Excitation temperature via Boltzmann plot technique

```
%%%
```

```
%%
%Import and average data;
for i=1:Slices      %Slices
    for j=1:Points
        if j<10
    FileName=sprintf('%d00%d',i,j); %Sequential file name read
        else
    FileName=sprintf('%d0%d',i,j); %Sequential file name read
        end

   NewFileName=sprintf('DataFiles/Clean%d00%d',i,j); %New file names
   NewFileNameUnCal=sprintf('DataFiles/UnCal%d00%d.txt',i,j); %New file names
   TempData=importdata(FileName);
   TempData(1,:)=[];TempData(1,:)=[];TempData(1,:)=[];TempData(1,:)=[];
   TempData(:,1)=[];
   TempDataAvg=(sum(TempData')/length(TempData(1,:)))'; %Average spectrum
   TempUnCal=[Wavelengths TempDataAvg]; % For Diagnostics
   TempDataFinal=(TempDataAvg-DarkAvg).*Cal; %Subtract dark spectrum and calibrate
   TempDataFinal=(abs(TempDataFinal)+TempDataFinal)/2;   %Eliminate negative values
   save(NewFileName,'TempDataFinal','-ascii','-tabs'); %save new file
   save(NewFileNameUnCal,'TempUnCal','-ascii','-tabs'); %save new file
   fprintf('saving file%s\n',NewFileName);

    end
end
%% Reorganize data into seperate files for each point
clear FileName;
```

```
clear NewFileName;
clear ReadyMatrix;

for i=1:Slices       %Slices
    NewFileName=sprintf('DataFiles/Spectra_%d',i); %New file names
    for j=1:Points
    FileName=sprintf('DataFiles/Clean%d00%d',i,j); %New file names
    TempDataFinal=importdata(FileName);
    ReadyMatrix(:,Points-j+1)=TempDataFinal;
    end
    save(NewFileName,'ReadyMatrix','-ascii','-tabs'); %save new file
   fprintf('saving file%s\n',NewFileName);
   clear ReadyMatrix;
end
%% Check data
clear tempReady
for i=8:8
 File=sprintf('DataFiles/Spectra_%d',i);
    tempReady=importdata(File);
end


%%  Integrate Lines prior to abel inversion
clear FileName
clear NewFileName
```

```
for i=1:Slices
FileName=sprintf('DataFiles/Spectra_%d',i);
NewFileName=sprintf('DataFiles/IntegratedSpectra_%d',i);
FinalData=importdata(FileName);

Lines=importdata('DataFiles/Lines.txt');    % Import spectral line data
Lines_Wavelengths=Lines.data(:,1);          % Center wavelengths
Lines_LdivAulGu=Lines.data(:,2);            % Lambda/gk Aki
Lines_Ek=Lines.data(:,3);                   % Energy of upper level
Lines_Width=Lines.data(:,4);                % Approximate spectral width
Lines_HalfWidth=ceil(Lines_Width/2);        % Approximate half-width
Lines_Index=Lines.data(:,5);        %wavelength index of input data
for j=1:Points
    Ytemp=FinalData(:,j);

for k=1:length(Lines_Wavelengths)
    Index_left=Lines_Index(k)-Lines_HalfWidth(k);
    Index_right=Lines_Index(k)+Lines_HalfWidth(k);
    %right hand side of boltzman eq. sorted by energy
    Line_Int(k)=sum(Ytemp(Index_left:Index_right)-mean([Ytemp(Index_left) Ytemp(Index_right)]))*0.06;
    if Line_Int(k)<0
        Line_Int(k)=0;
    end
end
Line_Int_Final(:,j)=Line_Int;

end
```

```
save(NewFileName,'Line_Int_Final','-ascii','-tabs'); %save new file
   fprintf('saving file%s\n',NewFileName);
end



%% Abel inverstion of data based on fitting to a 10th degree even
%%%%polynomial
clear FileName;
clear NewFileName;
clear ReadyMatrix;
x=(0:Points)/(Points);  %scale x axis
R=1;
for i=1:Slices
 FileName=sprintf('DataFiles/IntegratedSpectra_%d',i);
 NewFileName=sprintf('DataFiles/InvertedData%d',i);
 ReadyMatrix=importdata(FileName);
 ReadyMatrix=[ReadyMatrix zeros(length(ReadyMatrix(:,1)),1)];

%%%Fit Spectra to tenth degree polynomial then invert analytically%%%
for j=1:length(ReadyMatrix(:,1))
    Q=ReadyMatrix(j,:)-min(ReadyMatrix(:,Slices));
    ft_1 = fittype({'X^10', 'X^8', 'X^6', 'X^4', 'X^2', '1'},'dependent',{'y'},'independent',{'X'},
    'coefficients',{'fF', 'eE', 'dD', 'cC', 'bB','aA'});
    % Fit this model using data%
    [fit_one,goodness_one]= fit(x',Q',ft_1);
    aA=fit_one.aA;
```

```
    bB=fit_one.bB;
    cC=fit_one.cC;
    dD=fit_one.dD;
    eE=fit_one.eE;
    fF=fit_one.fF;
    %%%%%%%%%%%%%%%%%%%%%%%%%%
%%Compare data to fit%%
%hold all;
%plot(fit_one,'--');
%plot(x,Q);
%%%%%%%%%%%%%%%%%%%%%%
r=x;
%analytical solution to abel transform%
fit_poly=(-1/pi)*(2/315*sqrt(-r.^2+R^2).* (315*bB+8*r.^4.*(63*dD+72*eE*r.^2+80*fF*r.^4)+4*r.^2.*(63*dD+72*eE*r.^2
+80*fF*r.^4).*R^2+3.*(63*dD+72*eE*r.^2+80*fF*r.^4).*R^4+20*(9*eE+10*fF*r.^2)*R^6+175*fF*R.^8+210*cC*(2*r.^2+R^2)));
InvertedData(j,:)=fit_poly;
fprintf('Section %d of %d\n',j, length(ReadyMatrix(:,1)));   %Output progress
end
%%%%%%%%%%%%%%%%%%%
```

```
FinalData=importdata(FileName);
%% %% LTE temperature measurement using Ar I lines
clear FileName;
clear NewFileName;
clear Texc_Boltz_Final;
clear boltz_Y;
clear boltz_X;

Lines_Ek=Lines.data(:,3);
%%%Delete all lines except for 706 969 675 and 641 nm%%%
Lines_Ek(9)=[];
Lines_Ek(8)=[];
Lines_Ek(4)=[];
Lines_Ek(4)=[];
%%%%%%%%%%%%%%%%%%%%%%%%%%%%%%%%%%%%%%%%%%%%%%%%%%%%%%%%%%%
for i=1:Slices
FileName=sprintf('DataFiles/InvertedData%d',i);
FinalData=importdata(FileName);
for j=1:Points-1
FinalData=importdata(FileName);

%Right hand side of boltzman eq. sorted by energy
boltz_Y=log(FinalData(:,j).*Lines_LdivAulGu);
%%%Delete all lines except for 706 969 667 675 and 641 nm%%%
boltz_Y(9)=[];
boltz_Y(8)=[];
boltz_Y(4)=[];
```

```
boltz_Y(4)=[];
%%%
```

```
%Capture 14 recoreded at -10 mm OFD

Xaxis=0:.2:0.2*length(Texc_Boltz_Final(1,:))-.2;
for m=1:length(Texc_Boltz_Final(:,1))
    Yaxis(m)=16-m*2+2;
end
hold all;
ylim([0 22]);
contour(Yaxis,Xaxis,11600*Texc_Boltz_Final',DisplayName','T_{exc}');
```

A.1.1 lines.txt

```
Wavelength Lambda/gkAki Ek [eV] MaxWidth [Pixels] Index
706.7218 3.71959E-14 13.30222662 34 3481
696.5431 3.62783E-14 13.3278562 28 3084
667.7282 2.82936E-12 13.47988596 15 2047
693.7664 2.25249E-13 14.69363882 35 2979
687.1289 8.23896E-14 14.71089717 40 2733
675.2834 6.99776E-14 14.74253992 62 2309
641.6307 1.10626E-13 14.83881006 42 1196
703.0251 5.24646E-14 14.83881006 64 3341
660.4853 7.25808E-12 14.97152141 29 1806
```

A.2 Matlab Code: Calculating electron density via stark broadening of hydrogen-alpha line

```
%%%
```

```
%Import and average data;
for i=1:Slices      %Slices
    for j=1:Points
        if j<10
    FileName=sprintf('%d00%d',i,j) %Sequential file name read
        else
    FileName=sprintf('%d0%d',i,j) %Sequential file name read
        end

   NewFileName=sprintf('DataFiles/Clean%d00%d',i,j); %New file names
   NewFileNameUnCal=sprintf('DataFiles/UnCal%d00%d.txt',i,j); %New file names
   TempData=importdata(FileName);
   TempData(1,:)=[];TempData(1,:)=[];TempData(1,:)=[];TempData(1,:)=[];
   TempData(:,1)=[];
   TempDataAvg=(sum(TempData')/length(TempData(1,:)))'; %Average spectrum
   TempUnCal=[Wavelengths TempDataAvg]; % For Diagnostics
   TempDataFinal=(TempDataAvg-DarkAvg).*Cal; %Subtract dark spectrum and calibrate
   TempDataFinal=(abs(TempDataFinal)+TempDataFinal)/2;   %Eliminate negative values
   save(NewFileName,'TempDataFinal','-ascii','-tabs'); %save new file
   save(NewFileNameUnCal,'TempUnCal','-ascii','-tabs'); %save new file
   fprintf('saving file%s\n',NewFileName);

    end
end
%% Abel inversion around 656.28 nm line (index=1663) +/ 150 indexes to
 %(wavelength range for able inversion from 652.456 to 660.065 nm)%
Window_H=125; %Number of indexes contating line
```

```
center=1663;     %Index of center wavelength (656.28nm)
HalphaWavelengths=Wavelengths(center-Window_H:center+Window_H);
dWavelengths=(HalphaWavelengths(1+2*Window_H)-HalphaWavelengths(1))/(2*Window_H);
LinearBackground=0;
clear FileName;
clear NewFileName;

for i=1:Slices
    NewFileName=sprintf('DataFiles/HalphaReadyMatrix%d',i); %New file names
    for j=1:Points
        %%%Import calbirated spectra%%%
    FileName=sprintf('DataFiles/Clean%d00%d',i,j); %Calibrated files
    TempDataFinal=importdata(FileName);
        %%%%%%%%%%%%%%%%%%%%%%%%%%%%%%%%
        %%%Remove coninuum via linear fit%%%
        for k=1:2*Window_H+1
        LinearBackground(k)=(TempDataFinal(center+Window_H)-TempDataFinal(center-Window_H))/(2*Window_H+1)*k
        +TempDataFinal(center-Window_H);
        end
    ReadyForInversion=TempDataFinal(center-Window_H:center+Window_H)-LinearBackground';
        %%%%%%%%%%%%%%%%%%%%%%%%%%%%%%%%%%%%%
    ReadyMatrix(:,Points-j+1)=ReadyForInversion;    %Reorder matrix
        %%%Save max intensity and total intensity%%%
    MaxHalpha(i,Points-j+1)=max(TempDataFinal(center-10:center+10));
    TotalHalpha(i,Points-j+1)=sum(TempDataFinal)*dWavelengths;
    %%%%%%%%%%%%%%%%%%%%%%%%%%%%%%%%%%%%%%%%%%%%%%%%%%%
    end
```

```
    save(NewFileName,'ReadyMatrix','-ascii','-tabs'); %save new file
   fprintf('saving file%s\n',NewFileName);
   clear ReadyMatrix;
end
save('HalphaTotalIntensity','TotalHalpha','-ascii','-tabs'); %save new file
save('HalphaIntensity','MaxHalpha','-ascii','-tabs'); %save new file

%% Abel inverstion of data based on fitting to a 10th degree even
%%%%polynomial
clear FileName;
clear NewFileName;
clear ReadyMatrix;
x=(0:Points)/(Points);  %scale x axis
R=1;
for i=1:Slices
 FileName=sprintf('DataFiles/HalphaReadyMatrix%d',i);
 NewFileName=sprintf('DataFiles/InvertedData%d',i);
 ReadyMatrix=importdata(FileName);
 ReadyMatrix=[ReadyMatrix zeros(2*Window_H+1,1)];

%%%Fit Spectra to tenth degree polynomial then invert analytically%%%
for j=1:length(ReadyMatrix(:,1))
    Q=ReadyMatrix(j,:)-min(ReadyMatrix(:,Slices));
    ft_1 = fittype({'X^10', 'X^8', 'X^6', 'X^4', 'X^2', '1'},'dependent',{'y'},'independent',{'X'},
    'coefficients',{'fF', 'eE', 'dD', 'cC', 'bB','aA'});
    % Fit this model using data%
    [fit_one,goodness_one]= fit(x',Q',ft_1);
```

```
    aA=fit_one.aA;
    bB=fit_one.bB;
    cC=fit_one.cC;
    dD=fit_one.dD;
    eE=fit_one.eE;
    fF=fit_one.fF;
    %%%%%%%%%%%%%%%%%%%%%%%%%%
%%Compare data to fit%%
%hold all;
%plot(fit_one,'--');
%plot(x,Q);
%%%%%%%%%%%%%%%%%%%%%%%%
r=x;
%analytical solution to abel transform%
fit_poly=(-1/pi)*(2/315*sqrt(-r.^2+R^2).* (315*bB+8*r.^4.*(63*dD+72*eE*r.^2+80*fF*r.^4)+4*r.^2.*(63*dD+72*eE*r.^2+
80*fF*r.^4).*R^2+3.*(63*dD+72*eE*r.^2+80*fF*r.^4).*R^4+20*(9*eE+10*fF*r.^2)*R^6+175*fF*R.^8+210*cC*(2*r.^2+R^2)));
InvertedData(j,:)=fit_poly;
fprintf('Section %d of %d\n',j,2*Window_H+1);   %Output progress
end
%%%%%%%%%%%%%%%%%%%
```

```
FinalData=importdata(FileName);
%%

%% Calculate electron density by fitting to Lorentizan profile and measuring FWHM

clear FileName;
clear NewFileName;

for i=1:Slices;
FileName=sprintf('DataFiles/InvertedData%d',i);
FinalData=importdata(FileName);
for j=1:Points
Ytemp=FinalData(:,j);
for k=1:length(Ytemp)                %Use linear approximation for continuum
LinearBackground(k)=(Ytemp(length(Ytemp))-Ytemp(1))/(length(Ytemp))*k+Ytemp(1);
end
Ytemp=Ytemp-LinearBackground';       %Subtract continuum
Ytemp=Ytemp/(sum(Ytemp));            %Normalize Spectrum

%%Fit each spectra to a Lorenzian profile%%
fo_ = fitoptions('method','NonlinearLeastSquares','Lower',[0 0 653],'Upper',[Inf 10 659]);
st_ = [3.14 1 656.27999999999997];
set(fo_,'Startpoint',st_);
ft_= fittype('B/(A*((x-x0)^2+B^2))','dependent',{'y'},'independent',{'x'},'coefficients',{'A', 'B', 'x0'});
[fit_Lorentz,goodness_Lorentz]=fit(HalphaWavelengths,Ytemp,ft_,fo_);
Acoeff=fit_Lorentz.A;
Bcoeff=fit_Lorentz.B;       %HWHM of lorenzian
```

```
Ccoeff=fit_Lorentz.x0;      %Center wavelength
tempFWHM(i,j)=Bcoeff*2;     %FWHM of lorenzian
tempRsqr(i,j)=goodness_Lorentz.rsquare;
%%%%%%%%%%%%%%%%%%%%%%%%%%%%%%%%%%%%%%%%%%%%
%%Compare data to fit%%
%hold all;
%plot(HalphaWavelengths,Ytemp);
%plot(fit_Lorentz,'--');
%%%%%%%%%%%%%%%%%%%%%%%
end
end
save('DataFiles/FWHM_Profile','tempFWHM','-ascii','-tabs'); %save new file
save('DataFiles/FWHM_Rsqr','tempRsqr','-ascii','-tabs'); %save new file
%% Used Gingosos1996 table to calculate electron density%%
Gingosos1996=importdata('DataFiles/gigosos1996_stark_parameters.txt');
T=Gingosos1996(1,:); T(1)=[];   %Extract Temperature
Ne=Gingosos1996(:,1); Ne(1)=[]; %Extract Wavelengths
Z=Gingosos1996(2:length(Ne)+1,2:length(T)+1);   %Extract broadening FWHM
[X,Y]=meshgrid(T,Ne);   %Generate mesh for interpolation
for i=1:Slices;
for j=1:Points;
FWHM_Profile=importdata('DataFiles/FWHM_Profile');
Difference=0;
DiffMin=1e3;
[X,Y]=meshgrid(T,Ne);
    %%%Loop over possiable Te and Ne to find matching FWHM%%%
    for Nesearch=1e14:5e14:1*10^(17.67)
```

```
    for Tsearch=5000:5000:20000
    FWHMSearch=interp2(X,Y,Z,Tsearch,Nesearch);
    Difference=abs(FWHMSearch-FWHM_Profile(i,j));
        if Difference<DiffMin
          DiffMin=Difference;
          Tmin=Tsearch;
          Nemin=Nesearch;
        else
            break;
        end
    end
    end
    %%%%
```

```
        if FWHM_Rsqr(i,j)>=0.965
            Ne_Stark_Final(i,j)=Ne_Stark(i,j);
        else
            break;
        end
    end
end

%% Scale axis and contour plot based of focal position
%   \  / -OFD
%    \/
%  Focus
%    /\
%   /  \ +OFD
%Capture 1 recoreded at 16 mm OFD
%Capture 14 recoreded at -10 mm OFD

Xaxis=0:.2:0.2*length(Ne_Stark_Final(1,:))-.2;
for m=1:length(Ne_Stark_Final(:,1))
    Yaxis(m)=16-m*2+2;
end
hold all;
%xlim([0 22]);
%contour(Xaxis,Yaxis ,10^6*Ne_Stark_Final,'DisplayName','Electron Density');
ylim([0 22]);
contour(Yaxis,Xaxis,10^6*Ne_Stark_Final',’DisplayName’,’Electron Density’);
```

Appendix B

Axi-symmetric model code

B.1 Header file

```
/*************************************/
/*Sample header file (LSP_UDF.h) ******/
/*************************************/
double RAD_LOSS(cell_t, Thread);
double ELEC_DEN(double);
double POW_INC(cell_t, Thread);
double INV_BREM_COEFF(double);
double ABS_LEN(cell_t, Thread);
double POW_ABS(cell_t, Thread);
```

B.2 C file

```
/*****************************************************************************************/
/*Sample user-defined function used to model argon LSP assuming LTE material properties********/
/*
/*****************************************************************************************/
#include "LSP_UDF.h"  /* Header file containing subroutines */
#include "udf.h"      /* Required Flunet header*/
#include "mem.h"      /* Required Fluent header--allows acces to node values and cell properties*/

/* Global constants*/

int ZONE_ID=3;       /*Identifies the laser zone   */
int LASER_MODE=3 ;/*0-TEM00; 1-TEM01*; 2-D_MODE, 3-Q_MODE*/
double PI=M_PI;        /*defines pi using flunet macro*/
double Pre=1.01325e5;       /*Atmospheric pressure   [N/m^2]*/
double Ptot=1900;     /*Laser power [W]  <This parameter is modified based on the model>*/
double VEL=5.5;       /*Gas speed [m/s]  <This parameter is modified based on the model>*/
double ESQ_LP=30.0; /*number light pipes within e-squared radius <This parameter is modified based on the model>*/
double X_LAST=0.095; /* x coordinate to find the last cell <This parameter is modified based on the model>*/

/* Macro to set initial solution values*************************************************************/
DEFINE_INIT(temp_init, domain)
{
cell_t c;
Thread *t;
real xc[ND_ND];  /* array of locations of cell centroid; ND_ND equals 2 in the 2-D */
int count;
/* loop over all cell threads (zones) in the domain */
```

```
Message("initializing temperature in the domain\n");
count=0;
thread_loop_c (t, domain)
{
/* loop over all cells */
   begin_c_loop_all (c,t)
     {
       C_CENTROID(xc,c,t);
   if (xc[1]<100E-06&&fabs(xc[0])<2.9E-03)  /*cells near laser focus are assigned temperature of 14,000 K*/
   {
    C_T(c,t)=14000;
count=count+1;
}
       else
{
         C_T(c,t)=300;
}
       C_P(c,t)=0.0;
       C_U(c,t)=VEL;                            /* The velocity is initalized equal to VEL for all cells */
       C_V(c,t)=0.0;
     }     /* end cell loop*/
   end_c_loop_all (c,t)
} /* end thread loop*/
Message("number of cells initiallized ::%d\n",count); /* Output the number of cells assigned 14, 000 K*/
}
/*end of Macro ***********************************************************************************************/
```

```
/* Macro defining the source in the energy equation*************************************************************/
DEFINE_SOURCE(ener_sc, c, t, dS, eqn)
{
double source=0;
/* Radiation loss for the cell*/
if(C_T(c,t)<8000.0) /*no radiation loss or absorption below 8000 K*/
return source;
source=-1*RAD_LOSS(C_T(c,t)); /*Source set to radiation losses (see RAD_LOSS function) */
if (THREAD_ID(t)!=ZONE_ID) /*If the cell is not within the laser zone, /*
return source;                                  /* only radiative losses take place*/
/*source inside the laser zone*/
source=source
+POW_INC(c,t)*exp(-1*POW_ABS(c,t))*(1-exp(-1*INV_BREM_COEFF(C_T(c,t))*ABS_LEN(c,t)))/(2*(PI)*C_VOLUME(c,t));
/**POW_INC(c,t) is the initial power entering a light pipe; */
exp(-1*POW_ABS(c,t)) is power remaning after absorption by up-stream cells*/
/**INV_BREM_COEFF is the inverse bremsstrahlung absorption coefficient; ABS_LEN is the length of the cell;*/
/** 2*(PI) is necessary to account for the cell volume in axi-symmetric mode*/
return source;
}
/*End of Source Macro*****************************************************************************************/

/* Macro defining viscosity as a function of temperature*********************************************************/
DEFINE_PROPERTY(cell_viscosity,c,t)
{
/* Coefficients taken from Chen1995_Critical analysis of viscosity data of thermal argon plasmas at...*/
double A0,A1,A2,A3,A4,A5,A6;
```

```
double B0,B1,B2,B3,B4,B5,B6;
double C0,C1,C2,C3,C4,C5,C6;
double D0,D1,D2,D3,D4,D5,D6;
double visc;
double T;
T=C_T(c,t);
/*T< 2000*/
A0=-1.2901940032E-12;
A1=1.0183396590E-07;
A2=-9.3186162829E-11;
A3=7.9179938250E-14;
A4=-4.1540632566E-17;
A5=1.1922960073E-20;
A6=-1.4284392204E-24;
/* 2000<T<10000 */
B0=2.6801341470E-06;
B1=5.8581388296E-08;
B2=-1.1403793050E-11;
B3=2.4434611751E-15;
B4=-3.3873975059E-19;
B5=2.5526498290E-23;
B6=-7.8712548005E-28;
/*10000<T<12000*/
C0=-3.3638459373E-01;
C1=2.0960949967E-04;
C2=-5.4183875997E-08;
C3=7.4413524700E-12;
```

```
C4=-5.7262365757E-16;
C5=2.3413417289E-20;
C6=-3.9751183148E-25;
/*12000<T<20000*/
D0=-1.1051989982E-01;
D1=4.0286780091E-05;
D2=-6.0095708464E-09;
D3=4.7195193788E-13;
D4=-2.0645964614E-17;
D5=4.7805168030E-22;
D6=-4.5842445161E-27;

if (T<2000)
visc=A0+A1*T+A2*pow(T,2)+A3*pow(T,3)+A4*pow(T,4)+A5*pow(T,5)+A6*pow(T,6);
else if (T>=2000&&T<10000)
visc=B0+B1*T+B2*pow(T,2)+B3*pow(T,3)+B4*pow(T,4)+B5*pow(T,5)+B6*pow(T,6);
else if (T>=10000&&T<12000)
visc=C0+C1*T+C2*pow(T,2)+C3*pow(T,3)+C4*pow(T,4)+C5*pow(T,5)+C6*pow(T,6);
else if (T>=12000&&T<20000)
visc=D0+D1*T+D2*pow(T,2)+D3*pow(T,3)+D4*pow(T,4)+D5*pow(T,5)+D6*pow(T,6);
else
visc=4.6769E-5 -1.2256E-9*T;
return visc;
}
/* End of viscosity Macro*****************************************************************************/

/* On-demand Macro to check convergence of solution*************************************************/
```

```
DEFINE_ON_DEMAND(ConvCheck)
{
double power,tpower,RadLoss,RadTot,xc[ND_ND];
Domain *d;
Thread *t;
cell_t c;
d = Get_Domain(1); /*Required because domain is not passed to On Demand Macros*/
power=0;
tpower=0;
RadLoss=0;
RadTot=0;
thread_loop_c(t,d)
{
begin_c_loop_all(c,t)
{
if(C_T(c,t)>8000)
{
RadLoss=RAD_LOSS(C_T(c,t));
}
else
{
RadLoss=0;
}
RadTot=RadTot+2*PI*C_VOLUME(c,t)*RadLoss;     /*2 Pi accounts for volume in axi-symmetric mode*/
}
end_c_loop_all(c,t)
}
```

```
thread_loop_c(t,d)
{
if (THREAD_ID(t)==ZONE_ID)    /*Calculated energy absoprition in laser zone*/
{
begin_c_loop_all(c,t)
{
C_CENTROID(xc,c,t);
if(xc[0]>X_LAST)   /*If the cell is at the end (exit) of a the light pipe*/
{
tpower=tpower+POW_INC(c,t); /*The total power traveling along in all light pipes */
power=power+POW_INC(c,t)*exp(-1*POW_ABS(c,t));  /* Total power incident on the last cells,*/
}                                               /* (portion not absorbed by previous cells)*/
}
end_c_loop_all(c,t)
}
}

    Message("Total P::%e, Trans P::%e, Abs P::%e, % Power Abs::%f\n",tpower, power
, tpower-power, 100*(tpower-power)/tpower);
    Message("Radiated P::%e, Absorbed-Radiated::%e\n",RadTot,tpower-power-RadTot);
/*Convergence when energy flux out of domain (check via Fluent GUI) is within */
/*1% of the total energy absorbed minus the radiative losses*/
}
/* End of convergence check Macro*****************************************************************************/

/* Function to calculate radiative losses of a cell*****************************************************************/
double RAD_LOSS(double T)
```

```
{
double Ne, radloss;
double h, esqr, mcsqr, vc, Zeff, kbT;
/*Constants used to calculate radiation loss (constans are in eV, cm and s units)*/
h=2*(PI)*6.5821220E-16; /* eV s*/
esqr=1.439962E-7; /* eV cm*/
mcsqr=5.10999E5; /* eV*/
vc=6.89E14; /*threshold frequency at which continuum is no longer optically thin [Hz] */
Zeff=sqrt(1.50);

Ne=ELEC_DEN(T); /*Electron denisty in 1/cm^3*/
kbT=T*8.615E-5; /*T is in K, kbT is in eV */
/*Radiation loss*/
/*Equation due to Ottinger1967_Unified Treatment of the relaxation phenomenon in radiating...*/
/*Doubling losses following Glumb1986_Two-dimensional model of laser-sustained plasmas...*/
radloss=2*1.69E-13*64*(vc+kbT/h)*pow(esqr,3)*pow(PI,1.5)*Ne*Ne*Zeff*Zeff/(3*pow(mcsqr,1.5)*sqrt(6*kbT));
return radloss;
}
/* End of function to calculate radiative losses*****************************************************************/


/* Function to calculate electron density  of a cell*************************************************************/
double ELEC_DEN(double T)
{
/* This subroutine claculates Ne in 1/cm^3 */
double Ne, Nh, Z_ratio, saha_fac, x;
Nh=Pre*pow(10,23)/(1.38065*T);         /* Neutral gas density assuming atmospheric pressure*/
```

```
/*Partation Ratio determined by fitting Ratio of Ar I and Ar II partition functions Vs. temperature */
/*Ralchenko, Yu., Kramida, A., Reader, J. and NIST ASD Team (2011). NIST Atomic Spectra Database (version. 4.1). */
/*Available: http://physics.nist.gov/asd. National Institute of Standards and Technology, Gaithersburg, MD.*/
if(T<30000)
Z_ratio=-2.3077E-29*pow(T,7)+2.3474E-24*pow(T,6)-8.8453E-20*pow(T,5)
+1.4851E-15*pow(T,4)-9.843E-12*pow(T,3)-1.2477E-8*pow(T,2)+0.00047534*T+3.7971;
else if (T<50000)                        /*Not used since first-degree ionization assumed*/
Z_ratio=9.9694E-18*pow(T,4)-1.7996E-12*pow(T,3)+1.2266E-7*pow(T,2)-0.0037512*T+43.814;
else                                    /*Not used since first-degree ionization assumed*/
Z_ratio=3.9694E-06*T+0.044951;
saha_fac=Z_ratio*(2.0/Nh)*1.68391E20*pow(2.0*(PI)*T,1.5)*exp(-1*15.6*1.6E-19/(1.3E-23*T));
x=(sqrt(saha_fac*saha_fac+saha_fac)-saha_fac);
Ne=1E-06*x*Nh; /*Electron density in cm^-3*/
return Ne;
}
/* End of function to calculate electron density*****************************************************************/

/* Function to calculate power incident on the light pipe to which a cell belongs*******************************/
double POW_INC(cell_t c, Thread *t)
{
cell_t c_l,c_l_next,c_n_1,c_n_0;
face_t f;
Thread *tf;
double lx, P, xc_l[ND_ND],xc_n_0[ND_ND], xc_n_1[ND_ND];
double P_TEM00,P_TEM01s,P_TEM02s,P_TEM10;
int i, count;
c_l=c; /*current cell index*/
```

```
count=0;
while (c_l>=0) /*continue looping over all cells untill the cell neighboring the axis of symmetry is reached*/
{ /*IMPORTANT: If begin_c_loop_all is used instead to loop over all cells, */
                                                /*           an infinite loop will result!*/
C_CENTROID(xc_l,c_l,t);         /*assign centroid of current cell to xc*/
lx=fabs(xc_l[0]-NODE_X(C_NODE(c_l,t,1))); /*measuring distance from x coordinates of cell center to any node*/
c_l_next=-10; /*IMPORTANT: ensures that loop ends if no conditions below are not met*/
for (i=0;i<=3;i++) /*loop over all faces*/
{
       f=C_FACE(c_l,t,i);     /*assign current face*/
       tf=C_FACE_THREAD(c_l,t,i); /*assign current face thread*/
           c_n_0=F_C0(f,tf);
   if(c_n_0>=0) /*Sequence is only necessary to account for cells at zone boundary.*/
   {
   if(THREAD_ID(THREAD_T0(tf))==ZONE_ID) /*assigns C0 cell index (see fluent UDF manual for (C0 and C1) as c_n_1*/
   {
   C_CENTROID(xc_n_0,c_n_0,t);
   }
   else
   {
   c_n_0=c_l;
   }
   }
   c_n_1=F_C1(f,tf);   /*assigns C1 cell index adjacent to face (see UDF manual) as c_n_1*/
   if(c_n_1>=0)
   {
if(THREAD_ID(THREAD_T1(tf))==ZONE_ID)
```

```
{
 C_CENTROID(xc_n_1,c_n_1,t); /*assigns xc_n_1 as centroid corrdinate for C1 if in laser zone*/
 }
 else
{
c_n_1=c_l; /*ensure C1 will fail if statement below*/
}
}
/*move to C0 next*/
   if (c_n_0>=0&&c_n_0!=c_l && xc_n_0[1]<xc_l[1] && fabs(xc_n_0[0]-xc_l[0])<lx)
/* if C0 is closer to axis of symmetry than C1 && C0 and C1 are neighbors (similar x) of parallel light pipes */
   c_l_next=c_n_0;
   if (c_n_1>=0&&c_n_1!=c_l && xc_n_1[1]<xc_l[1] && fabs(xc_n_1[0]-xc_l[0])<lx)
/* if C1 is closer to axis of symmetry than C0 && C0 and C1 are neighbors (similar x) of parallel light pipes */
   c_l_next=c_n_1;                          /* Keep moving towards axis of symmetry*/
}
count=count+1;     /*count the distance between the current cell and axis of symmetry*/
c_l=c_l_next;
}
/* Defination of required TEM modes; s specifies "star"*/
P_TEM00=exp(-2*pow((count-1)/ESQ_LP,2))-exp(-2*pow(count/ESQ_LP,2));
P_TEM01s=(1+2*pow((count-1)/ESQ_LP,2))*exp(-2*pow((count-1)/ESQ_LP,2))
-(1+2*pow((count)/ESQ_LP,2))*exp(-2*pow(count/ESQ_LP,2));
P_TEM02s=exp(-2*pow((count-1)/ESQ_LP,2))*(1+2*pow(count-1,4)/pow(ESQ_LP,4)+2*pow(count-1,2)/pow(ESQ_LP,2))
-exp(-2*pow(count/ESQ_LP,2))*(2*pow(count,4)+2*pow(count*ESQ_LP,2)+pow(ESQ_LP,4))/pow(ESQ_LP,4);
P_TEM10=exp(-2*pow((count-1)/ESQ_LP,2))*(1+4*pow(count-1,4)/pow(ESQ_LP,4))
-exp(-2*pow(count/ESQ_LP,2))*(4*pow(count,4)+pow(ESQ_LP,4))/pow(ESQ_LP,4);
```

```
/*Calculate fraction of laser power enter the light pipe to which the cell belongs*/
if (LASER_MODE==0) /*TEM00 Mode*/
P=Ptot*(exp(-2*pow((count-1)/ESQ_LP,2))-exp(-2*pow(count/ESQ_LP,2)));
/*Can set P=Ptot*P_TEM00 instead of writing P_TEM00 in long form*/
else if (LASER_MODE==1) /*TEM01* Mode*/
P=Ptot*((1+2*pow((count-1)/ESQ_LP,2))*exp(-2*pow((count-1)/ESQ_LP,2))
-(1+2*pow((count)/ESQ_LP,2))*exp(-2*pow(count/ESQ_LP,2)));
else if (LASER_MODE==2) /*PRC Laser Corp D-Mode*/
P=Ptot*(0.6*((1+2*pow((count-1)/ESQ_LP,2))*exp(-2*pow((count-1)/ESQ_LP,2))
-(1+2*pow((count)/ESQ_LP,2))*exp(-2*pow(count/ESQ_LP,2)))+0.4*(exp(-2*pow((count-1)/ESQ_LP,2))
-exp(-2*pow(count/ESQ_LP,2))));
else if (LASER_MODE==3) /*PRC Laser Corp Q-Mode*/
P=Ptot*(0.14*P_TEM00+0.14*P_TEM10+0.36*P_TEM01s+0.36*P_TEM02s);
else
Message("THE SUBROUTINE DOES NOT RECOGNIZE THE MODE\n");
return P;
}
/* End of function to calculate power incident on the light pipe to which a cell belongs***********************/

/* Function to calculate inverse bremsstrahlung absorption coefficint*****************************************/
double INV_BREM_COEFF(double T)
{
double alpha, KTe, vp, coul, Ne;
/*note: units are in eV, cm, s*/
Ne=ELEC_DEN(T);
KTe=(T)*8.617E-5;
vp=8980*sqrt(Ne);
```

```
coul=23-log(sqrt(Ne)*pow(KTe,-1.5));
alpha=100*7.8E-9*Ne*Ne*coul/(2.82823E13*2.82823E13*pow(KTe,1.5)*sqrt(1-(vp*vp)/(2.82823E13*2.82823E13)));
return alpha;
}
/* End of function to inverse bremsstrahlung coefficient*************************************************************/

/*Function to calculate cell absorption length ******************************************************************/
double ABS_LEN(cell_t c, Thread *t)
{
double xmin=0, ymin=0, xmax=0, ymax=0, xf[ND_ND], len;
face_t f;
Thread *tf;
int i;
c_face_loop(c,t,i)  /*loop over all faces of cell */
{
       f=C_FACE(c,t,i);
       tf=C_FACE_THREAD(c,t,i);
           F_CENTROID(xf,f,tf); /*assign current face's centroid as xf*/
   if (i==0) /*for first face, assign its x and y centroid as both max and mins */
   {
   xmin=xf[0];
   xmax=xf[0];
   ymin=xf[1];
   ymax=xf[1];
   }
   else
   {
```

```
if (xf[0]<xmin) /* assign xmin and ymin*/
{
xmin=xf[0];
ymin=xf[1];
}
if (xf[0]>xmax) /* assign xmax and ymax*/
{
xmax=xf[0];
ymax=xf[1];
                }
   }
}
if (xmax-xmin<=0)
Message("Error xmin-xmax<=0 OR yman-ymin<=0 !!!\n");  /* Just in case*/
len=sqrt(pow(xmin-xmax,2)+pow(ymin-ymax,2));          /* calculate cell length */
return len;
}
/*end of function to calculate cell absorption length ************************************************************/


/*Function to calculate fraction of power incident on the current cell*****************************************/
double POW_ABS(cell_t c, Thread *t)
{
cell_t c_t,c_n_0,c_n_1,c_t_next;
double lx, atten, xc[ND_ND], xc_t[ND_ND],xc_n_0[ND_ND],xc_n_1[ND_ND],len;
face_t f;
Thread *tf;
```

```
int i;
C_CENTROID(xc,c,t); /*assign xc as centroid to current cell*/
lx=fabs(xc[0]-NODE_X(C_NODE(c,t,1))); /*measure distance from x coordinates of cell center to any node*/
for (i=0;i<=3;i++) /*loop over all faces of current cell*/
{
       f=C_FACE(c,t,i);
       tf=C_FACE_THREAD(c,t,i);
   c_n_0=F_C0(f,tf);
   if(c_n_0>=0)    /*only necessary to take account of cells on zone boundary*/
   {
   if(THREAD_ID(THREAD_T0(tf))==ZONE_ID)    /*if C1 is in laser zone, calculate its centroid*/
   {
   C_CENTROID(xc_n_0,c_n_0,t);
   }
   else
   {
    c_n_0=c;
}
     }
   c_n_1=F_C1(f,tf);

   if(c_n_1>0)
   {
   if(THREAD_ID(THREAD_T1(tf))==ZONE_ID)  /*if C1 is in laser zone, calculate its centroid*/
   {
   C_CENTROID(xc_n_1,c_n_1,t);
   }
```

```
   else
   {
    c_n_1=c; /*if statement will not be satisfied if C1 is not in laser zone*/
}
}
   if (c_n_0>=0&&c_n_0!=c && xc_n_0[0]<xc[0] && fabs(xc_n_0[0]-xc[0])>lx)
   c_t=c_n_0;
   if (c_n_1>=0&&c_n_1!=c && xc_n_1[0]<xc[0] && fabs(xc_n_1[0]-xc[0])>lx) /* if C1 is upstream of C0  */
   c_t=c_n_1; /*set c_t as unpsream neighbor of C0*/
}
atten=0;
while(c_t>=0) /*continue looping over all cells untill all upstream cells are accounted for*/
{
c_t_next=-10; /* Similar logic to function to calculate power incident on the light pipe*/
C_CENTROID(xc_t,c_t,t);
len=ABS_LEN(c_t,t); /*calculate cell length*/
/*calculate absorption (alpha * cell lenght) in cells starting with upstream neighbor of current cell (c) */
atten=atten+len*INV_BREM_COEFF(C_T(c_t,t));
lx=fabs(xc_t[0]-NODE_X(C_NODE(c_t,t,1)));
for (i=0;i<=3;i++) /*Similar logic to above to move to neighboring upstream cells*/
{
       f=C_FACE(c_t,t,i);
       tf=C_FACE_THREAD(c_t,t,i);
   c_n_0=F_C0(f,tf);
   if(c_n_0>=0)
   {
   if(THREAD_ID(THREAD_T0(tf))==ZONE_ID)
```

```
   {
   C_CENTROID(xc_n_0,c_n_0,t);
   }
   else
   {
    c_n_0=c_t;
}
}
   c_n_1=F_C1(f,tf);
   if (c_n_1>=0)
   {
   if(THREAD_ID(THREAD_T1(tf))==ZONE_ID)
   {
   C_CENTROID(xc_n_1,c_n_1,t);
   }
   else
   {
    c_n_1=c_t;
}
           }
   if (c_n_0>=0&&c_n_0!=c_t && xc_n_0[0]<xc_t[0] && fabs(xc_n_0[0]-xc_t[0])>lx)
   c_t_next=c_n_0;
   if (c_n_1>=0&&c_n_1!=c_t && xc_n_1[0]<xc_t[0] && fabs(xc_n_1[0]-xc_t[0])>lx)
   c_t_next=c_n_1;
}
c_t=c_t_next;
}
```

```
return atten;
}
```

Appendix C

Cross-sectional and top surface images

Included in this appendix are higher magnification versions of figures 4.22, 4.25, 4.26, 4.27, 4.29, 4.30, 4.31, 4.32 4.34, 4.36, 4.40, 4.41, 4.45, 4.46 and 4.46.

Top surface images showing single-trail samples processed using a nitrogen LSP at an off-focal distance of 8 mm as a function of translation speed. Magnified from figure 4.22.

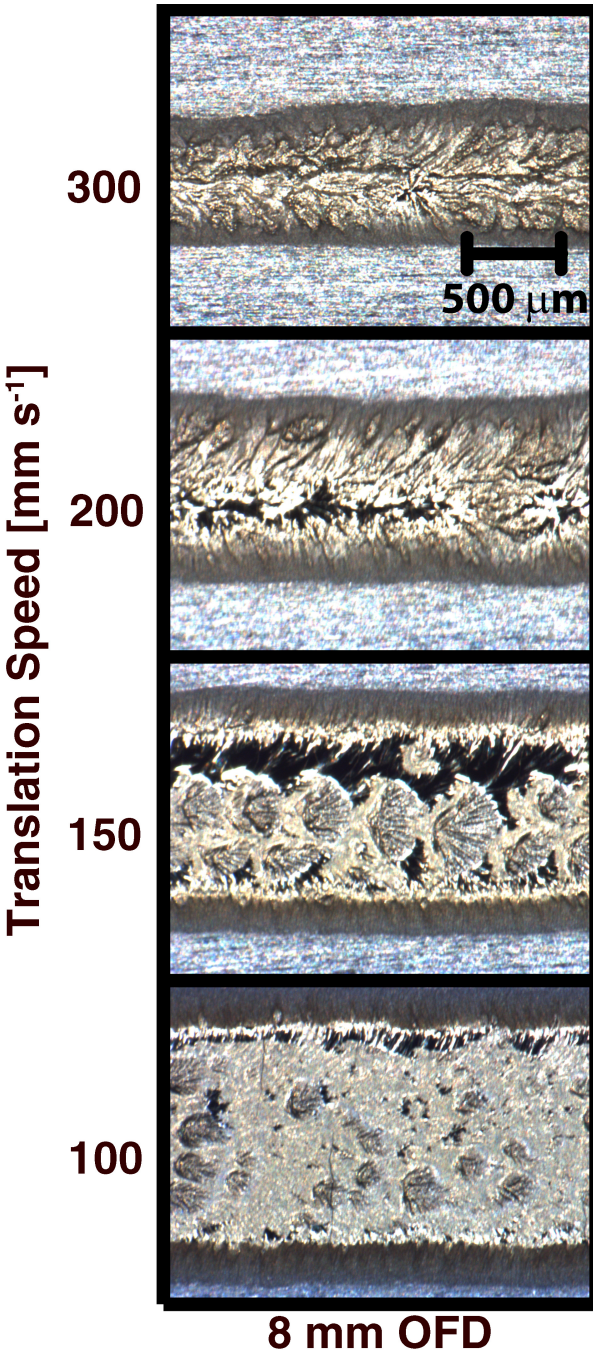

Top surface images showing single-trail samples processed using a nitrogen LSP at an off-focal distance of 6 mm as a function of translation speed. Magnified from figure 4.22.

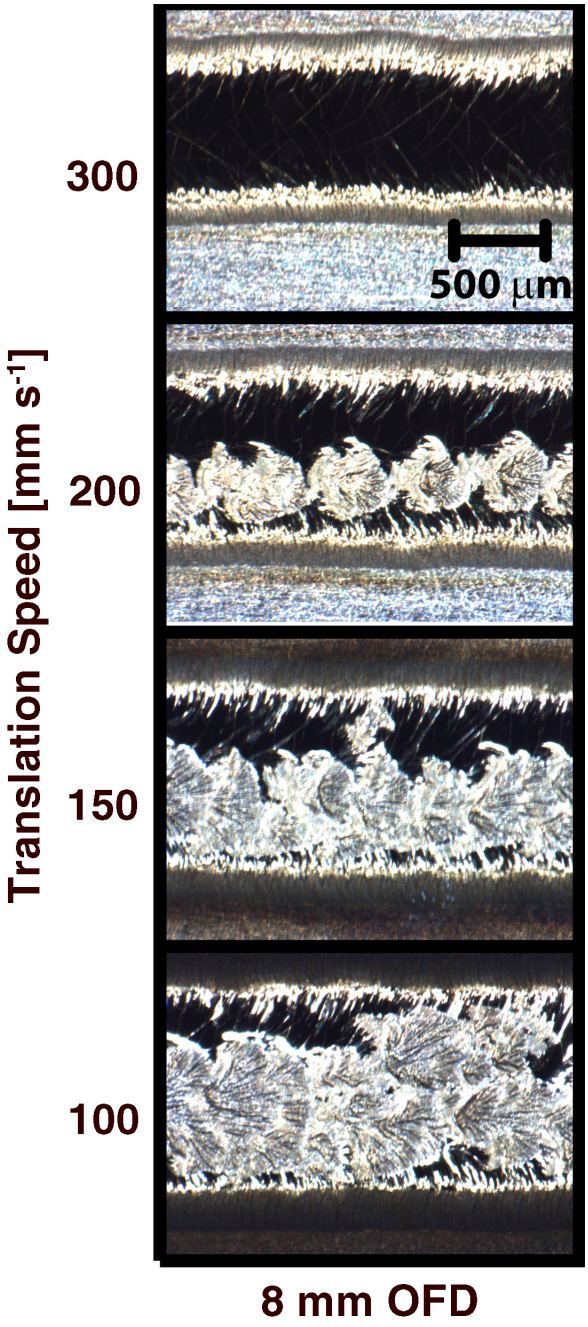

Top surface images showing single-trail samples processed using a nitrogen LSP at an off-focal distance of 4 mm as a function of translation speed. Magnified from figure 4.22.

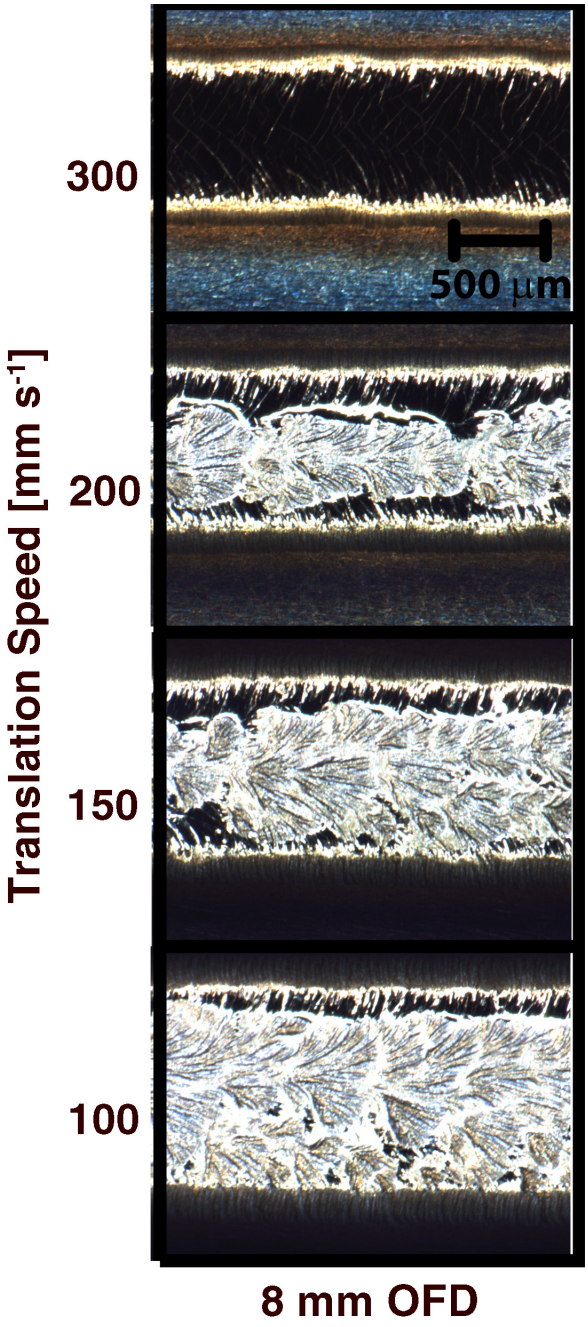

Top surface images showing single-trail samples processed using CO_2 laser, without plasma formation, and nitrogen gas at an off-focal distance of 8 mm as a function of translation speed. Magnified from figure 4.25.

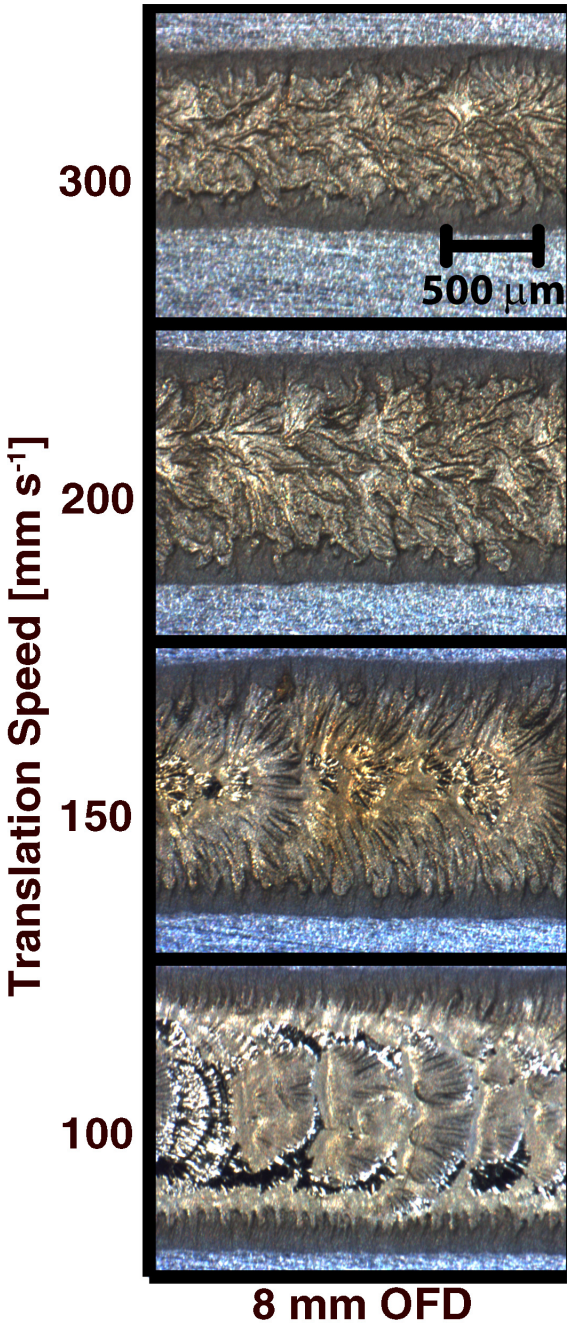

Top surface images showing single-trail samples processed using CO_2 laser, without plasma formation, and nitrogen gas at an off-focal distance of 6 mm as a function of translation speed. Magnified from figure 4.25.

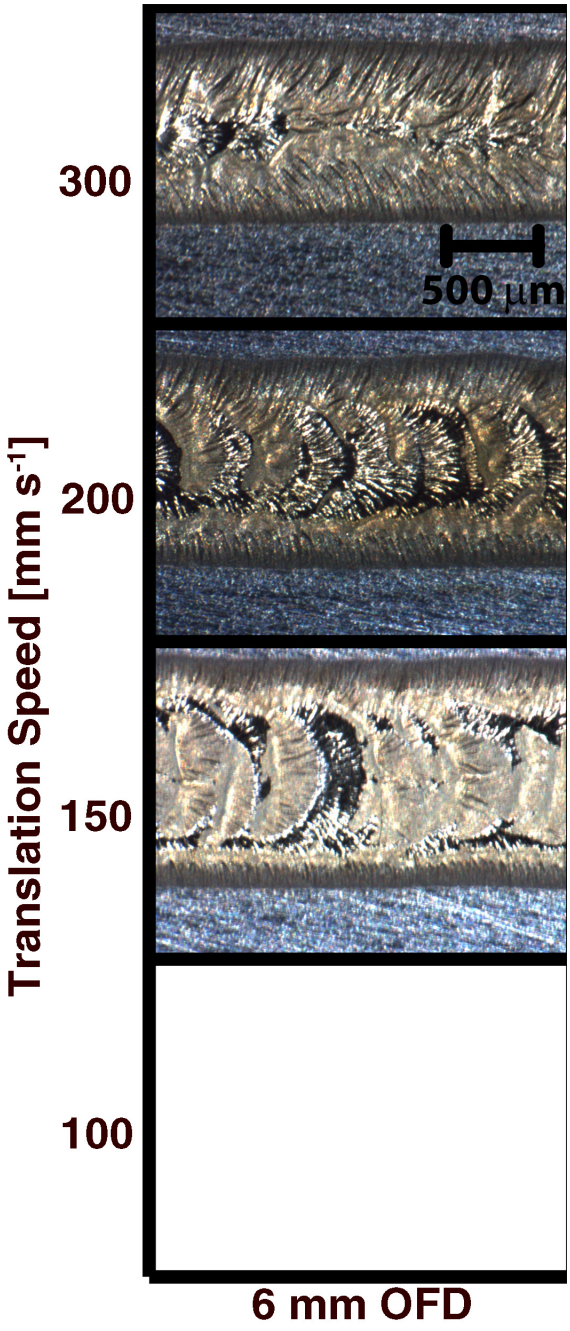

Cross-sectional micrographs of samples processed using a pure nitrogen LSP at an off-focal distance of 8 mm as a function of translation speed. Magnified from figure 4.26.

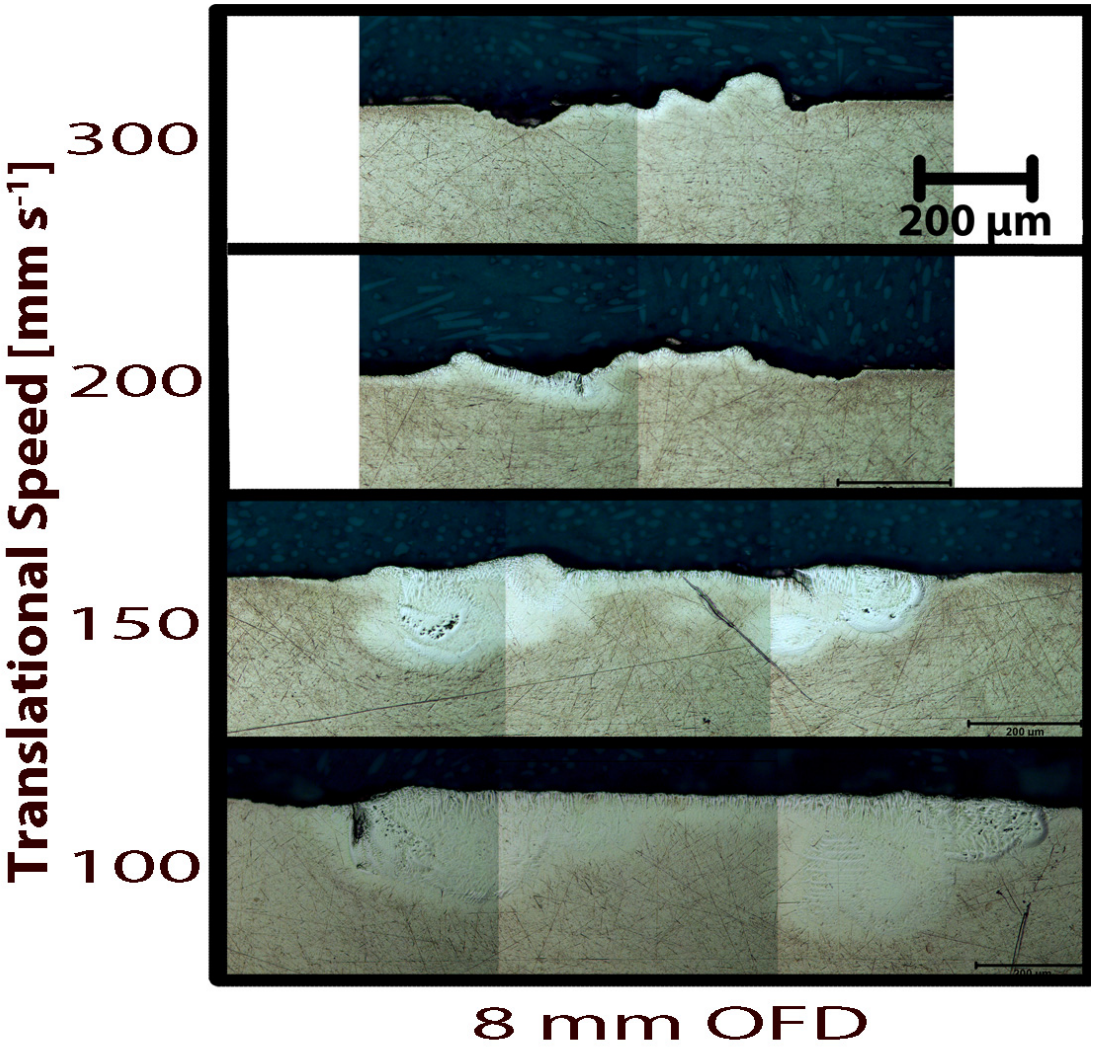

Cross-sectional micrographs of samples processed using a pure nitrogen LSP at an off-focal distance of 6 mm as a function of translation speed. Magnified from figure 4.26.

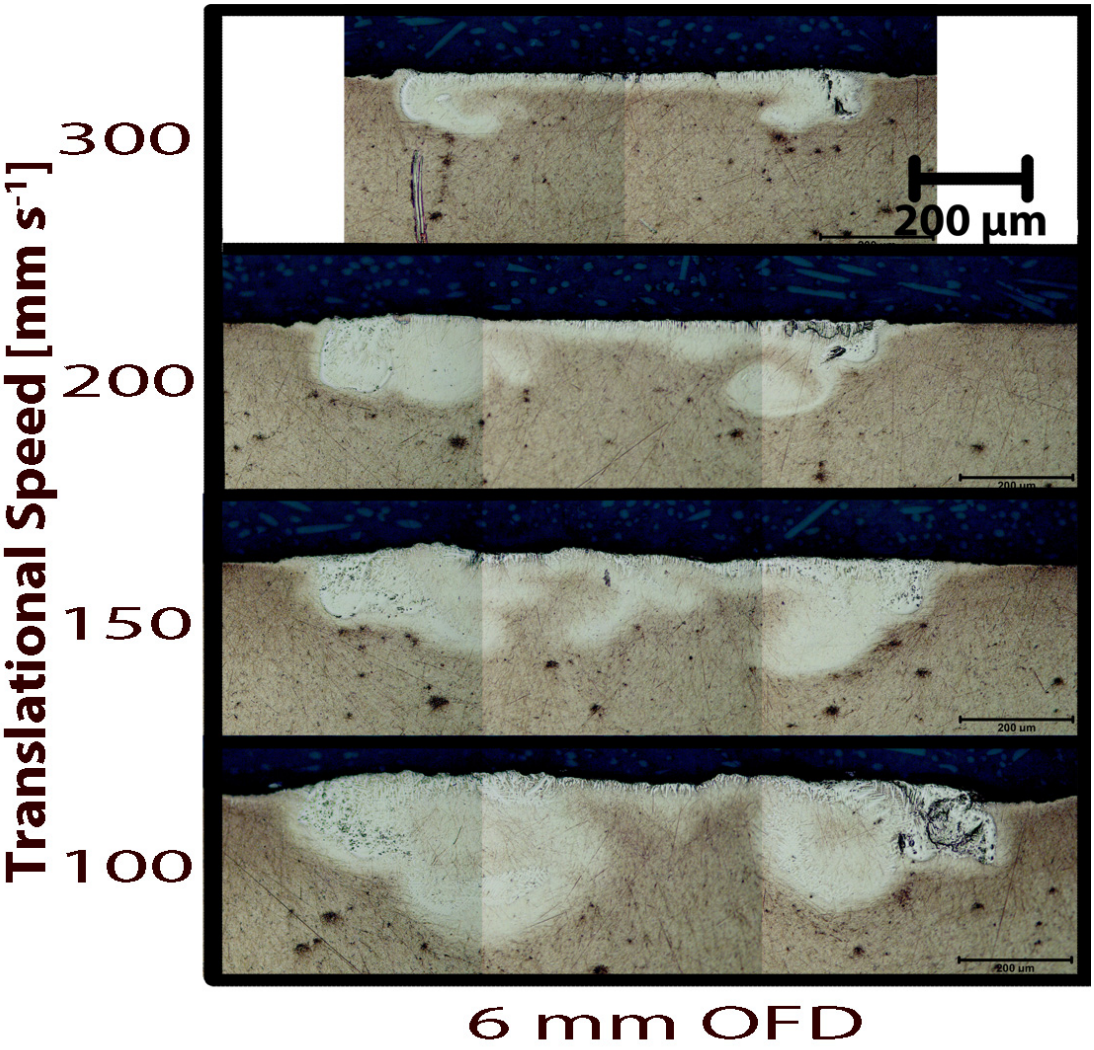

Cross-sectional micrographs of samples processed using a pure nitrogen LSP at an off-focal distance of 4 mm as a function of translation speed. Magnified from figure 4.26.

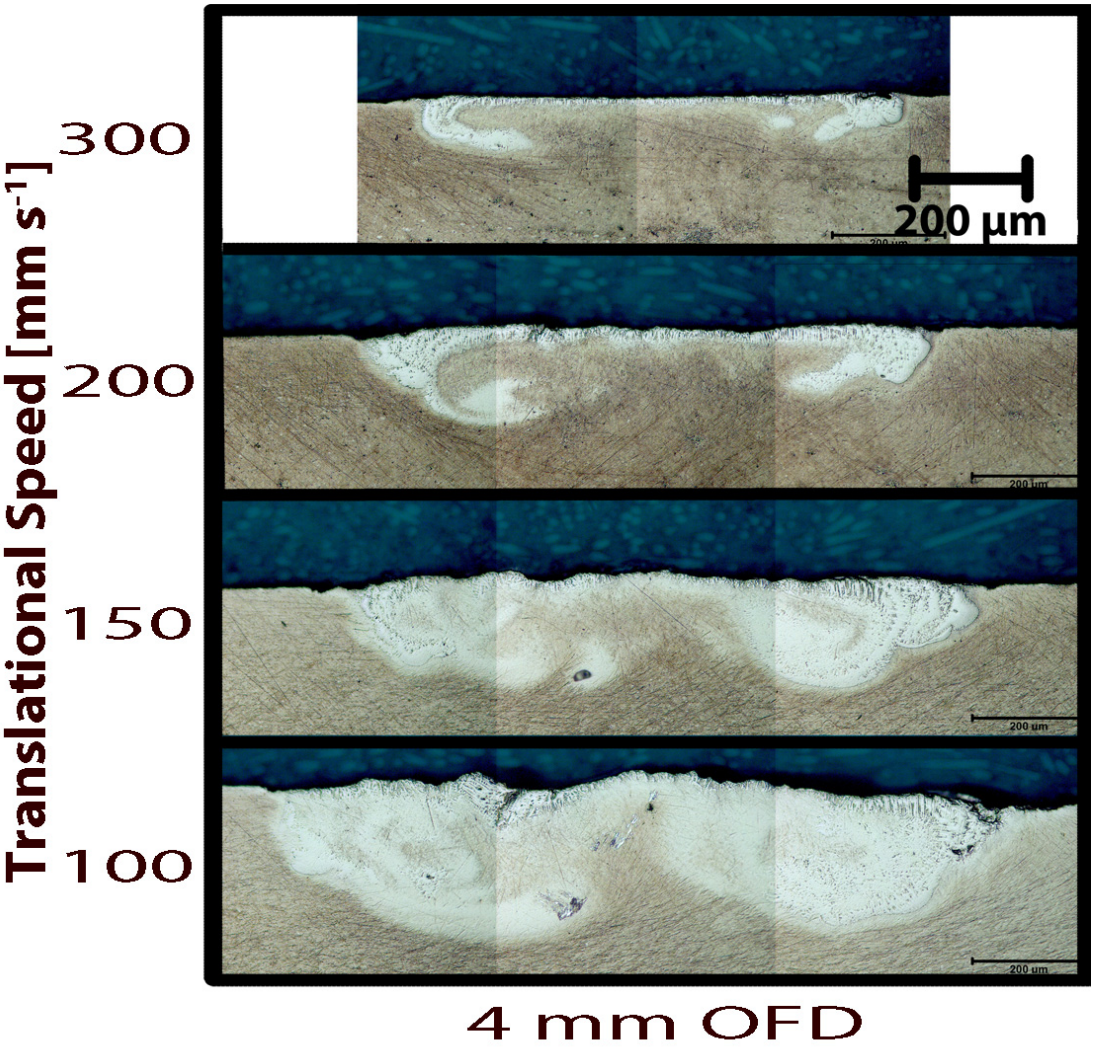

Cross-sectional micrographs of samples processed using a CO_2 laser and nitrogen gas, without plasma formation, at an off-focal distance of 8 mm as a function of translation speed. Magnified from figure refCh4::CrossSectionsN2NoLSPHighSpeed.

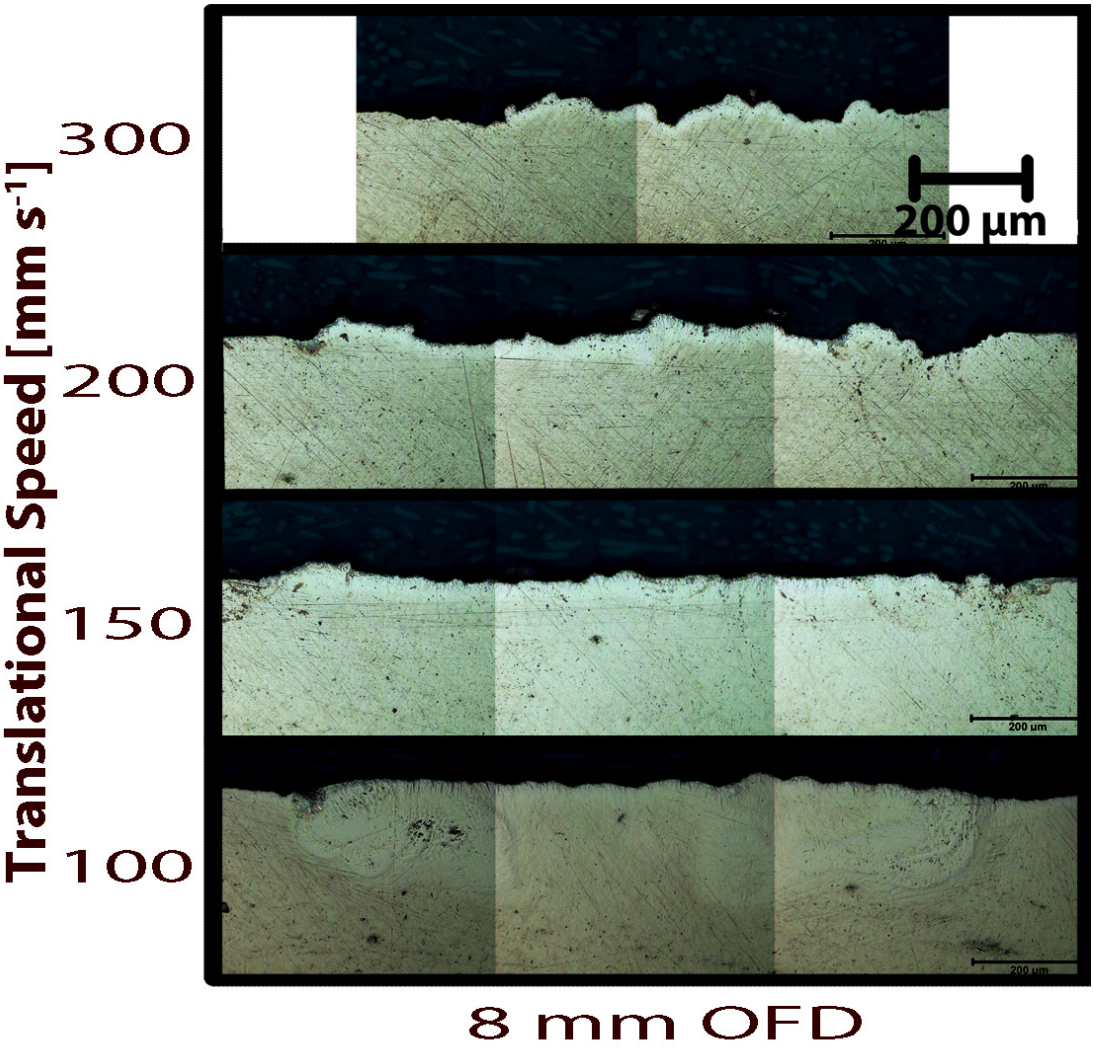

Cross-sectional micrographs of samples processed using a CO_2 laser and nitrogen gas, without plasma formation, at an off-focal distance of 6 mm as a function of translation speed. Magnified from figure 4.27.

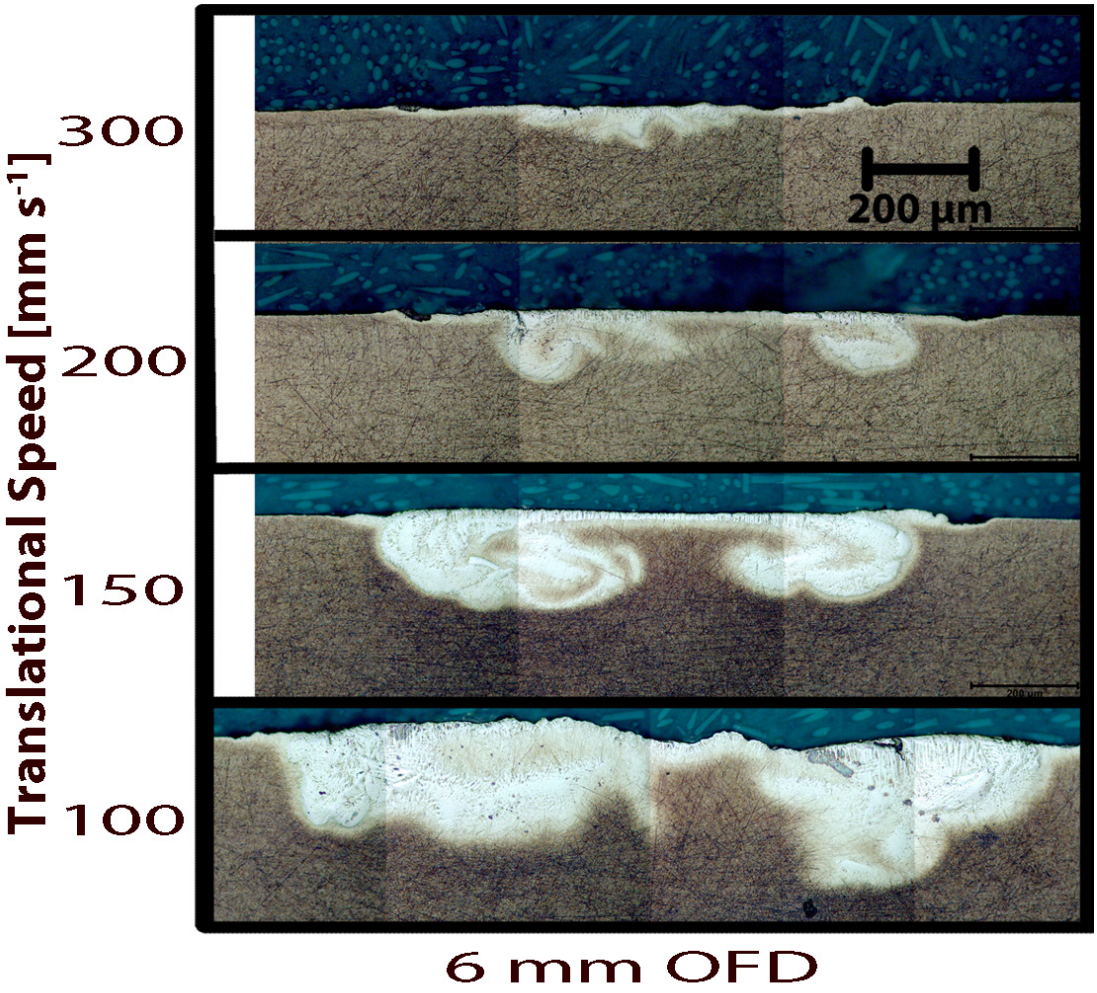

Top surface images of samples processed using a $49.2 \pm 2\,\%$ N_2–Ar LSP at an off-focal distance of 8 mm as a function of translation speed. Magnified from figure 4.29.

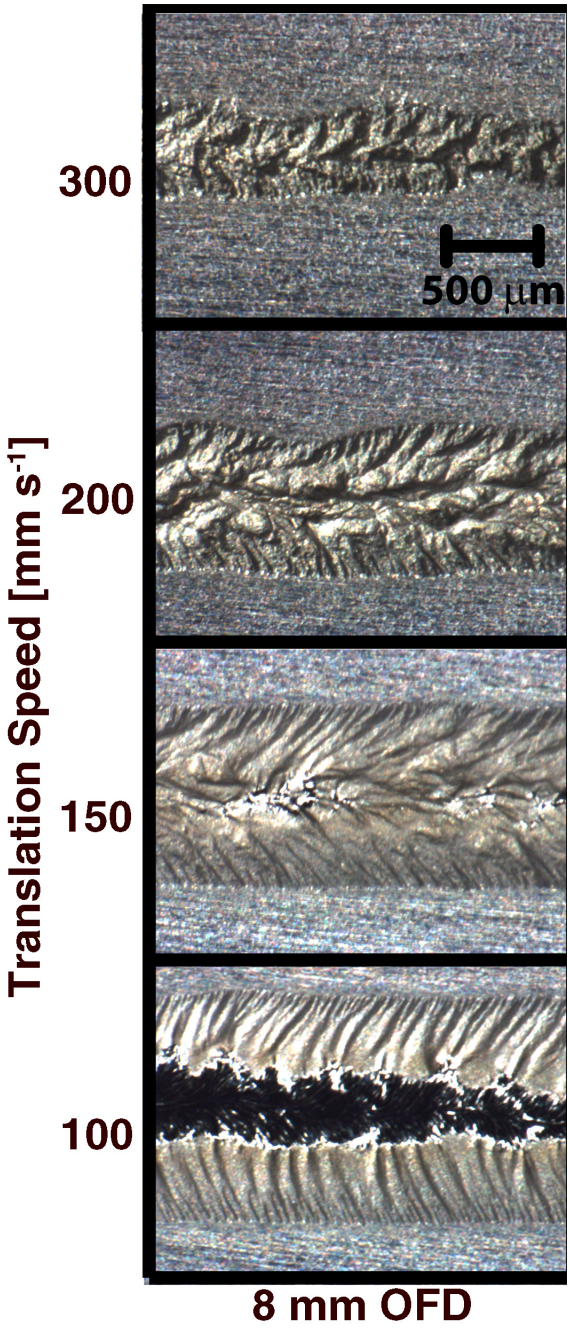

Top surface images of samples processed using a $49.2 \pm 2\,\%$ N_2–Ar LSP at an off-focal distance of 6 mm as a function of translation speed. Magnified from figure 4.29.

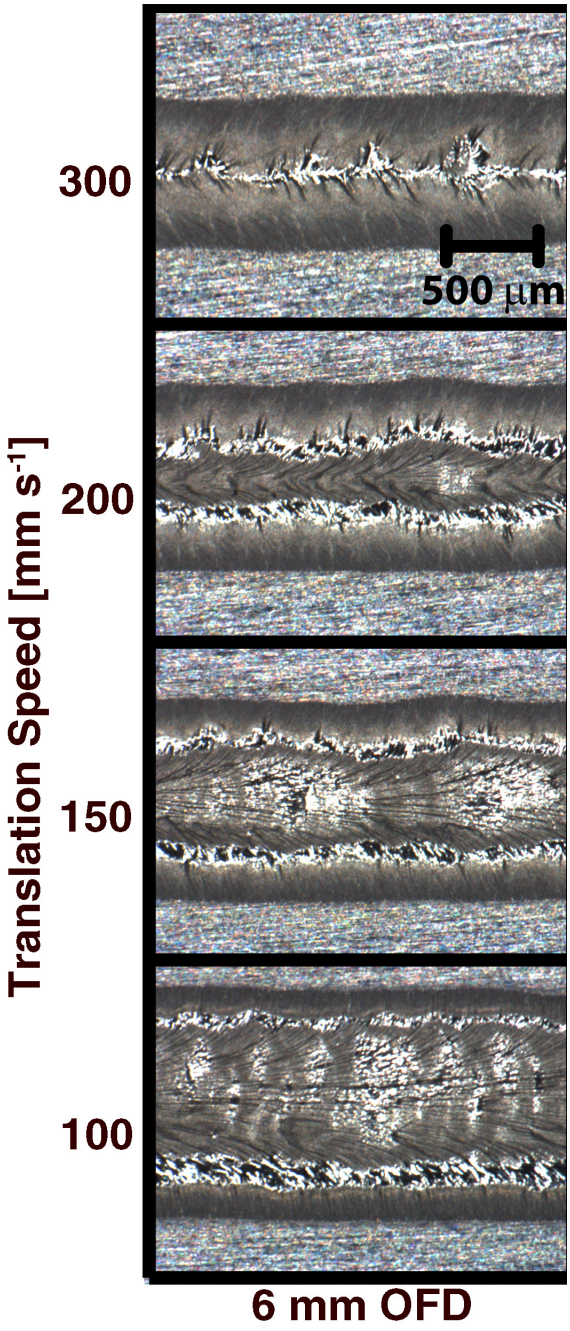

Top surface images of samples processed using a $49.2 \pm 2\,\%$ N_2–Ar LSP at an off-focal distance of 4 mm as a function of translation speed. Magnified from figure 4.29.

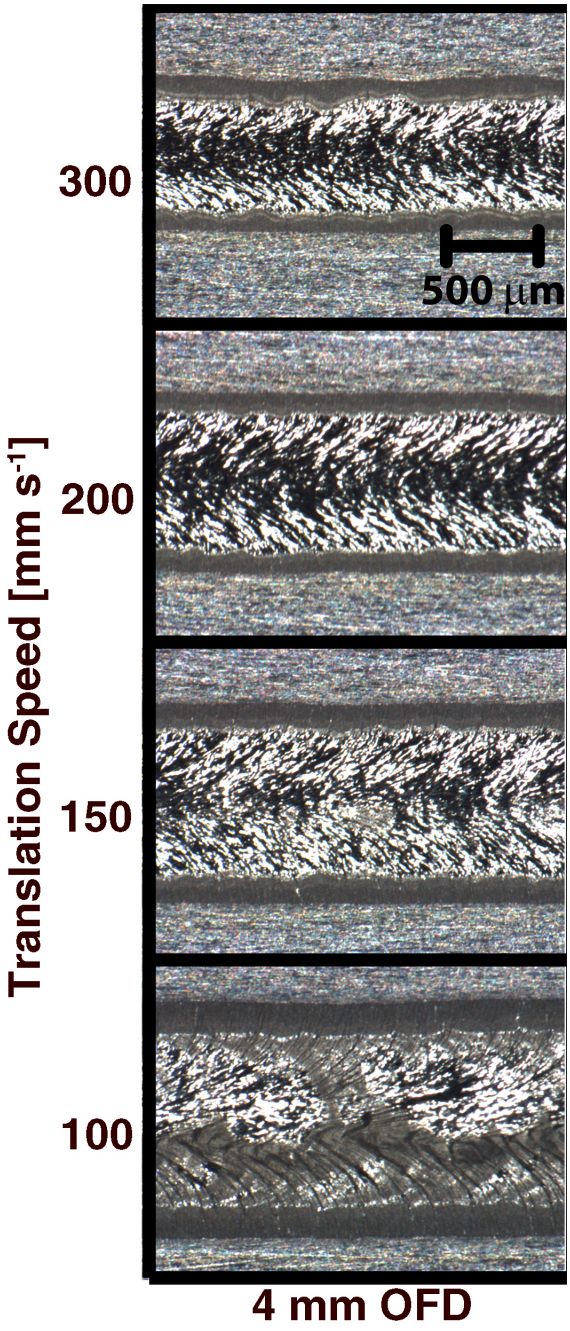

Top surface images showing single-trail samples processed using a CO_2 laser, without plasma formation, and a 49.2 ± 2 % N_2–Ar gas mixture at an off-focal distance of 8 mm as a function of translation speed. Magnified from figure 4.30.

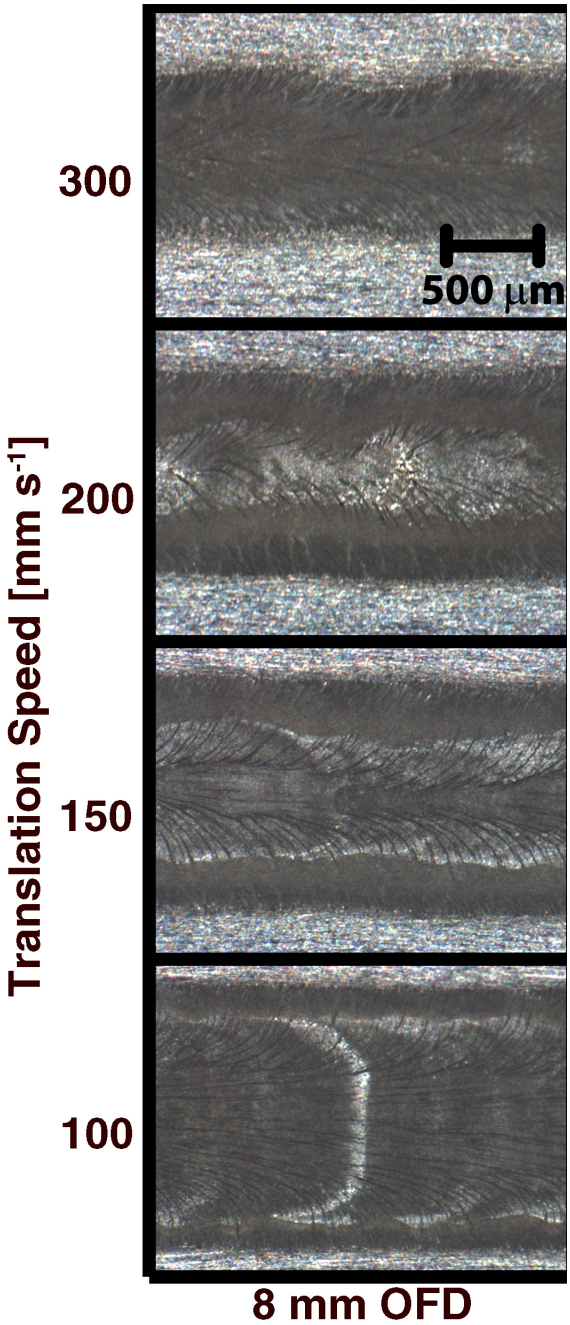

Top surface images showing single-trail samples processed using a CO_2 laser, without plasma formation, and a 49.2 ± 2 % N_2–Ar gas mixture at an off-focal distance of 6 mm as a function of translation speed. Magnified from figure 4.30.

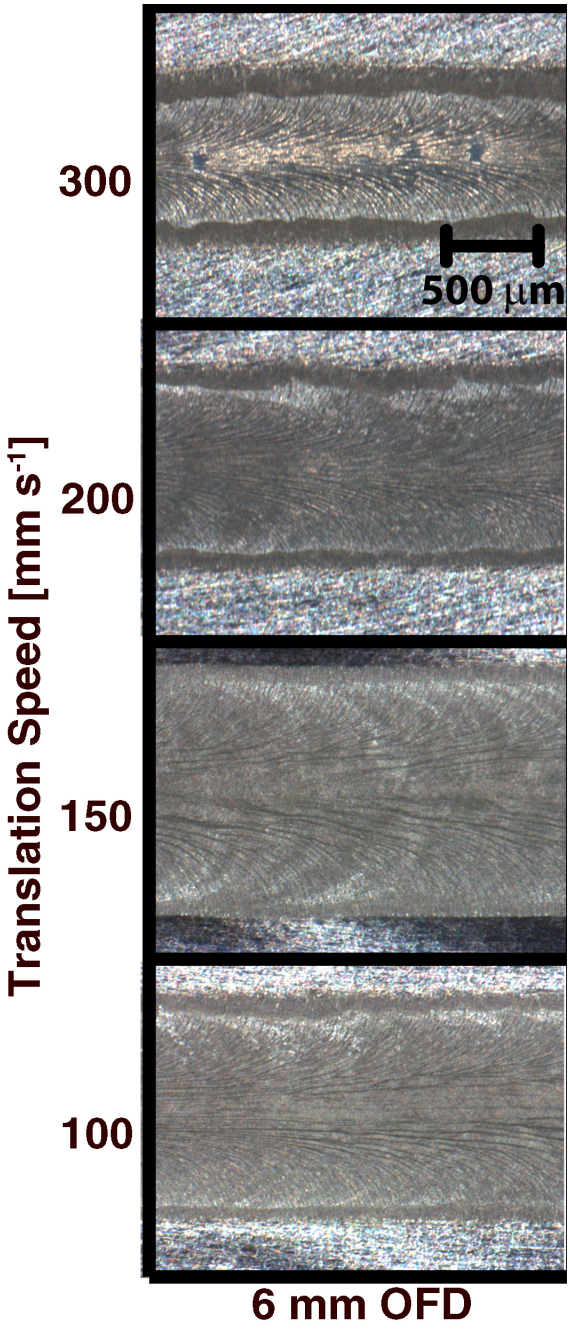

Cross-sectional micrographs of samples processed using a $49.2 \pm 2\,\%$ N_2-Ar LSP at an off-focal distance of 8 mm as a function of translation speed. Magnified from figure 4.31.

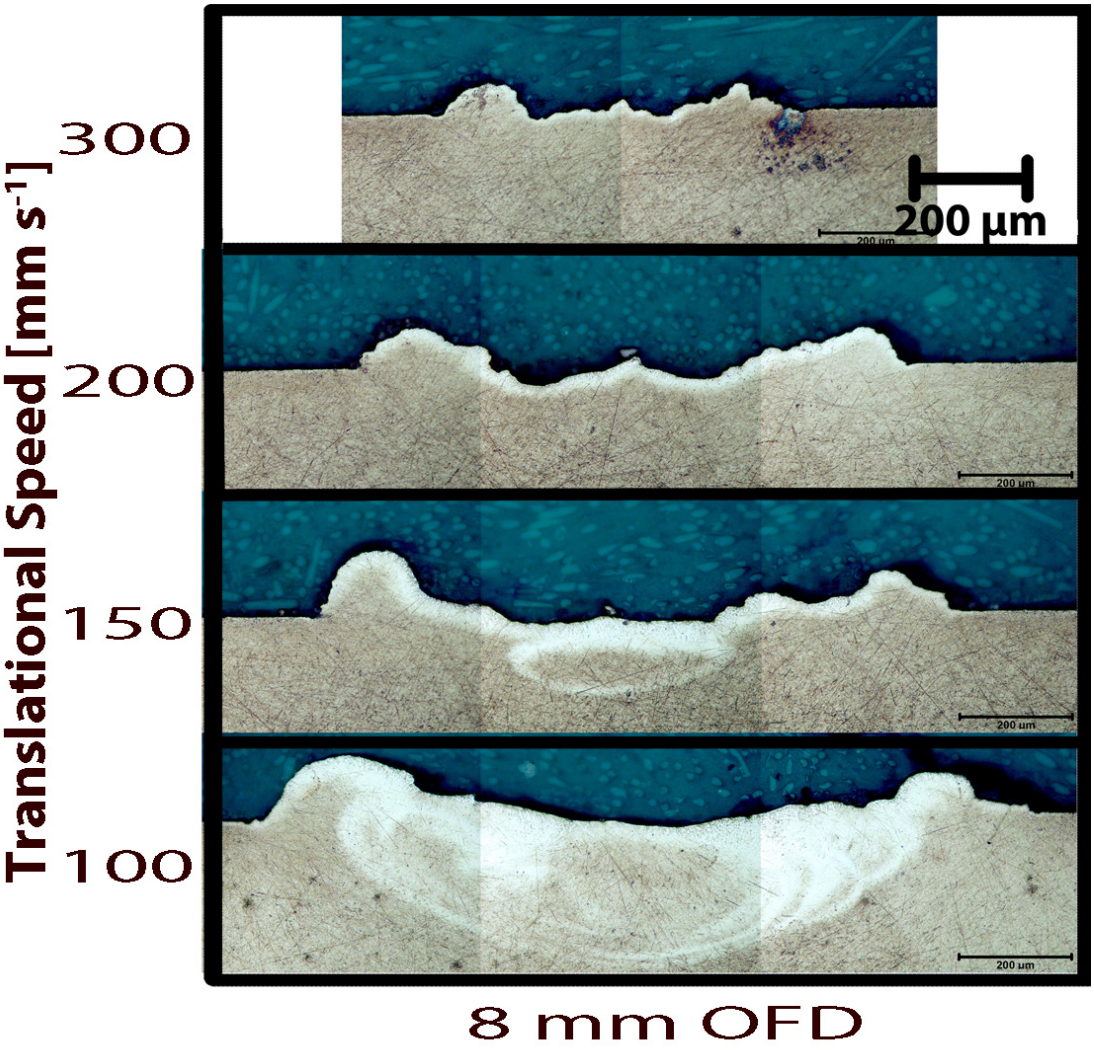

Cross-sectional micrographs of samples processed using a $49.2 \pm 2\,\%$ N_2-Ar LSP at an off-focal distance of 6 mm as a function of translation speed. Magnified from figure 4.31.

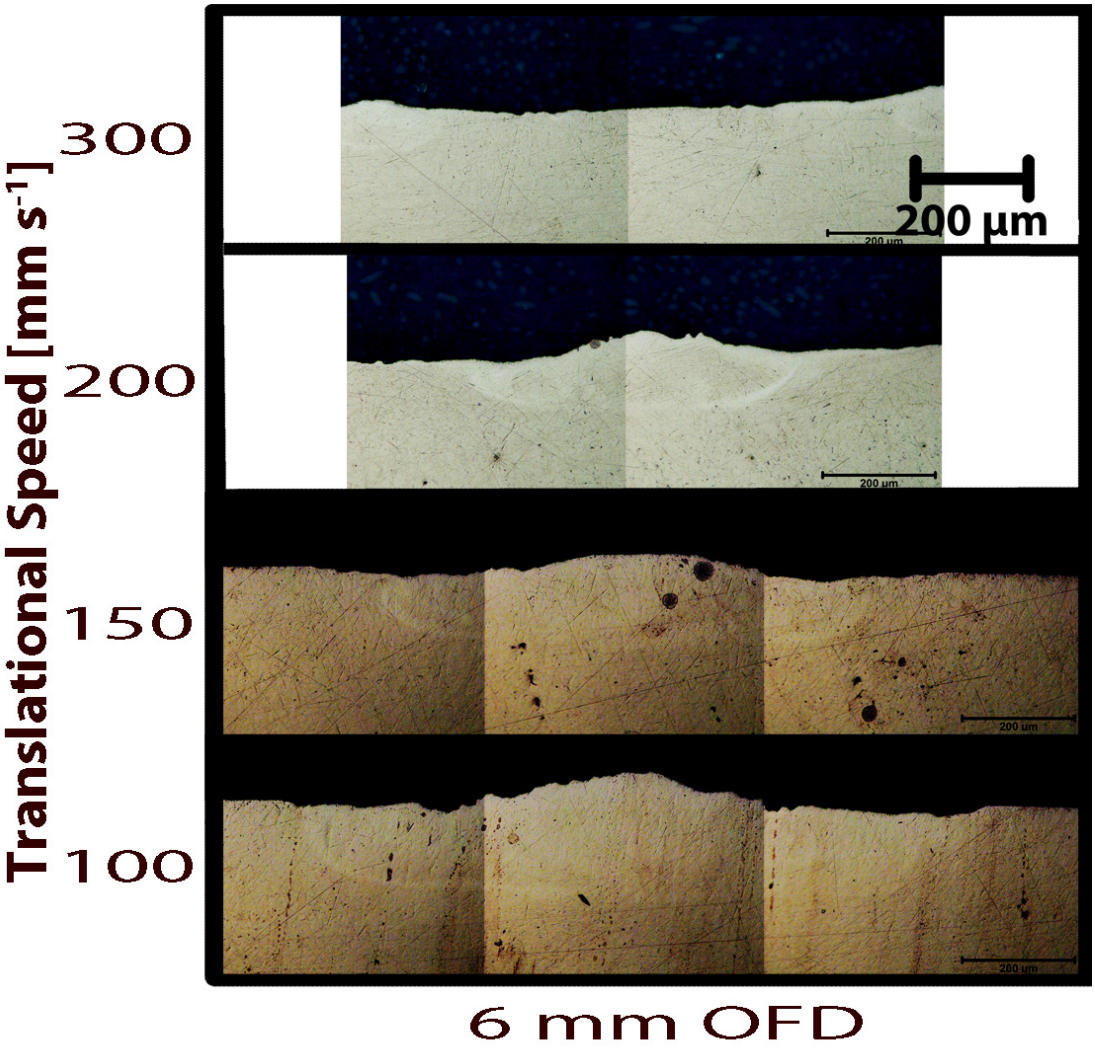

Cross-sectional micrographs of samples processed using a $49.2 \pm 2\,\%$ N_2-Ar LSP at an off-focal distance of 4 mm as a function of translation speed. Magnified from figure 4.31.

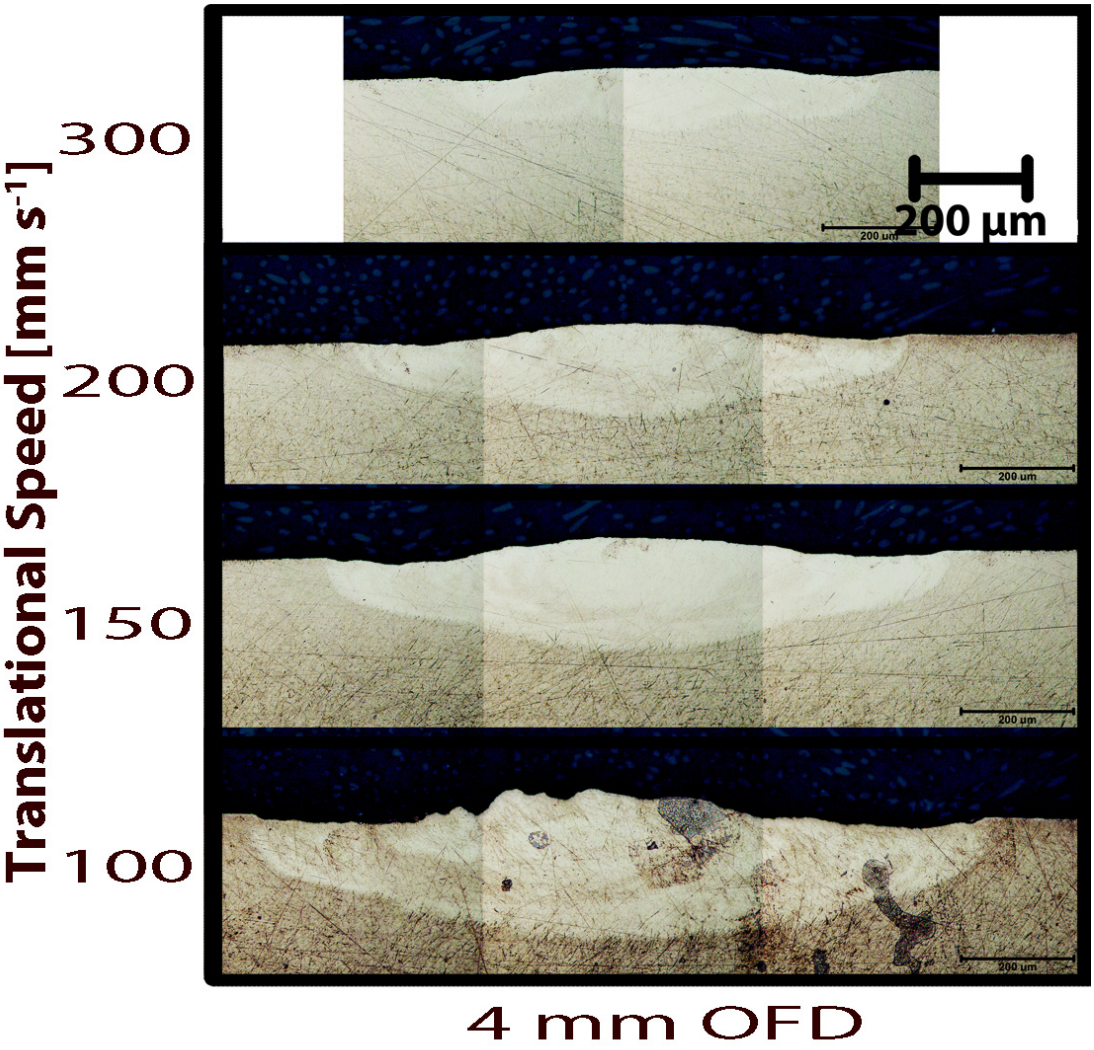

Cross-sectional micrographs of samples processed using a CO_2 laser and a $49.2 \pm 2\,\%$ **N_2-Ar gas mixture, without plasma formation, at an off-focal distance of 8 mm as a function of translation speed. Magnified from figure 4.32.**

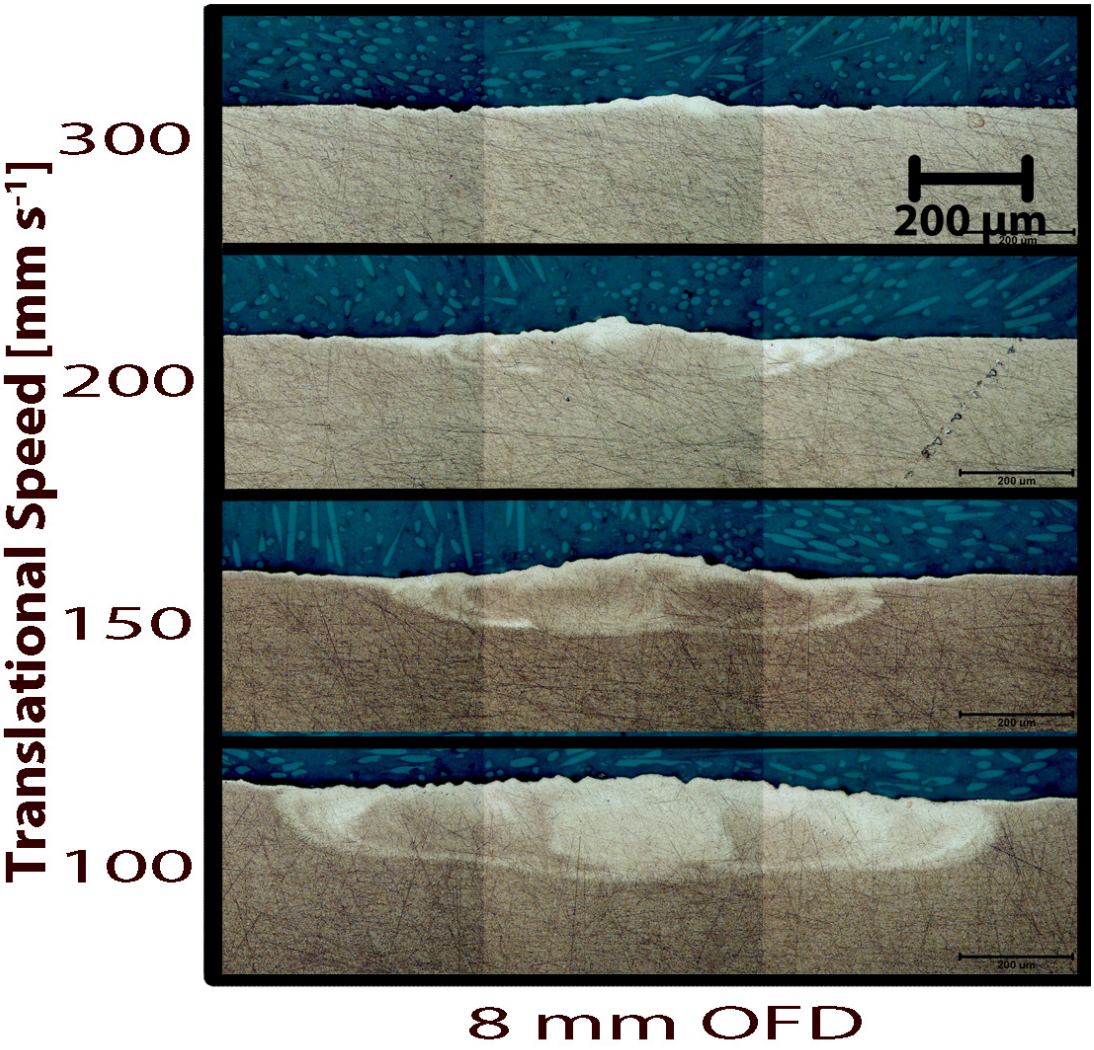

Cross-sectional micrographs of samples processed using a CO_2 laser and a $49.2 \pm 2\,\%$ **N_2-Ar gas mixture, without plasma formation, at an off-focal distance of 6 mm as a function of translation speed. Magnified from figure 4.32.**

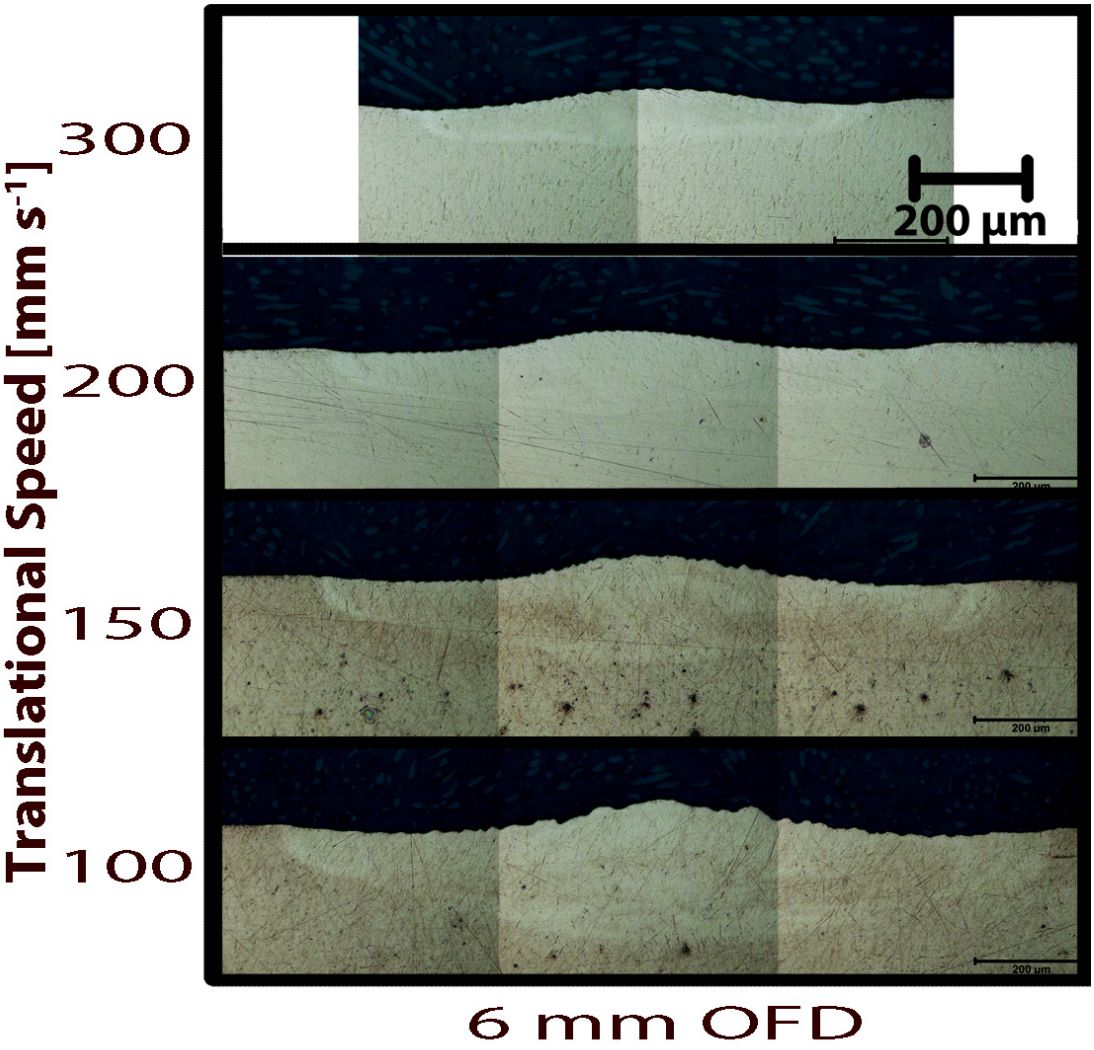

Top surface images of samples processed using a $49.2 \pm 2\,\%$ N_2–Ar LSP at an off-focal distance of 8 mm as a function of low translation speeds. Magnified from figure 4.34.

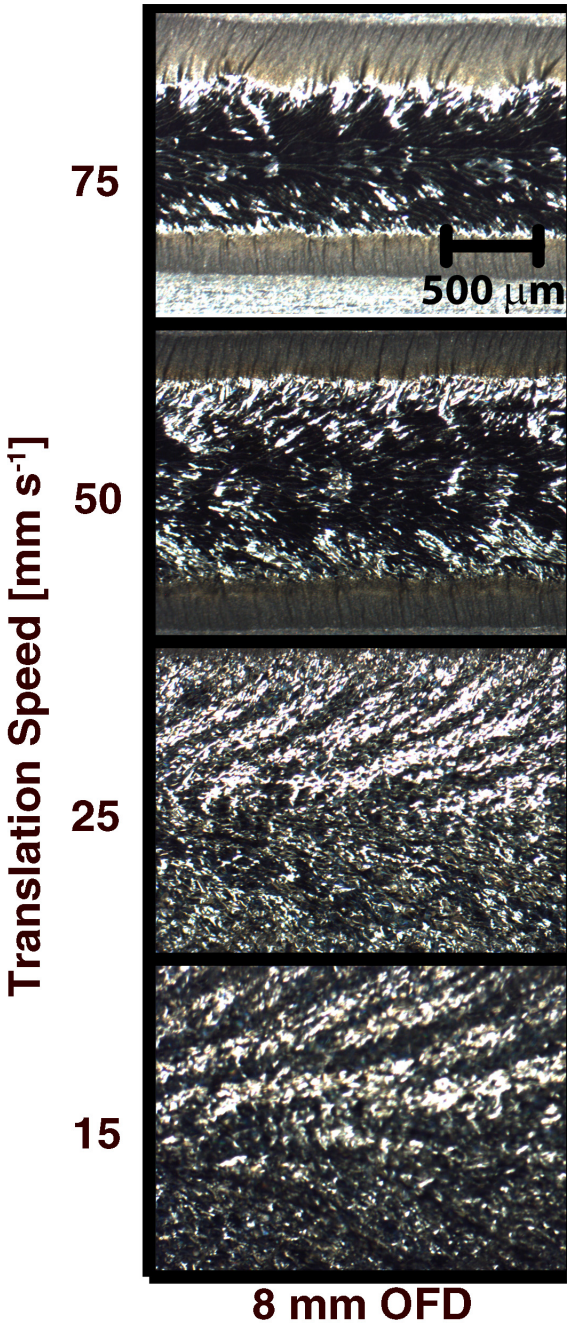

Top surface images of samples processed using a $49.2 \pm 2\,\%$ N_2–Ar LSP at an off-focal distance of 6 mm as a function of low translation speeds. Magnified from figure 4.34.

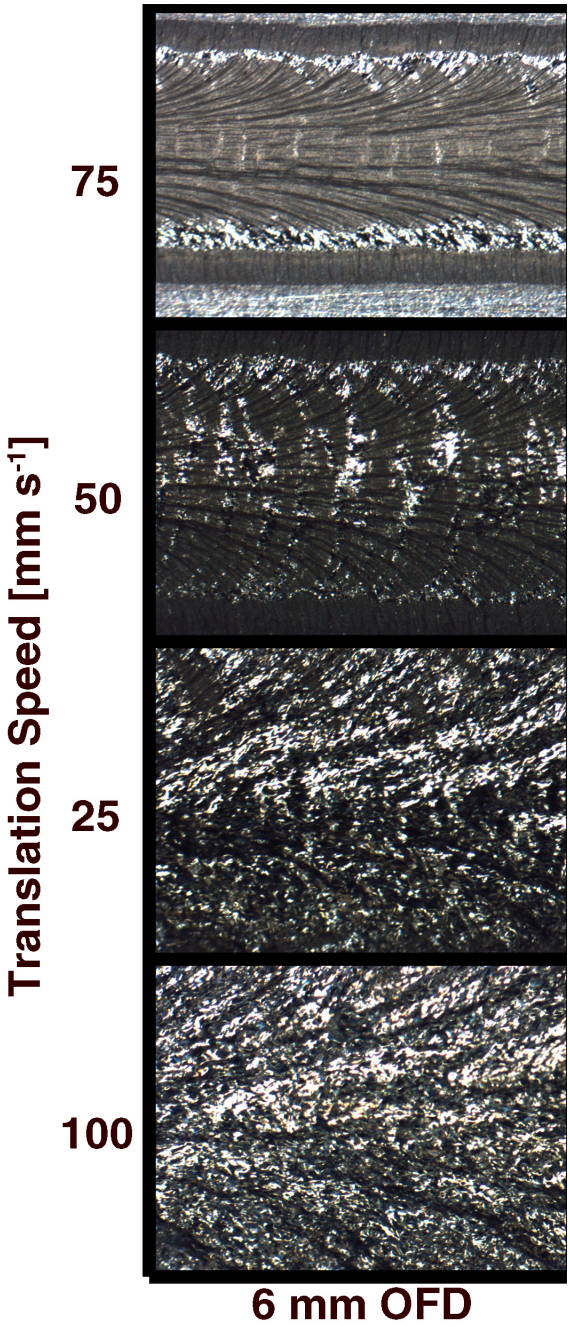

Top surface images of samples processed using a $49.2 \pm 2\,\%$ N_2–Ar LSP at an off-focal distance of 4 mm as a function of low translation speeds. Magnified from figure 4.34.

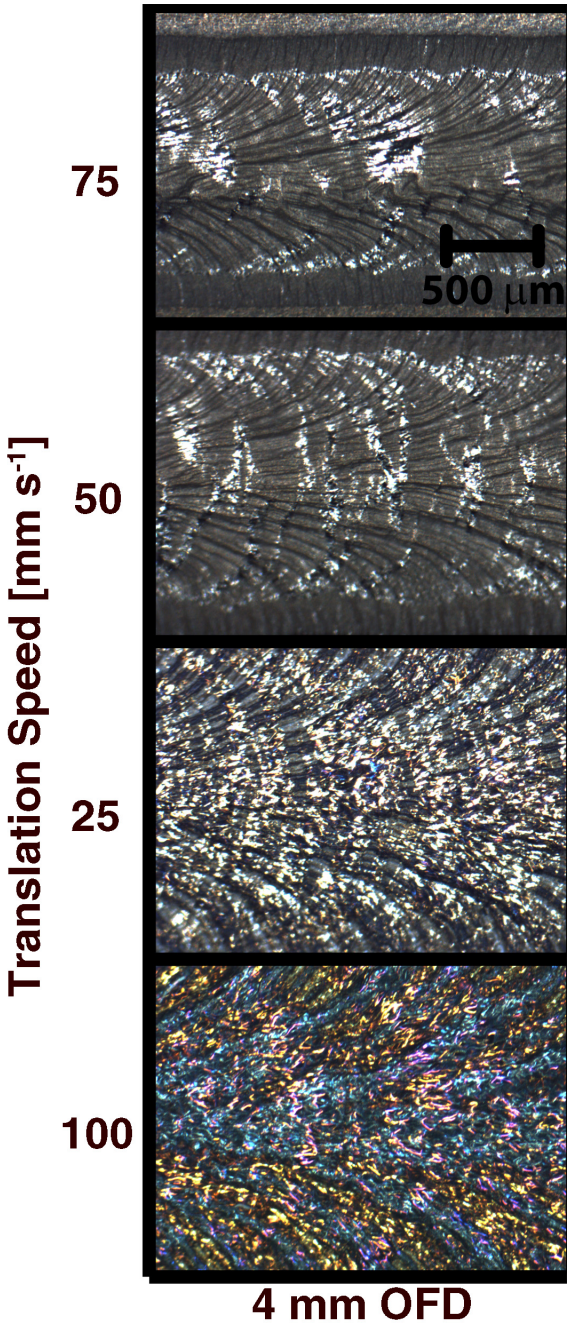

Cross-sectional micrographs of samples processed using a $49.2 \pm 2\,\%$ N_2-Ar LSP at an off-focal distance of 8 mm as a function of translation speed. Magnified from figure 4.36.

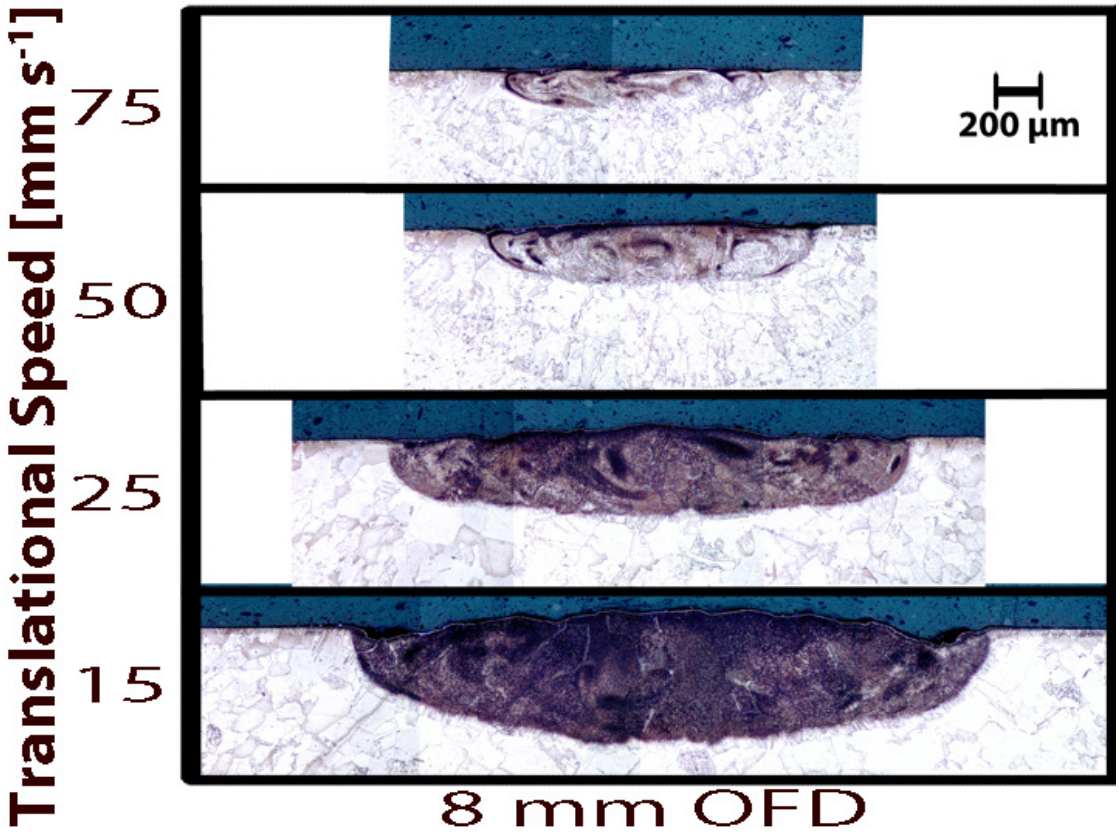

Cross-sectional micrographs of samples processed using a $49.2 \pm 2\,\%$ N_2-Ar LSP at an off-focal distance of 6 mm as a function of translation speed. Magnified from figure 4.36.

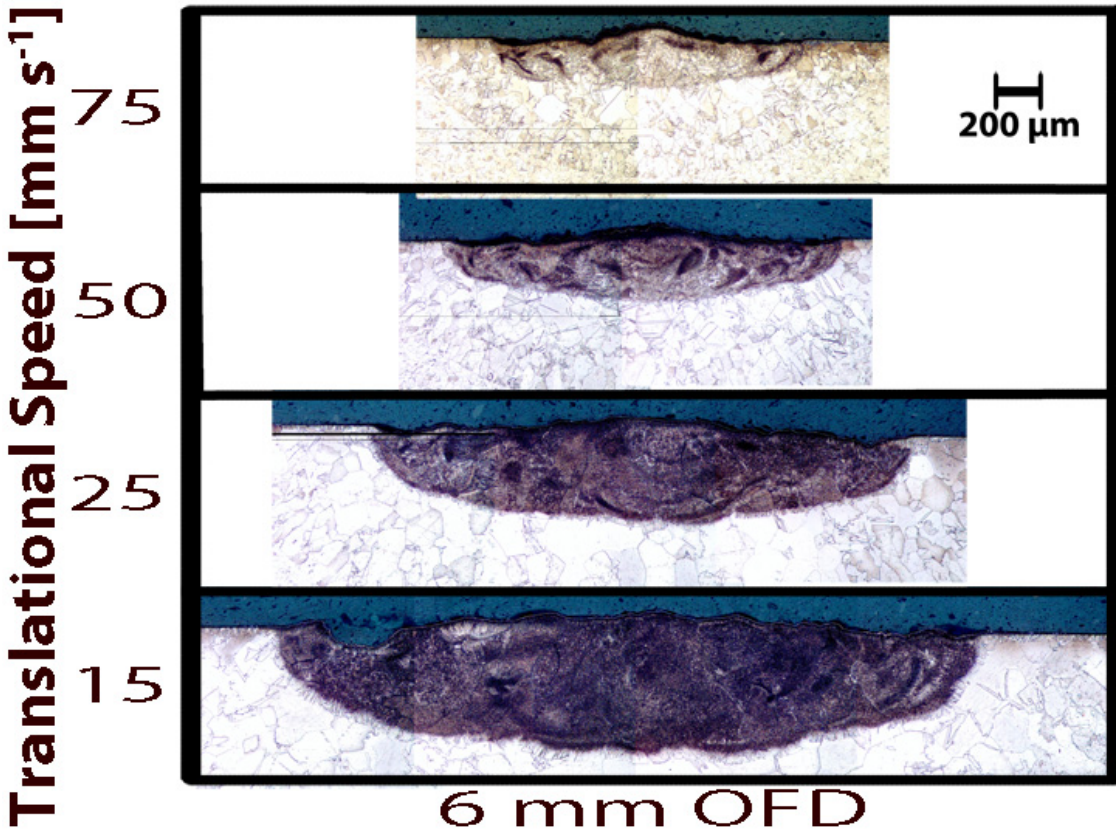

Cross-sectional micrographs of samples processed using $49.2 \pm 2\,\%$ N_2-Ar LSP at an off-focal distance of 4 mm as a function of translation speed. Magnified from figure 4.36.

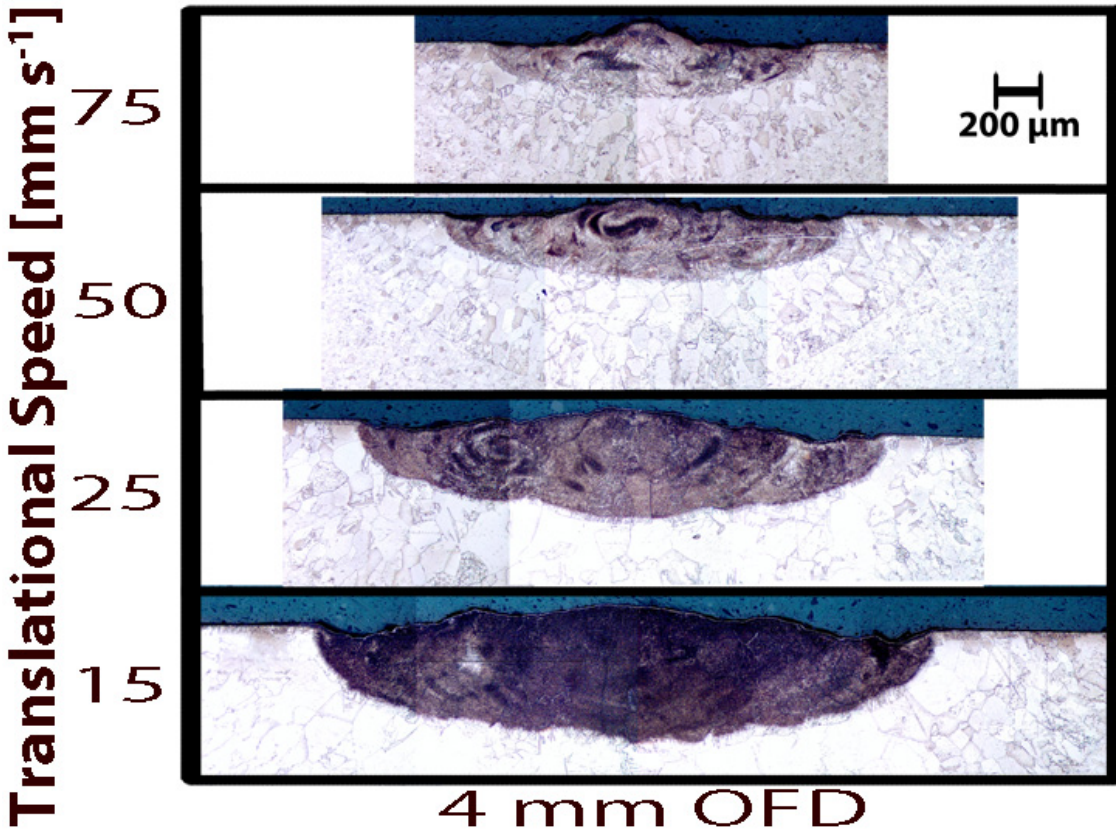

Cross-sectional micrographs of multi-trail samples processed using nitrogen with (top) and without LSP (bottom) at an off-focal distance of 8 mm as a function of translation speed. Magnified from figure 4.40.

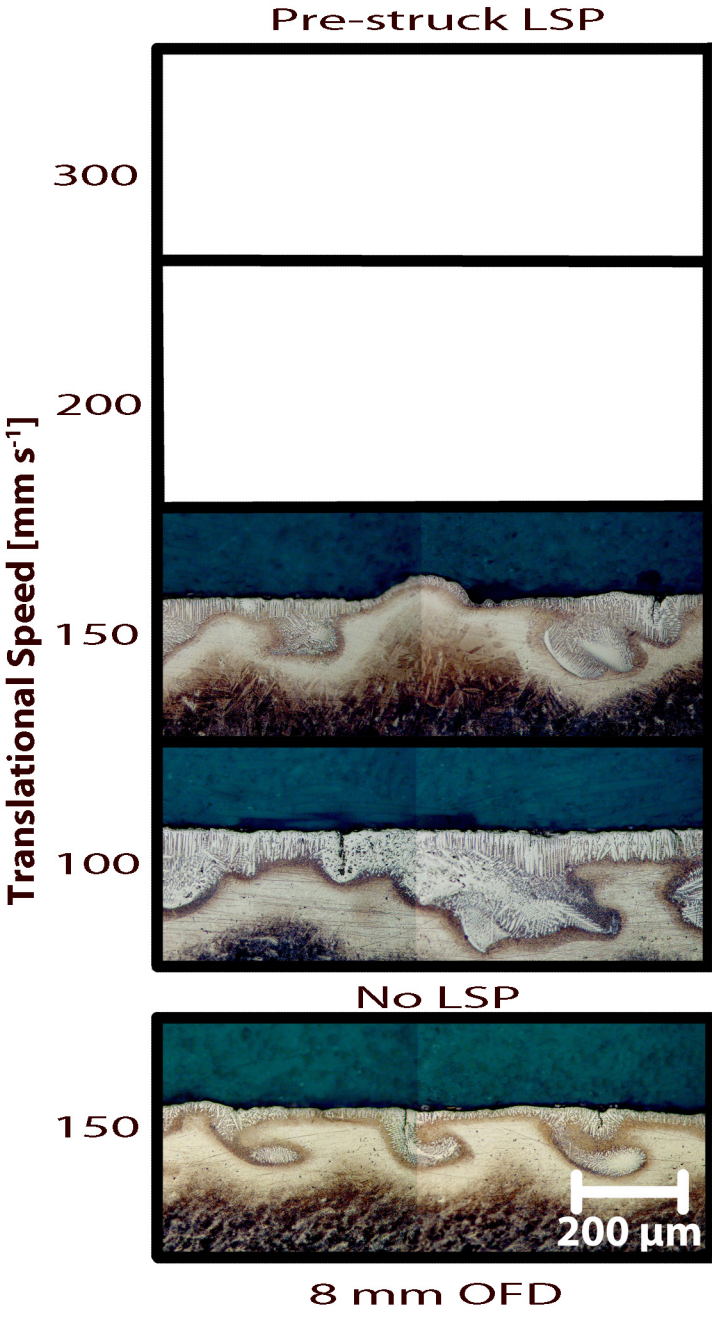

Cross-sectional micrographs of multi-trail samples processed using nitrogen with (top) and without LSP (bottom) at an off-focal distance of 6 mm as a function of translation speed. Magnified from figure 4.40.

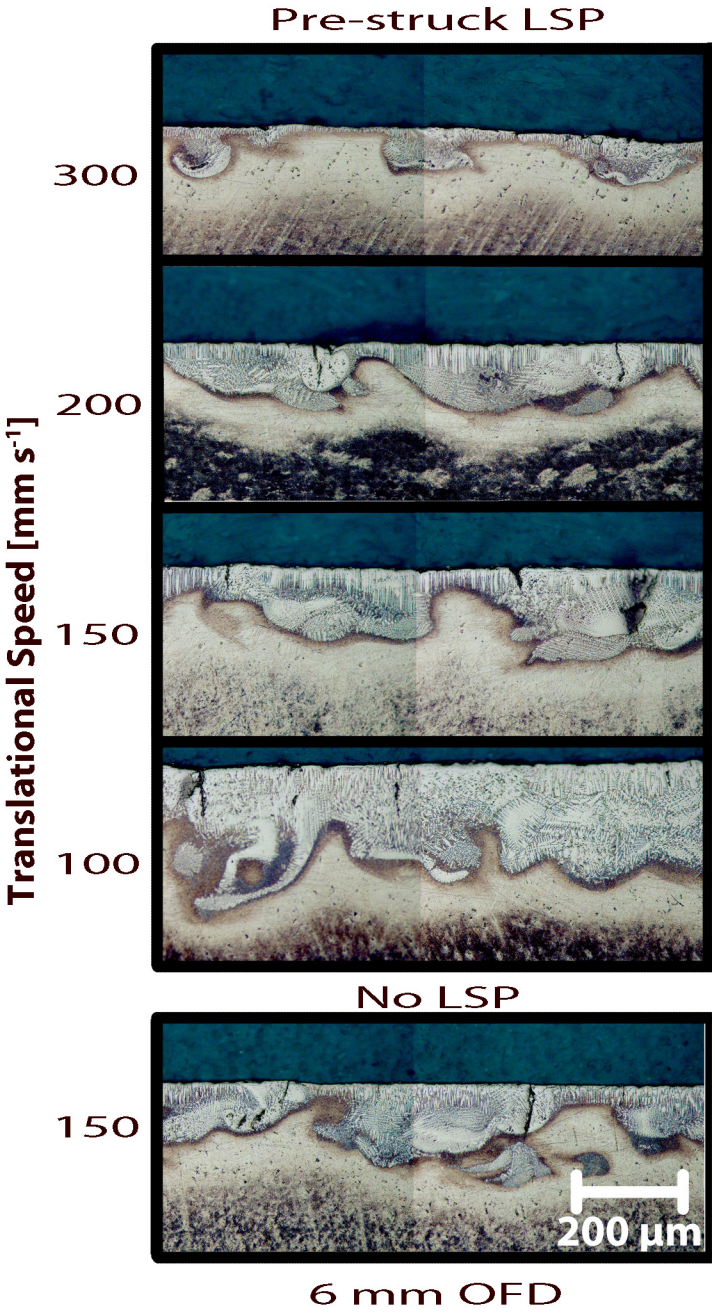

Cross-sectional micrographs of multi-trail samples processed using a nitrogen LSP at an off-focal distance of 4 mm as a function of translation speed. Magnified from figure 4.40.

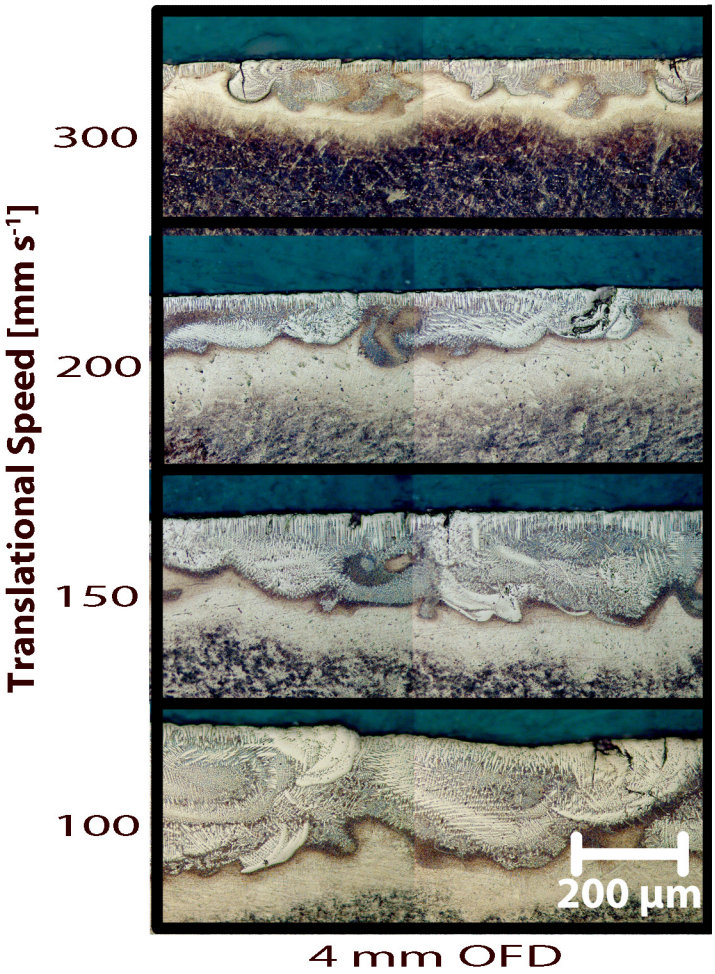

Top surface images of samples processed with (left) and without (right) a nitrogen LSP at an off-focal distance of 8 mm as a function of high translation speeds. Magnified from figure 4.41.

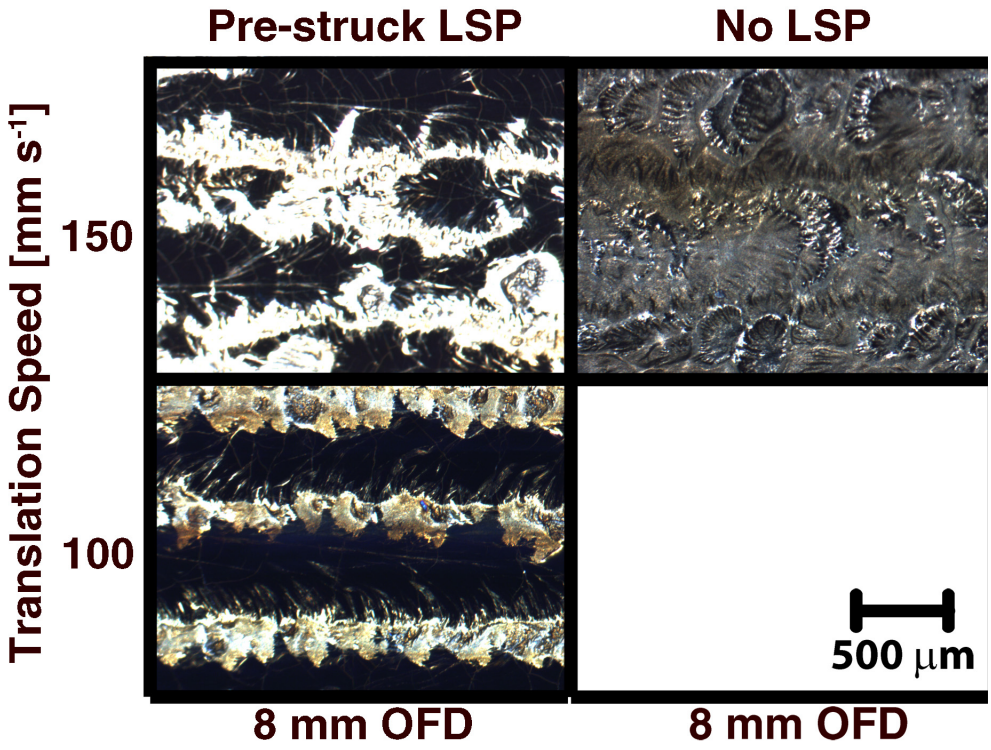

Top surface images of samples processed with (left) and without (right) a nitrogen LSP at an off-focal distance of 6 mm as a function of high translation speeds. Magnified from figure 4.41.

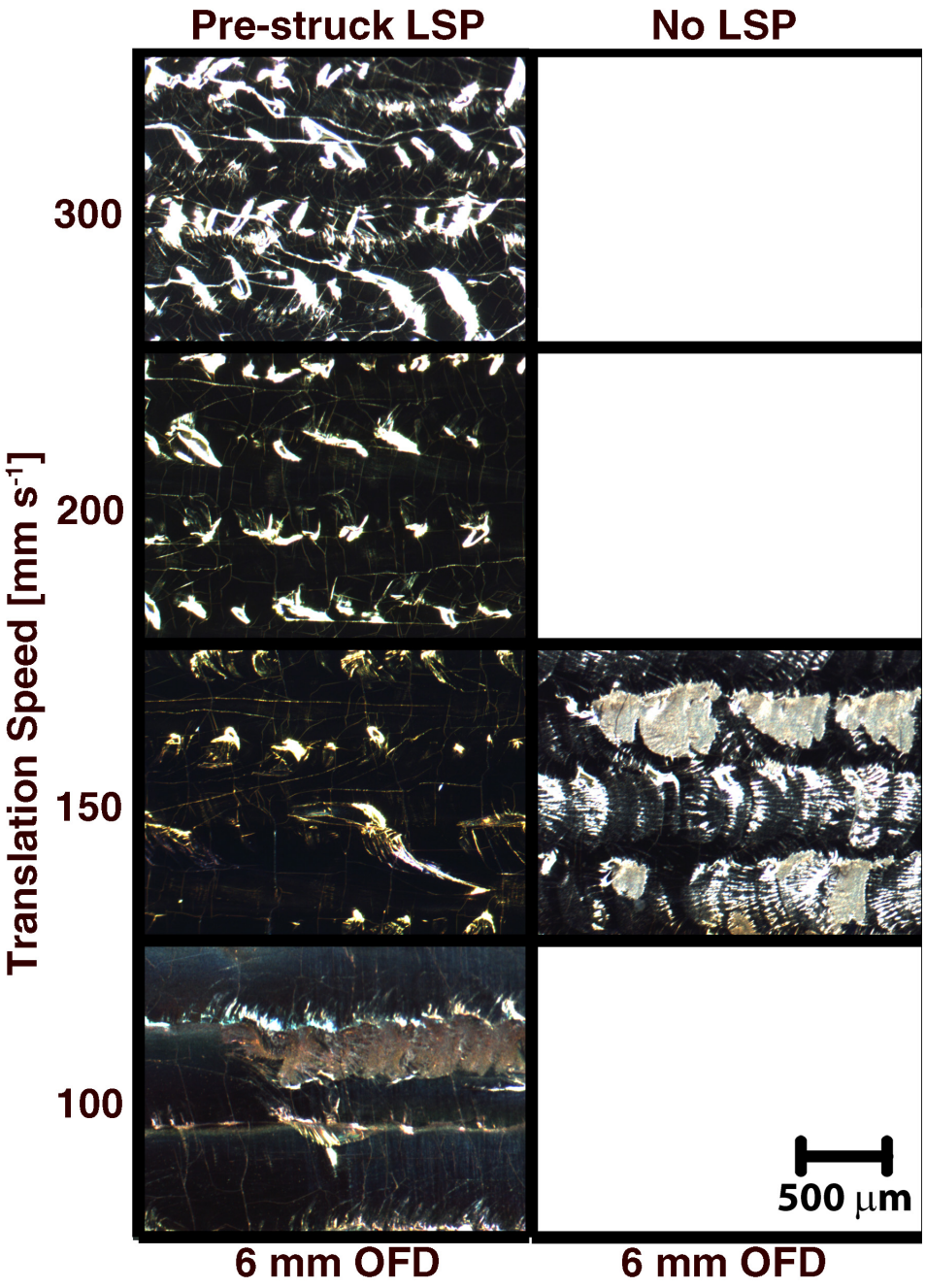

Top surface images of samples processed with a nitrogen LSP at an off-focal distance of 4 mm as a function of high translation speeds. Magnified from figure 4.41.

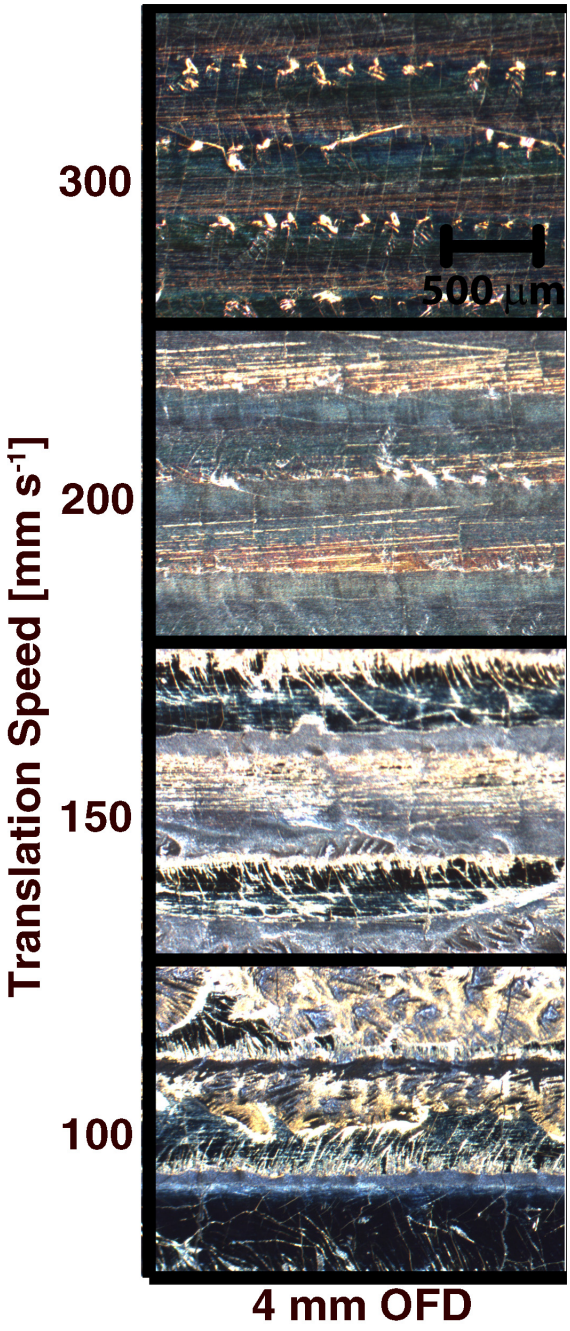

Cross-sectional micrographs of multi-trail samples processed using a $49.2 \pm 2\,\%$ nitrogen–argon mixture, with (top) and without (bottom) LSP an off-focal distance of 8 mm as a function of translation speed. Magnified from figure 4.45.

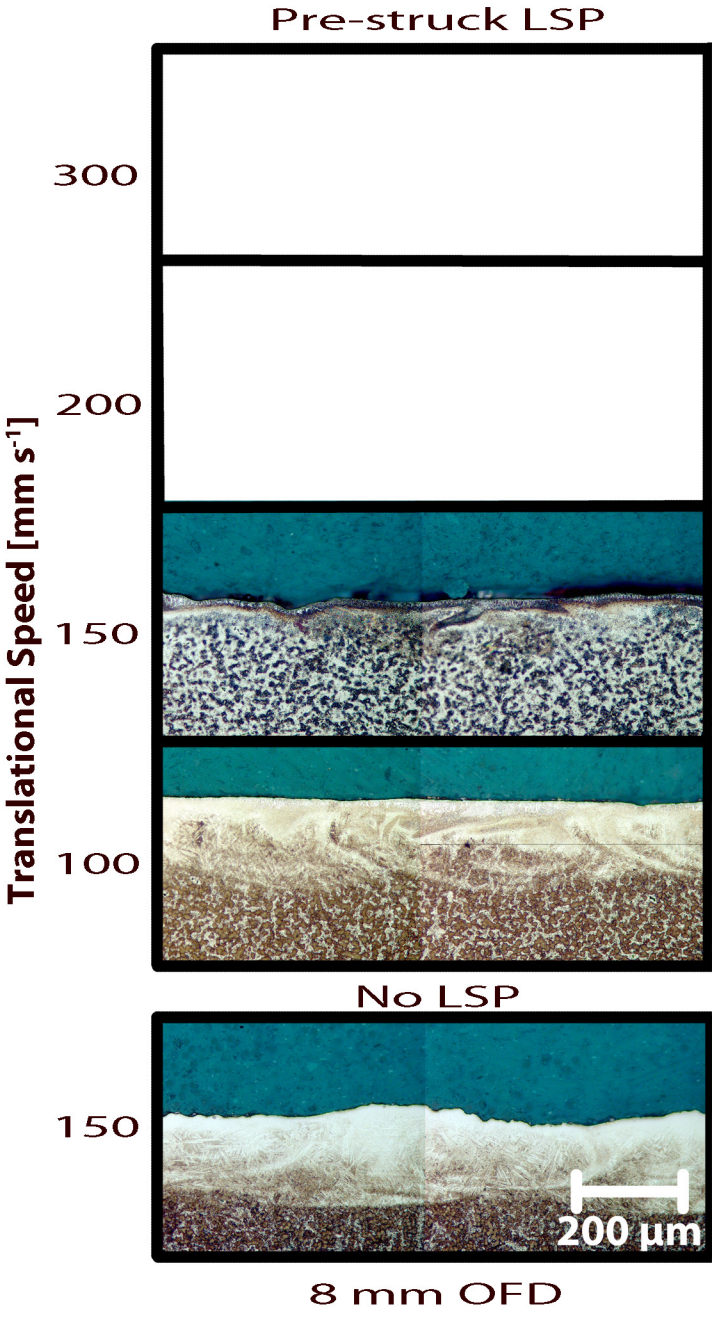

Cross-sectional micrographs of multi-trail samples processed using a $49.2 \pm 2\,\%$ nitrogen–argon mixture, with (top) and without (bottom) LSP an off-focal distance of 6 mm as a function of translation speed. Magnified from figure 4.45.

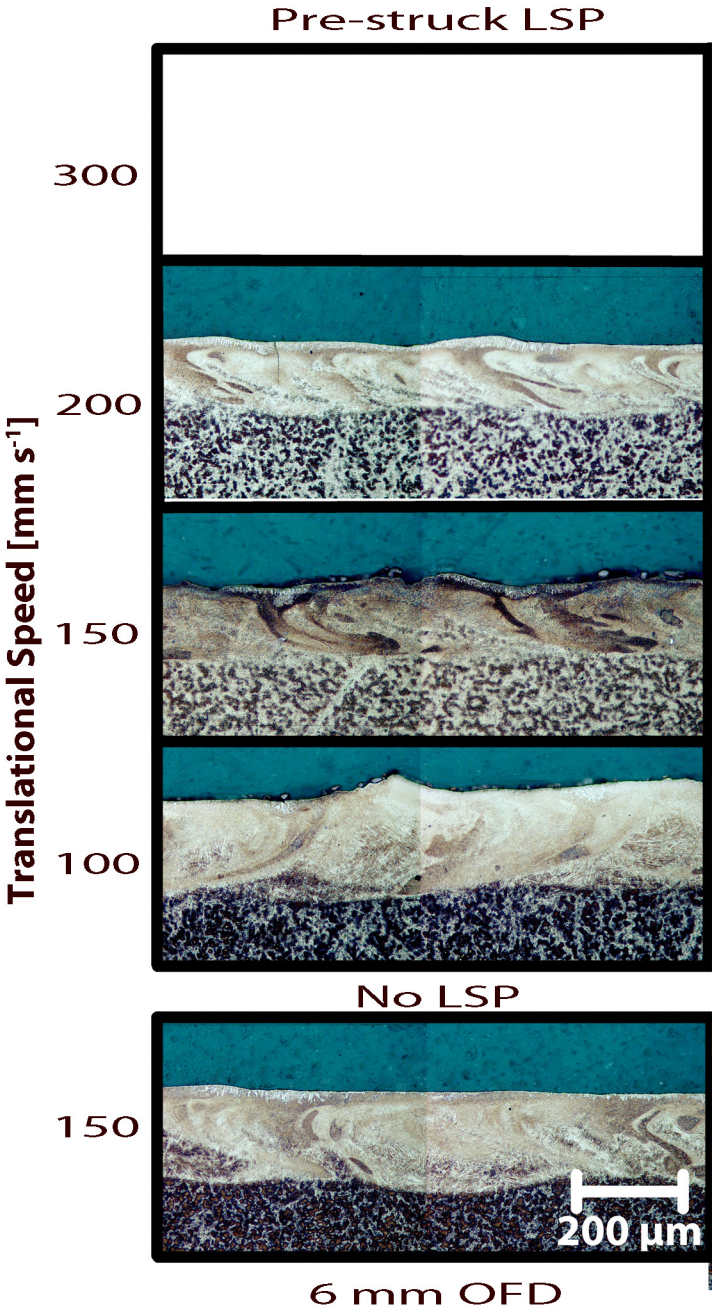

Cross-sectional micrographs of multi-trail samples processed using a $49.2 \pm 2\,\%$ nitrogen–argon mixture, with (top) and without (bottom) LSP an off-focal distance of 4 mm as a function of translation speed. Magnified from figure 4.45.

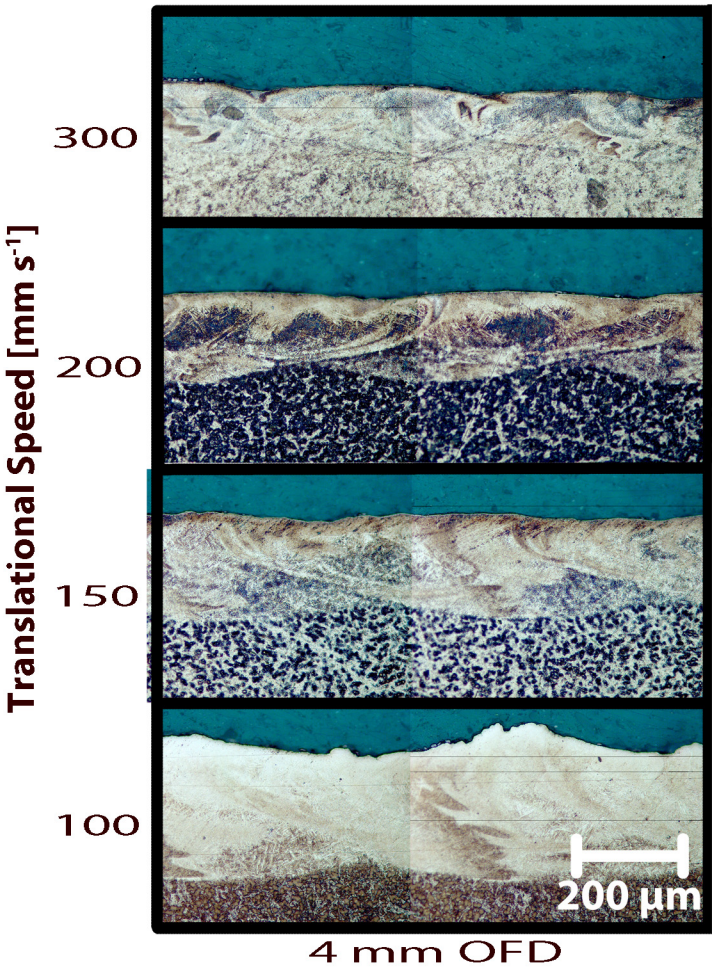

Top surface images of multi-trail samples processed with (left) and without (right) a $49.2 \pm 2\,\%$ nitrogen–argon mixture LSP at an off-focal distance of 8 mm as a function of high translation speeds. Magnified from figure 4.46.

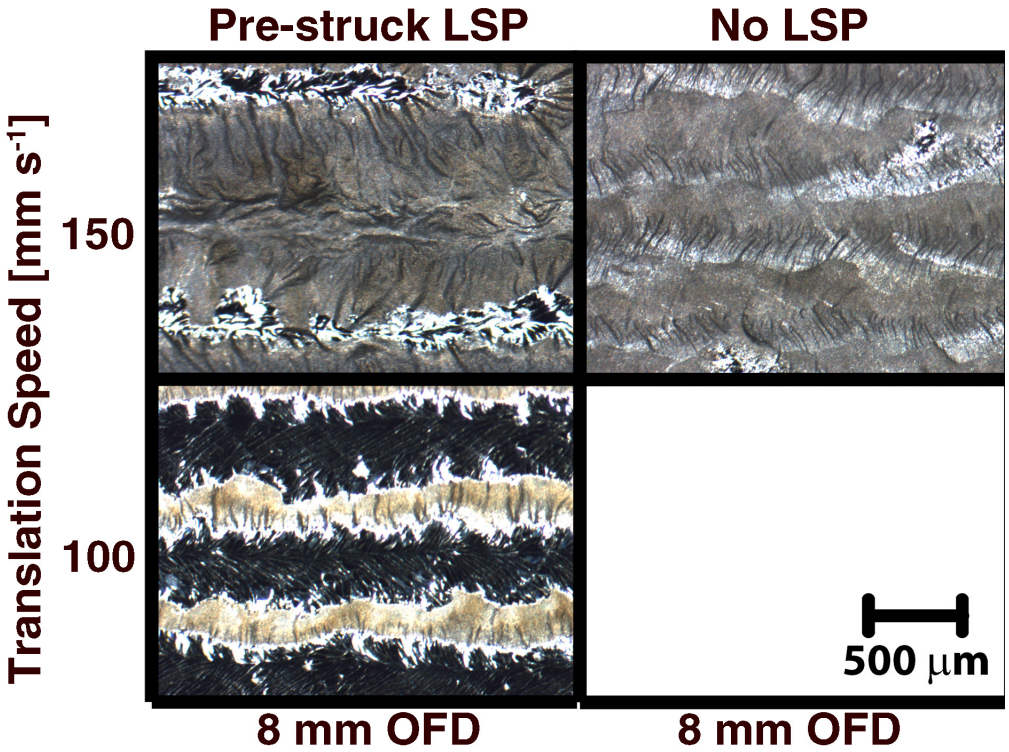

Top surface images of multi-trail samples processed with (left) and without (right) a $49.2 \pm 2\,\%$ nitrogen–argon mixture LSP at an off-focal distance of 6 mm as a function of high translation speeds. Magnified from figure 4.46.

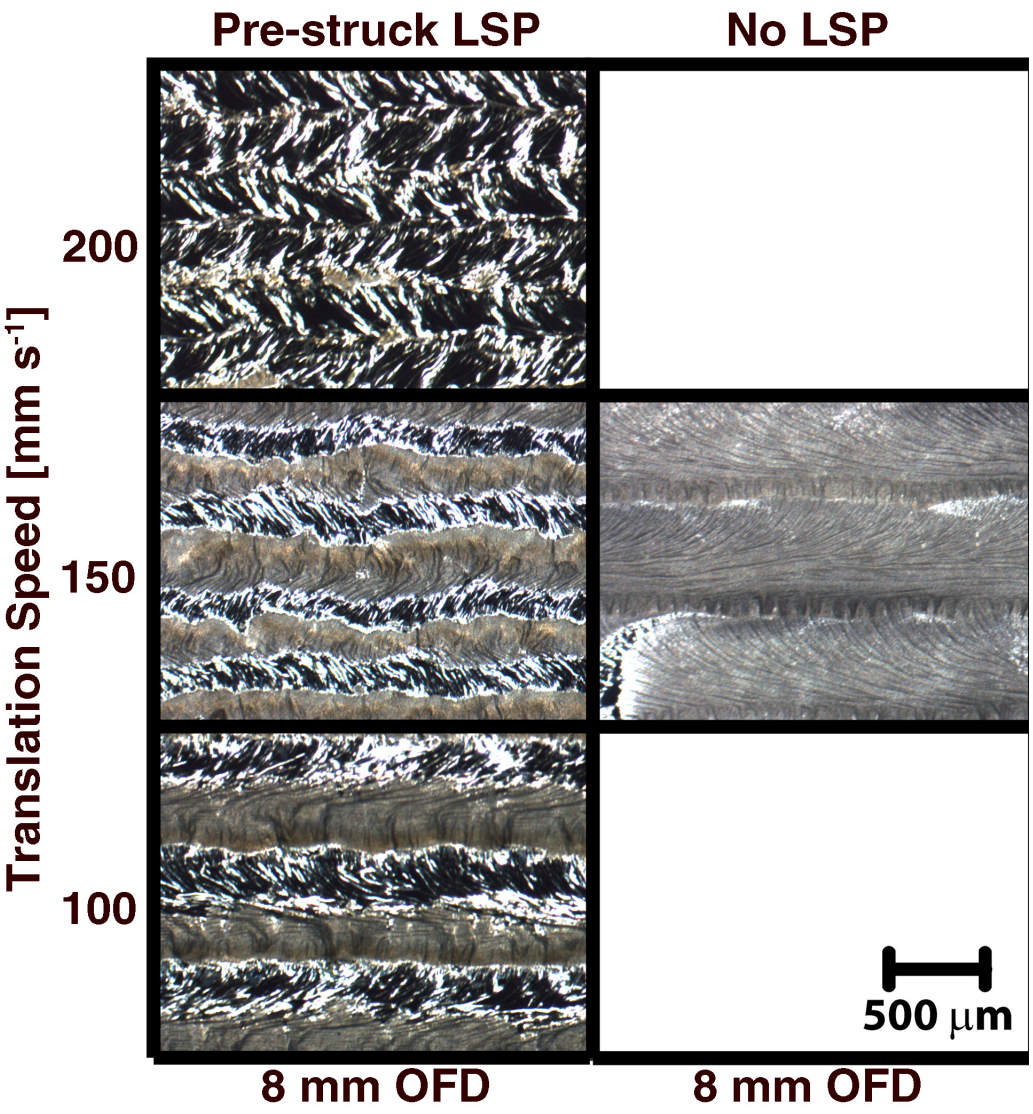

Top surface images of multi-trail samples processed with a $49.2 \pm 2\,\%$ nitrogen–argon mixture LSP at an off-focal distance of 4 mm as a function of high translation speeds. Magnified from figure 4.46.

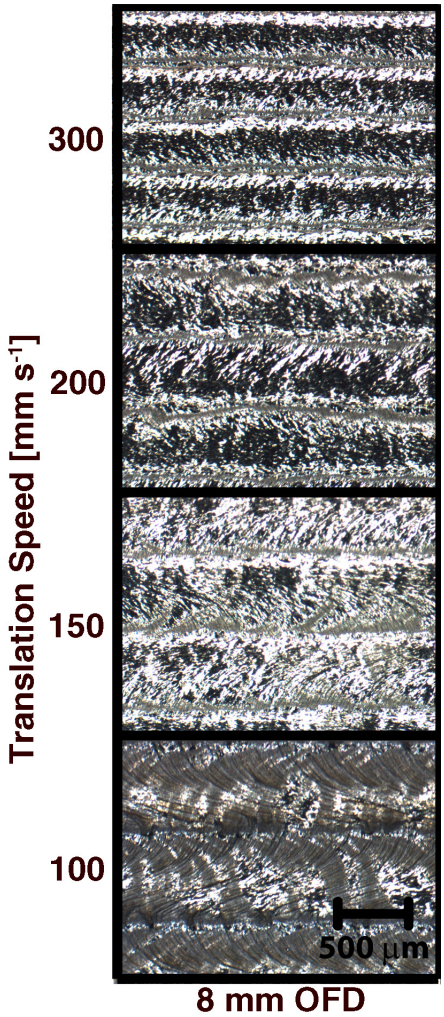

Appendix D

Non-technical abstract

Many modern materials processing techniques involve the use of plasma. Plasma, often referred to as the fourth state of matter, is a collection of ionized and neutral atoms or molecules. In this excited state, plasma can enable chemical reactions which are not otherwise typically possible with solids, liquids or gases. Most commonly, plasma is formed in an enclosed chamber at a low pressures by passing an electric current though a gas or by using microwaves or other types of electromagnetic energy sources. Plasma can also be formed near the focal point of a laser beam. If the laser energy is sufficient, plasma can be sustained away from any confining surface. This phenomena is termed a laser-sustained plasma (LSP). LSP differs from other types of plasma because it is hotter, more dense and can be sustained at atmospheric pressure. Another unique property of LSP is that it can be moved remotely by moving the focal position of the laser beam.

While under some conditions laser processing results in the formation of (surface-struck) plasma, the effect of this plasma on the processing is not well understood. Practically speaking, the only difference between a surface-struck (or near-surface) plasma and a LSP is that LSP can be sustained once the focal position of the laser beam is moved away from a surface. In order to form, LSP must be surface struck or ignited by another plasma. This is analogous to a lighter flame. The lighter flame can be sparked by striking flint or using another flame but will only be sustained if there is a sufficient, continuous flow of lighter fluid.

Because LSP can be made to interact with a surface under conditions where the interaction of a laser beam alone would not result in plasma formation, it is a powerful tool for distinguishing the effect of plasma from laser beam interactions with a surface. This work is the first attempt to conduct such an investigation. In doing so, plasma is characterized by looking at the colors of light it radiates, by constructing mathematical equations which model its behavior and by analysing metal surfaces processed with and without LSP.

By measuring the amount of light emitted at various colors (wavelengths) it was possible to measure the temperature of the plasma. Also, by investigating the degree to which one specific color was spread out (broadened), the number of electrons and ions per unit volume (plasma

density) was measured. The temperature and density were compared to the results of a mathematical model. The model results compared well with the measurements. The assumptions of both the measurement techniques and the model were tested and discussed. The constructed mathematical model differed from previous models in that it allowed for different energy distributions within the laser beam. Different energy distributions were found to influence plasma properties.

A major contribution of this work was in better explaining the role of plasma in laser nitriding of titanium. Laser nitriding is a process wherein nitrogen gas or a nitrogen gas mixture is introduced above a titanium melt pool formed using a laser beam. Previous researchers either ignored the role of plasma, which was likely surface-struck, tried to suppress it or did not present evidence as to its role. Using a LSP, this work presented new insights into the role of plasma in the laser nitriding process. Among the findings was that plasma plays an important role in transferring energy from the laser beam to the titanium metal and that it can both result in new chemical reactions above the surface and prevent the reaction of oxygen with the melt.

Bibliography

[1] Ireland, C. (2004) *Handbook of laser technology and applications*, vol. III, chap. Materials processing, Institute of Physics Publishing, Bristol, UK, pp. 1559–1560.

[2] Majumdar, J. D. and I. Manna (2003) "Laser processing of materials," *Sadhana*, **28**(3 and 4), pp. 495–562.

[3] Steen, W. M. and J. Mazumder (2010) *Laser materials processing*, 4th ed., Springer-Verlag London Limited.

[4] Bäuerle, D. (2011) *Laser processing and chemistry*, 4th ed., Springer Berlin Heidelberg.

[5] Keefer, D. R. (1989) *Laser-induced Plasmas and Applications*, chap. Laser-Sustained Plasmas, Marcel Dekker, INC., pp. 169–206.

[6] Raizer, Y. P. (1991) *Gas Discharge Physics*, Springer-Verlag.

[7] Glumb, R. J. and H. Krier (1986) "Two-Dimensional Model of Laser-Sustained Plasmas in Axisymmetric Flowfields," *AIAA Journal*, **24**(4), pp. 1331–1336.

[8] Cremers, D. A., F. L. Archuleta, and R. J. Martinez (1985) "Evaluation of the Continous optical discharge for spectrochemical analysis," *Spectrochimica Acta Part B: Atomic Spectroscopy*, **40**(4), pp. 665–679.

[9] Bolshakov, A. P., V. I. Konov, V. G. Vostrikov, V. Y. Dubrovskii, F. K. Kosyrev, V. G. Naumov, and L. V. Shachkin (2008) "Study of the optical-discharge plasma in multicomponent mixtures of molecular gases," *Quantum Electronics*, **38**(2), pp. 165–168.

[10] Konov, V. I., A. M. Prokhorov, S. A. Uglov, A. P. Bolshakov, I. A. Leontiev, F. Dausinger, H. Hugel, B. Angestenberger,

G. Sepold, and S. Metev (1998) "Laser Driven Plasma CVD of Thin Films," *SPIE*, **3484**.

[11] Metev, S., H. Brecht, J. Schwarz, and G. Sepold (2002) "New technology for high rate synthesis of PC-diamond coatings in air with photon plasmatron," *Diamond and Related Materials*, **11**, pp. 472–477.

[12] Schwarz, J., K. Meteva, A. Grigat, A. Schubnov, S. Metev, and F. Vollertsen (2005) "Synthesis of diamond coatings on tungsten carbide with photon plasmatron," *Diamond and Related Materials*, **14**, pp. 302–207.

[13] Schaaf, P. (2000) "Laser nitriding of metals," *Progress in Materials Sciences*, **47**(1), pp. 1–161.

[14] Chen, F. F. (2006) *Introduction To Plasam Physics And Controlled Fussion*, Springer Science Business Media, LLC.

[15] Mihailescu, I. N. and J. Hermann (2010) *Laser Processing of Materials*, chap. Laser-plasma interactions, Springer Berlin Heidelberg, pp. 49–88.

[16] Weyl, G. M. (1989) *Laser-induced plasmas and applications*, chap. Physics of laser-induced breakdown: An update, CRC Press, pp. 1–67.

[17] Arzuov, M. I., A. I. Barchukov, F. V. Bunkin, V. I. Konov, and A. M. Prokhorov (1975) "Self-maintence of a continuous optical discharge near solid targets," *Soviet journal of quantum electronics*, **5**(5), pp. 523–525.

[18] Cooper, J. (1966) "Plasma Spectroscopy," *Reports on Progress in Physics*, **23**(35).

[19] Griem, H. R. (1963) "Validity of local thermal equilibrium in plasma spectroscopy," *Physical Review*, **131**(3), pp. 1170–1176.

[20] Zerkle, D. K. and H. Krier (1994) "Nonlocal Thermodynamic Equilibrium in Laser-Sustained Plasmas," *AIAA*, **32**(2), pp. 324–332.

[21] Lochte-Holtgreven, W. (ed.) (1968) *Plasma Diagnostics*, North-Holland Publishing Company.

[22] Hunddlestone, R. H. and S. L. Leonard (eds.) (1965) *Plasma Diagnostic Techniques*, Academic Press.

[23] Giacomo, A. D. (2003) "Experimental characterization of metallic titanium-laser induced plasma by time and space resolved optical emission spectroscopy," *Spectrochimica Acta Part B*, **58**, pp. 71–83.

[24] Generalov, N. A., V. P. Zimakov, G. I. Kozlov, V. A. Masyukov, and Y. P. Raizer (1970) "Continuous Optical Discharge," *Journal of Experimental and Theoretical Physics Letters*, **11**, pp. 302–304.

[25] Raizer, Y. P. (1970) "The feasibility of an optical plasmotron and its power requirement," *JETP Letters*, **11**(3), pp. 120–123.

[26] Generalov, N. A., V. P. Zimakov, G. I. Kozlov, V. A. Masyukov, and Y. P. Raizer (1970) "Gas breakdown under the influence of long-wave infrared radiation of a CO2 laser," *Journal of Experimental and Theoretical Physics Letters*, **11**(7), pp. 228–231.

[27] Fowler, M. C. and D. C. Smith (1975) "Ignition and maintenance of subsonic plasma waves in atmospheric pressure air by cw C02 laser radiation and their effect on laser beam propagation," *Journal of Applied Physics*, **46**, pp. 138–150.

[28] Generalov, N. A., A. M. Zakharov, V. D. Kosynkin, and Y. M. Yakimov (1986) "Stability of a continuous optical discharge in an atmospheric-air flow," *Combustion, Explosion and Shock Waves*, **22**(2), pp. 91–94.

[29] Carlhoff, C., E. Krametz, J. H. Schafer, K. Schildbach, J. Uhlenbusch, and D. Wroblewski (1981) "Continous optical discharges at very high pressure," *Physica B+C*, **103**, pp. 439–337.

[30] Raizer, Y. P. (1979) "Optical discharges," *Journal De Physique*, **40**(C7), pp. C7–141 – C7–147.

[31] Gerasimenko, M. V., G. I. Kozlov, and V. A. Kuznetsov (1983) "Laser Plasmatron," *Soviet Journal of Quantum Electronics*, **13**(4), pp. 438–443.

[32] Keefer, D. R., B. B. Henriksen, and W. F. Braerman (1975) "Experimental study of stationaly laser-sustained air plasma," *Journ*, **46**(3), pp. 1080–1083.

[33] Fowler, M. C. (1981) "Measured molecular absorptivities for a laser thruster," *AIAA Journal*, **19**(9), pp. 1009–1014.

[34] Mazumder, J., T. J. Rockstroh, and H. Krier (1987) "Spectroscopic studies of plasma during cw laser gas heating in flowing argon," *Journal of Applied Physics*, **62**(12), pp. 4712–4718.

[35] Krier, H., J. Mazumder, T. J. Rockstroh, T. D. Bender, and R. J. Glumb (1986) "Continous wave laser gas heating by sustained plasma in flowing argon," *AIAA J*, **24**(10), pp. 1656–1662.

[36] Welle, R., D. Keefer, and C. Peters (1986) "Energy conversion efficiency in high-flow laser-sustained argon plasmas," in *AIAA and ASME, Joint Fluid Mechanics, Plasma Dynamics and Lasers Conference, 4th, Atlanta, GA, May 12-14.*

[37] Kozlov, G. I. (1978) "Flowing-gas laser plasmotron," *Soviet Technical Physics Letters*, **4**(5), pp. 234–235.

[38] Glumb, R. J. (1986) *Experimental and Theoretical studies of laser-sustained argon plasma for application to laser-supported rocket propulsion*, Ph.D. thesis, University of Illinois at Urban-Champaign.

[39] Conrad, R., Y. P. Raizer, and S. T. Sarzhikov (1996) "Continous Optical Discharge Stabbalized by gas flow in weakly focused laser beam," *AIAA Jour*, **34**(8), pp. 1584–1588.

[40] Giren, B. G. (1993) "Steel Surface Processing by a Continous Optical Discharge Plasma," *Plasma Chemistry and Plasma Processing*, **13**(1), pp. 133–140.

[41] ——— (1991) "Absorption of laser radiation in an optical discharge plasma in a gas mixture stream," *Journal of Physics D: Applied Physics*, **24**, pp. 1086–1087.

[42] Cross, J. B. and D. A. Cremers (1986) "High kinetic energy (1-10 eV) laser sustained atom beam source," *Nuclear Instruments & Methods in Physics Research, Section*, **B13**(1-3), pp. 658–662.

[43] Chen, X. and J. Mazumder (1989) "Emission spectroscopy of CW C02 laser-sustained argon plasma: Effects of gas flow speed," *Journal of Applied Physics*, **66**(12), pp. 5756–5762.

[44] Mazumder, J., H. Krier, and X. Chen (1988) *Spectroscopic diagnostics of electron temperature and energy conversion efficiency of laser-sustained plasma in flowing argon*, *Tech. Rep. APOSR-TR. 89-0442*, Air Force Office of Scientific Research, Department of Mechanical and Industrial Engineering, University of Illinois at Urban-Champaign.

[45] Glumb, R. J. and H. Krier (1983) "Concepts and status of laser-supported rocket propulsion," *AIAA Jo*, **21**(1), pp. 70–79.

[46] Matsui, M., T. Inoue, K. Komurasaki, and Y. Arakawa (2007) "High enthalpy flow generation by a 2 kW class CW laser," in *45th AIAA Aerospace Sciencces metting and Exhibit 8-11 January 2007, Reno Nevada.*

[47] Cremers, D. A., J. Castro, and K. marcus (1985) "Evaluation of the continuous optical discharge for spectrochemical analysis," *Spectrochimica Acta Part B: Atomic Spectroscopy*, **40**(4), pp. 665–679.

[48] Bolshakov, A., V. Konov, A. Prokhorov, S. Uglov, and F. Dausinger (2001) "Laser plasma CVD diamond reactor," *Diamond and Related Materials*, **10**, pp. 1559–1564.

[49] Konov, V. I., A. M. Prokhorov, S. A. Uglov, A. P. Bolshakov, I. A. Leontiev, F. Dausinger, H. Hugel, B. Angestenberger, G. Sepold, and S. Metev (1998) "CO2 laser-induced plasma CVD synthesis of diamond," *Applied Physics A*, **66**, pp. 575–578.

[50] Naumov, V. G., V. E. Cherkovetch, V. U. Dubrovckii, F. K. Kosyrev, V. G. Vostriko, V. I. Konov, A. Bolshakov, and V. R. chenko (2008) "Laser plasmatron for CVD synthesis of diamond in open air," Proceedings of SPIE 6344,.

[51] Githens, A. (2012) *Preliminary exploration of diamond formation at atmospheric pressure using laser sustained plasmas*, Honors thesis, Pennsylvania State University.

[52] Griem, H. R. (1964) *Plasma spectroscopy*, McGraw-Hill.

[53] ——— (1974) *Spectral line broadening by plasmas*, Academic Press, London.

[54] Jansson, P. A. (1997) *Deconvolution of images and spectra*, 2nd ed., Academic Press,.

[55] Gigosos, M. A. and V. Cardeoso (1996) "New plasma diagnosis table of hydrogen stark broadening including ion dynamics," *Journal of Physics B: Atomic, Molecular and Optical Physics*, **29**(20), pp. 4795–4838.

[56] Aparicio, J. A., M. A. Gigosos, V. R. Gonzlez, C. Prez, M. I. de la Rosa, and S. Mar (1998) "Measurement of Stark broadening and shift of singly ionized Ar lines," *Journal of Physics B: Atomic, Molecular and Optical Physics*, **31**, pp. 1029–1048.

[57] Gigosos, M. A., M. . Gonzlez, and V. Cardeoso (2003) "Computer simulated Balmer-alpha, -beta and -gamma Stark line profiles for non-equilibrium plasmas diagnostics," *Spectrochimica Acta Part B: Atomic Spectroscopy*, **58**, pp. 1489–1504.

[58] Huang, X. and Y. L. Yung (2003) "A common misunderstanding about the Voigt line profile," *Journal of The Atmospheric Sciences*, **61**, pp. 1630–1632.

[59] Bockasten, K. (1960) "Transformation of observed radiances into radial distribution of the emission of a plasma," *Journal of The Optical Society of America*, **51**, pp. 943–947.

[60] Krempl, P. W. (2007) *Semi-integrals and Semi-derivatives in Particle Physics*, chap. Semi-integrals and Semi-derivatives in Particle Physics, Springer Netherlands, pp. 139–154.

[61] Kilbas, A. A., H. M. Srivastava, and J. J. Trujillo (2006) *Theory and applications of fractional differential equations*, Elsevier.

[62] Nestor, O. H. and H. N. Olsen (1960) "Numerical methods for reducting line and surface probe data," *SIAM Review*, **2**, pp. 200–207.

[63] Chvala, F. and J. Hlina (2006) "Numerical aspects of evaluating the radial distribution of radiation intensity in plasma jets," *Czechoslovak Journal of Physics*, **56**, pp. B761–B766.

[64] Ralchenko, Y., A. Kramida, J. Reader, and NIST ASD Team (2011), "NIST Atomic Spectra Database (version 4.1)," Online. URL `http://physics.nist.gov/asd`

[65] Szymanski, Z., Z. Peradzynski, J. Kurzyna, J. Hoffman, M. Dudeck, M. de Graff, and V. Lago (1997) "Spectroscopic study of a supersonic jet of laser-heated argon plasma," *Journal of Physics D: Applied Physics*, **30**, pp. 998–1006.

[66] Lebehot, A. and R. Campargue (1996) "Properties of an argon plasma free jet generated from a continuous optical discharge," *Physics of Plasmas*, **3**(7), pp. 2502–2510.

[67] Dimitrijevic, M. S., M. Christova, and S. Sahal-Brechot (2007) "Stark broadening of visible Ar I spectral lines," *Physica scripta*, **75**(6), pp. 809–819.

[68] Navráatil, Z., D. Trunec, R. šmíd, and L. Lazar (2006) "A software for optical emission spectroscopy - problem formulation and application to plasma diagnostics," *Czechoslovak Journal of Physics*, **56**(Suppl. B), pp. B944–951, http://dx.doi.org/10.1007/s10582-006-0308-y.

[69] Akarapu, R., A. R. Nassar, S. M. Copley, and J. A. Todd (2009) "Numerical Model of a laser-sustained argon plasma," *Journal of Laser Applications*, **21**, pp. 169–175.

[70] Raizer, Y. P. (1970) "Subsonic propagation of a light spark and threshold conditions for the maintenance of plasma by radiation," *Soviet Physics JETP*, **31**(6), pp. 1148–1154.

[71] Jackson, J. P. and P. E. Nielsen (1974) "Role of radiative transport in propagation of laser supported combustion waves," *AIAA Journal*, **12**(11), pp. 1498–1501.

[72] Kemp, N. H. and R. G. Root (1979) "Analytical study of laser-supported combustion waves in hydrogen," *Journal of Energy*, **3**(1), pp. 40–49.

[73] ——— (1977) *Analytical study of laser supported combustion waves in hydrogen*, *Tech. Rep. NASA-CR-135349*, NASA Lewis Research Center.

[74] Keefer, D., C. Peters, and H. Crowder (1985) "A re-examination of the laser-supported combustion wave," *AIAA Journal*, **23**(8), pp. 1208–1212.

[75] Batteh, J. H. and D. R. Keefer (1974) "Two dimensional generalization of Raizer's analysis for the subsonic propagation of laser sparks," *IEEE Transactions on Plasma Science*, **PS-2**, pp. 122–129.

[76] Keefer, D., H. Crowder, and R. Elkins (1982) "A two-dimensional model of the hydrogen plasma for a laser powered rocket," *AIAA Paper*, **82-0404**.

[77] Muller, S. and J. Uhlenbusch (1982) "Theoretical model for a continuous optical dis," *Physica*, **112C**, pp. 259–270.

[78] Jeng, S. M. and D. R. Keefer (1986) "Theoretical investigation of laser-sustained argon plasmas," *Journal of Applied Physics*, **60**(7), pp. 2272–2279.

[79] Jeng, S.-M., R. Litchford, and D. Keefer (1988) *Computational design of an experimental laser-powered thruster*, *Tech. Rep. NASA-CR-183587*, NASA Marshall Space and Flights Center.

[80] Keefer, D., S.-M. Jeng, and R. Welle (1987) "Laser thermal propulsion using laser sustained plasmas," *Acta Astronautica*, **15**(6/7), pp. 367–376.

[81] Girard, J. M., A. Lebehot, and R. Campargue (1993) "Generation conditions of a laser-sustained argon plasma," *Journal of Physics D: Applied Physics*, **26**, pp. 1382–1293.

[82] Surzhikov, S. T. and A. A. Chenstov (1996) "Numerical study of the stability of optical discharges in an air flow," *Plasma Physics Reports*, **22**(11), pp. 957–963.

[83] Komurasaki, K., P. Molina-Morales, K. Toyoda, and Y. Arakawa (2001) "Numerical analysis of CW laser propulsion," *Transactions of the Japan Society for Aeronautical and Space Sciences*, **44**(144), pp. 67–72.

[84] Derllishak, K. S., C. F. Knopp, and A. B. Cambel (1963) "Partition Functions and Thermodynamic Propertis of Argon Plasma," *The Physics of Fluids*, **6**(9), pp. 1280–1288.

[85] Devoto, R. S. (1973) "Transport coefficients of ionized argon," *The Physics of Fluids*, **16**(5), pp. 616–623.

[86] Murphy, A. B. and C. J. Arudell (1994) "Transport coefficients of argon, nitrogen, oxygen, argon-nitrogen, and argon-oxygen plasmas," *Plasma Chemistry and Plasma Processing*, **14**(4), pp. 451–490.

[87] Kuznetsova, T. D. and D. A. Frank-Kamentskii (1962) "Radiative Thermal Conductivity of a Fully Ionized Plasma," *Soviet Astronomy*, **6**, p. 191.

[88] Menart, J., J. Heberlein, and E. Pfender (1996) "Theoretical radiative emission results for argon/copper thermal plasmas," *Pla*, **16**(1), pp. 245S–265S.

[89] Chen, W. L. T., J. Heberlein, and E. Pfender (1996) "Critical Analysis of Viscosity Data of Thermal Argon Plasmas at Atmospheric Pressure." *Plasma Chemistry and Plasma Processing.*, **16**(4), pp. 635–650.

[90] Saha, M. N. (1921) "On a Physical Theory of Stellar Spectra," *Proceedings of the Royal Society of London Series A*, **99**(697), pp. 135–153.

[91] Johnston, T. W. and J. Dawson (1973) "Correct values for high-frequency power absorption by inverse bremsstrahlung in plasmas," *Physics of Fluids*, **16**(5), p. 722.

[92] Naval Research Laboratory (2007) *NRL Plasma Formulary*, vol. NRL/PU/6790-07-500, Naval Research Laboratory.

[93] Oettinger, P. E. and D. Bershader (1967) "A Unified Treatment of the Relaxation Phenomenon in Radiating Argon Plasma Flows," *AIAA Journal*, **5**(9), pp. 1625–1632.

[94] Horn, K. P. (1966) *Radiative behavior of shock generated argon plasma flows*, Ph. d. thesis, Stanford University.

[95] Fluent, inc. (2006) "Fluent 6.3 Users Guide," .

[96] Pantankar, S. V. and D. B. Spalding (1972) "Calculation procedure for heat, mass and momentum transfer in three-dimensional parabolic flow," *International Journal of Heat and Mass Transfer*, **15**(10), pp. 1787–1806.

[97] Szymanski, Z. and S. Filipkowski (1991) "Nonstationary laser-sustained plasma," *Journal of Applied Physics*, **69**(6), pp. 3480–3484.

[98] Marotta, A. (1994) "Determination of axial thermal plasma temperatures without Abel inversion," *Journal of Physics D: Applied Physics*, **27**(2), pp. 268–272.

[99] Nassar, A. R., R. Akarapu, S. M. Copley, and J. A. Todd (2012) "Investigations of laser-sustained plasma and its role in laser nitriding of titanium," *Journal of Physics D: Applied Physics*, **45**(18), p. 185401. URL `http://dx.doi.org/10.1088/0022-3727/45/18/185401`

[100] Mordike, B. L. (1986) "NATO ASI Series, Series E: Applied Sciences (San Miniato, Italy)," in *NATO ASI Series, Series E: Applied Sciences* (C. W. Draper and P. Mazzoldi, eds.), vol. 115, NATO Advanced Study Institute on Laser Treatment of Metals, Dordrecht: Martinus Nijhoff Publ, San Miniato, Italy,, pp. 389–412.

[101] Xue, L., M. U. Islam, A. K. Koul, M. Bibby, and W. Wallace (1997) "Laser Gas Nitriding of Ti-6Al-4V Alloy: I. Optimization of the Process," *Materials and Manufacturing Processes*, **4**, pp. 25–47.

[102] Bell, T., P. H. Morton, and A. Bloyce (1994) "Towards the design of dynamically loaded titanium engineering components," *Materials Science and Engineering*, **A184**, pp. 73–86.

[103] Bonss, S., B. Brenner, and E. Beyer (2001) "Laser gas alloying of titanium - New possibilities for severe wear loaded components in medicine," *MATERIALWISSENSCHAFT UND WERKSTOFFTECHNIK*, **32**(2), pp. 160–165.

[104] Abboud, J. H., A. F. Fidel, and K. Y. Benyounis (2008) "Surface nitriding of Ti-6Al-4V alloy with a high power CO2 laser," *Optics & Laser Technology*, **40**, pp. 405–414.

[105] Weerasinghe, V. M., D. R. F. West, and J. deDamborenea (1996) "Laser surface nitriding of titanium and titanium alloy," *Journal of Materials Processing Technology*, **58**, pp. 79–86.

[106] Chen, X., G. Wu, R. Wang, W. Guo, J. Yang, X. Chen, G. Wu, R. Wang, W. Guo, and J. Yang (2007) "Laser nitriding of titanium alloy in the atmosphere environment," *Surface and Coatings Technology*, **201**(9-11), pp. 4843–4846.

[107] Thomann, A. L., E. Sicard, C. Boulmer-Leborgne, C. Vivien, J. Hermann, C. Andreazza-Vignolle, P. Andreazza, and C. Meneau (1997) "Surface nitriding of titanium and aluminium by laser-induced plasma," *Surface and Coatings and Technology*, **97**, pp. 448–452.

[108] Nwobu, A. I. P., R. D. Rawlings, and D. R. F. West (1999) "Nitride formation in titanium based substrates during laser surface melting in nitrogen-argon atmospheres," *ACTA MATERIALIA*, **47**(2), pp. 631–643.

[109] Raaif, M., F. M. El-Hossary, N. Z. Negm, S. M. Khalil, A. Kolitsch, D. Hche, J. Kaspar, S. Mandl, and P. Schaaf (2008) "CO2 laser nitriding of titanium," *Journal of Physics D: Applied Physics*, **41**(8), p. 085208.

[110] Selamat, M. S., T. N. Baker, and L. M. Watson (2001) "Study of the surface layer formed by the laser processing of Ti-6Al-4V alloy in a dilute nitrogen envirnment," *Journal of Materials Processing Technology*, **113**, pp. 509–515.

[111] Kloosterman, A. B. and J. T. M. DeHosson (1995) "Microstructural characterization of laser nitrided titanium," *Scripta Metallurgica et Materialia*, **33**(4), pp. 567–573.

[112] Mridha, S. and T. N. Baker (1998) "Effects of nitrogen gas flow rates on the and properties of laser-nitrided IMI318 titanium alloy (Ti-4V-6Al)," *Journal of Materials Processing Technology*, **77**, pp. 115–121.

[113] Yilbas, B. S., M. Sunar, Z. Gasem, and B. J. A. Aleem (2009) "Laser gas assisted nitriding and TiN coating of Ti6Al4V alloy: Experimental and numerical investigation of mechanical properties," *Journal of Materials Processing Technology*, **209**(3), pp. 1199–1208.

[114] Santos, E. C., M. Morita, M. Shiomi, K. Osakada, and M. Takahashi (2006) "Laser gas nitriding of pure titanium using CW and pulsed Nd:YAG lasers," *Surface & Coatings Technology*, **201**(3-4), pp. 1635–1642.

[115] Carpene, E., P. Schaaf, M. Han, K. P. Lieb, and M. Shinn (2002) "Reactive surface processing by irradiation with excimer laser, Nd : YAG laser , free electron laser and Ti : sapphire laser in nitrogen atmosphere," *Applied Surface Science*, **186**(1-4), pp. 195–199.

[116] Dai, J. J. and S. Q. Hou (2009) "Laser Gas Nitriding Of Titanium And Titanium Alloys," *Surface Review and Letters*, **16**(9), p. 789796.

[117] D'Anna, E., M. L. Giorgi, G. Leggieri, A. Luches, M. Martino, A. Perrone, I. N. Mihailescu, P. Mengucci, and A. V. Drigo (1992) "Oxidation interference in direct laser nitridation of titanium: relative merits of various ambient gases," *Thin Solid Films*, **213**(2), pp. 197–204.

[118] Höche, D., M. Shinn, S. Mller, and P. Schaaf (2009) "Diffusion, convection, and solidification in cw-mode free electron laser nitrided titanium," *Journal of Applied Physics*, **105**(8), p. 083503.

[119] Höche, D., M. Shinn, J. Kaspar, G. Rapin, and P. Schaaf (2007) "Laser pulse structure dependent texture of FEL synthesized TiNx coatings," *Journal of Physics D: Applied Physics*, **40**(3), pp. 818–825.

[120] Höche, D. and P. Schaaf (2011) "Laser nitriding: investigations on the model system TiN. A review," *Heat and Mass Transfer*, **47**(5), pp. 519–540.

[121] Jianglong, L., L. Qiquan, and Z. Zhirong (1993) "Laser gas alloying of titanium alloy with nitrogen," *Surface and Coatings Technology*, **57**, pp. 191–195.

[122] Mridha, S. and T. N. Baker (1994) "Crack-Free Hard Surfaces Produced By Laser Nitriding of Commercial Purity Titanium," *Material Science and Engineering: A*, **188**(1-2), pp. 229–239.

[123] ——— (1991) "Characteristic features of laser-nitrided surfaces of two titanium alloys," *Materials Science and Engineering: A*, **142**(1), pp. 115–124.

[124] Yu, H., F. Sun, and J. Zhang (2009) "Laser and plasma nitriding of titanium using CW-CO2 lasers in the atmosphere," *Current Applied Physics*, **9**, pp. 227–233.

[125] Thomann, A. L., C. Boulmer-Leborgne, C. Andreazza-Vignolle, P. Andreazza, J. Hermann, and G. Blondiaux (1996) "Metal surface nitriding by laser-induced plasma," *Journal of Applied Physics*, **80**(8), pp. 4673–4684.

[126] Thomann, A. L., J. Hermann, and C. Boulmer-Leborgne (1994) "TiN layer synthesis by laser-plasma," *Thin Solid Films*, **241**(1-2), pp. 39–43.

[127] Akarapu, R. K., P. Dua, A. Campbell, D. Scott, A. Nassar, J. Todd, and S. Copley (2008) "Characterization of Spectral Emissions from Laser Irradiated Titanium," *Materials Research Society Symposium Proceedings*, **1040**, pp. 25–30, boston, MA.

[128] Nielsen, P. E. (1979) "High-intensity laser-matter coupling in a vacuum," *Journal of Applied Physics*, **50**, pp. 3938–3943.

[129] Liu, J., F. Sun, and H. Yu (2005) "Nitridation of iron by the mixing technology with laser and plasma beams," *Applied Surface Science*, **252**, pp. 921–928.

[130] Moulder, J. F., W. F. Stickle, P. E. Sobol, and K. D. Bomben (1995) *Handbook of X Ray Photoelectron Spectroscopy: A Reference Book of Standard Spectra for Identification and Interpretation of Xps Data*, Physical Electronics, Eden Prairie, MN.

[131] Saha, N. C. and H. G. Tompkins (1992) "Titanium nitride oxidation chemistry: An x-ray photoelectron spectroscopy study," *Journal of Applied Physics*, **72**(7), pp. 3072–3079.

[132] Hofmann, S. (1986) "Characterization of nitride coatings by Auger electron spectroscopy and X-ray photoelectron spectroscopy," *Journal of Vacuum Science & Technology A: Vacuum, Surfaces, and Films*, **4**(6), pp. 2789–2796.

[133] Porte, L., L. Roux, and J. Hanus (1983) "Vacancy effects in the x-ray photoelectron spectra of TiNx," *Physical Review B (Condensed Matter)*, **28**(6), pp. 3214–3224.

[134] Arora, A., G. G. Roy, and T. DebRoy (2009) "Unusual wavy weld pool boundary from dimensional analysis," *Scripta Materialia*, **60**(2), pp. 68–71.

[135] Copley, S. M., D. G. Beck, O. Esquivel, and M. Bass (1981) "Solidification of continuous laser melted trails," in *Proceedings of a Symposium held at the 110th AIME Annual Meeting*, vol. Lasers in Metallurgy, pp. 11–19.

[136] Dickerman, P. J. and W. Deuel (1965) "Technique for Measuring Self-Absorption of Spectral Lines in Plasmas," *Review of scientific instruments*, **35**(8), pp. 978–981.

[137] Devoto, R. S. (1967) "Transport coefficients of partially ionized argon," *The Physics of Fluids*, **10**(3), pp. 354–364.

Vita

Abdalla Ramadan Nassar

Abdalla Ramadan Nassar was born in El-Mahalla El-Kubra, Egypt in April of 1986 to Rakia Saleh and Ramadan Nassar. At the age of seven, Abdalla was lucky enough to have moved with his family to Bloomsburg, "the only incorporated TOWN in Pennsylvania." He attend the Central Columbia school district until graduating from high school in 2004. After high school, Abdalla studied engineering at the Hazleton commonwealth campus of Penn State University for two years before transferring to the University Park campus in his junior year. While at the Hazleton campus, Abdalla was awarded the President's Freshman Award, the President Sparks Award and the Scholar's Lion Award. He also became a member of the Schreyer Honors College in 2006. As an undergraduate at the University Park campus, Abdalla earned the Evan Pugh Scholar Award and became a member of Tau Beta Pi, the oldest engineering honor society in the United States.

Abdalla earned a Bachelor of Science degree, with highest honors, in Engineering Science from the Department of Engineering Science and Mechanics and the Schreyer Honors College in the spring of 2008. That same year, he received the Kerns/McNitt Award, for service to the department, and served as the Student Marshall for his graduating class.

As a graduate student, Abdalla studied laser–materials interactions, with special emphasis on the role of plasma, and played an active role in the Engineering Science Graduate Student Council, where he held the offices of President (2009-2010), Outreach Director (2010-2011) and Treasurer (2011-2012). In 2009 he was awarded a National Science Foundation Graduate Research Fellowship. In addition to numerous conference presentations, Abdalla's publications include

- Nassar A R, Akarapu R, Copley S M, and Todd J A 2012 *Investigations of laser-sustained plasma and its role in laser nitriding of titanium* Journal of Physics D, Applied Physics **45** 185401

- Francis A, Nassar A R and Mehta K *Are we formal yet? The evolving role of informal lending mechanisms to support entrepreneurship and poverty alleviation in central Kenya* International Journal of Social Entrepreneurship and Innovation **(Accepted 2012)**

- Akarapu R, Nassar A R, Copley S M, and Todd J A 2009 *Numerical model of a laser-sustained argon plasma* Journal of Laser Applications **21** 169-75

- Akarapu, R K, Dua, P, Campbell, A, Scott, D, Nassar, A, Todd, J A and Copley, S M 2007 *Characterization of Spectral Emissions from Laser Irradiated Titanium* Materials Research Society Proceedings **1040-Q08-02**.